Schweizerische Eidgenossenschaft
Confédération suisse
Confederazione Svizzera
Confederaziun svizra

Failure Behaviour of Cantilever Retaining Walls

Soil-Retaining Wall Interaction

Bruchverhalten von Winkelstützmauern

Boden-Wand Interaktion

Comportement de rupture des murs de soutènement à semelles

Intéraction sol-mur

**ETH Zürich
David Perozzi
Prof. Dr. Alexander Puzrin**

Schweizerische Eidgenossenschaft
Confédération suisse
Confederazione Svizzera
Confederaziun svizra

Failure Behaviour of Cantilever Retaining Walls

Soil-Retaining Wall Interaction

Bruchverhalten von Winkelstützmauern

Boden-Wand Interaktion

Comportement de rupture des murs de soutènement à semelles

Intéraction sol-mur

ETH Zürich
David Perozzi
Prof. Dr. Alexander Puzrin

Impressum

Forschungsstelle und Projektteam
Projektleitung
Prof. Dr. Alexander Puzrin

Mitglied
David Perozzi

Begleitkommission
Präsident
Dr. Hansrudolf Ganz

Mitglieder
Stéphane Cuennet
Dr. Armand Fürst
Dr. Eckart Hars
Fritz Ruchti

KO-Finanzierung des Forschungsprojekts
Bundesamt für Verkehr
Institut für Geotechnik, ETH Zürich

Antragsteller
Arbeitsgruppe Brückenforschung (AGB)

Bezugsquelle
Das Dokument kann kostenlos von http://www.mobilityplatform.ch heruntergeladen werden.

Inhaltsverzeichnis

Summary

The current state of preservation of cantilever retaining walls has attracted considerable attention in the last decade in Switzerland, as destructive tests have detected strongly localised corrosion of the main reinforcement in many walls built in the 1970s. This has been identified as a potential threat that could lead to an unpredictable brittle collapse of the wall, which may cause severe damage to high-traffic roads and even victims. Typically, retaining walls are designed to withstand active earth pressure. This condition implicitly presupposes certain soil deformations, which require the wall to have a sufficient rotation capacity. However, corrosion damage can significantly reduce structural rotation capacity. Therefore, quantifying the earth pressure acting on corrosion-damaged cantilever retaining walls is essential to assess their safety reliably. This work studies the evolution of the earth pressure as a function of corrosion-driven wall displacement. Analytical, numerical, and experimental analyses are performed to quantify the history of earth pressure, from the construction of the wall to the moment of possible corrosion-induced collapse. The obtained results are generally valid for any problem involving the same failure mode as that resulting from a corrosion of the main reinforcement.

The relevant failure mode is identified as a rigid-body rotation around its toe. The limit load is determined using a static and a kinematic solution based on the limit analysis theorems and compared to conventional design methods. This failure mode is further analysed in scaled experiments, where different initial conditions and soil parameters are investigated. Loose, contractive soil requires much larger rotations to reach the residual state than dense soil. In addition, the unloading process is influenced by the initial stress state in the backfill. In uncompacted soil, the initial earth pressure is bilinearly distributed, whereas higher stresses are measured close to the soil surface in statically compacted samples. Slightly larger wall rotations are required to reach the active state in compacted backfills.

By imposing the rotation of a single wall section, it is shown how an inhomogeneous distribution of the corrosion degree over the wall length can lead to a decreased limit load on the failing wall section due to the stress redistribution occurring in the backfill. Consequently, neighbouring sections must withstand increased loads.

A numerical framework for quantifying the earth pressure on cantilever retaining walls is developed based on experimental observations and widely known constitutive laws to guarantee practical applicability. The framework is generally applicable and provides reliable results as it is validated using experimental data. The material behaviour is calibrated through virtual element tests performed using the Level Set Discrete Element Method. In plane strain tests, the mobilised soil strength is higher than in triaxial tests, which confirms the experimental observations.

Furthermore, the Level Set Discrete Element Method is used to analyse the earth pressure coefficient at rest, showing a correlation between the coefficient and the peak friction angle, which does not imply causation.

Then, the developed numerical models are applied to some case studies. Taking into account a more accurate structural model, it is apparent that actions and reactions can be decoupled to assess the safety of walls, as the precise modelling of the elastoplastic wall behaviour does not significantly influence the earth pressure. Furthermore, the effects of cyclic atmospheric temperature changes are simulated and discussed, considering the implications for wall monitoring.

Finally, a verification procedure for cantilever retaining walls is proposed, considering the wall and soil behaviour.

Zusammenfassung

Der aktuelle Erhaltungszustand von Winkelstützmauern hat in den letzten zehn Jahren in der Schweiz grosse Aufmerksamkeit erregt, da bei zerstörenden Prüfungen in vielen Mauern, die in den 1970er Jahren gebaut wurden, eine stark lokalisierte Korrosion der Hauptbewehrung festgestellt wurde. Dies wurde als potenzielle Gefährdung erkannt, die zu einem unvorhersehbaren spröden Versagen der Mauer führen kann, was schwere Schäden an stark befahrenen Strassen und sogar Opfer verursachen kann. Den Untersuchungen zufolge ist eine schlechte Betonqualität (die zur Bildung von Kiesnester führt) die Hauptursache für die Korrosion, die sich direkt über der Konstruktionsfuge zwischen der Bodenplatte und die Wand befindet. Die Korrosion führt zu einem Querschnittsverlust, der in der Regel auf einige Zentimeter über die Länge der Stäbe begrenzt ist. Diese lokale Verschlechterung stellt eine Schwachstelle in der Hauptbewehrung dar, die zu einem lokalen Spannungszuwachs und damit zu einer erhöhten Dehnung und Wandverschiebung führt. Unter diesen Umständen kann die Entwicklung eines plastischen Gelenks an der Arbeitsfuge angenommen werden, die zu einer korrosionsbedingten Wandrotation und zu einer Bodenentlastung führt.

Üblicherweise werden Stützmauern so bemessen, dass sie dem aktiven Erddruck widerstehen. Diese Bedingung setzt implizit bestimmte Bodenverformungen voraus, die eine ausreichende Rotationskapazität der Wand erfordern. Korrosionsschäden können jedoch die Rotationskapazität der Struktur stark verringern. Daher ist die Quantifizierung des Erddrucks, der auf korrosionsgeschädigte Winkelstützmauern einwirkt, von entscheidender Bedeutung, um deren Sicherheit zuverlässig zu bewerten.

Aufgrund des potenziell spröden Versagensverhaltens ist die Anwendbarkeit der Beobachtungsmethode fragwürdig, da vor dem Einsturz nur geringe Wandverschiebungen auftreten können. Darüber hinaus ergeben sich bei der statischen Überprüfung von Stützmauern häufig Schwierigkeiten aufgrund fehlender statischer und geotechnischer Unterlagen. Ausserdem ist es schwierig, den aktuellen Zustand der Hauptbewehrung mit zerstörungsfreien Prüfungen zu untersuchen, da sie sich auf der Seite der Hinterfüllung befindet. Aus diesen Gründen sind zuverlässige und prädiktive Modelle erforderlich, um die Sicherheit bestehender Mauern zu beurteilen und Sicherheits- und Verstärkungsmassnahmen zu planen. Aus diesem Grund hat das ASTRA eine Ausschreibung für Forschungsprojekte lanciert, die zu besseren Erkenntnissen über den aktuellen Erhaltungszustand von Stützmauern führen sollen.

Das vorliegende Forschungsprojekt untersucht die Entwicklung des Erddrucks in Abhängigkeit der korrosionsbedingten Wandverschiebung. Es werden analytische, numerische und experimentelle Analysen durchgeführt, um den Verlauf des Erddrucks von der Konstruktion der Mauer bis zum Zeitpunkt eines möglichen korrosionsbedingten Einsturzes zu quantifizieren. Die erzielten Ergebnisse gelten im Allgemeinen für jedes Problem, bei dem der gleiche Versagensmodus wie bei einer Korrosion der Hauptbewehrung auftritt.

Die Hauptziele dieser Arbeit sind:

1. Die Identifizierung des relevanten Bodenversagensmodus für durch Korrosion geschädigten Stützmauern und die Definition der einwirkenden Lasten im Grenzzustand der Tragfähigkeit;

2. Die Durchführung einer umfassenden experimentellen Studie, die es ermöglicht, die wichtigsten Einflussparameter auf die Entwicklung des Erddrucks zu ermitteln;

3. Die Entwicklung numerischer Modelle zur Simulation der korrosionsbedingten Wandentlastung, wobei die genaue Modellierung der Boden-Wand-Interaktion und des Bodenentlastungsverhaltens im Vordergrund steht;

4. Quantifizierung möglicher dreidimensionaler Auswirkungen auf die Grenzbelastung; und

5. Die möglichen Anwendungen der entwickelten Modelle für die Sicherheitsbewertung und Überwachung bestehender Bauwerke aufzuzeigen.

Der Schwerpunkt der vorliegenden Arbeit liegt auf körnigen Böden. Bodenarten, die als Hinterfüllung von Wänden in Frage kommen, werden als körnige Böden eingestuft, die in

der Regel eine sehr geringe bis keine Kohäsionsfestigkeit aufweisen. Mit anderen Worten, die Festigkeit von körnigen Böden ist nicht durch Kohäsion aufgrund von van der Waals-Wechselwirkungen wie bei Ton gekennzeichnet. Stattdessen wird die Kohäsion, die manchmal im Labor an körnigen Proben gemessen wird, ausschliesslich von den Saug-kräften gegeben, die sich aus der natürlich vorhandenen Feuchtigkeit im Boden ergeben. Daher ist diese Kohäsion stark vom Feuchtigkeitsgehalt abhängig, der wiederum von Fak-toren wie der geografischen Lage und dem Klima abhängt, und sollte bei der Bemessung und Überprüfung der Wände nicht berücksichtigt werden.

Erddrucktheorien und übliche Bemessungsmethoden

Die Kenntnis der herkömmlichen Methoden zur Bemessung von Stützmauern ist für die Beurteilung ihrer Sicherheit und Stabilität von wesentlicher Bedeutung, da sie einen Ein-blick in die Perspektive des Planers und eine Abschätzung der Tragfähigkeit einer Mauer im Falle fehlender Bauwerksakten ermöglicht. Aus diesem Grund werden in Abschnitt 2 die üblichsten Erddrucktheorien und historischen Bemessungsmethoden für Winkelstützmau-ern beschrieben.

Die Grössenordnung des Erddrucks, der auf eine Wand wirkt, hängt unter anderem von der Wandverschiebung ab und wird durch zwei Werte begrenzt: den aktiven und den pas-siven Erddruck. Diese beiden Werte werden bei einer bestimmten Wandverschiebung er-reicht, die eine vollständige Mobilisierung der Scherfestigkeit der Hinterfüllung bewirkt. Wenn keine Wandverschiebung auftritt, wirkt der initiale Erddruck auf die Wand. In der Ingenieurpraxis wird häufig angenommen, dass der initiale Erddruck dem Erdruhedruck entspricht. In Wirklichkeit handelt es sich bei der Hinterfüllung einer Stützmauer um einen gestörten Boden, derer initiale Horizontalspannung von vielen Faktoren abhängt, wie z. B. dem Grad der Verdichtung und der Wandreibung.

In der Vergangenheit wurden verschiedene Theorien zur Bestimmung des Erddrucks vor-geschlagen. Die Coulomb'sche Lösung wird beispielsweise in der Praxis immer noch häu-fig für die Bestimmung des aktiven Erddrucks verwendet. Coulomb setzte der Einfachheit halber der Bruchfläche in der Hinterfüllung als eine Ebene voraus und vernachlässigte zu-nächst die Wandreibung. Somit löste er die globalen Gleichgewichtsgleichungen für einen Bruchkeil, um den aktiven Erddruck zu ermitteln. Seine Theorie wurde später weiterentwi-ckelt, um eine geneigte Hinterfüllung und andere Randbedingungen zu berücksichtigen. Später schlug Poncelet ein grafisches Verfahren zur Bestimmung des Coulomb'schen Erddrucks vor. Verbesserte Lösungen für den aktiven Erddruck wurden dann von Boussi-nesq, Caquot und Kérisel sowie von Sokolovskii vorgeschlagen. Sie berücksichtigten näm-lich gekrümmte Versagenslinien, die eine höhere Genauigkeit im Falle einer endlichen Wandreibung ermöglichten.

Mit der Einführung neuer Bautechniken und Materialien wie Stahlbeton begannen die Bau-ingenieure, die Bemessung von Stützmauern zu optimieren, um die Zugfestigkeit der ein-gesetzten Baustoffe voll auszunutzen. Diese Optimierung führte dazu, dass leichtere und schlankere Winkelstützmauern bemessen wurden. Einer der bedeutendsten Beiträge zur Bemessung von Winkelstützmauern wurde 1925 von Mörsch veröffentlicht. Seine Arbeit basierte auf den Theorien von Coulomb, Poncelet und Rankine und stützte sich auf die in kleinmassstäblichen Experimenten gesammelten Erkenntnisse, in denen er die Versa-gensmechanismen untersuchte, die durch eine horizontale Wandbewegung (d. h. eine Starrkörpertranslationsbewegung) in der Hinterfüllung von Winkelstützmauern ausgelöst werden. Mörsch entwickelte ein Berechnungsmodell für die Bestimmung des auf die Wände wirkenden Erddrucks. Seine Methode wurde in der Vergangenheit häufig für die Bemessung von Stützmauern verwendet.

Die konventionelle Bemessungsmethode, die in der Praxis üblich für Stützmauern einge-setzt wurde, wird in Abschnitt 2 beschrieben. Sie betrachtet entkoppelte Systeme, bei de-nen die Einwirkungen und die Widerstände aus dem Boden separat bestimmt werden, wo-bei die Kinematik des Gesamtsystems vernachlässigt wird.

Der Grenzzustand der Tragsicherheit von korrosionsbeschädigten Winkelstützmauern

In Abschnitt 3 werden zunächst verschiedene Versagensarten von Winkelstützmauern vorgestellt und diskutiert. Bei einem geotechnischen Bauwerk sind mehrere Versagensarten möglich. Sie lassen sich in zwei Kategorien einteilen: geotechnische Versagensarten und strukturelle Versagensarten. Geotechnisches Versagen kann global oder lokal auftreten. Ein globales Versagen bedeutet ein Versagen der Böschung, während ein lokales Versagen als reines Gleiten oder als Kombination von Gleiten und Grundbruch auftritt. Strukturelles Versagen kann als Scher- oder Biegeversagen der Wand auftreten. In dieser Arbeit wird der Schwerpunkt auf das durch Korrosion der Bewehrung induzierte Strukturversagen gelegt, bei dem das Biegeversagen massgebend ist. Infolge der Korrosion der Stäbe, die an der Arbeitsfuge lokalisiert ist, entsteht ein plastisches Gelenk. Dadurch rotiert die vertikale Wand um die Arbeitsfuge und die Hinterfüllung versagt. Jede Versagensart ist durch eine andere Kinematik gekennzeichnet, die zu unterschiedlichen Erddrücken auf die Wand führt. Aus diesem Grund ist es wichtig, für jede Bemessungssituation den richtigen Versagensmodus zu berücksichtigen.

Danach wird eine Grenzlösung auf der Grundlage der Plastizitätstheorie entwickelt. Die Lösung bietet dem Ingenieur ein ausgezeichnetes Werkzeug, um numerische Lösungen zu überprüfen und die Sicherheit und den Entwurf bestehender Bauwerke zu beurteilen. Es wurde dann gezeigt, dass das Problem einer Drehung um den Wandfuss für die relevantesten Parameterbereiche einer Wandtranslation entspricht (aus Sicht der Grenzlast). Darüber hinaus lieferte der entwickelte Einkeilmechanismus häufig eine ausreichend genaue Lösung. Das bedeutet, dass Wände, die unter der Annahme des aktiven Coulomb'schen Erddrucks bemessen wurden, richtig bemessen waren. Es hat sich gezeigt, dass die vorgeschlagene Lösung im Allgemeinen die exakte Lösung präzise eingrenzt. Die entwickelte statische Lösung ist in der Anwendung nicht komplizierter als die Coulombsche Lösung und kann in der Praxis mühelos eingesetzt werden. Ihr Vorteil ist, dass sie näher an der sicheren Seite liegt. Anschliessend wurden die Auswirkungen der Dilatanz diskutiert. Nicht assoziiertes Fliessen führt zu einer Dehnungslokalisierung und einer höheren Grenzlast (laut der Plastizitätstheorie). Darüber hinaus wurde beobachtet, dass die Neigung der Scherbänder vom Dilatanzwinkel abhängt. In Finite-Elemente-Berechnungen wurde die höhere Grenzlast nur bei ausreichend feinen Mesh erreicht, während gröbere Mesh den gleichen Grenzzustand wie bei der Annahme der assoziierten Fliessregel erreichten. Somit wurde gezeigt, dass das Problem "kinematisch uneingeschränkt" ist. Nämlich ist der versagende Boden frei, der Wandbewegung folgend und in Richtung der Bodenoberfläche zu "fliessen". Daher behindert kein kinematischer Zwang eine Volumenausdehnung und die Dilatanz beeinflusst in diesem Sinne die Grenzlast nicht weiter. Für praktische Zwecke wurde gezeigt, wie die nach konventionellen geotechnischen Verfahren abgeleitete Festigkeit direkt in die Lösungen der Grenzanalyse oder für Finite-Elemente-Berechnungen verwendet werden kann. In letzterem Fall ist bei der Wahl der Meshgrösse Vorsicht geboten.
Schliesslich werden die konventionellen Methoden auf der Grundlage der neu gewonnenen Erkenntnisse überprüft. Es wurde gezeigt, dass unterschiedliche Annahmen oft zu konservativeren Kräften führen als die genauere Lösung der Grenzwertanalyse, was zu höheren Sicherheitsreserven gegen Biegeversagen führt.

Um die innere Tragsicherheit von Winkelstützmauern zu bemessen und nachzuweisen, muss also ein plastisches Gelenk in der Struktur berücksichtigt werden. Das am plastischen Gelenk im Grenzzustand wirkende Moment kann nach dem folgenden Verfahren berechnet werden:

1. Bestimmung der Wandgeometrie, der Bodenparameter und der Reibung an der Wandoberfläche.
2. Bestimmung des im Grenzzustand wirkenden Moments mit Hilfe von Gleichung (3.17) (kinematische Lösung) oder den Gleichungen (3.31) und (3.41) (statische Lösung).

Alternativ kann der aktive Erddruck nach Coulomb entlang der Wandhöhe integriert werden. Die kinematische Lösung entspricht der Coulomb'schen Lösung und liegt auf der unsicheren Seite (allerdings mit einem oft vernachlässigbaren Fehler). Der so ermittelte Wert

kann zur Beurteilung der Sicherheit von Winkelstützmauern oder zum Benchmarking von Finite-Elemente-Berechnungen verwendet werden.

Korrosionsbedingte Wandentlastung

In Abschnitt 4 wird der korrosionsbedingte Entlastungsprozess von Winkelstützmauern qualitativ beschrieben. Es wird gezeigt, wie sich der Erddruck vom Bau der Wand bis zu ihrem Lebensende unter Berücksichtigung von Korrosionsschäden entwickelt. Korrosion führt zu einem Festigkeitsverlust und einer Abnahme der Rotationskapazität der Wände. Aus diesem Grund kann die Wand versagen, bevor die Hinterfüllung vollständig bis zum aktiven Zustand entlastet werden kann, was die Wichtigkeit der Untersuchung des vollständigen Entlastungsprozesses zwischen dem Ausgangszustand und dem Bodenversagen hervorhebt.

Eine qualitative Analyse der Boden-Wand-Interaktion zeigt, wie sich das Bodenversagen in einer Hinterfüllung mit einer anfänglichen linearen Spannungsverteilung von oben nach unten ausbreitet. In den ersten Phasen der Entlastung stützt die Wand den nachgebenden Boden und erzeugt einen Bogeneffekt, der später verschwindet, wenn der Grenzzustand erreicht ist. Die Spannungsverteilung zum Zeitpunkt des Versagens ist linear, wie es die Lösung der Grenzwertanalyse in Abschnitt 3 vorhersagt.

Schliesslich zeigt eine begrenzte parametrische Studie die einflussreichsten Parameter für das Entlastungsverhalten des Bodens. Die wichtigsten Parameter sind die Steifigkeit und die Festigkeit des Bodens (im Allgemeinen das elastoplastische Bodenverhalten) und der anfängliche Spannungszustand. Diese Ergebnisse werden im folgenden Abschnitt bei der Konstruktion des Versuchsaufbaus berücksichtigt.

Experimentelle Untersuchung des korrosionsbedingten Wandentlastungsprozesses: Aufbau und Programm

Die Bemessung des Versuchsaufbaus und das Versuchsprogramm werden in Abschnitt 5 vorgestellt. Zunächst werden die Merkmale der Versuchsvorrichtungen vorgestellt, wobei aufgezeigt wird, welche Anforderungen zu der gewählten Konstruktion führten. Es wurden zwei Arten von Wänden gebaut und verwendet: eine flexible Winkelstützmauer und eine sehr steife Stahlwand. Anschliessend werden die Materialparameter aufgeführt.

Schliesslich wird das Versuchsprogramm dargestellt. Die Wände werden zunächst hinterfüllt; dann wird eine Drehung der vertikalen Wand aufgezwungen. Das daraus resultierende Momenten-Rotations-Verhalten wird zusammen mit anderen Grössen überwacht. Bei einigen Versuchen wird die Hinterfüllung der Wände zusätzlich statisch verdichtet, um die Effekte von erhöhten initialen Spannungen zu untersuchen. Darüber hinaus wird die Erddruckverteilung auf der sehr steifen Stahlwand untersucht.

Experimentelle Untersuchung des korrosionsbedingten Wandentlastungsprozesses: Ergebnisse

In Abschnitt 6 werden die Ergebnisse einer experimentellen Studie über den auf korrosionsgeschädigte Winkelstützmauern wirkenden Erddruck vorgestellt. Die wichtigsten Einflussparameter, d. h. der Initialspannungszustand und das elastoplastische Bodenverhalten, werden in einem skalierten Versuchsaufbau untersucht. Die Zuverlässigkeit und Wiederholbarkeit der erzielten Ergebnisse werden auf verschiedene Weise nachgewiesen.

Zunächst wird die vollständige Entwicklung des Erddrucks über die gesamte Lebensdauer einer Wand, von ihrer Herstellung bis zum Versagen der Struktur aufgrund von Korrosionsschäden, erklärt. Wenn der Boden ohne Verdichtung eingebracht wird, ergibt sich am Ende der Hinterfüllung eine bilineare Erddruckverteilung. In lockeren Böden wurden höhere Drücke gemessen als in dicht gelagerten Böden, was auf die langsamere Mobilisierung der Festigkeit in lockeren Böden zurückzuführen ist. Eine Drehung der Wand um ihren Fusspunkt führte zu einer Entlastung des Bodens und damit zu einer Verringerung des auf die Wand wirkenden Drucks. Es wird das typische Verhalten von lockerem, kontraktantem und

dichtem, kontraktantem-dilatantem Boden beobachtet, wobei das Moment in der dichten Probe bei einer Drehung von etwa 5-10 mrad ein Minimum erreicht, bevor es aufgrund der Entfestigung des Bodens zunimmt. Im Gegensatz dazu nimmt das Moment in der lockeren Probe monoton und langsamer ab. Darüber hinaus werden in beiden Proben Stick-Slip-Ereignisse beobachtet, die beschrieben und deren Ursprung erklärt wird. Die erhaltenen Erddruckkoeffizienten bei aktivem Versagen sind relativ niedrig, was auf eine hohe Festigkeit hindeutet, die durch die im Labor durchgeführten Triaxialversuche nicht erklärt werden kann.

Ferner werden verdichtete Proben hergestellt, indem nach dem Aufbringen der einzelnen Schichten eine statische Last auf die Bodenoberfläche aufgebracht wird. Im Vergleich zu den unverdichteten Proben wird am Ende der Hinterfüllungsphase ein höherer Spannungszustand festgestellt. Insbesondere ergibt sich eine andere Erddruckverteilung, die durch einen Maximalwert im oberen Teil der Hinterfüllung gekennzeichnet ist. Infolgedessen wirkte die resultierende Erddruckkraft an einer höheren Stelle. Aus diesem Grund und wegen der höheren Bodensteifigkeit war das Moment-Rotations-Verhältnis der verdichteten Proben durch eine steile Entlastung gekennzeichnet, obwohl etwas grössere Rotationen als für unverdichtete Proben erforderlich sind, um aktives Versagen zu erreichen. Im Allgemeinen ist das Verhalten der verdichteten Proben dem der unverdichteten Proben ähnlich.

Im Weiteren wird das Entlastungsverhalten von unverdichteten Proben für dreidimensionale Bedingungen untersucht. Die Situation eines einzelnen korrodierten Wandabschnitts wird getestet, indem nur der mittlere Wandabschnitt gedreht wird. In der Hinterfüllung kam es zu einer Spannungsumlagerung, die zu einem tieferen Grenzzustand und einem gekrümmten Versagensmechanismus führte. Infolgedessen wurde an den benachbarten Wandabschnitten eine Momentenerhöhung gemessen.

Schliesslich wird der Erddruck auf eine nahezu starre Wand während der Hinterfüllung und Verdichtung gemessen. Es wird gezeigt, dass die Wandreibung zur bilinearen Verteilung des auf reale Wände wirkenden Erddrucks beiträgt.

Numerische Analyse: Wandentlastung

In Abschnitt 7 wird ein Verfahren zur Simulation des auf beschädigte Winkelstützmauern wirkenden Erddrucks vorgestellt. Es basiert auf einem Finite-Elemente-Modell der Wand und ihrer Hinterfüllung und erfordert die Kenntnis des Spannungszustands des Bodens unter Gebrauchsbedingungen. Letztere können durch numerische Analysen (wie im folgenden Abschnitt) oder durch Annahmen aufgrund von Erfahrungen gewonnen werden. Direkte Messungen (wie sie in dieser Arbeit zur Verfügung standen) sind in der Regel nicht verfügbar und im Allgemeinen im Feld schwer zu erhalten. Das verwendete Stoffgesetz basiert auf druckabhängiger isotroper Elastizität und dem Mohr-Coulomb-Versagenskriterium. Es wurde eine eigene Verfestigungsregel auf der Grundlage von experimentellen Daten verwendet. Alternativ könnte die Verfestigungsregel des Modells "Hardening Soil" für annähernde Ergebnisse angenommen werden.

Das numerisch ermittelte Bodenverhalten wurde mit den experimentellen Ergebnissen verglichen. Die unverdichteten Proben zeigten eine ausgezeichnete Übereinstimmung, sowohl in Bezug auf die Spannung als auch auf die Verformungen. Bei den unverdichteten Proben breitet sich das Bodenversagen von oben nach unten aus. Die Genauigkeit der Lösung der Grenzanalyse wurde in diesem Abschnitt ebenfalls durch den Vergleich mit den experimentellen und numerischen Ergebnissen bestätigt. Es wurde festgestellt, dass die mit den in Abschnitt 3.3 vorgeschlagenen Lösungen erhaltene Grenzlast eine gute, konservative Abschätzung der Grenzlast im Restzustand liefert. Bei der Abschätzung des minimalen Biegemoments, das durch den Erddruck unter Annahme des maximalen Reibungswinkels entsteht, wurde hingegen ein etwas unkonservatives Ergebnis erzielt. Der Zustand, bei dem die gesamte Hinterfüllung gleichzeitig die maximale Festigkeit mobilisiert, ist nämlich nicht gegeben. Andererseits wurde bestätigt, dass die Grenzlast, die unter Annahme der nicht assoziierten Fliessregel ermittelt wurde, das Moment überschätzt, da der Reibungswinkel mit der herkömmlichen geotechnischen Methode kalibriert wurde (siehe Abschnitt 3.5.1).

Die numerische Simulation der verdichteten Versuche zeigte ebenfalls eine gute Übereinstimmung mit den experimentellen Daten. Lediglich bei der dichten Probe wurde eine leichte Unterschätzung des Moments und des Erddrucks im Verfestigungsregime beobachtet. Der Grund dafür ist vermutlich, dass der Testboden mit (fast) seiner maximalen Dichte abgelagert wurde, die durch Abscheren während des Verdichtungsvorgangs abnahm. Das vorgeschlagene Stoffgesetz betrachtet jedoch nur die Bodendichte als eine Konstante während der gesamten Analyse.

Daraus wird gefolgert, dass das vorgeschlagene numerische Modell für zuverlässige Abschätzungen des auf die beschädigten Wände ausgeübten Erddrucks verwendet werden kann. Zur Reproduktion des in den Versuchen beobachteten Stick-Slip-Effekts könnte ein Rate-and-State-Modell angenommen werden. Die Wand sollte jedoch immer in der Lage sein, einen Gleichgewichtszustand entlang der unteren Umhüllenden der Moment-Rotations-Kurve zu finden, da die Periode der Schwingungen klein ist.

Im zweiten Teil des Abschnitts wird der dreidimensionale Grenzzustand mit Hilfe der Software OptumG3 analysiert. Es zeigt sich eine gute Übereinstimmung mit den experimentellen Ergebnissen, obwohl die Dimensionen des Versagensmechanismus aufgrund der impliziten Annahme der assoziativen Fliessregel in der Grenzwertanalyse nicht perfekt übereinstimmen. Der Einfluss der assoziierte Fliessregel wird dann mit Hilfe der Finite-Elemente-Methode und eines einfachen linear-elastischen, perfekt plastischen Stoffgesetzes untersucht. Es wird gezeigt, dass assoziiertes Fliessen keinen Einfluss auf die Ergebnisse hat, da die Scherfestigkeit des Bodens unter der Annahme einer Grenzwertlösung auf die in einem Elementversuch gemessene Grenzlast zurückgerechnet wurde. Der Grund dafür ist, dass das Problem nicht kinematisch eingeschränkt ist. Wenn das Mesh in einer Finite-Elemente-Simulation jedoch fein genug ist, würde sich die Verformung in dünnen Scherbändern lokalisieren, was zu einer erhöhten Grenzbelastung führen würde. In diesem Fall sollte die Kalibrierung der Bodenfestigkeit jedoch auch die Lokalisierung der Verformung berücksichtigen.

Darüber hinaus werden die Herausforderungen bei der Modellierung dreidimensionaler Bedingungen aufgezeigt und mögliche Gegenmassnahmen vorgeschlagen.

Empfehlungen für die Praxis

Das Entlastungsverhalten der Hinterfüllung einer Wand kann mit kommerziellen Finite-Elemente-Codes wie Abaqus oder Plaxis quantifiziert werden. Während für Abaqus ein benutzerdefiniertes Stoffgesetz erforderlich ist, kann die Implementierung des "hardening soil model" von Plaxis ohne weiteres verwendet werden. Das "hardening soil model" ermöglicht eine recht genaue Modellierung des Verfestigungsverhaltens des Bodens, nicht jedoch die Modellierung der Entfestigung des Bodens, die häufig in dichten Böden beobachtet wird. Für den Nachweis von Winkelstützmauern ist die genaue Modellierung der Verfestigung jedoch wesentlich kritischer, da korrodierte Wände in der Regel nicht über eine ausreichende Rotationskapazität verfügen, damit der Boden die Entfestigungsphase erreichen kann. Wie in dieser Arbeit gezeigt wurde, ist die Modellierung der Entfestigung auch immer mit einer Meshabhängigkeit in FEM verbunden, die, wenn sie nicht korrekt berücksichtigt wird, zu fehlerhaften Ergebnissen führen kann.
Folglich sollte der Ingenieur die maximale Festigkeit von dichtem Boden vernachlässigen und das Stoffgesetz nur unter Berücksichtigung des residualen Zustands kalibrieren. In bestimmten Fällen kann jedoch eine höhere Festigkeit als die Restfestigkeit berücksichtigt werden, sofern der Spannungszustand an jedem Punkt unterhalb der maximalen Scherfestigkeit des Materials bleibt. In diesem Fall muss der Ingenieur überprüfen und nachweisen, dass die maximale Scherfestigkeit nirgendwo im Modell mobilisiert wird. Andernfalls liefert das Modell falsche Ergebnisse, und der Ingenieur erhält eine unsichere Schätzung.

Nach der korrekten Kalibrierung des Stoffgesetzes kann die Entlastung der Wand mit einem Modell ähnlich dem in Abschnitt 7.2.1 vorgestellten simuliert werden. Der initiale Spannungszustand wird entweder im Modell initialisiert (auf der Grundlage einiger Annahmen) oder direkt durch Simulation des Bauvorgangs berechnet (wie in Abschnitt 8). Möglicherweise könnte das Modell von Abschnitt 7.2.1 durch Hinzufügen einer Fundamentschicht erweitert werden, obwohl ihr Einfluss auf den Entlastungsprozess vernachlässigbar

ist. Abschliessend ist zu erwähnen, dass das Stoffgesetz in dieser Arbeit durch biaxiale Versuche kalibriert wurde. In Anhang II.2.2 wurde gezeigt, dass die Bodenfestigkeit unter ebenen Dehnungsbedingungen höher ist, was bedeutet, dass eine Kalibrierung durch Tri-axialversuche möglicherweise zu konservative Resultate führt.

Numerische Analyse: Initiale Spannungsbedingungen

Im ersten Teil von Abschnitt 8 wird eine Untersuchung des Erdruhedrucks auf der Parti-kelskala durchgeführt. Ein gutes Verständnis des Erddrucks bei eindimensionalen Verfor-mungszuständen ist eine Voraussetzung für das Verständnis des Erddrucks auf Stützmau-ern im Gebrauchszustand (d. h. nicht im Grenzzustand der Tragfähigkeit). Das numerische Modell des Anhangs II.2 wird zur Durchführung von Ödometerversuchen verwendet. Es zeigt sich, dass der Erdruhedruck-Koeffizient K_0 umgekehrt proportional zur gemittelten Koordinationszahl der Probe ist, was zu höheren Werten bei lockeren Proben führt. Ande-rerseits zeigt der Koeffizient K_0 während der Entlastung einen steileren Anstieg mit zuneh-mendem Überkonsolidierungsgrad (OCR) in dichteren Proben. Die in der Literatur häufig angenommene empirische Potenzgesetzfunktion, die den K_0-Koeffizienten von überkon-solidiertem Boden mit dem OCR in Beziehung setzt, erweist sich bei der Entlastung als vernünftige, obwohl nicht sehr genaue, Schätzung für praktische Anwendungen. Anschlies-send wurden die Kontrollparameter des Erdruhedrucks untersucht. Für normal verfestigte Böden wird keine Korrelation zwischen K_0 und den elastischen Parametern nachgewiesen, während eine gute Korrelation mit der intergranulären Reibung gefunden wurde. Folglich korreliert der Erdruhedruckkoeffizient gut mit der Höchstscherfestigkeit des Bodens, ob-wohl keine Kausalität impliziert wird. Obwohl die Formel von Jáky auf einer schwachen theoretischen Grundlage beruht, wird festgestellt, dass sie eine gute, konservative Schät-zung von K_0 für dichten Perth Sand liefert. Die durch die Formel geschätzten Werte über-schätzen die numerischen Daten für die lockere Probe, bleiben aber konservativ. Es sind jedoch weitere Untersuchungen zu anderen Kornformen erforderlich.

Im zweiten Teil des Abschnitts wird das in Abschnitt 7 eingeführte numerische Modell er-weitert, um das Konsolidierungsverhalten von Boden zu berücksichtigen und die Boden-verdichtung zu modellieren. Es werden numerische Simulationen der Wandversuche durchgeführt und die erhaltenen Ergebnisse mit den experimentellen Ergebnissen vergli-chen. Die Simulationen der unverdichteten Proben zeigten eine gute Übereinstimmung mit den Versuchsergebnissen. Die Erddruckverteilung in diesen Proben ist bilinear, gekenn-zeichnet durch einen höheren Erddruckkoeffizienten im untersten Teil der Hinterfüllung und beeinflusst durch die Wanddurchbiegungen und die Reibungsfläche. Die Simulation der verdichteten Proben führte zu einer etwas weniger genauen Vorhersage der Anfangsspan-nung, was hauptsächlich auf einige Schwierigkeiten bei der Modellierung des betrachteten Problems mit der Finite-Elemente-Methode zurückzuführen ist. Infolgedessen führten die geschätzten Drücke dazu, dass das am Wandfuss wirkende Moment im dichten Probekör-per unterschätzt und im lockeren Probekörper überschätzt wurde. Bessere Ergebnisse lies-sen sich durch den Einsatz einer meshfreien Methode erzielen. Ausserdem wird die ana-lytische Lösung von Broms verifiziert. Es zeigt sich, dass konservative Ergebnisse erzielt werden, obwohl ihre Anwendung insbesondere bei dichtem Boden wahrscheinlich zu einer zu hohen Sicherheit führen würde.

Empfehlungen für die Praxis

Die Empfehlungen des vorherigen Abschnittes gelten auch für diesen Abschnitt. Da in die-sem Abschnitt die initialen Spannungsbedingungen durch die Modellierung der Bauphasen bestimmt werden, kann jedoch die Berücksichtigung der elastoplastischen Bodenfunda-mentschicht unter der Wand die resultierende initiale Spannung der Wand beeinflussen. Während der Hinterfüllung wird sich die Wand nämlich unter dem Bodengewicht und dem Erddruck setzen, was zu einer teilweisen Entlastung der bereits abgelagerten Hinterfüllung führt. Die Vernachlässigung der Fundamentschicht führt daher zu konservativen Ergebnissen. Zweifellos kann das vorgeschlagene Stoffgesetz zur Simulation komplexerer Baupha-sen eingesetzt werden, z. B. zur Simulation eines Böschungseinschnitts, der Errichtung der Mauer und der Hinterfüllung.

Weitere Untersuchungen

In Abschnitt 9 werden verschiedene Analysen durchgeführt, um das Verständnis der Boden-Wand-Interaktion weiter zu verbessern. Zunächst wird eine Analyse des Entlastungsverhaltens unter Berücksichtigung eines verfeinerten Strukturmodells durchgeführt. Die Ergebnisse zeigen, dass das Entlastungsverhalten des Bodens nicht von der richtigen Modellierung des elastoplastischen Wandverhaltens abhängt. Tatsächlich wird die gleiche Erddruckentlastung für eine korrodierte Wand und für eine intakte Wand, der eine Drehung an ihrem Fusspunkt aufgezwungen wurde, beobachtet. Es wird also gezeigt, dass die Einwirkungen und Widerstände bei der Auswertung des Versagens korrosionsgeschädigter Wände entkoppelt werden können. Die Sicherheit der Wände kann dann durch Überlagerung der Einwirkungen und Reaktionen wie in Abbildung 63 bewertet werden.

Anschliessend wird die thermische Analyse einer bestehenden Wand durchgeführt. Auf der Grundlage frei verfügbarer meteorologischer Daten ist es möglich, das Temperaturfeld einer Stützmauer mit einer guten Genauigkeit zu simulieren. Es wird gezeigt, wie Temperaturänderungen eine zyklische Wirkung auf die Mauer haben, die zu einer zusätzlichen Verschiebung führt. Die im Feld gemessenen Wandverschiebungen können erklärt werden, wenn auch nur teilweise (da der 24-Stunden-Mittelwert berücksichtigt werden musste).

Ausserdem wird das entwickelte numerische Modell zur Simulation von Bauwerken in Originalgrösse verwendet. Es zeigt sich, dass das Entlastungsverhalten unempfindlich gegenüber den Wandabmessungen ist und dass die zuvor gemachten Aussagen für jede Wandabmessung gelten. Darüber hinaus wird der Einfluss der Neigung der Hinterfüllung untersucht. Auch in diesem Fall wird nur ein geringer Einfluss auf das Entlastungsverhalten des Bodens festgestellt.

Schliesslich wird eine Parameterstudie durchgeführt, um die Auswirkungen der Bodenreibung und der Geometrie der Wandabschnitte auf den dreidimensionalen Grenzzustand zu untersuchen. Eine höhere Reibung und höhere Wandabschnitte ermöglichen eine bessere Spannungsumlagerung in der Hinterfüllung, was zu einem niedrigeren Grenzzustand und einem höheren Anstieg des auf die benachbarten Abschnitte wirkenden Moments führt.

Sicherheitsbewertung von Winkelstützmauern

Abschnitt 10 bildet die Synthese der beiden Forschungsprojekte AGB 2015/028 *"Tragwiderstand und Verformungsvermögen von Winkelstützmauern bei lokaler Korrosion der Bewehrung"* und AGB 2015/029 *"Failure Behaviour of Cantilever Retaining Walls - Soil-Retaining Wall Interaction"* und ist in enger Zusammenarbeit erstellt worden.

Zur Überprüfung der Tragsicherheit von Stützmauern mit korrodierender Bewehrung wird eine mehrstufige Überprüfungsstrategie vorgeschlagen, bei welcher der Überprüfungsaufwand je Stufe erhöht wird. Es ist fallweise zu entscheiden, ob sich der Aufwand für eine Stufe lohnt (in Abhängigkeit des Bauwerkalters, dessen allgemeinen Zustands, übergeordneter Projektziele, des Aufwands für Verstärkungsmassnahmen und hinsichtlich Datenerhebung), oder ob direkt Verstärkungsmassnahmen oder ein Ersatzneubau geprüft werden sollen.

Zunächst wird eine Triage vorgenommen, wobei mit vereinfachten analytischen Kriterien festgestellt wird, ob sich eine genügende Tragsicherheit nachweisen lässt.
Ist dies nicht der Fall, wird eine entkoppelte Analyse durchgeführt. Hierbei werden das Last-Verformungsverhalten der Stützmauer und der Hinterfüllung getrennt voneinander ermittelt und erst für den Nachweis zusammengeführt. Auf dieser Stufe werden einfache, konservative Annahmen hinsichtlich des Korrosionsschadens getroffen. Eine möglicherweise bereits erfolgte Abnahme des Erddrucks infolge Verkippung der Stützmauer um den Fusspunkt wird vernachlässigt.
Ergibt die einfache entkoppelte Analyse eine ungenügende Tragsicherheit, kann eine verfeinerte entkoppelte Analyse mit weniger konservativen Annahmen zur Korrosionsverteilung oder der Fundationssteifigkeit durchgeführt werden, sofern entsprechende Daten mit vertretbarem Aufwand erhoben werden können.

Wenn die Möglichkeit einer Lastumlagerung in Längsrichtung besteht, beispielsweise falls nur einzelne Segmente einer dilatierten Stützmauer von Korrosion betroffen sind, kann eine gekoppelte Analyse angebracht sein. Dabei werden die Verformung der Mauer und die Reaktion des Erddrucks in jedem Berechnungsschritt unter Berücksichtigung der Boden-Bauwerks-Interaktion ermittelt, so dass der Einfluss angrenzender Segmente erfasst werden kann.

Lässt sich die Tragsicherheit auch mit einer vertieften Analyse nicht nachweisen, sind geeignete Verstärkungsmassnahmen oder ein Ersatzneubau zu planen.

Nachfolgend wird die Überprüfungsstrategie anhand eines Fallbeispiels illustriert.

Anschliessend werden einige praxisbezogene und auf den zwei Projekten basierende Bemerkungen gegeben.

Résumé

L'état de conservation actuel des murs de soutènement à semelles a suscité une grande attention en Suisse au cours des dix dernières années, car des essais destructifs ont révélé une corrosion très localisée de l'armature principale dans de nombreux murs construits dans les années 1970. Cette situation a été reconnue comme un danger potentiellement grave qui pourrait provoquer une rupture fragile et imprévisible du mur, causant ainsi de graves dommages aux routes très fréquentées, ou même des victimes. Selon les essais, la mauvaise qualité du béton (qui conduit à la formation de nids de gravier) est la principale cause de la corrosion qui se produit juste au-dessus du joint de construction entre le radier et le mur. La corrosion provoque une perte de section qui se limite généralement à quelques centimètres sur la longueur des barres. Cette détérioration locale constitue un point faible dans l'armature principale, qui génère une augmentation locale des contraintes et, par conséquent, une augmentation de la déformation et du déplacement du mur. Dans ces conditions, on peut supposer le développement d'une charnière plastique au niveau du joint de construction, ce qui cause une rotation du mur due à la corrosion et un allègement du sol.

Habituellement, les murs de soutènement sont dimensionnés pour résister à la poussée active du sol. Cette condition présume implicitement certaines déformations du sol qui exigent une capacité de rotation suffisante du mur. Cependant, les dommages causés par la corrosion peuvent réduire considérablement la capacité de rotation de la structure. Il est donc essentiel de quantifier la poussée des terres exercée sur les murs de soutènement à semelles endommagés par la corrosion afin d'évaluer leur sécurité de manière fiable.

En raison du comportement de rupture potentiellement fragile, l'applicabilité de la méthode observationnelle est discutable, car seuls de faibles déplacements de murs peuvent se produire avant l'effondrement. En outre, le contrôle statique des murs de soutènement se heurte souvent à des difficultés dues à l'absence de documents statiques et géotechniques. De plus, il est difficile d'examiner l'état actuel de l'armature principale avec des contrôles non destructifs, car elle se trouve du côté du remblai. Pour ces raisons, des modèles fiables et prédictifs sont nécessaires pour évaluer la sécurité des murs existants et planifier des mesures de sécurité et de renforcement. C'est pourquoi l'OFROU a lancé un appel à propositions pour des projets de recherche qui devraient permettre d'acquérir de meilleures connaissances sur l'état de conservation actuel des murs de soutènement.

Le présent projet de recherche étudie l'évolution de la poussée des terres en fonction du déplacement des murs dû à la corrosion. Des analyses analytiques, numériques et expérimentales sont effectuées afin de quantifier l'évolution de la poussée des terres depuis la construction du mur jusqu'au moment d'un éventuel effondrement dû à la corrosion. Les résultats obtenus s'appliquent généralement à tous les problèmes caractérisés par le même mode de rupture que celui causée par une corrosion de l'armature principale.

Les principaux objectifs de ce travail sont :

1. l'identification du mode de rupture du sol correspondant pour les murs de soutènement endommagés par la corrosion et la détermination des charges appliquées à l'état limite ultime ;

2. la conduite d'une étude expérimentale complète permettant d'identifier les principaux paramètres influençant l'évolution de la poussée des terres ;

3. le développement de modèles numériques pour simuler la décharge des murs due à la corrosion, en mettant l'accent sur la modélisation précise de l'interaction sol-mur et du comportement du sol ;

4. la quantification de possibles effets tridimensionnels sur la charge limite ; et

5. de montrer les applications possibles des modèles développés pour l'évaluation de la sécurité et la surveillance des ouvrages existants.

Le présent travail se concentre sur les sols granuleux. Les types de sols envisageables pour le remblayage des murs sont classés comme des sols granuleux, qui présentent pas de cohésion, ou très fiable. Autrement dit, la résistance des sols granuleux n'est pas caractérisée par la cohésion due aux interactions de van der Waals comme pour l'argile. Au contraire, la cohésion parfois mesurée en laboratoire sur des échantillons granulaires, est exclusivement dérivée des forces de succion résultant de l'humidité naturellement présente

dans le sol. Par conséquent, cette cohésion dépend fortement de la teneur en humidité, qui dépend elle-même de facteurs tels que la situation géographique et le climat, et ne devrait pas être prise en compte lors du dimensionnement et de la vérification des murs.

Théories de la poussée des terres et méthodes de dimensionnement conventionnelles

La connaissance des méthodes traditionnelles de dimensionnement des murs de soutènement est essentielle pour évaluer leur sécurité et leur stabilité, car elle permet de se mettre dans la perspective du planificateur et d'estimer la capacité portante d'un mur en cas d'absence de dossier de construction. C'est pourquoi la section 2 décrit les théories de la poussée des terres les plus courantes et les méthodes historiques de dimensionnement des murs de soutènement à semelles.

L'ordre de grandeur de la poussée des terres exercée sur un mur dépend notamment du déplacement du mur et est limité par deux valeurs : la poussée des terres active et la poussée des terres passive. Ces deux valeurs sont atteintes pour un déplacement du mur spécifique, qui implique une mobilisation complète de la résistance au cisaillement du remblai. S'il n'y a pas de déplacement de la structure, la poussée des terres initiale agit. Dans la pratique du génie civil, on suppose souvent que la poussée initiale des terres correspond à la poussée des terres au repos. En réalité, le remblayage d'un mur de soutènement est un sol perturbé dont la contrainte horizontale initiale dépend de nombreux facteurs, tels que le degré de compactage et le frottement du mur.

Dans le passé, plusieurs théories ont été proposées pour déterminer la poussée des terres. La solution de Coulomb, par exemple, est encore souvent utilisée dans la pratique pour déterminer la poussée des terres active. Pour simplifier, Coulomb a supposé que la surface de rupture dans le remblai était un plan et a d'abord négligé le frottement entre le sol et la structure. Il a ainsi résolu les équations d'équilibre global pour un coin de rupture afin de déterminer la poussée des terres active. Sa théorie a ensuite été développée pour tenir compte d'un remblai incliné et d'autres conditions limites. Plus tard, Poncelet a proposé une méthode graphique pour déterminer la poussée des terres de Coulomb. Des solutions améliorées pour la poussée des terres actives ont ensuite été proposées par Boussinesq, Caquot et Kérisel, ainsi que par Sokolovskii. Ils ont en effet pris en compte des lignes de rupture courbes qui permettaient une plus grande précision dans le cas d'un coefficient de friction fini de la paroi.

Avec l'introduction de nouvelles techniques de construction et de nouveaux matériaux comme le béton armé, les ingénieurs ont commencé à optimiser le dimensionnement des murs de soutènement afin d'exploiter pleinement la résistance à la traction des matériaux de construction utilisés. Cette optimisation a conduit au dimensionnement de murs de soutènement à semelles plus légers et plus minces. L'une des contributions les plus importantes au dimensionnement des murs de soutènement à semelles a été publiée en 1925 par Mörsch. Son travail était basé sur les théories de Coulomb, Poncelet et Rankine et s'appuyait sur les connaissances acquises lors des expérimentations en échelle réduite, dans lesquelles il étudiait les mécanismes de rupture provoqués par un mouvement horizontal du mur (c'est-à-dire un mouvement de translation du corps rigide) dans le remblayage des murs de soutènement à semelles. Mörsch a développé un modèle de calcul pour déterminer la poussée des terres agissant sur les murs. Sa méthode a été fréquemment utilisée dans le passé pour le dimensionnement des murs de soutènement.

La méthode de dimensionnement conventionnelle, couramment utilisée dans la pratique pour les murs de soutènement, est décrite dans la section 2. Elle considère des systèmes découplés, dans lesquels les actions et les réactions du sol sont déterminées séparément, en négligeant la cinématique globale du système.

L'état-limite ultime des murs de soutènement à semelles endommagés par la corrosion

Dans la section 3, différents types de défaillance des murs de soutènement à semelles sont tout d'abord présentés et discutés. Plusieurs types de défaillance sont possibles pour un ouvrage géotechnique. Elles peuvent être classées en deux catégories : les modes de défaillance géotechniques et les modes de défaillance structurels. La défaillance géotechnique peut être globale ou locale. Une défaillance globale implique une défaillance du talus, alors qu'une défaillance locale se présente sous la forme d'un glissement pur ou d'une combinaison entre un glissement et une défaillance de la fondation. La défaillance structurelle peut se produire en cisaillement ou en flexion du mur. Dans ce travail, l'accent est mis sur la défaillance structurelle induite par la corrosion des armatures, pour laquelle la défaillance en flexion est déterminante. Suite à la corrosion des barres, localisée au niveau du joint de travail, une charnière plastique se forme. Le mur vertical tourne alors autour du joint de construction et le remblayage est en défaillance. Chaque forme de défaillance se caractérise par une cinématique différente, qui entraîne des poussées des terres différentes sur le mur. C'est pourquoi il est important de prendre en compte le mode de rupture approprié pour chaque situation de dimensionnement.

Dans la suite de cette section, une solution limite basée sur la théorie de la plasticité est développée. Cette solution offre à l'ingénieur un excellent outil pour vérifier les solutions numériques et évaluer la sécurité et la conception des structures existantes. Il est ensuite démontré que le problème d'une rotation autour de la base du mur correspond à une translation du mur pour les domaines de paramètres les plus pertinents (du point de vue de la charge limite). En outre, le mécanisme à un seul coin proposé a généralement fourni une solution suffisamment précise. Cela signifie que les murs dimensionnés en supposant la poussée des terres active de Coulomb étaient correctement dimensionnés. Il s'est montré que la solution proposée délimite en général la solution exacte avec précision. La solution statique développée n'est pas plus compliquée à appliquer que la solution de Coulomb et peut être utilisée sans effort dans la pratique. Son avantage est qu'elle se situe plus près de la sécurité. Les effets de la dilatance ont ensuite été discutés. L'écoulement plastique non associé conduit à une localisation de la déformation et à une charge limite plus élevée (selon la théorie de la plasticité). En outre, il a été observé que l'inclinaison des bandes de cisaillement dépend de l'angle de dilatance. Dans les calculs par éléments finis, la charge limite plus élevée n'a été obtenue que pour les mesh suffisamment fins, tandis que les mesh plus larges ont atteint le même état-limite qu'en supposant la loi d'écoulement associée. D'autre part, il a été démontré que le problème est "cinématiquement illimité". En effet, le sol en défaillance est libre de "couler" en suivant le mouvement du mur et en direction de la surface du sol. Par conséquent, aucune contrainte cinématique n'empêche l'expansion du volume et la dilatance n'a donc pas d'influence supplémentaire sur la charge limite. A des fins pratiques, il a été montré comment la résistance déduite selon les méthodes géotechniques conventionnelles peut être utilisée directement dans les solutions analytiques ou pour des calculs par éléments finis. Dans ce dernier cas, il faut être prudent dans le choix de la taille du mesh.

Enfin, les méthodes conventionnelles sont réexaminées sur la base des nouvelles connaissances acquises. Il a été démontré que différentes hypothèses conduisent souvent à des forces plus conservatrices que la solution plus précise proposée dans ce travail, ce qui conduit à des réserves de sécurité plus élevées contre la défaillance en flexion.

Pour dimensionner et vérifier la sécurité structurale interne des murs de soutènement à semelles, il faut donc prendre en compte une charnière plastique dans la structure. Le moment agissant sur la charnière plastique à l'état-limite peut être calculé selon la procédure suivante :

1. Détermination de la géométrie du mur, des paramètres du sol et du coefficient de friction du mur.
2. Détermination du moment agissant à l'état-limite à l'aide de l'équation (3.17) (solution cinématique) ou des équations (3.31) et (3.41) (solution statique).

Il est également possible d'intégrer la poussée des terres active selon Coulomb le long de la hauteur du mur. La solution cinématique correspond à la solution coulombienne et se situe du côté incertain (mais avec une erreur souvent négligeable). La valeur ainsi obtenue peut être utilisée pour évaluer la sécurité des murs de soutènement à semelles ou pour évaluer les calculs par éléments finis.

Décharge des murs à cause de la corrosion

La section 4 décrit qualitativement le processus de décharge des murs de soutènement à semelles provoqué par la corrosion. Elle montre comment la poussée des terres évolue depuis la construction du mur jusqu'à sa fin de vie, en tenant compte des dommages causés par la corrosion. La corrosion entraîne une perte de résistance et une diminution de la capacité de rotation des murs. Pour cette raison, le mur peut céder avant que le remblai ne soit complètement déchargé jusqu'à l'état actif, ce qui souligne l'importance d'étudier le processus complet de décharge entre l'état initial et la défaillance du sol.

Une analyse qualitative de l'interaction sol-mur montre comment la défaillance du sol se propage de haut en bas dans un remblai avec une distribution initiale linéaire des contraintes. Dans les premières phases de la décharge, le mur soutient le sol qui cède et crée un effet d'arc qui disparaît plus tard, lorsque l'état-limite est atteint. La distribution des contraintes au moment de la défaillance est linéaire, comme le prédit la solution de l'analyse limite de la section 3.

Enfin, une étude paramétrique limitée montre les paramètres les plus influents sur le comportement de décharge du sol. Les paramètres les plus importants sont la rigidité et la résistance du sol (en général, le comportement élastoplastique du sol) et l'état de contrainte initial. Ces résultats sont pris en compte dans la section suivante lors de la construction du modèle expérimental.

Étude expérimentale du comportement du mur en cas de décharge due à la corrosion : dispositif et programme

Le dimensionnement du dispositif expérimental et le programme d'expérimentation sont présentés dans la section 5. Les caractéristiques des dispositifs expérimentaux sont d'abord présentées, en montrant quelles exigences ont conduit à la construction choisie. Deux types de murs ont été construits et utilisés : un mur de soutènement à semelles flexibles et un mur en acier très rigide. Les paramètres des matériaux sont ensuite présentés.

Enfin, le programme d'essai est présenté. Les murs sont d'abord remblayés, puis une rotation du mur vertical est imposée. La relation entre moment et rotation qui en résulte est surveillé en même temps que d'autres grandeurs. Dans certains essais, le remblayage des murs est également compacté statiquement afin d'étudier les effets de l'augmentation des contraintes initiales. En outre, la distribution de la pression des terres sur le mur en acier est étudiée.

Étude expérimentale du comportement du mur en cas de décharge due à la corrosion : résultats

La section 6 présente les résultats d'une étude expérimentale sur la poussée des terres exercée sur les murs de soutènement à semelles dégradés par la corrosion. Les principaux paramètres d'influence, notamment l'état de contrainte initial et le comportement élastoplastique du sol, sont étudiés dans un dispositif expérimental à l'échelle. La fiabilité et la répétabilité des résultats obtenus sont démontrées de plusieurs manières.

Tout d'abord, l'évolution complète de la poussée des terres sur toute la durée de vie d'un mur, depuis sa construction jusqu'à l'effondrement de la structure due aux dommages causés par la corrosion, est expliquée. Lorsque le sol est déposé sans être compacté, on obtient une répartition bilinéaire de la pression de terre à la fin du remplissage du mur. Des pressions plus élevées ont été mesurées dans les sols meubles que dans les sols denses,

ce qui s'explique par la mobilisation plus lente de la résistance dans les sols meubles. Une rotation du mur autour de son pied a entraîné un déchargement du sol et donc une diminution de la pression exercée sur le mur. On observe le comportement typique des sols meubles contractants et des sols denses contractants-dilatants, dont le moment obtenu avec un sol dense atteint un minimum pour une rotation d'environ 5 à 10 mrad avant d'augmenter en raison du phénomène d'adoucissement du sol. Au contraire, dans le cas du sol meuble, le moment diminue de manière monotone et moins rapidement. En outre, des événements de stick-slip sont observés dans les deux types d'échantillons, ils sont décrits et leur origine est expliquée. Les coefficients de pression de terre obtenus en cas de défaillance active sont relativement faibles, ce qui indique une résistance élevée qui ne peut pas être expliquée par les essais triaxiaux réalisés en laboratoire.

En outre, des essais compactés sont réalisés en appliquant une charge statique à la surface du sol après l'application des différentes couches. Par rapport aux essais non compactés, on constate un état de contrainte plus élevé à la fin de la phase de remblayage. Il en résulte notamment une autre répartition de la pression du sol, caractérisée par une valeur maximale dans la partie supérieure du remblayage. Par conséquent, la force résultante de la poussée des terres a agi à un point plus élevé. Pour cette raison, et en raison de la plus grande rigidité du sol, le rapport moment/rotation des essais compactés était caractérisé par une décharge abrupte, même si des rotations légèrement plus grandes sont nécessaires pour obtenir une défaillance active. En général, le comportement des échantillons compactés est similaire à celui des échantillons non compactés.

Par la suite, le comportement de décharge des échantillons non compactés est étudié pour des conditions tridimensionnelles. La situation où une seule section du mur est corrodée est testée en ne faisant tourner que la section centrale. Une redistribution des contraintes s'est produite dans le remblai, ce qui a conduit à un état-limite inférieur et à un mécanisme de rupture incurvé. En conséquence, une augmentation du moment a été mesurée sur les sections de mur adjacentes.

Enfin, la poussée des terres sur un mur presque rigide est mesurée pendant le remblayage et le compactage. Il est montré que l'interface de frottement contribue à la distribution bilinéaire de la poussée des terres.

Analyse numérique : décharge des murs

La section 7 présente une méthode de simulation de la poussée des terres agissant sur des murs de soutènement à semelles endommagées. Elle est basée sur un modèle d'éléments finis du mur et de son remblai et nécessite la connaissance de l'état de contrainte du sol dans les conditions de service. Ces dernières peuvent être obtenues par des analyses numériques (comme dans la section suivante) ou par des hypothèses basées sur l'expérience. Les mesurages directs (comme ceux dont nous disposions dans ce travail) ne sont normalement pas disponibles et sont généralement difficiles à obtenir sur le terrain. La loi de comportement du sol utilisée est basée sur l'élasticité isotrope dépendant de la pression et sur le critère de rupture de Mohr-Coulomb. Une loi de durcissement personnalisée a été utilisée sur la base de données expérimentales. Alternativement, la loi de durcissement du modèle "Hardening Soil" pourrait être adoptée pour obtenir des résultats approximatifs.

Le comportement du sol déterminé numériquement a été comparé aux résultats expérimentaux. Les échantillons non compactés ont montré une excellente concordance, à la fois en termes de contraintes et de déformations. Dans les échantillons non compactés, la défaillance du sol se propage du haut vers le bas. La précision de la solution de l'analyse limite a également été confirmée dans cette section par la comparaison avec les résultats expérimentaux et numériques. Il a été constaté que la charge limite obtenue avec les solutions proposées dans la section 3.3 fournit une bonne estimation conservative de la charge limite à l'état résiduel. En revanche, l'estimation du moment de flexion minimal généré par la poussée des terres en supposant l'angle de frottement maximal a donné un résultat peu conservateur. En effet, l'état dans lequel l'ensemble du remblai mobilise simultanément la résistance maximale n'existe pas. D'autre part, il a été confirmé que la charge limite déterminée en supposant la loi d'écoulement nonassociée surestime le moment, car

l'angle de frottement a été calibré avec la méthode géotechnique traditionnelle (voir section 3.5.1).

La simulation numérique des essais compactées a également montré un bon accord avec les données expérimentales. Seule une légère sous-estimation du moment et de la poussée des terres dans le régime de durcissement a été observée pour l'échantillon dense. La raison en est probablement que le sol du test a été déposé avec (presque) sa densité maximale, qui a diminué par cisaillement pendant le processus de compactage. Cependant, la loi de comportement du sol proposée ne considère que la densité du sol comme une constante tout au long de l'analyse.

On en déduit que le modèle numérique proposé peut être utilisé pour faire des estimations fiables de la poussée des terres exercée sur les murs endommagés. Pour reproduire l'effet de stick-slip observé lors des essais, on pourrait adopter un modèle rate-and-state. Cependant, le mur devrait toujours être en mesure de trouver un état d'équilibre le long de l'enveloppe inférieure de la courbe moment-rotation, car la période des oscillations est petite.

Dans la deuxième partie de la section, l'état-limite tridimensionnel est analysé à l'aide du logiciel OptumG3. On constate une bonne concordance avec les résultats expérimentaux, bien que les dimensions du mécanisme de défaillance ne correspondent pas parfaitement en raison de l'hypothèse implicite de la règle d'écoulement associative dans l'analyse de la valeur limite. L'influence de la loi d'écoulement associée est ensuite étudiée à l'aide de la méthode des éléments finis et d'une loi de comportement du sol simplifiée, linéaire et élastique, parfaitement plastique. Il est démontré que l'écoulement associé n'a pas d'influence sur les résultats, car la résistance au cisaillement du sol a été recalculée en supposant une solution limite à la charge limite mesurée dans un essai par éléments. La raison en est que le problème n'est pas limité cinématiquement. Cependant, si le mesh est suffisamment fin dans une simulation par éléments finis, la déformation se localiserait dans de fines bandes de cisaillement, ce qui conduirait à une charge limite plus élevée. Cependant, dans ce cas, la calibration de la résistance du sol devrait également prendre en compte la localisation de la déformation.

En outre, les défis liés à la modélisation de conditions tridimensionnelles sont mis en évidence et des contre-mesures possibles sont proposées.

Recommandations pour la pratique

Le comportement de décharge du remblai d'un mur peut être quantifié à l'aide de codes d'éléments finis commerciaux tels qu'Abaqus ou Plaxis. Alors qu'une loi de comportement du sol définie par l'utilisateur est nécessaire pour Abaqus, l'implémentation du "hardening soil model" de Plaxis peut être utilisée sans difficultés. Le "hardening soil model" permet une modélisation assez précise du comportement de durcissement du sol, mais pas la modélisation de l'adoucissement du sol, qui est souvent observé dans les sols denses. Or, pour la vérification des murs de soutènement à semelles, la modélisation précise du durcissement est beaucoup plus critique, car les murs corrodés n'ont généralement pas une capacité de rotation suffisante pour que le sol puisse atteindre la phase de adoucissement. Comme il a été démontré dans ce travail, la modélisation de l'adoucissement est également toujours liée à une dépendance du mesh dans FEM qui, si elle n'est pas correctement prise en compte, peut conduire à des résultats erronés.

En conséquence, l'ingénieur devrait négliger la résistance maximale d'un sol dense et calibrer la loi de comportement du sol en tenant compte uniquement de l'état résiduel. Toutefois, dans certains cas, une résistance supérieure à la résistance résiduelle peut être prise en compte, à condition que l'état de contrainte en tout point reste inférieur à la résistance maximale au cisaillement du matériau. Dans ce cas, l'ingénieur doit vérifier et démontrer que la résistance maximale au cisaillement n'est mobilisée nulle part dans le modèle. Dans le cas contraire, le modèle fournit des résultats erronés et l'ingénieur obtient une estimation incertaine.

Une fois la loi de comportement du sol correctement calibrée, la décharge du mur peut être simulée à l'aide d'un modèle similaire à celui présenté à la section 7.2.1. L'état de contrainte initial est soit initialisé dans le modèle (sur la base de quelques hypothèses), soit calculé directement en simulant le processus de construction (comme dans la section 8). Il est possible que le modèle de la section 7.2.1 puisse être étendu en ajoutant une couche de fondation, bien que son influence sur le processus de décharge soit négligeable. Pour conclure, il convient de mentionner que la loi de comportement du sol a été calibrée dans ce travail par des essais biaxiaux. L'annexe II.2.2 a montré que la résistance du sol est plus élevée dans des conditions de déformation planes, ce qui signifie qu'une calibration par des essais triaxiaux peut conduire à des résultats trop conservateurs.

Analyse numérique : contraintes initiales

La première partie de la section 8 est dédiée à l'étude des poussées des terres au repos à l'échelle des particules. Une bonne compréhension de la poussée des terres dans des conditions de déformation unidimensionnelles est indispensable pour comprendre la poussée des terres sur les murs de soutènement dans l'état de service (c'est-à-dire pas dans l'état-limite ultime). Le modèle numérique de l'annexe II.2 est utilisé pour réaliser des essais œdométriques. Il s'avère que le coefficient de poussées des terres au repos K_0 est inversement proportionnel au coefficient de coordination moyen de l'échantillon, ce qui conduit à des valeurs plus élevées pour les échantillons meubles. D'autre part, le coefficient K_0 montre une augmentation plus marquée pendant la décharge avec l'augmentation du degré de surconsolidation (OCR) dans les échantillons plus denses. La fonction de loi de puissance empirique, souvent adoptée dans la littérature, qui relie le coefficient K_0 du sol surconsolidé à l'OCR, s'avère être une estimation raisonnable, bien que pas très précise, pour des applications pratiques lors de la décharge. Les paramètres de contrôle des poussées des terres au repos ont ensuite été étudiés. Pour les sols normalement consolidés, aucune corrélation n'est démontrée entre K_0 et les paramètres élastiques, alors qu'une bonne corrélation a été trouvée avec le frottement intergranulaire. Par conséquent, le coefficient de poussée des terres est bien corrélé à la résistance maximale au cisaillement du sol, même si aucune causalité n'est impliquée. Bien que la formule de Jáky repose sur une base théorique peu solide, on constate qu'elle fournit une bonne estimation conservative de K_0 pour le sable dense de Perth. Les valeurs estimées par la formule surestiment de manière plus importante les résultats numériques pour l'échantillon meuble. Des études supplémentaires sur d'autres échantillons sont toutefois nécessaires.

Dans la deuxième partie de la section, le modèle numérique introduit dans la section 7 est étendu afin de prendre en compte le comportement de consolidation du sol et de modéliser la compaction du sol. Des simulations numériques des essais expérimentaux sont effectuées et les résultats obtenus sont comparés. Les simulations des échantillons non compactés ont montré une bonne concordance avec les résultats expérimentaux. La distribution de la poussée de terre dans ces échantillons est bilinéaire, caractérisée par un coefficient de la poussée des terres plus élevé dans la partie la plus basse du remblai et influencée par les déflexions du mur et le frottement du mur. La simulation des échantillons compactés a conduit à une prédiction moins précise de la contrainte initiale, principalement en raison de certaines difficultés rencontrées lors de la modélisation du problème considéré par la méthode des éléments finis. Par conséquent, les pressions estimées ont conduit à une sous-estimation du moment agissant au pied du mur dans un échantillon dense et à une surestimation dans un échantillon meuble. L'utilisation d'une méthode sans mesh permettrait d'obtenir de meilleurs résultats. En outre, la solution analytique de Broms est vérifiée. Il s'avère que des résultats conservateurs sont obtenus, bien que leur application conduirait probablement à une sécurité trop élevée, en particulier dans les sols denses.

Recommandations pour la pratique

Les recommandations de la section précédente s'appliquent également à cette section. Toutefois, étant donné que dans cette section, les conditions de contrainte initiales sont déterminées par la modélisation des phases de construction, la prise en compte de la couche de fondation de sol élastoplastique sous le mur peut influencer la contrainte initiale résultante du mur. En effet, pendant le remblayage, le mur se tassera sous le poids du sol et la poussée des terres, ce qui entraînera un allègement partiel du remblai déjà déposé.

Négliger la couche de fondation conduit donc à des résultats conservatifs. Il ne fait aucun doute que la loi de comportement du sol proposée peut être utilisée pour simuler des phases de construction plus complexes, par exemple pour simuler l'excavation d'un talus, la construction du mur et le remblayage.

Analyses supplémentaires

Dans la section 9, différentes analyses sont effectuées afin de poursuivre la compréhension de l'interaction sol-mur. Tout d'abord, une analyse de la décharge des murs est effectuée en tenant compte d'un modèle structurel affiné. Les résultats montrent que le comportement de décharge du sol ne dépend pas d'une modélisation correcte du comportement élastoplastique du mur corrodée. En effet, on observe la même décharge de pression du sol pour un mur corrodé et pour un mur intact auquel on a imposé une rotation à sa base. Il est donc démontré que les actions et les résistances peuvent être découplées lors de l'évaluation de la défaillance des murs endommagés par la corrosion. La sécurité des murs peut alors être évaluée en superposant les actions et les réactions comme dans la figure 63.

Ensuite, l'analyse thermique d'un mur existant est effectuée. Sur la base de données météorologiques disponibles librement, il est possible de simuler le champ de température d'un mur de soutènement avec une bonne précision. On montre comment les changements de température ont un effet cyclique sur le mur, ce qui entraîne un déplacement supplémentaire. Les déplacements du mur mesurés sur le terrain peuvent être expliqués, même si ce n'est que partiellement (car la moyenne sur 24 heures a dû être prise en compte).

En outre, le modèle numérique développé est utilisé pour simuler des ouvrages en échelle réelle. Il s'avère que le comportement de décharge n'est pas sensible aux dimensions du mur et que les affirmations faites précédemment sont valables pour chaque dimension de mur. En outre, l'influence de l'inclinaison du remblai est étudiée. Dans ce cas également, on ne constate qu'une faible influence sur le comportement de décharge du sol.

Enfin, une étude paramétrique est réalisée afin d'examiner les effets de l'angle de frottement interne du sol et de differentes géométries des sections du mur sur l'état-limite tridimensionnel. Un angle de frottement interne plus haut et des sections plus hautes permettent une meilleure redistribution des contraintes dans le remblai, ce qui conduit à des forces plus faibles sur la section corrodée dans l'état limite et à une augmentation plus importante de la force résultante sur les sections adjacentes.

Évaluation de la sécurité des murs de soutènement à semelles

La section 10 constitue la synthèse des deux projets de recherche AGB 2015/028 *"Tragwiderstand und Verformungsvermögen von Winkelstützmauern bei lokaler Korrosion der Bewehrung"* et AGB 2015/029 *"Failure Behaviour of Cantilever Retaining Walls - Soil-Retaining Wall Interaction"*.

Pour vérifier la sécurité structurale des murs de soutènement avec des armatures corrodées, une stratégie de vérification en plusieurs phases est proposée, dans laquelle l'effort de vérification est augmenté à chaque phase. Il faut décider dans chaque cas si l'effort pour une phase est justifié (en fonction de l'âge de l'ouvrage, de son état général, des objectifs supérieurs du projet, des dépenses pour les mesures de renforcement et pour la collecte des données), ou si des mesures de renforcement ou une nouvelle structure de remplacement doivent être examinées directement.

Dans un premier stade, on procède à un triage en utilisant des critères analytiques simplifiés pour déterminer s'il est possible de démontrer une sécurité structurale suffisante.
Si ce n'est pas le cas, une analyse découplée est effectuée. Dans ce cas, le comportement force-déplacement du mur de soutènement et celui du remblai sont déterminés séparément et ne sont réunis que pour la vérification. A ce stade, des estimations prudentes et simples sont faites concernant les dommages dus à la corrosion. Une éventuelle diminution de la poussée des terres due au basculement du mur de soutènement autour de son pied est négligée.

Si l'analyse découplée simple révèle une sécurité structurale insuffisante, une analyse découplée plus détaillée peut être effectuée avec des suppositions moins conservatrices concernant la répartition de la corrosion ou la rigidité de la fondation, pour autant que les données correspondantes puissent être collectées à un coût raisonnable.

S'il existe une possibilité de transfert de force dans le sens longitudinal, par exemple si seuls certains segments d'un mur de soutènement dilaté sont touchés par la corrosion, une analyse couplée peut être indiquée. Dans ce cas, la déformation du mur et la réaction de la poussée des terres sont déterminées à chaque étape du calcul en tenant compte de l'interaction du sol avec la structure, ce qui permet de saisir l'influence des segments adjacents.

Si la sécurité structurale ne peut pas être démontrée même avec une analyse approfondie, des mesures de renforcement appropriées ou une nouvelle structure de remplacement doivent être planifiées.

La stratégie de vérification est ensuite illustrée à l'aide d'un exemple de référence.

Quelques remarques pratiques, basées sur les deux projets, sont ensuite formulées.

1   Introduction

Retaining walls constitute a significant part of the building infrastructure along roads in Switzerland. Therefore, their safety is crucial and is periodically monitored and reassessed throughout their lifetime. To this end, the Federal Roads Office (FEDRO) launched a campaign in 2006 to investigate the state of cantilever retaining walls located along national highways and built in the 1970s [1]. Destructive tests were carried out to evaluate the condition of the main reinforcement bars. The results showed advanced and strongly localised corrosion, which represents a potential threat to wall safety and can lead to an unpredictable and brittle wall collapse [1], [2].

According to the investigations, poor concrete quality (leading to the formation of honeycombs) is the main cause of corrosion, located just above the construction joint between the base slab and the stem (see the magnified detail in Fig. 1, left) [1], [2]. Corrosion leads to a cross-sectional loss that is usually limited to a few centimetres over the length of the bars [2]. This local deterioration represents a weak point in the main reinforcement that leads to a local stress increase, resulting in increased strain and wall displacement. Under these circumstances, the development of a plastic hinge at the construction joint can be assumed. Consequently, a wall rotation driven by corrosion arises, leading to the unloading of the soil (Fig. 1, right).
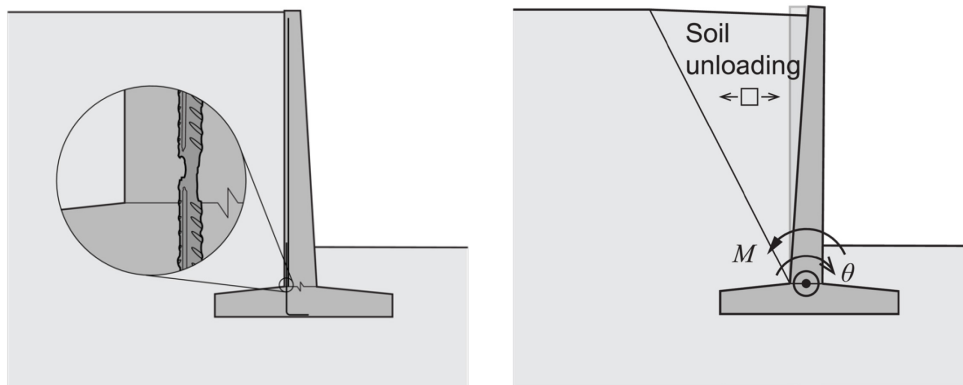
Fig. 1: *On the left: cross-section of a corrosion-damaged cantilever retaining wall. As observed in [1], the corrosion is localised at the construction joint. On the right: corrosion-induced soil unloading.*

Due to the potentially brittle failure behaviour, the applicability of the observational method is questionable, as only small wall displacements could occur before its collapse. Furthermore, difficulties often arise in evaluating retaining walls due to the lack of structural and geotechnical documentation. Additionally, inspecting the current state of the main reinforcement with nondestructive tests is challenging as it is located on the side of the backfill. For these reasons, reliable and predictive models are needed to assess the safety of existing walls and to plan safety and strengthening measures. Thus, the FEDRO launched a call for research projects aiming at bringing improved knowledge on:

1. the identification of potential risks to existing retaining walls;
2. the failure behaviour of cantilever retaining walls;
3. the monitoring of unanchored retaining walls.

In total, five different projects were approved and funded. These are the projects AGB 2015/026, AGB 2015/028, AGB 2015/029 (the present work), AGB 2015/034_OBF, and AGB 2016/002. The present work focuses on the failure behaviour of corrosion-damaged cantilever retaining walls; more precisely, on the corrosion-driven wall unloading process and the soil-structure interaction. As this is strongly related to the structural failure behaviour of the wall, there was a continuous exchange of information and collaboration with

project AGB 2015/028 [3], conducted at the Institute of Structural Engineering of ETH Zurich. The collaboration allowed the investigation of the most relevant aspects of the failure behaviour and of the wall-structure interaction in the most realistic way. Additionally, information was occasionally exchanged with the other projects, particularly with project AGB 2015/034_OBF [4].

In the past, a pilot study [1] was carried out. It studied the failure behaviour of corrosion-damaged cantilever retaining walls using simplified models for the structural behaviour of locally corroded reinforcement and the evolution of the loads acting on the wall. However, it remained unclear whether the reduction of the stresses in the backfill due to increasing deformation would inevitably lead to a brittle failure and how large the possible deformation capability of such walls could be. In particular, the evolution of stresses acting in the backfill on the retaining wall following a corrosion-induced wall displacement is subject to significant uncertainties. Specifically,

- it is unclear how large the displacement of a cantilever retaining wall has to be to develop active soil failure in the backfill and how fast the unloading takes place depending on the displacement;
- corrosion influences the kinematics of the wall at failure, leading to the formation of a plastic hinge at the base of the stem and, thus, to the rotation of the stem;
- the resulting evolution of the stresses in the backfill and the load acting on the retaining wall are poorly understood.

These uncertainties in assessing the stresses in the backfill affected by the wall displacement make the investigation of the evolution of the loads acting on cantilever retaining walls a necessary step towards achieving the goals of the FEDRO research initiative.

1.1 Aim and objectives of this research project

This work aims to improve the understanding and quantification of the earth pressure acting on corrosion-damaged cantilever retaining walls. In particular, the evolution of the earth pressure from construction to the onset of corrosion is studied and the influence of several parameters, such as different soil behaviours and initial stress conditions, is investigated. The combination of numerical, analytical, and physical modelling contributes to an advanced understanding and leads to criteria for assessing the soil-retaining wall interaction. The results, combined with the results of project AGB 2015/028 [3], will provide practitioners with the basis to assess the safety of corrosion-damaged retaining walls.

The main objectives of this work are:

1. to identify the relevant soil failure mode for corrosion-damaged retaining walls and define the acting loads at the ultimate limit state;
2. to perform a comprehensive experimental study, allowing to identify the most influential parameters on the earth pressure evolution;
3. to develop numerical models to simulate the corrosion-driven wall unloading, prioritising the accurate modelling of the soil-wall interaction and the soil behaviour;
4. to quantify potential three-dimensional effects on the limit load; and
5. to demonstrate the potential applications of the developed models to the safety assessment and monitoring of existing structures.

The focus of the present work lies on purely frictional soil. In fact, soil types that qualify to be used as a wall backfill (see, e.g., [5], [6]) are classified as granular soil, which usually has very low to no pure cohesive strength. In other words, the strength of granular soil is not characterised by cohesion resulting from van der Waals interactions as in clay. Instead, the cohesion that is sometimes measured in the laboratory in granular samples is purely derived from the suction forces resulting from the naturally present moisture in the soil. Therefore, this cohesion is highly dependent on the moisture content (e.g., [7], [8]), which in turn depends on factors such as geographical position and climate, and should not be considered in the design and verification of the walls.

1.2   Structure of the report

This report is divided into eleven sections. Sections 1-2 introduce the reader to the research topic. In particular, Section 2 reviews the theories of earth pressure and the conventional wall design methods used in practice to design retaining walls, providing the knowledge required to assess the design of existing walls.

Section 3 defines the ultimate limit state of corrosion-damaged cantilever retaining walls from a geotechnical perspective. First, the reader is introduced to the most fundamental concepts and theorems of limit analysis, which will be further applied to determine the limit load. Then, the relevant failure mode induced by corrosion damage is defined. Next, limit analysis is used to seek a bounded solution of the limit load that acts on the wall when it collapses. Its applicability to real situations involving nonassociated flow is verified. In addition, the obtained solution is used to verify the conventional design methods presented in Section 2.

As a sufficiently large wall rotation capacity, which is not guaranteed in corrosion-damaged walls, is needed to reach the limit state, the following sections deal with the corrosion-driven unloading behaviour of the walls, from the initial stress state to the ultimate state. Section 4 introduces the reader to the unloading behaviour and the soil-wall interaction in a qualitative manner. The gained knowledge is then used in Section 5 to design an appropriate test setup capable of reliable and repeatable testing conditions. In addition, it presents the testing procedures and the programme and a description of the materials. An experimental study is carried out in Section 6. The most influential parameters identified in Section 4 are investigated and the results are presented.

In the following sections, a numerical framework for quantifying the earth pressure is developed and validated. In Section 7, a numerical model is developed that can accurately model the wall unloading process and the soil-wall interaction. The unloading phase of the wall tests is modelled assuming the initial stress state from the experimental results, and the proposed numerical model is validated. Furthermore, the limit state under three-dimensional conditions is studied numerically. The initial stress state is modelled in Section 8, which is divided into two main sections. First, numerical simulations are carried out to study the earth pressure at rest at a fundamental particle-scale level. Then, the gained knowledge is used to extend the constitutive model proposed in Section 7 to consider volumetric yielding and accurately model the behaviour of one-dimensional consolidation problems. The numerical model is then used to simulate the soil deposition and compaction phases that preceded unloading in the wall tests in Section 6. Finally, the model is validated against the experimental data. Then, the developed numerical framework is applied to some real applications in Section 9, where the analysis of a real wall is carried out considering a proper structural model to simulate the elastoplastic wall behaviour during corrosion. In addition, the effects of changes in temperature on an existing wall are studied. The results obtained are verified against field measurements. Furthermore, the influence of the wall height and the backfill inclination is studied using the developed numerical models. In the last part of the section, a parametric study is carried out to study the influence of soil friction and wall geometry on the three-dimensional limit state. Finally, Section 10 discusses the verification procedure for cantilever retaining walls, considering the wall and soil response.

Sections 1-9 and all the appendices are a condensed version of the doctoral thesis [1] titled "*Quantification of the Earth Pressure Acting on Corrosion Damaged Cantilever Retention Walls: An analysis of the soil-structure interaction*" [9], submitted to ETH Zurich on December 2022 by David Perozzi under the direction of Prof. Dr. Alexander Puzrin. Some original content was added to the present report as *recommendations for the practice* to allow a more straightforward implementation of the results to practical problems. Section 10 was written jointly with Severin Häfliger and Prof. Dr. Walter Kaufmann (Institute of structural engineering, ETH Zurich) and is published in German in [3].

---

[1] The full text of the thesis can be found online (open access) at: https://doi.org/10.3929/ethz-b-000591353

2 Earth pressure theories and conventional design methods

Familiarity with the conventional historical methods used to design retaining walls is essential to assess their safety and stability, as it allows insight into the designer's perspective and estimation of the strength of a wall in the event of missing building files.
Among the most crucial information needed to design a wall is the quantification of the actions to which it is subject. The most significant actions on retaining walls are the earth pressure, the pressure exerted by groundwater, surcharge loads, compaction loads, and temperature-related actions such as thermal effects caused by a temperature gradient across the wall thickness or soil freezing pressure. However, since the primary focus of the present work is the earth pressure, the water pressure, surcharge loads, and soil freezing pressure are neglected.

This section is divided into two parts. First, the most common theories of earth pressure are reviewed. Then, the focus is shifted to historical design methods for cantilever retaining walls. Despite the technological advancement in the last fifty years, the state of the art in wall design has not changed much. In situations that do not require detailed numerical analyses, the methods used in the 1970s are still often used today (see, e.g., [10], [11]) and implemented in software (e.g. [12]).

2.1 Earth pressure theories

The earth pressure is the pressure exerted by the soil on embedded and backfilled structures, and its correct quantification is crucial for the design and verification of retaining walls. The earth pressure value is bounded between two limits (Fig. 2). The lower limit is defined by the active earth pressure E_a, which is reached when the wall moves away from the soil mass, while the upper limit is defined by the passive earth pressure, developed in the case of a wall moving towards the soil mass. The wall displacement must be sufficiently large to reach one of these limits (i.e. the limit state). Instead, if the wall does not move and is perfectly rigid, the earth pressure E_0 acts on the wall. In this work, E_0 is called *initial earth pressure*. In engineering practice, E_0 is often assumed to correspond to the earth pressure at rest. In reality, the backfill of a retaining wall is a disturbed soil and the valute E_0 depends on many factors, such as the degree of compaction and the wall friction.
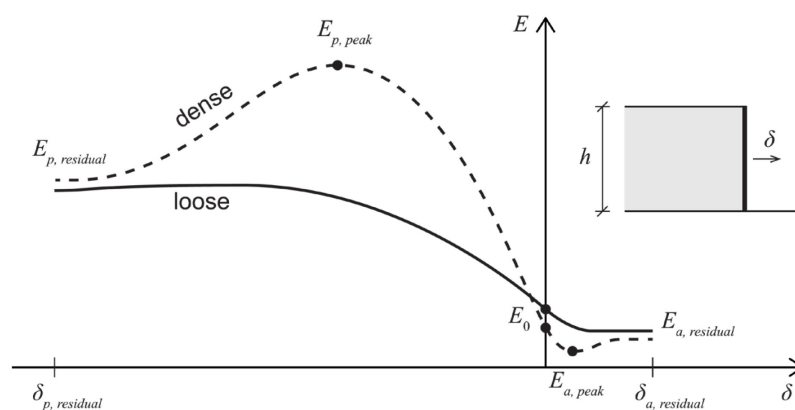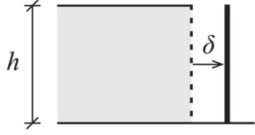
Fig. 2: *Development of the earth pressure as a function of the wall displacement for dense and loose soil.*

Fig. 2 shows how the earth pressure depends on the soil behaviour and the wall displacement. While the earth pressure is a monotonically decreasing curve in loose soil, in dense soil two extremal values are reached when the peak shear strength is mobilised. A steady value is reached by all soil types at $\delta_{a/p,residual}$. The $\delta_{a/p,residual}$ value depends, among other factors, on the type of wall displacement and on the soil packing density. Eurocode 7 [13]

suggests the values in Tab. 1 for the active earth pressure. These values are said to be valid if the initial coefficient of lateral earth pressure is $K_0 < 1$ (i.e. low or no compaction). Between K_0 and K_a it is suggested to interpolate linearly.

***Tab. 1:** Required wall displacement to reach the active limit state according to [13].*

Displacement mode	Loose soil	Dense soil
	$\dfrac{\delta_a}{h} \in [0.004, 0.005]$	$\dfrac{\delta_a}{h} \in [0.001, 0.002]$
	$\dfrac{\delta_a}{h} \approx 0.002$	$\dfrac{\delta_a}{h} \in [0.0005, 0.001]$

In the following subsections, the relevant earth pressure theories are reviewed. In particular, this includes the active earth pressure, the earth pressure at rest, and the compaction-induced earth pressure. In addition, a review of studies on the earth pressure unloading to the active state is included.

2.1.1 The active earth pressure

Since the Early Modern period, engineers have needed to quantify the force required to stabilise backfilled walls. French military engineers provided the first significant contributions to the earth pressure theory beginning in the late 17th century (e.g. [14]–[17]), as they had to design tall walls for fortifications and other large military constructions [18]. In the beginning, they almost exclusively focused on quantifying the active earth pressure, as it was the only quantity of interest for designing their walls (e.g. [19]). Early attempts to quantify the earth pressure were based purely on experience (e.g. [14]) or simple geometric reasoning (e.g. [15]) and led to simplified results in which the variable soil properties (e.g. the friction angle) remained ignored.

The most relevant earth pressure theories are given chronologically in the following. This section aims not to cover the complete development of the earth pressure theory but rather to overview the most common theories used in Switzerland between the 1960s and the present.

Coulomb's theory

The first significant contribution to the earth pressure theory was made in 1776 by C. A. Coulomb [19]. Assuming homogeneous soil properties, Coulomb investigated the equilibrium state of the soil wedge *CBa* depicted in Fig. 3a.

Three forces support the wedge *CBa*: the force exerted by the wall at point F, the soil frictional resistance, and the cohesive resistance. By solving the force equilibrium equations, Coulomb determined the force exerted by the wall (i.e., the active earth pressure) as [19, p. 358]:

$$E_a = \frac{G(h - \mu_{\text{soil}}x) - c(h^2 + x^2)}{x + \mu_{\text{soil}}h},$$
(2.1)

where $\mu_{\text{soil}} = \tan\varphi$ is the soil friction coefficient and c is the cohesion.
Coulomb noted that the wall must not only support a given wedge *CBa*, but, among all possible surfaces, the surface *CBeg* that leads to the highest possible pressure (Fig. 3a). In his experience, the failed portion of a wall's backfill is a "surface very similar to a triangle" [19, p. 360]. Thus, he optimised Equation (2.1) to get the maximum force exerted on the wall neglecting curved surfaces.
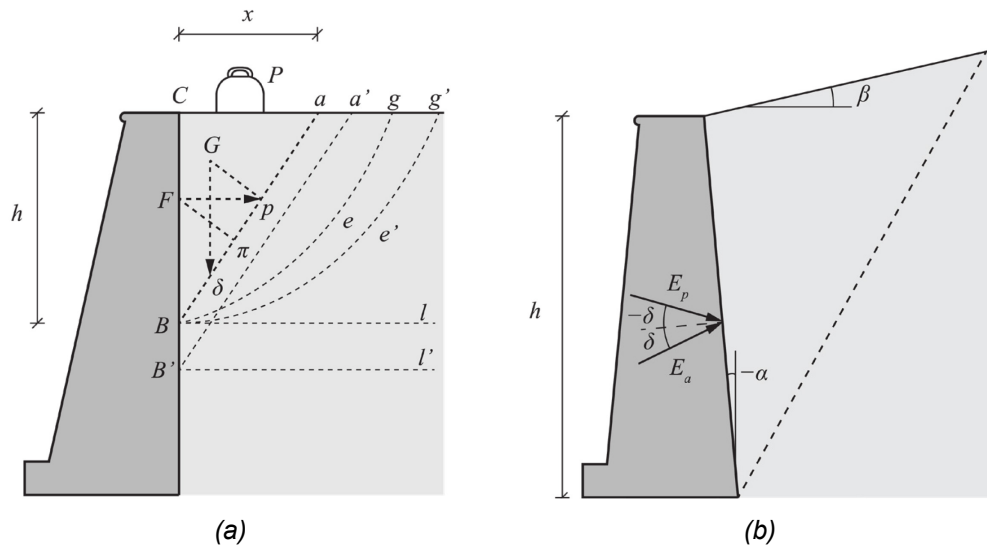
(a)   (b)

Fig. 3: *(a) Coulomb's illustration for his earth pressure theory. Adapted from [19]. (b) General boundary conditions for the earth pressure theory.*

Coulomb finally included wall friction in his solution, which Culmann later criticised as he argued that moment equilibrium on the wedge was not satisfied in the presence of wall friction [20, p. 629].

Coulomb's theory was further studied and extended in the early 19th century by Prony, Mayniel, and Français [21]–[23], among other authors. They developed solutions for the earth pressure under more general boundary conditions, such as a wall or a backfill inclination (Fig. 3b), by borrowing Coulomb's assumptions (e.g. [23, p. 160]). Later, the corresponding equations were developed for the passive earth pressure (e.g. [24, p. 262]). Today, these extended theories are widely known simply as *Coulomb's theory*. The coefficient of active earth pressure is commonly given as (e.g. [11, p. 163]):

$$\bar{K}_{\mathrm{a}} = \frac{\cos^2(\varphi + \alpha)}{\cos^2 \alpha \cos(\delta - \alpha) \left[1 + \sqrt{\dfrac{\sin(\varphi + \delta)\sin(\varphi - \beta)}{\cos(\delta - \alpha)\cos(\alpha + \beta)}} \right]^2}, \tag{2.2}$$

where φ is the soil friction angle, δ the wall interface friction angle, and α and β geometrical parameters according to Fig. 3b.

The coefficient of earth pressure is defined as:

$$\bar{K}_{\mathrm{a}} = \frac{E_{\mathrm{a}}}{\gamma h^2 / 2}, \tag{2.3}$$

where E_{a} is the active earth pressure acting on a wall of height h and backfilled with soil of weight γ. The horizontal and the vertical components read

$$\bar{K}_{\mathrm{ah}} = \bar{K}_{\mathrm{a}} \cos(\delta - \alpha)\,, \text{ and} \tag{2.4}$$

$$\bar{K}_{\mathrm{av}} = \bar{K}_{\mathrm{a}} \sin(\delta - \alpha)\,. \tag{2.5}$$

Coulomb's equations have been widely used in engineering practice. In particular, Equation (2.2) is still broadly used in practice to estimate the active earth pressure (see, e.g., [10], [25], [26]).

Graphical methods: Poncelet and Culmann

Different graphical methods were developed during the 19th century to determine the earth pressure in cohesionless granular soils. Using these methods, the engineers could graphically determine the inclination of the failure lines, even for more complicated geometries. In particular, Poncelet's and Culmann's methods have been intensively applied in the 20th century and are sometimes still applied today.

Poncelet translated Coulomb's analytical equations into a purely geometrical construction [24, p. 102]. However, Culmann argued that the engineer would have to keep in mind the original analytical solution (i.e. Coulomb's solution, which could be superseded at a certain point) to use Poncelet's solution [20, p. V–VI]. Thus, he developed a geometric solution from scratch, ignoring existing analytical solutions. Nevertheless, Culmann's assumptions are very similar to Coulomb's. In fact, he assumed the failure line to be straight and got the same resulting force diagram as Coulomb [20, pp. 548–549]. However, his method allows one to consider arbitrary wall and backfill geometries [20, pp. 563–571]. These two procedures are presented in Appendix I.

Rankine's theory

Rankine published his contribution to the earth pressure theory in 1857 [27]. His main concern was that "previous researches … are based … on some mathematical artifice or assumption, such as Coulomb's 'wedge of least resistance' [that], although leading to true solutions of many special problems, are both limited in the application of their results, and unsatisfactory in a scientific point of view" [27, p. 9].

Instead, he only assumed Coulomb's frictional law

$$\tau = \sigma \tan \varphi \ ,$$ (2.6)

and examined the stress equilibrium in a cohesionless granular medium.
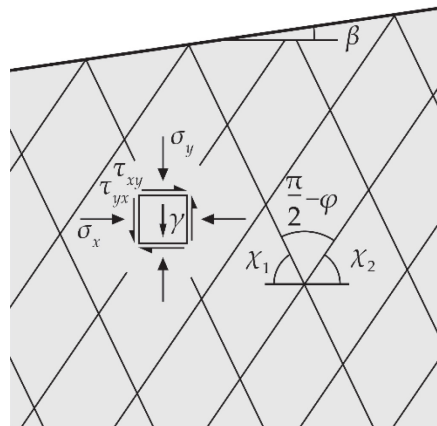
Fig. 4: Rankine's solution.

By solving the equilibrium equations for an arbitrarily inclined slope entirely in a state of failure, Rankine proved that the planes of equal stress in an infinite slope are parallel to the free surface. He then could establish the inclination of the failure planes

$$\chi_1 = \frac{\pi}{4} + \frac{\varphi - \beta}{2} + \frac{1}{2}\arcsin\left(\frac{\sin \beta}{\sin \varphi}\right) ,$$

$$\chi_2 = \frac{\pi}{4} + \frac{\varphi + \beta}{2} - \frac{1}{2}\arcsin\left(\frac{\sin \beta}{\sin \varphi}\right) ,$$ (2.7)

the earth pressure acting along a vertical plane [16, p. 26]

$$\sigma_x = \gamma y \frac{\cos^4 \beta}{\cos^2 \varphi} \left[1 - \sqrt{1 - \frac{\cos^2 \varphi}{\cos^2 \beta}} \right]^2, \tag{2.8}$$

and the shear stress acting along a vertical plane

$$\tau_{yx} = \sigma_x \tan \beta . \tag{2.9}$$

The last two equations show that the stress direction depends solely on the slope geometry. Rankine then determined the earth pressure acting on a retaining wall using Equations (2.8) and (2.9), noting that the wall friction angle must be greater than or equal to the soil friction angle, $\delta_{\text{wall}} \geq \varphi$ [27, pp. 21–22]. In reality, the condition is slightly looser, as the wall friction angle shall be greater than or equal to the slope inclination:

$$\delta_{\text{wall}} \geq \beta. \tag{2.10}$$

Therefore, Rankine's solution can only be directly used to determine the earth pressure on a wall in a handful of cases because of this restriction.

In the particular case of a horizontal backfill, $\beta = 0°$, the wall would be assumed to be smooth, and the following stress components result

$$\sigma_x = \gamma y \frac{1 - \sin \varphi}{1 + \sin \varphi}, \tag{2.11}$$

$$\tau_{yx} = 0.$$

This shows that Rankine's solution is of little practical use for the design of retaining walls, as there are no perfectly smooth surfaces.

Boussinesq-Caquot-Kérisel Theory

Boussinesq recognised the limitations of Coulomb's and Rankine's approaches, which only considered straight failure lines, and laid the foundation for determining the equations of curved slip lines and the rotation of the stress state. He formulated the equilibrium equations for the soil element in Fig. 5a and found an approximate solution for some particular cases [28, p. 264]. Later, Caquot and Kérisel found a more generalised solution to Boussinesq's equations valid for more diverse geometries and active and passive cases.
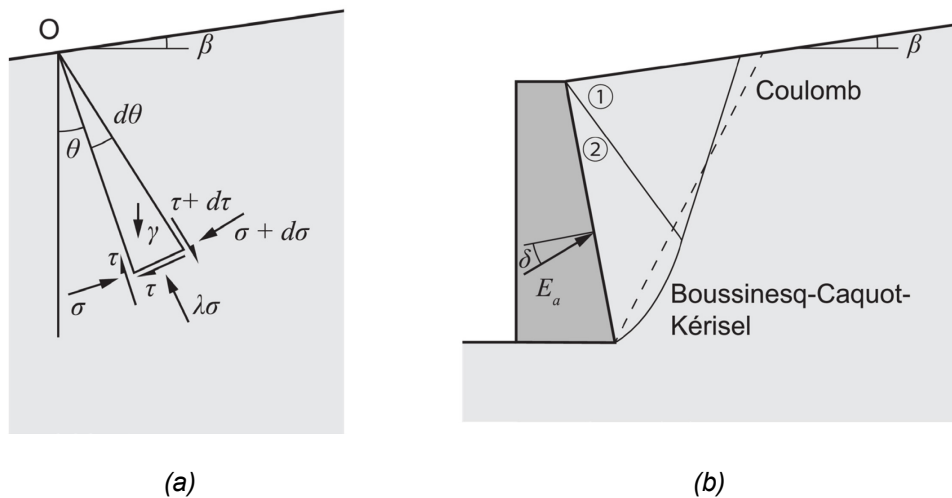

(a)   *(b)*

Fig. 5: *Boussinesq-Caquot-Kérisel's assumptions and resulting failure mechanism.*

Boussinesq-Caquot-Kérisel Theory assumes a centre of similarity at point O (Fig. 5a). Thus, the stress states of all points along a ray with initial point O are similar. In other words, the stress acting on a radial plane passing through O has a constant direction. In addition, it is assumed that the stress is proportional to the vertical distance from the surface of the soil.

The equilibrium state of the soil element depicted in Fig. 5a is described by:

$$\begin{cases} \dfrac{d\sigma}{d\theta} = 3\tau - \sin\theta \\ \dfrac{d\tau}{d\theta} = m\sigma - \cos\theta \end{cases}, \tag{2.12}$$

where $m = 2\lambda - 1$, and $\lambda = \sigma'/\sigma$ is the ratio between two conjugate normal stresses σ, σ' [28, p. 271]. [2]

The system of differential equations (2.12) has no closed-form solution. However, it can be shown that Rankine's solution is a particular solution [28, p. 271].

Caquot and Kérisel proposed an approximation method based on a Taylor expansion to integrate Equation (2.12) for different wall and backfill inclinations. The interested reader is referred to their book [28, pp. 271–291]. The resulting earth pressure coefficients for stand-ard parameter sets are given in tabular or in graphical form in books and national codes (e.g. [25, p. 78], [29, p. 226]).

The resulting failure lines are depicted in Fig. 5b. The stress state in region ① corresponds to Rankine's stress state. This region extends from the soil surface to the first Rankine failure line. In fact, Ravizé showed that in a granular soil mass with a plane surface of inclination $\beta = [-\varphi, \varphi]$ there is no other solution than Rankine's between the failure line and the free surface [30]. In region ②, the stress state rotates to satisfy the boundary condition at the wall interface.

This theory provides the same results as Coulomb's and Rankine's theories for the case $\beta = 0°$, $\delta = 0°$. Since an arbitrary wall friction δ can be considered and a nonplanar failure surface is assumed, however, Caquot and Kérisel's solution to Equation (2.12) gives more accurate results for arbitrary values β, δ. In fact, when considering arbitrary values β, δ the assumption of a planar failure is not conservative.

Caquot and Kérisel extended their solution to consider surface loads and cohesive soils by applying the method of superposition [28, pp. 291–300], which – when applied to solutions of the plasticity theory – only leads to approximate solutions (see, e.g., [31, p. 353]).

Sokolovskii's Theory

Sokolovskii considered the equilibrium equations of a soil medium

$$\begin{cases} \dfrac{\partial \sigma_x}{\partial x} + \dfrac{\partial \tau_{xy}}{\partial y} = 0 \\ \dfrac{\partial \sigma_y}{\partial y} + \dfrac{\partial \tau_{yx}}{\partial x} = \gamma \end{cases}, \tag{2.13}$$

and Mohr-Coulomb's failure criterion

$$\tau = c + \sigma \tan\varphi. \tag{2.14}$$

Based on Kötter's work [32], Sokolovskii applied the method of characteristics (often named the slip-line method) to obtain a numerical solution for the active earth pressure [33, pp. 110–120].

---

[2] Two stresses σ and σ' are conjugate if the stress σ acts on a surface element that coincides with the direction of the other stress σ' and vice versa.
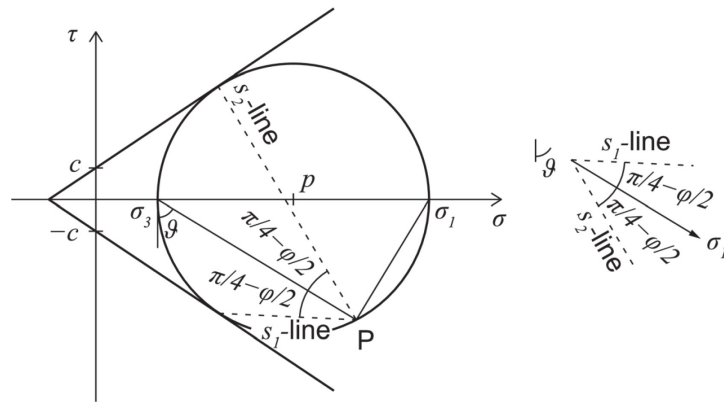
Fig. 6: Mohr's circle and stress characteristics.

For plane strain conditions and plastic failure, the stress state of a point can be described by two variables, namely the mean effective stress p and the direction of the major principal stress ϑ (see Fig. 6):

$$\sigma_{x,y} = p \mp \cos 2\vartheta \, (p \sin \varphi + c \cos \varphi)$$

$$\tau_{xy} = \sin 2\vartheta \, (p \sin \varphi + c \cos \varphi)$$

(2.15)

Inserting Equation (2.15) into Equation (2.13) results in a system of hyperbolic partial differential equations with characteristics [33], [34]:

$$\frac{\mathrm{d}x}{\mathrm{d}y} = \tan\left[\vartheta \pm \left(\frac{\pi}{4} - \frac{\varphi}{2}\right)\right].$$

(2.16)

Thus, the stress characteristics are inclined by $\vartheta \pm \left(\frac{\pi}{4} - \frac{\varphi}{2}\right)$ to the vertical, which corresponds to the inclination of the slip lines postulated by Sokolovskii, i.e. the s_1-line and s_2-line in Fig. 6 [33, p. 24]. Combining Equations (2.13), (2.15), and (2.16), it is possible to compute the stress state in a boundary value problem.
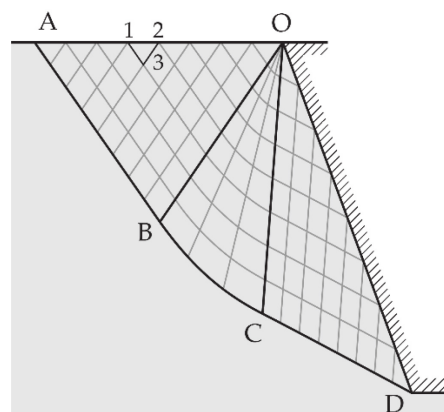
Fig. 7: Stress characteristics in the backfill of a retaining wall in the active state (adapted by the authors from [33]).

In the boundary value problem depicted in Fig. 7, the stress state is subdivided into three regions: OAB, OBC, and OCD. OB and OC are discontinuity lines. Sokolovskii showed that a discontinuity line corresponds to a slip line [33, p. 24]. Within a stress region, the spatial derivatives of the stresses and of the principal directions are continuous; across a discontinuity line, they are discontinuous.

The free surface OA is stress-free and the principal direction $\vartheta = 90°$. On OD, the principal direction ϑ is given by the interface friction. Region OBC is a fan centred at O, which is a

singularity point in the stress field. The stress characteristics and the change in stress can be calculated using Eqs. (2.13), (2.15), and (2.16) within a chosen discretisation mesh starting from the free surface OA. In Fig. 7, point 3 results from the intersection of the characteristics passing through 1 and 2. Next, all points at the same level as point 3 are determined before proceeding to the next level until the stress along OD can be determined. For a more detailed example, the reader is referred to [33], [34].

Sokolovskii's theory provides accurate results for the most common parameters, depending on the chosen discretisation size. In engineering practice, it is often used to estimate the passive earth pressure; tabled values based on this theory are sometimes even given in national design codes (e.g., [35, p. 21]). While accurate results are usually obtained, it is unknown whether the slip line method solution is an upper or a lower bound of the exact solution since the stress field is determined only in a finite region [31, p. 6].

2.1.2 Earth pressure theories for cantilever retaining walls

With the introduction of new building techniques and materials, such as reinforced concrete, civil engineers started to optimise the design of retaining walls to take full advantage of the tensile strength of the materials. This optimisation led to the design of lighter and slenderer cantilever retaining walls. The first documented technical notes on the design methods for cantilever retaining walls date to the beginning of the 20th century (see, e.g., [36]).

While different authors developed methods to design cantilever retaining walls in the 1910s (e.g. [37]–[40]), one of the most influential contributions was published by Mörsch in 1925 [41] in his work based on Coulomb's, Poncelet's, and Rankine's theories.
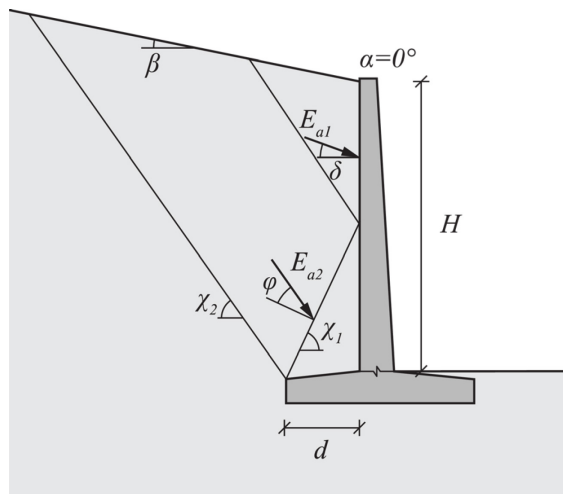
Fig. 8: Earth pressure acting on a retaining wall according to Mörsch [31].

Supported by the evidence collected in small-scale experiments, Mörsch proposed the model depicted in Fig. 8. In his experiments, Mörsch studied the failure mechanisms induced by a horizontal wall movement (i.e. a rigid body translational motion) that developed in the backfill of cantilever retaining walls. He observed the development of the sliding mechanism shown in Fig. 8, composed of three failure lines. The first failure line, inclined by χ_1 to the horizontal, defines a soil wedge resting on the wall base and the second, inclined by χ_2, delimits the failure region. The third failure line was observed only for the case $\chi_1 < \arctan \frac{H}{d}$, i.e. when the first failure intersects the wall and divides the failing body into two blocks. Mörsch could then show that the inclination of the failure lines χ_1, χ_2 correspond to those resulting from Rankine's theory, Equation (2.7). On the basis of these observa-

tions, he developed a graphical procedure to calculate the earth pressure at failure on cantilever retaining walls. This graphical method was still used in the 1960s and later (see, e.g., [42]). The procedure was as follows [42, pp. 50–54]:

1. Determine the angle χ_1 following Mörsch's graphical procedure (see Appendix I.3).
2. Calculate the earth pressure using Poncelet's method.

An equivalent (and, nowadays, less time-consuming) procedure is the following:

1. Determine the angle χ_1 using Equation (2.7).
2. Calculate the earth pressures E_{a1} and E_{a2} (Fig. 8) using Coulomb's formula, Equation (2.2):
    i. E_{a1} acts on a vertical wall ($\alpha = 0°$; in the specific case of Fig. 8) with wall friction angle δ;
    ii. E_{a2} acts on a fictitious wall with inclination $\alpha = \frac{\pi}{2} - \chi_1$ and wall friction angle $\delta = \varphi$.

The two procedures are equivalent since Mörsch's graphical procedure results in the same angles as Rankine's theory, and Poncelet's method is just a graphical translation of Coulomb's theory.

2.1.3   3D active earth pressure

The earth pressure acting on narrow walls (i.e., characterised by a high height-to-width ratio h/b) is lower than on wide walls. In fact, excessive displacement of a narrow wall will lead to a spatial stress redistribution caused by arching, which leads to a lower force on the wall. Previous studies have investigated the 3D earth pressure and have suggested different simplified analytical methods to quantify it. For example, Piaskowski and Kowalewski [43] proposed a simple and widespread method based on a limit equilibrium solution. However, their solution can only be treated as a rough approximation, as the assumed mechanism is not kinematically admissible. Karstedt later proposed a kinematically admissible mechanism (with the assumption of associated flow) [44], but the determination of the earth pressure was subject to some assumptions (above all, the location of the resultant earth pressure force) and a practical description of the procedure is not available [45]. Walz and Prager [46] extended Terzaghi's earth pressure theory [47] to solve three-dimensional problems. This method assumes a soil wedge and solves the equilibrium by considering infinitely thin horizontal slices. On the two lateral sides, a frictional force is assumed. Although the considered mechanism is not kinematically admissible, this method was found to best match experimental results in [45].

The method found in DIN 4085 [35] is often used in engineering practice. It is based on Piaskowski and Kowaleski's method [43] and defines the 3D earth pressure as a reduction of the plane strain value:

$$E_{ah}^{3D} = \mu_{ah} \cdot E_{ah}^{2D}. \tag{2.17}$$

The reduction factor is defined as:

$$\mu_{ah} = 1 - \frac{2}{\pi}\left[\left(1 + \frac{1}{\hat{\varphi}^2}\right) \cdot \arctan \hat{\varphi} - \frac{1}{\hat{\varphi}}\right], \tag{2.18}$$

where

$$\hat{\varphi} = \frac{\varphi \cdot h}{2b}, \tag{2.19}$$

with h as the wall height and b as the wall width. This method is only valid for $\alpha = 0°$, $\beta = 0°$, $\delta = 0°$; in all other cases, it is stated that the method provides only an approximation [35]. However, due to the kinematical inadmissibility of the assumed mechanism, the solution should be treated for all cases as an approximate solution.

Tom Wörden conducted a thorough study of 3D earth pressure, including experimental and numerical analyses [45]. He observed that a height-to-width ratio $\frac{h}{b} = 3$ led to a reduction in earth pressure of about 25-35% compared to the plane strain case. Due to the stress redistribution, a stress increase was observed on both sides of the wall to a distance ranging from $0.5b$ to b. Furthermore, the evolution of the earth pressure was measured. A rotation about the foot between 3 and 5 mrad was needed to reach the minimum earth pressure value. The experiments were used to validate a FEM model used to carry out a parametric study. The parametric study showed that the most influential parameter in the reduction of the three-dimensional earth pressure is the ratio h/b, while the influence of the soil friction was less important and the wall friction angle only had a marginal role. Additionally, numerical simulations based on the discrete element method (DEM) were carried out to study the stress redistribution at a particle level, although only at a qualitative level, as rather simplistic assumptions were made (i.e. all particles had the same radius).

2.1.4 Earth pressure at rest

The following definition of the earth pressure at rest was given by Terzaghi [48, pp. 26–27]: "If the nature of a mass of soil and its geological history justify the assumption that the ratio σ_{h0}/σ_{v0} is approximately the same for every point of the mass, it will be called the coefficient of earth pressure at rest and designated by the symbol K_0". In general, the "rest state" in the soil is defined as the state characterised by zero horizontal deformation, as in an infinite half-space. Thus, the stress state corresponds to that observed in a uniaxial consolidation (e.g. in an oedometer test).

In engineering practice, the earth pressure at rest is commonly assumed for the design of nearly undeformable structures or when it is necessary to minimise the deformations of the backfill. However, knowledge of the earth pressure at rest is also needed if it cannot be guaranteed that a wall has sufficient deformation capacity to allow a complete soil unloading to the active state before reaching structural failure. In the case of walls damaged by corrosion, knowledge of soil behaviour in a one-dimensional consolidation is needed to define the actual earth pressure acting on the wall.

Based on experience, Terzaghi proposed the following values for the coefficient of earth pressure at rest: $K_0 \approx 0.5$ for dense and $K_0 \approx 0.4$ for loose sand. If the soil is compacted layer by layer, the value should instead be $K_0 \approx 0.8$ [49, p. 148]. Alternatively, two theories define the earth pressure at rest. The first assumes an isotropic, linear elastic half-space defined by a horizontal plane subjected to gravity and defines the coefficient of earth pressure at rest as (e.g. [48, p. 372]):

$$K_0 = \frac{\nu}{1 - \nu}. \tag{2.20}$$

This results from the equilibrium equations, Hooke's law, and the additional requirement that $\varepsilon_h = 0$. ν is the Poisson's ratio. The drawback of this method is that it does not consider the soil volumetric yield observed in the soil (e.g. in an oedometer test). Furthermore, it is challenging to precisely determine the Poisson's ratio in the laboratory.

Jáky [50] proposed a second approach. Jáky considered the soil wedge OAE depicted in Fig. 9 and asserted that the horizontal stress acting on the plane OC is the earth pressure at rest. The stress value was calculated by solving the equilibrium equations assuming Rankine's failure in regions OAB and ODE and by guessing the distribution of the shear stresses in the region OBD, which cannot be in a state of failure. The resulting coefficient of earth pressure at rest was:

$$K_0 = (1 - \sin\varphi) \cdot \frac{1 + \frac{2}{3}\sin\varphi}{1 + \sin\varphi}, \tag{2.21}$$

where φ is the soil internal friction angle. In a later publication, Jáky then cited his previously developed formula for the earth pressure at rest as we know it today [51], [52]:

$$K_0 = 1 - \sin\varphi , \qquad (2.22)$$

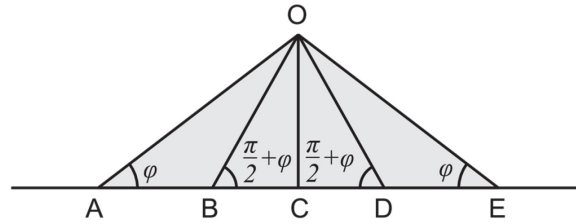which results in a slightly higher coefficient.

Fig. 9: *The soil wedge considered by Jáky in [40].*

Different studies have confirmed the validity of Jáky's Equation (2.22) experimentally, although with somewhat contrasting conclusions: Mesri and Hayat [53] showed good experimental agreement on cohesionless soil and normally consolidated clay for $\varphi = \varphi_{cv}$, whereas Mayne and Kulhawi [54] argued that it is more accurate for normally consolidated clay and only fairly agrees with experimental data on cohesionless soil. Lee et al. [55] argued that two different friction angles should be applied on loosely and densely packed granular soil, i.e. the interparticle friction angle for loose soil, and the residual friction angle φ_{cv} for dense soil. In a further study, they showed that a correlation between K_0 is effective only for spherical glass beads, while it may be inaccurate for angular grains [56]. Talesnick et al. [57] further argued that all experimental data obtained in previous research was influenced by the deflection of the used pressure sensors and boundary effects (i.e. frictional resistance) and is therefore not conclusive. They carried out oedometric tests using null soil pressure gauges [58] (i.e. nondeflecting pressure sensors), showing that deflecting sensors lead to unreliable results.

Jáky's theoretical assumptions were instead criticised by Michalowski [52]. First, Michalowski argued that Jáky's assumption of a soil wedge is wrong since the strain state is two-dimensional (and not one-dimensional, as it should be). Second, he showed that Jáky's assumption of the shear stress distribution in OBD leads to unrealistic normal stress distributions on the base BD. Third, he questions the meaning of the relation of the stress state at rest to the shear resistance φ, although the soil is below the yielding level (in shearing).

The discrete element method has been recently used to study the earth pressure coefficient at rest in oedometric tests. Gu et al. showed that K_0 decreases as the soil relative density increases and found that Jáky's formula gives a better prediction of the earth pressure at rest for $\varphi = \varphi_{\mathrm{peak}}$ [59]. In a later study, the same authors found a good correlation between K_0 and the small strain shear stiffness.

K_0 in the unloading phase

The evolution of the stresses during axial unloading of a radially confined soil sample (e.g. in an oedometer test) was determined experimentally on clay by Brooker and Ireland [60]. They showed that the coefficient of earth pressure at rest in the unloading phase depends on the stress history. For an overconsolidation ratio (OCR) larger than 20, K_0 approached the coefficient of passive earth pressure K_p. Based on these results, Schmidt [60] suggested the following relationship between the coefficient of earth pressure at rest during virgin loading K_0 and during unloading K_0':

$$K_0' = K_0 \cdot \left(\frac{\sigma_{v,\mathrm{max}}}{\sigma_v}\right)^a =: K_0 \cdot \mathrm{OCR}^a , \qquad (2.23)$$

where a is an exponent (sometimes called the rebound exponent, e.g. in [54]) that can be fitted empirically. Schmidt suggested a relationship between the exponent a and the soil friction angle φ. Mayne and Kulhawy recommended $a = \sin\varphi$ based on an extensive study on clay, silt and sand [54]. Again, the empirical results were disproved by Talesnick et al. [57], who obtained lower values for the exponent a (i.e. $a \approx 0.37$ on sand; using Mayne and Kulhawy's formula, a way too low friction value of $\varphi \approx 22°$ would result).

2.1.5 Effects of soil compaction

The effects of soil compaction on the soil are twofold. First, soil compaction causes a shear strain accumulation accompanied by volumetric compression or dilation [61], [62]. Second, increased stresses remain in the soil. Previous studies investigated the effects of compaction on the soil lateral stress. For example, Spotka [63] observed experimentally that the lateral soil stress increases with increasing compaction work (as a result of strain accumulation) and that the maximum lateral stress is reached inside the influence depth of the compacting device (i.e. where the device causes an actual increase in vertical stress). He further observed that the compaction-induced stresses tend to disappear with increasing depth. These results were later proven by Chen and Fang [64]. They also showed that the vertical stress after removing the compaction load is a linear function of the depth and unit weight. Further, they observed that the lateral earth pressure close to the soil surface approaches the passive earth pressure while it tends to the earth pressure at rest with increasing depth (i.e. outside the compaction influence depth). Among the analytical methods proposed in the past (e.g. [63], [65], [66]), the most considered method in practice is that proposed by Broms [65] and depicted in Fig. 10.
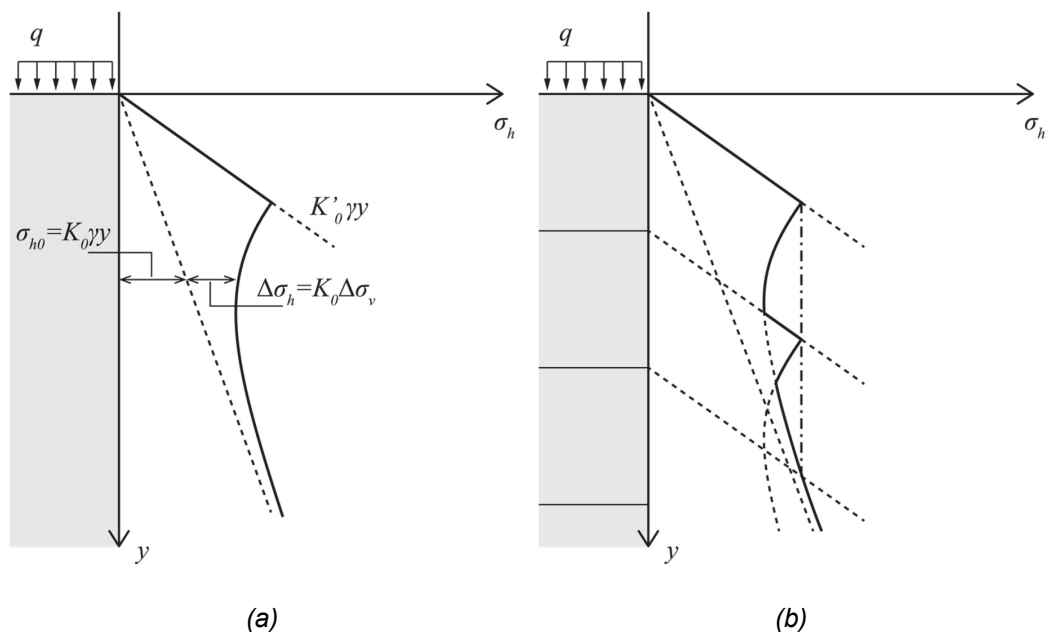

Fig. 10: Compaction-induced earth pressure according to Broms [65]: (a) for a single layer; (b) for multiple layers.

Broms considered a cohesionless soil load characterised by the coefficient of earth pressure at rest K_0 during loading and K_0' during unloading. In a sample calculation, Broms assumed $K_0 = 0.5$ and $K_0' = 2.0$. The first results from Jáky's formula and a friction angle of 30°; the second is also said to correspond to the same friction angle, although it is not explained how it was obtained [65, p. 380]. The horizontal earth pressure is then defined as (Fig. 10a):

$$\sigma_{h0} = \min\{K_0(\gamma y + \Delta\sigma_v), K_0'\gamma y\}\,, \tag{2.24}$$

where $\Delta\sigma_v$ is the additional vertical stress due to the compaction load q according to Boussinesq's solution [67]. If the compaction is carried out on multiple layers, the same formula is applied to the single layers as in Fig. 10b, and the outer envelope is considered. Sometimes, the procedure is simplified by assuming the dash-dotted envelope in Fig. 10b.
Despite its simplicity, this procedure is theoretically inaccurate under multiple aspects. First, the vertical stresses induced by the compacting device are calculated based on an elastic theory (i.e. Boussinesq's theory), whereas yielding occurs during compaction, as shown by Chen et al. [64]. Second, the compaction-induced lateral stress is computed assuming the coefficients K_0 and K_0', which implicitly presupposes a one-dimensional strain path, while it is two-dimensional because of the finite size of the compacting device. Third,

the coefficient of earth pressure at rest during unloading K_0' is assumed to be constant over the soil depth, while in reality it is not. Indeed, it decreases with depth, as the OCR does (see Equation (2.23)).

Later, Duncan and Seed [68] proposed a similar procedure, assuming a more sophisticated hysteretic model for the K_0-loading. Their procedure generally results in lower pressures than Broms'. Duncan and Seed validated their method against field experiments concluding that it agreed well with the measurements. Chen et al. [64] later showed that both methods agree with laboratory experiments in the upper backfill region. In contrast, they tend to overestimate the horizontal stresses in the middle region. To be noted is that the agreement of Broms' method with reality is highly dependent on the assumed value for K_0'.

2.1.6 Earth pressure behind rotating walls and displacement-dependent evolution

The active and passive limits of the earth pressure represent the lower and upper values that the earth pressure on a wall may assume. Any intermediate value is admissible during the lifetime of a retaining wall. Although the two limits can be determined assuming a rigid plastic material using techniques such as limit analysis or the limit equilibrium, the earth pressure evolution between the two limits is more complicated to quantify. Different studies conducted in the past investigated the displacement-dependent evolution of the earth pressure experimentally, numerically, and analytically. Sherif et al. [69] conducted a series of tests on rigid retaining walls rotating at their base. They concluded that with increasing wall rotation, the state of active stress propagates downward from the surface of the soil to the wall foundation leading, in the wall, ultimately leading to a linear distributed earth pressure corresponding to Coulomb's solution. Fang and Ishibashi confuted this last result two years later [70]. They showed evidence that a steady state was reached after the imposed rotation of 8 mrad by pointing out that the total earth load and its point of application and the mobilised wall friction reached a constant value. It was then argued that Coulomb's solution would underestimate the earth pressure acting on walls rotating about the base, as a fully active state will not be achieved in the backfill as a region of increased stress was observed in the lower part of the wall. In fact, they showed that the point of application of the total earth load was 0.28H above the foundation and would never reach 0.33H, which would be expected in the case of a linearly distributed pressure according to Coulomb (H is the height of the wall). However, the pressure distribution at steady state is not shown. Thus, it is difficult to judge whether the unexpected point of application results from noisy measurements since integrating the pressures (where random noise partially cancels out) leads to the value given by Coulomb's solution. One year earlier, Handy [71] had analytically shown how arching affects the earth pressure causing a nonlinear distribution. Hardy's and Fang and Ishibashi's results were later used to develop theories to quantify the evolution of the earth pressure or the active earth pressure acting on walls subjected to a rotation about the base. For example, Chang [72] developed a semiempirical method to determine the earth pressure distribution on rotating walls. The method could be used to model progressive failure behind the walls and qualitatively showed earth pressure distributions similar to those observed by Fang and Ishibashi. However, the model relies on some strong assumptions and simplifications, and its application in general practical cases remains dubious. More recently, Patel and Deb [73] developed an analytical model based on experimental observations to calculate the earth pressure distribution for an active stage when sufficient lateral movement of the wall has occurred. In support of their model, they experimentally showed that there is a "dead zone" caused by arching exists near the base of the rotating wall, where the soil does not yield. This dead zone was shown by PIV measurements and, according to the authors, leads to a nonlinear pressure distribution on the wall. However, boundary effects strongly affect PIV measurements (i.e. the wall friction mobilised on the interface between sand and glass wall). Nadukuru and Michalowski [74] studied the effect of arching on the active earth pressure running discrete element simulations showing that the active load for the translational and rotational (rotation about the bottom) modes are equivalent for a rough wall. The resulting pressure distribution at the active state was found to be linear in the case of a rotation about the bottom, confuting the results of previous studies.

2.2   Conventional design and verification of retaining walls

In Switzerland, as in many other European countries, the *limit state design* method is applied ([75], [76]). A distinction is made between *ultimate limit states* and *serviceability limit states* [75], [76]. The design of geotechnical structures is further subdivided into two main parts: the *geotechnical* design and the *structural* design. The geotechnical design aims to prevent global or local soil collapses, such as a general stability failure (Fig. 11a) or a foundation failure (i.e., bearing capacity failure or sliding; Fig. 11b-c). The structural design aims to prevent structural failure (e.g., bending or shear failure at the construction joint; Fig. 11d-e) and to satisfy the serviceability limit states (e.g., crack control, deflection control).

(a)

(b)   *(c)*

(d)   *(e)*
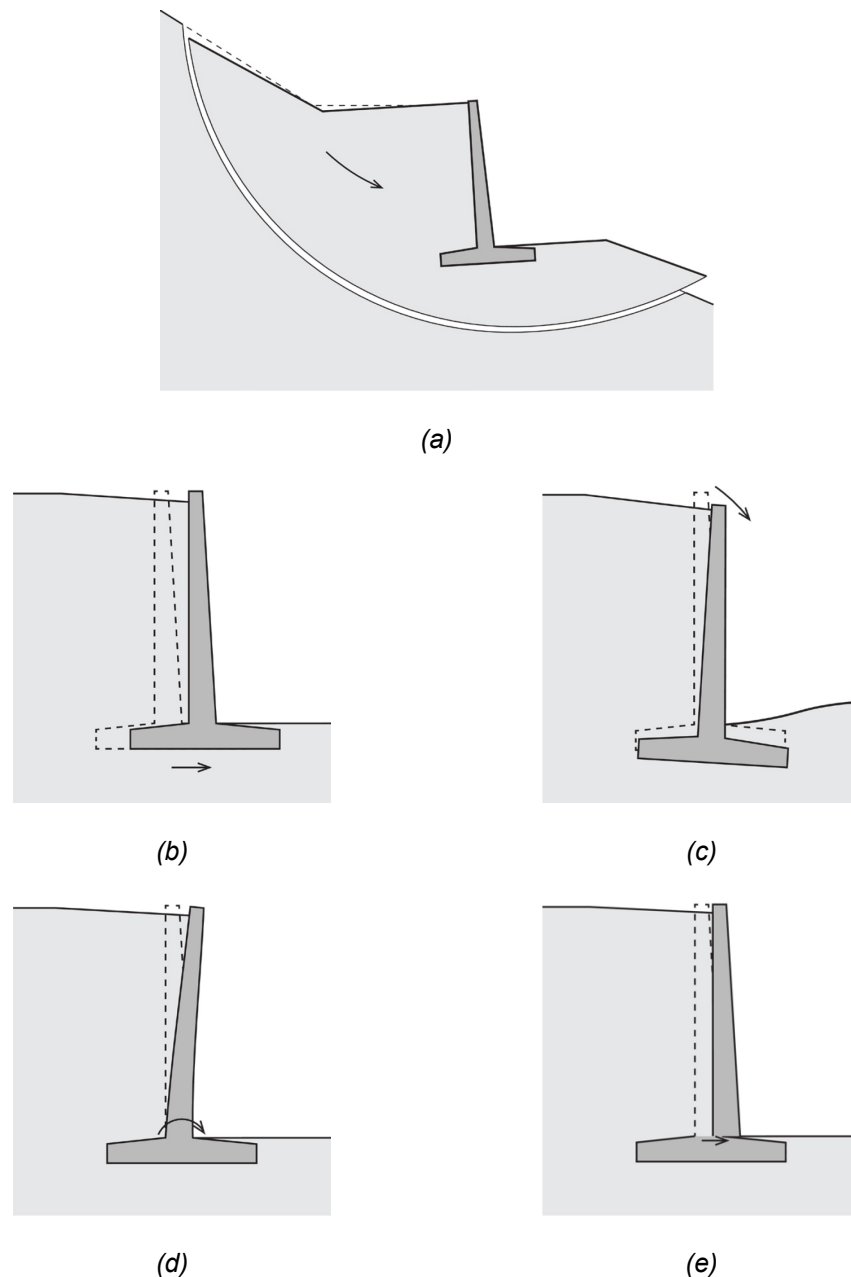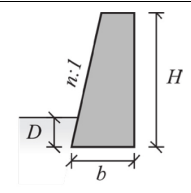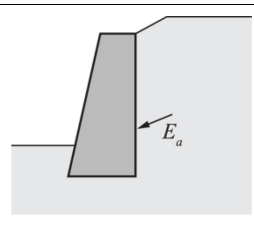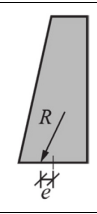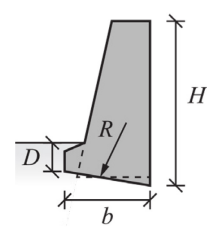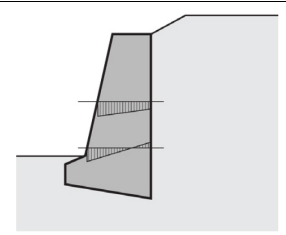
Fig. 11: Possible types of failure for cantilever retaining walls: (a) global soil failure, (b) sliding failure, (c) bearing capacity failure, (d) wall bending failure, and (e) wall shear failure.

In engineering practice, retaining walls are usually designed using simplified analytical approaches. The system is divided into three subsystems: the backfill, the wall, and the soil underneath the foundation. The wall must then be designed to withstand the pressure exerted by the backfill and transfer it to the foundation without causing sliding or bearing

capacity failure. Typically, the engineer relies on his experience to estimate the wall and foundation dimensions. The dimensions are then further refined to meet safety and economic requirements. In the second half of the 20th century, as computers were not yet widespread in the construction industry, this iterative procedure was seen as particularly time consuming [42, p. 14]. To relieve engineers of routine work, the Swiss Association of Road and Traffic Experts (VSS) decided to write and publish new guidelines and design tables for retaining walls [42, pp. 9–10]. The first volume was published in 1966. It describes the general design principles and methods for gravity and cantilever walls and contains design tables for gravity walls. Design tables for cantilever walls were planned for the second volume [42, p. 93] but were never published. The procedure for the design of retaining walls – valid for all retaining wall types – is presented in Tab. 2. This procedure has been applied extensively in the following years (e.g., [77, p. 1], [78, p. 15]) and is still commonly used today (e.g., [10, pp. 109–138]), with the only difference being that partial safety factors must be considered since the introduction of the national code SIA 267 [79].

Tab. 2: Procedure for the design of retaining walls as described in [42] (adapted by the authors).

1.	Determination of soil parameters.	γ, φ, c
2.	Selection of the type of wall and estimation of its dimensions.	
3.	Determination of the active earth pressure on the wall.	
4.	Determination of the resultant force (considering the earth pressure and the wall weight) at the base of the foundation. Verification of the "line of resultant pressure" (German *Drucklinie*). The resulting force must be within the wall body for its entire height (i.e., the wall must not overturn; see, e.g., [42, pp. 110–111]).	
5.	Design of the wall foundation (width and inclination) to provide safety against sliding and bearing capacity.	
6.	Verification of concrete and steel stresses.	

Furthermore, if necessary:

7. Verification of expected settlements and tilts.
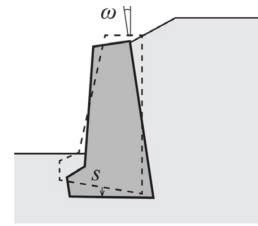
8. Verification of safety against global soil failure.
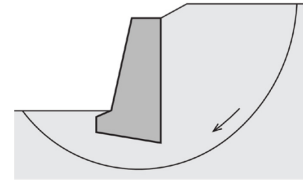
9. Verification of wall stability during each construction phase.
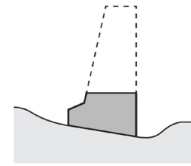
In the 1980s, the Heiniger & Partner company developed a computer program based on the VSS guidelines. The program reached at least version 3.0 [80] (see Fig. 12) and was often used by engineers to design retaining walls (e.g., [81, p. 2]).
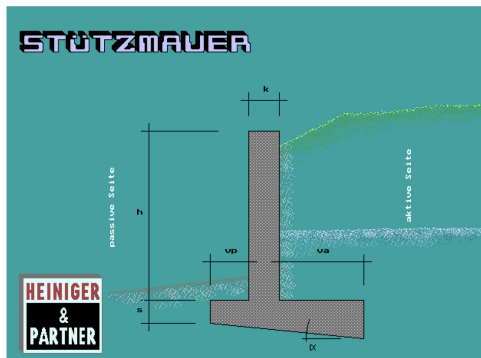
(a)   *(b)*

Fig. 12: *The third version of Stützmauer software by Heiniger & Partner running on MS-DOS [80]. (a) The splash screen; (b) The configuration page of a project. "VSS" is the default calculation method and is based on [42].*

The main steps of the geotechnical and structural design (steps 2 to 6 in Tab. 2) are depicted in Fig. 13 for a cantilever retaining wall.

All verifications are usually carried out in a decoupled fashion. The system is divided into two parts: the first includes the wall and the backfill and is used to determine the forces acting on the second subsystem, the wall foundation and the soil underneath it, which provides the resistance. The safety against different failure modes in Fig. 13b-f is assessed by comparing the actions with the resistances. In the following, the conventional procedure for each step in Fig. 13b-f is explained.
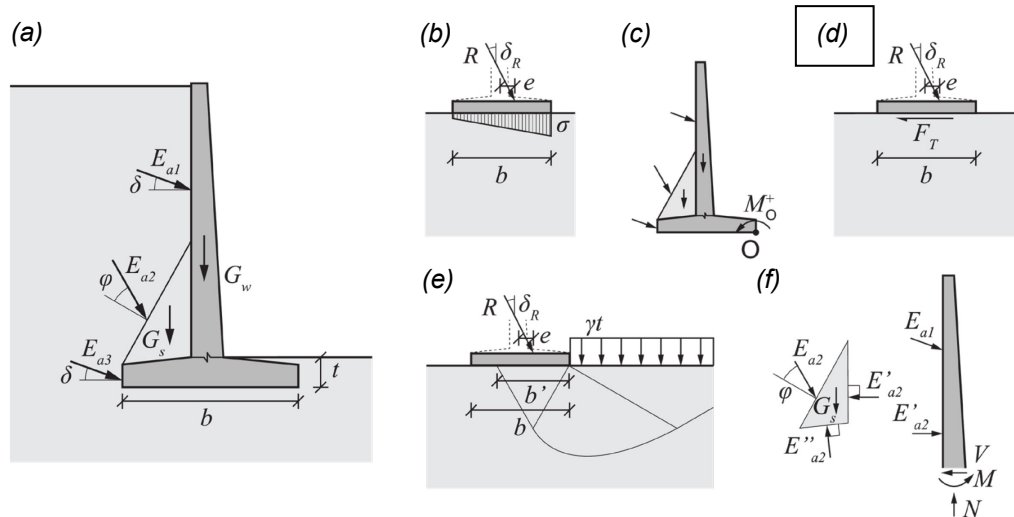
Fig. 13: *State-of-the-art design procedure for a retaining wall. (a) Determination of the earth pressure and the resultant force on the foundation; (b) verification against overturning through the eccentricity of the force resultant; (c) verification against overturning through the moment about O; (d) verification against sliding; (e) verification against bearing capacity failure; (f) verification against structural failure.*

2.2.1 Earth pressure determination (Fig. 13a)

As a first step, the earth pressures E_{ai} and the self-weights G_i are determined (Fig. 13a) as shown in Section 2.1.2.

As discussed previously, this limit equilibrium solution corresponds to a rigid body translation of the wall (i.e., sliding). However, the force resulting from it is used to verify all relevant failure modes Fig. 13b-e. This assumption is generally conservative (see Section 3.5.3).

The VSS guidelines suggested using $\delta = \frac{2}{3}\varphi$ as the friction in the soil-wall interface (for the backfill) [42, p. 98]. This value, as explained in [82, p. 72], is a mere conservative assumption based on the guidelines that prescribe a gravelly drainage layer behind every retaining wall. Based on experiments, the friction value between a concrete wall and gravel was determined as $\delta = 30°$. So, there are two cases. The first case represents a backfill with $\varphi < 30°$. In that case, the soil-wall interface is stronger than the soil itself, and failure will occur entirely in the soil. Therefore, the mobilised friction behind the wall is $\delta = \varphi$. The second case represents a backfill with $\delta \geq 30°$. In that case, the soil-wall interface is weaker than the soil and failure will occur at the interface. Therefore, the mobilised friction is $\delta = 30°$. Assuming $\delta = \frac{2}{3}\varphi$ is, therefore, a safe and reasonable assumption up to a soil friction angle of $\varphi = 45°$ [82, p. 72]. Today, this value is still widely accepted and recommended by several books and national codes (e.g. [11, p. 159], [25, p. 20]).

Passive earth pressure on retaining walls is generally not considered for safety reasons. Indeed, there is no guarantee that this will remain permanently effective after a wall has been built. In addition, the full passive earth pressure will hardly ever be achieved since the displacement required for its mobilisation is considerably greater than that for the active earth pressure [42, p. 62].

2.2.2 Safety against overturning (Fig. 13b-c)

This verification aims to prevent the wall from overturning without soil failure beneath the foundation (i.e., no bearing capacity failure). In engineering practice, two different failure modes are usually considered to cause the overturn.

In the first mode, Fig. 13b, it is assumed that the soil below the foundation undergoes purely elastic deformation. First, the resultant force R acting on the foundation and its eccentricity

e are determined based on the forces determined for the subsystem in Fig. 13a. The contact pressure at the soil-foundation interface is assumed to be linear, and no tensional stresses are allowed. Under these assumptions, the wall is stable against overturning, provided that the eccentricity of R is less than

$$ e_{\text{limit}} = \frac{b}{2} \cdot \frac{2}{3} = \frac{b}{3} \,. \tag{2.25} $$

So, the following relation must be fulfilled:

$$ e \leq e_{\text{limit}} = \frac{b}{3} \,. \tag{2.26} $$

In the second mode, Fig. 13c, it is assumed that the soil underneath the foundation is rigid. The only way for the wall to be overturned is, therefore, to rotate about the outermost point of the foundation O (Fig. 13c). Is the total moment M_O positive (positive direction as drawn in Fig. 13c), then the wall is stable. Before the publication of the national code SIA 267 – which first introduced the concept of partial safety factors [83, p. 267] –, the safety against overturning was commonly described by a safety factor, defined as:

$$ SF = \frac{\sum M_{\text{res}}^{O}}{\sum M_{\text{act}}^{O}} \,, \tag{2.27} $$

where $\sum M_{\text{res}}^{O}$ is the sum of all resisting moments (i.e., the positive moments according to Fig. 13c) and $\sum M_{\text{act}}^{O}$ the sum of all acting moments (i.e., the negative moments according to Fig. 13c). The required safety factor was not consistently defined and varied between 1.5 and 2.0 [84].

While today the first mode (Fig. 13b) is almost exclusively considered when designing a retaining wall (e.g., [10, pp. 119–120]), in the past, both modes were often considered (e.g., [78], [80]). However, it can be easily demonstrated that verifying the second mode (Fig. 13c) is less strict. For the case $SF = 1$, it follows:

$$ SF = 1 \iff \sum M_{\text{res}}^{O} = \sum M_{\text{act}}^{O} \iff M^{O} = 0 \iff e = \frac{b}{2} \,. \tag{2.28} $$

So when $SF = 1$ according to the failure mode in Fig. 13c, the system is still considered unstable according to the failure mode in Fig. 13b.

In the VSS guidelines and design tables, only the second failure mode (Fig. 13c) was considered [42, pp. 13 and 110–111].

2.2.3 Safety against sliding (Fig. 13d)

This verification aims to prevent the wall from sliding along the soil-foundation interface. First, the resultant force R acting on the foundation and its eccentricity e are determined based on the forces determined for the subsystem in Fig. 13a. The horizontal component $R_H = R \sin \delta_R$ is the acting force. The resisting force is calculated by assuming Coulomb's friction law. So,

$$ F_T = R_V \tan \delta_{\text{found}} = R \cos \delta_R \tan \delta_{\text{found}} \,, \tag{2.29} $$

where δ_{found} is the friction angle at the soil-foundation interface. Its value is often assumed to be equal to the friction angle of the soil itself [42, p. 68], $\delta_{\text{found}} = \varphi$. This assumption is usually safe, as the wall foundation is cast in place without a bottom formwork. Therefore, the concrete can build a rough interface with the soil, and it can be assumed that the failure occurs just underneath this interface (i.e. entirely in the soil).

Safety against sliding is provided if [42, p. 86]:

$$SF = \frac{\tan \delta_{\text{found}}}{\tan \delta_R} \geq 1.5 \ . \tag{2.30}$$

2.2.4 Safety against bearing capacity failure (Fig. 13e)

This verification aims to prevent the bearing capacity failure of the foundation layer. First, the resultant force R acting on the foundation and its eccentricity e are determined based on the forces determined for the subsystem in Fig. 13a. The bearing capacity of the soil σ_f is then estimated using the theory first proposed by Terzaghi [48] and later extended by several authors (e.g., [74], [75]), as described, e.g., in [11, pp. 142–153], [42, pp. 70–82], [85].

Safety against bearing capacity failure is provided if [42, p. 86]:

$$SF = \frac{\sigma_f \cdot B'}{R_V} \geq 2.0 \ . \tag{2.31}$$

where R_V is the vertical component of the resultant force R.

2.2.5 Safety against structural failure (Fig. 13f)

The structural design aims to prevent bending and shear failure of the wall. First, the stress resultants (i.e., the normal force, the shear force, and the bending moment) are determined. Then, the reinforcement is designed and verified so that

$$E \leq R \ . \tag{2.32}$$

where E is the acting stress resultant, and R is the structure's resistance.

The method used to calculate the stress resultants found was not univocal: two different assumptions (Fig. 14) are found in old documents, such as reports, construction files, and software.

(a)   *(b)*
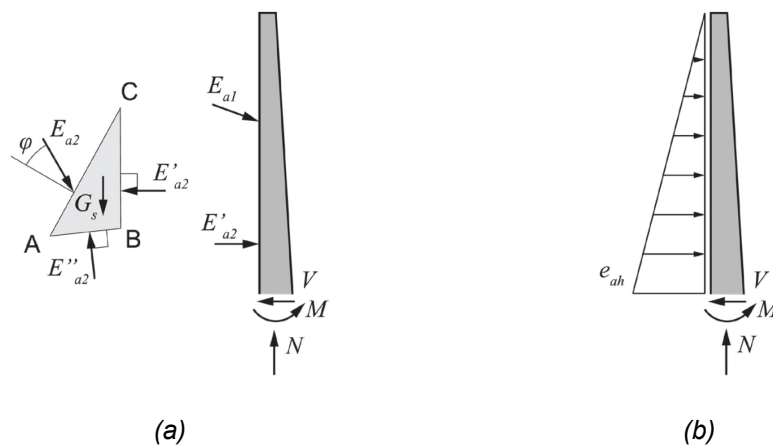
Fig. 14: *(a) Determination of the resultant stresses based on the earth pressures calculated in Fig. 13a; (b) Determination of the resultant stresses based on Coulomb's earth pressure directly applied behind the wall.*

The first assumption, depicted in Fig. 14a, is used by Heiniger & Partner's design software [80] and is used in old construction files of existing walls (e.g., [77]). This method assumes the earth pressure determined in Fig. 13a. The earth pressure E_{a2} is transferred to the wall using the limit equilibrium method by assuming that the soil wedge $\widehat{ABC}$ is at rest. Therefore, the forces E'_{a2} and E''_{a2} act perpendicular to the edges $\overline{AB}$ and $\overline{BC}$. The magnitude of E'_{a2} and

E_{a2}'' can be calculated by formulating the horizontal and vertical equilibrium equations. Often, the horizontal component of E_{a2}'' is ignored (e.g., in [80]), so that $E_{a2}' = E_{a2,h}$ even in the case that the base of the wedge is inclined. The earth pressure distribution is assumed to be linear.

The second assumption (Fig. 14b) is used in old construction files (e.g., [78]) and in a preliminary draft of VSS book [86]. Here, for the design of the wall reinforcement, it is assumed that Coulomb's earth pressure acts on the wall back face. The earth pressure is therefore given as:

$$e_{ah} = \gamma y \cdot \overline{K}_{ah} \tag{2.33}$$

where the coefficient of horizontal earth pressure $\overline{K}_{ah}$ results from Equation (2.4). It can be shown that this method represents a proper lower bound of the exact solution based on plasticity theory (see Section 3.4.1).

3 The ultimate state of corrosion-damaged retaining walls

In this section, the ultimate limit state of corrosion-damaged cantilever retaining walls is determined using limit analysis. First, the key concepts of limit analysis are briefly summarised. The reader is referred to [9] for a more thorough description. Then, the main failure modes of cantilever retaining walls are discussed, and the relevant failure mode for corrosion-damaged walls is discussed. Finally, an analytical solution for that failure mode is presented.

3.1 Introduction to limit analysis

The behaviour of granular soil is often described as an elastoplastic material. In the framework of elastoplasticity, soil loading (or unloading) is characterised by a first reversible elastic response followed by yielding and, eventually, failure (i.e., unconstrained plastic flow). Yielding is characterised by hardening, which leads to a peak stress value σ_{peak}, and softening, which leads to a stress reduction to the residual value σ_{res} (Fig. 15). While dense soils experience both hardening and softening, loose soils only experience hardening, and a peak stress value is never reached.
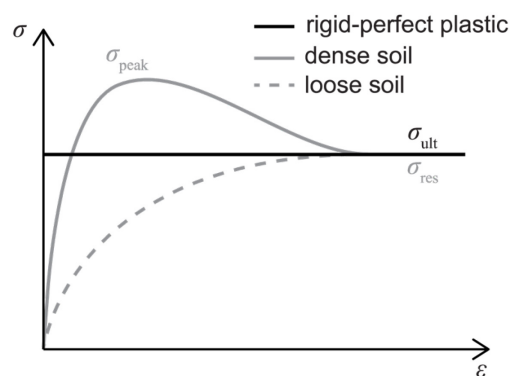

Fig. 15: Typical stress-strain behaviour of an elastoplastic soil (grey) and of a rigid-perfect plastic material (black).

A complete analysis of this process, even for simple boundary value problems, requires the use of numerical methods, such as the finite element method (FEM) and stress update algorithms for nonlinear materials (e.g., [87, pp. 294–308]) that have high computational costs. However, a complete analysis is often unnecessary in geotechnical engineering, as the ultimate limit state is decisive for many problems (e.g., the design of retaining structures or slope stabilising measures). In such problems, the engineer identifies the acting forces (i.e., surcharge loads, soil weight, etc.) and must design the structure to guarantee a prescribed safety margin against collapse. It is then clear that only the collapse load (i.e., the set of forces that leads to unconstrained plastic flow at constant stresses) is required.

In the history of geotechnical engineering, several methods have been developed and applied to determine the collapse load for common geotechnical problems. Limit equilibrium, slip-line method, and limit analysis are the most used. Although the first two methods provide only approximate solutions, the limit analysis provides proper lower and upper bounds of the exact solution based on plasticity theory.
When using the limit equilibrium method, the engineer must identify potential failure lines (straight or curved). Subsequently, the body enclosed between the failure lines is cut free, the acting forces are applied (mostly, Coulomb's friction is assumed), and the equilibrium equations are formulated. The position of the failure lines is then optimised to find the most critical failure mechanism, leading to the extreme value of the collapse load. As the stress

field in the whole soil body remains undefined, and the kinematic boundary conditions are not considered, the resulting solution is not guaranteed to be an upper or a lower bound of the exact solution [31, p. 7], [88, p. 37].

In a slip-line solution, it is usually assumed that the region near the structure (e.g., behind a retaining wall) is in plastic equilibrium. However, the stress equilibrium and yield conditions are generally only satisfied inside the region where the slip line field is defined. In addition, the stress-strain relationship is ignored in the slip-line method. For these reasons, the obtained solution is not guaranteed to be an upper or lower bound of the exact solution [31, pp. 6–7], [88, p. 29].

Limit analysis has been increasingly used to overcome the limits of the limit equilibrium and the slip-line methods. Two different principles are used to find the bounds of the true collapse load. The first, called the static principle, defines a stress field that satisfies the equilibrium equations and boundary conditions and nowhere violates the yield criterion. The second, called the kinematic principle, defines a velocity field compatible with the kinematic boundary conditions and satisfies the strain and velocity compatibility. It can be shown that the solutions of the two methods are rigorous bounds of the true collapse load.

The following is a brief introduction to the most relevant assumptions and theorems of limit analysis. For a complete description, the reader is referred, e.g., to [9], [31], [89], [90].

Material behaviour

As limit analysis aims to calculate the collapse load of a given boundary value problem, a rigid, perfectly plastic material can be assumed. The stress-strain response of such a material is a horizontal line (Fig. 15, black line) and is described by the failure criterion:

$$f\left(\underline{\sigma}\right) = 0, \tag{3.1}$$

where $\underline{\sigma}$ is the stress tensor. The failure criterion of a perfectly plastic material depends only on the stress state and is independent of the strains.

The assumption of perfect plasticity allows for the formulation of more straightforward analytical calculations. Under the assumption of a linear yield surface, the correctness of the resulting collapse load is not affected, provided that the correct value of the ultimate strength σ_{ult} is chosen. In general, the ultimate strength must be chosen equal to the residual strength, $\sigma_{ult} = \sigma_{res}$ (Fig. 15).

In this work, the linear Mohr-Coulomb failure criterion ([19], [91]) is assumed. In the framework of limit analysis, its formulation in the σ-τ-space is usually considered:

$$f(\sigma, \tau) = \tau - c - \sigma \tan \varphi = 0. \tag{3.2}$$

At a stress state for which $f(\sigma, \tau) < 0$ the material remains rigid. If $f(\sigma, \tau) = 0$ plastic flow occurs, while all stress states for which $f(\sigma, \tau) > 0$ are inadmissible.

Kinematics

The limit analysis theorems rely on the assumption of small strains [31, p. 33], [89, p. 386]. That is, the equilibrium and work equations are formulated for the undeformed configuration, and the strain rate tensor is defined as

$$\underline{\underline{\dot{\varepsilon}}} = \dot{\varepsilon}_{ij} = \frac{1}{2}\left(\dot{u}_{i,j} + \dot{u}_{j,i}\right). \tag{3.3}$$

Principle of virtual work

The principle of virtual work for a static system states that a body is in an equilibrium state if and only if the total virtual work of forces acting on the particle is zero for any virtual displacement ([87, p. 33], [92, p. 122], [93, p. 31]). In other words, the virtual work rate done by external forces $\dot{W}^{ext}$ applied on the body must be equal to the rate of internal dissipation $\dot{D}^{int}$. Thus,

$$W^{\text{ext}} - \dot{D}^{\text{int}} = 0, \tag{3.4}$$

The rate of external work is given by:

$$\dot{W}^{\text{ext}} = \int_S \underline{t} \cdot \underline{\dot{u}} \, \mathrm{d}S + \int_V \underline{b} \cdot \underline{\dot{u}} \, \mathrm{d}V, \tag{3.5}$$

where $\underline{t}$ are the prescribed tractions on the body surface S, $\underline{b}$ are the body forces acting over the whole body volume V, and $\underline{\dot{u}}$ is the rate of the virtual displacement field.

The rate of internal dissipation is given by:

$$\dot{D}^{\text{int}} = \int_V \underline{\underline{\sigma}} \cdot \underline{\underline{\dot{\varepsilon}}} \, \mathrm{d}V, \tag{3.6}$$

where $\underline{\underline{\sigma}}$ is the stress tensor in equilibrium with the body forces $\underline{b}$ and the surface tractions $\underline{t}$ and $\underline{\underline{\dot{\varepsilon}}}$ is the strain rate tensor, as defined in Equation (3.3), compatible with the rate of the virtual displacement field $\underline{\dot{u}}$. At failure, the plastic strain rate and the stress tensor are orthogonal (due to the normality of flow). Therefore, the frictional dissipation is zero:

$$\dot{D}^{\text{int}}_{\varphi} = 0. \tag{3.7}$$

It follows that in a Mohr-Coulomb type of soil, energy can only be dissipated by cohesion.

3.1.1 The limit analysis theorems

The limit analysis is based on two main theorems: the *static* and the *kinematic* principles.

The *static principle* states that if a statically admissible stress field can be found—i.e., a stress field that satisfies the prescribed tractions $\underline{t}$, is in equilibrium with the body forces $\underline{b}$, and is everywhere below yield, $f\left(\underline{\underline{\sigma}}\right) < 0$—, a collapse will not be induced by a set of forces more favourable (in terms of stability of the system) than $\underline{t}$, $\underline{b}$ ([31, pp. 8, 37], [94, p. 205]). By extension, the collapse forces $\underline{t}^c$, $\underline{b}^c$, compatible with a stress field at yield $\underline{\underline{\sigma}}^c$ (i.e., $f\left(\underline{\underline{\sigma}}^c\right) = 0$), represents either:

- a *lower bound* of the true limit load that induces soil collapse, [3] or
- an *upper bound* of the true limit load that provides resistance against soil collapse. [4]

Often, the static principle is misleadingly referred to as the "lower bound method", leading to confusion when applied to the active earth pressure problem.

The *kinematic principle* states that if a kinematically admissible velocity field can be found—i.e., a velocity field that satisfies compatibility, the flow rule, and the velocity boundary conditions—, plastic flow (i.e., collapse) is impending or has already taken place induced by the forces $\underline{t}$, $\underline{b}$ [31, pp. 9, 38], [89, p. 387], [94, p. 205], [95, p. 263]. By extension, the collapse forces $\underline{t}^c$, $\underline{b}^c$ represents either:

- an *upper bound* of the true limit load that induces soil collapse, or
- a *lower bound* of the true limit load that provides resistance against soil collapse.

---

[3] For example, the load acting on a foundation in the bearing capacity failure problem or the force acting on the wall in the passive earth pressure problem.

[4] For example, the force acting on the wall in the active earth pressure problem.

Often, the kinematic principle is misleadingly referred to as the "upper bound method", leading to confusion when applied to the active earth pressure problem. The bounds of the active earth pressure are depicted in Fig. 16.
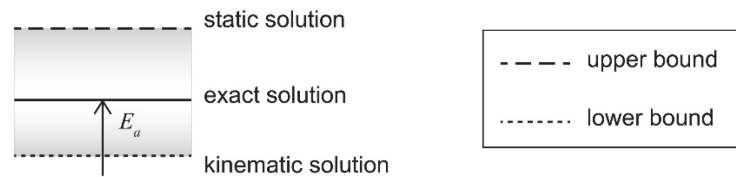

Fig. 16: Bounds of the active earth pressure as defined by the static and the kinematic principle.

3.1.2   The friction theorems

The two main limit analysis theorems summarised in Section 3.1.1 assume assemblages of perfectly plastic bodies that obey the associated flow rule. However, geotechnical problems often include frictional interfaces, e.g. the interface between a retaining wall and the backfill. Frictional interfaces are usually modelled assuming Coulomb friction, where the resistance to slip is given by the multiplication of a friction coefficient times the normal force acting on the interface, $T = \mu \cdot N$, where μ is usually expressed in terms of a friction angle: $\mu = \tan \delta$. The flow in frictional interfaces is assumed to be nondilatant, i.e. the virtual velocity increment of the block on the frictional interface is parallel to the tangential force. The fundamental difference between a friction interface and perfectly plastic soil is depicted in Fig. 17.

(a)   (b)
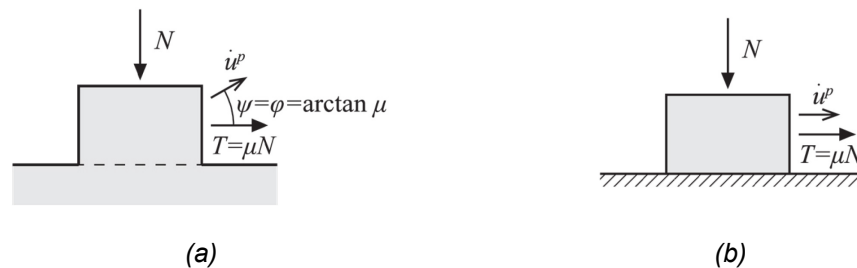
Fig. 17: (a): Shearing of a block of soil obeying the Mohr-Coulomb failure criterion and the associated flow rule; (b): sliding of a block of soil along a frictional interface obeying the Coulomb frictional law. Adapted by the authors from [89].

As the proofs of the static and kinematic principles are based on flow associativity, they do not hold for problems involving nondilatant frictional interfaces.

The virtual work equation must be extended to consider frictional interfaces. Adding the frictional dissipation at the interface to Equation (3.4), it follows:

$$\int_S \underline{t} \cdot \underline{\dot{u}} \, \mathrm{d}S + \int_V \underline{b} \cdot \underline{\dot{u}} \, \mathrm{d}V = \int_V \underline{\underline{\sigma}} \cdot \underline{\underline{\dot{\varepsilon}}} \, \mathrm{d}V + \int_I \underline{t}_{\text{int}} \cdot \underline{\dot{u}}_{\text{int}} \, \mathrm{d}I \,, \tag{3.8}$$

where $\underline{t}_{\text{int}}$ are the acting tractions and $\underline{\dot{u}}_{\text{int}}$ the relative velocity at the interface. I is the interface surface.

In two particular cases, the static and kinematic principles still hold for assemblages of perfectly plastic bodies with frictional interfaces [31, p. 42]:

- If the coefficient of friction is zero, as in that case the flow is associated: $\psi = \delta = 0°$.

- If there is no relative motion at the interface, i.e. the interface is rough, $\delta \geq \varphi$, and separation is not allowed. In that case, shearing occurs in the soil, which obeys the associated flow rule.

Two friction theorems can be formulated by considering these two cases as a reference.

Theorem 1. Any set of forces that produces collapse for the condition of no relative motion at the interfaces will produce collapse for the case of finite friction [90]. [5]

Theorem 2. Any set of forces that will not cause collapse when all coefficients of friction are zero will not produce collapse with any values of the coefficients [90].

Thanks to theorems 1 and 2, it is possible to find bounds for the collapse load of systems involving frictional interfaces. However, often, these bounds provide a relatively broad range [90, p. 74]. Drucker, therefore, formulated the third friction theorem:

Theorem 3. Any set of forces $\underline{t}$, $\underline{b}$ that will not cause the collapse of an assemblage of bodies with frictional interfaces will not produce collapse when the interfaces are "cemented" together with a cohesionless soil of friction angle $\varphi = \delta = \arctan \mu$ (i.e., when the frictional interfaces are assumed to dilate according to the associated flow rule: $\psi = \varphi = \delta$) [90].
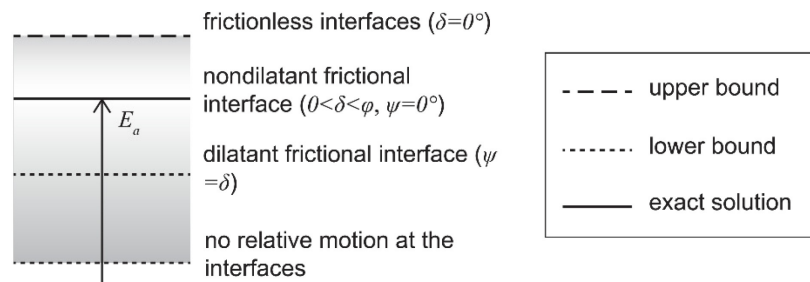

Fig. 18: Bounds of the active earth pressure for systems with frictional interfaces as defined by theorems 3-5.

From theorems 1–3, it follows that the limit load of an assemblage of bodies with frictional interfaces is bounded between (Fig. 18):

- the limit load for the same bodies with zero friction on the interfaces; and
- the limit load for no relative motion at the interfaces and the limit load for the same assemblage with dilatant interfaces.

The first bound provides a safe estimate of the limit load and the second set of bounds an unsafe estimate.

3.1.3 On the role of soil dilatancy

The assumption of associated flow, implying that the dilatancy angle is equal to the friction angle, is crucial for the validity of the limit analysis theorems, Section 3.1.1. However, it is well-known that the dilatancy angle of granular soils is significantly lower than its friction angle. Nonassociated flow rules are, therefore, frequently used to model the soil behaviour. The role of nonassociated flow on the limit load and, more in general, on the soil plastic behaviour has been discussed by several authors, e.g. [31], [34], [96]–[100]. Their main findings are summarised in [9].

In general, during plastic shearing, the direction of the principal stresses does not coincide with the direction of the strain increments [96, p. 135], [101]. However, as suggested by Hill [102], later confirmed experimentally by Roscoe [96], Thornton and Zhang [101], and Ai et

---

[5] "No relative motion" is more inclusive than "infinite friction" because separation is not permitted [90].

al. [103], the principal stress and principal strain increment directions are coaxial when unconstrained flow occurs. Since limit analysis aims at bounding the collapse load during unconstrained flow, only coaxial flow rules are assumed in this work.

Implications for the kinematic method

Because of the nonassociativity of the flow, Equation (3.7) does not hold anymore. Indeed, the frictional plastic dissipation is nonzero along a velocity discontinuity, as the strain increment is not orthogonal to the stress vector. Assuming the nonassociated flow rule, Drescher and Detournay write the plastic dissipation on a velocity discontinuity as [98]:

$$\dot{D}^{\text{int}}_{\text{NAFR}} = v \cos \psi \left[c^* + \sigma_n (\tan \varphi^* - \tan \psi) \right]. \tag{3.9}$$

The parameters c^* and φ^* were first given by Davis [34] as:

$$c^* = \eta c, \tag{3.10}$$

and

$$\tan \varphi^* = \eta \tan \varphi, \tag{3.11}$$

where

$$\eta = \frac{\cos \psi \cos \varphi}{1 - \sin \psi \sin \varphi}. \tag{3.12}$$

The variable v is the velocity jump across the discontinuity and σ_n is the normal stress acting on the discontinuity. This latter term is unknown in a kinematic solution, as the stress distribution is ignored. However, Drescher and Detournay showed that, for a mechanism composed of translational bodies, Equation (3.9) can be simplified to

$$\dot{D}^{\text{int}}_{\text{NAFR}} = c^* v \cos \varphi^* \tag{3.13}$$

if a flow rule associative to a fictitious Mohr-Coulomb surface characterised by c^* and φ^* is assumed [98].

Therefore, to calculate a kinematic solution assuming nonassociated flow and strength parameters c, φ, an associated flow rule and the reduced parameters c^*, φ^* can be considered. The procedure then remains the same as usual for associated materials.

(a)   (b)
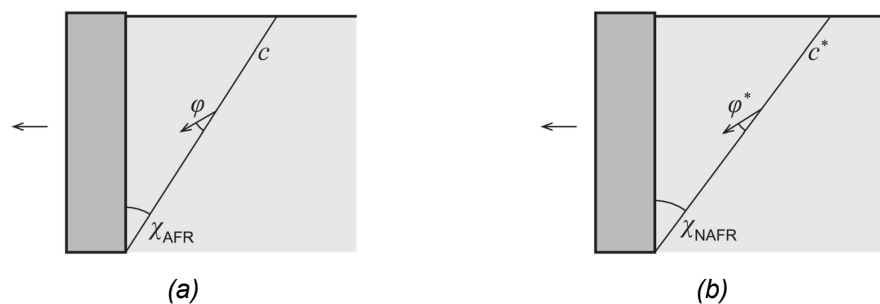
Fig. 19: *A simple kinematic mechanism for the earth pressure exerted by soil with strength parameters c, φ and (a) associated flow, (b) nonassociated flow. The parameters c^* and φ^* are determined from Eqs. (3.10), (3.11), and (3.12).*

Validity of the limit analysis theorems

The previous subsection showed how to apply the kinematic method to the case of nonassociativity of flow. However, a nonassociated flow rule has some implications on the validity of the limit analysis theorems, Section 3.1.1.

Static principle

In formulating a static solution, the kinematics of the problem remains ignored. Every static stress field that satisfies the equilibrium equations in the associated case will be a valid solution in the broader context of continuum mechanics, even if the exact solution does not obey the associated flow rule.

However, in the context of limit analysis, the proof of Theorem 1 (the static principle) requires the assumption that the exact solution satisfies the flow rule. As a consequence, it is not possible to ensure that a static solution represents a safe estimate of the collapse load, if the material obeys the nonassociated flow rule.

Kinematic principle

Contrary to the static principle, in formulating a kinematic solution, the kinematics of the problem must be considered. Also, the proof of Theorem 2 requires the assumption of the associated flow rule.

The modified procedure by Drescher and Detournay [98] can be used to obtain meaningful estimates of the actual limit load of nonassociated materials. In general, the so-obtained solution gives reasonable estimates of the limit load, as shown by Krabbenhoft et al. [99]. However, the solution may lie on the safe or on the unsafe side [99, pp. 1110, 1113]. This is, however, less of a concern, as a kinematic solution with the associated flow rule always lies on the unsafe side.

Theorem for nonassociated materials

Radenkovic formulated the following theorem for nonassociated materials [104]:

Theorem 6. "Any set of loads which produces collapse for the material with associated flow rule will produce collapse for the same material with nonassociated flow rules." [31, p. 44], [104]

It follows that a solution based on the associated flow rule represents an unsafe estimate of the exact solution for a material obeying the nonassociated flow rule.

Discussion

The associated flow rule is crucial to the validity of the limit analysis theorems. Nevertheless, the static and kinematic limit analysis methods can still obtain approximate solutions. A static solution does not require knowledge of the flow associativity to be constructed and is statically admissible even if nonassociated flow is assumed. However, it is not possible to ensure that a static solution lies on the conservative side if the flow is nonassociated. On the other hand, the formulation of a kinematic solution depends on the type of flow. An adapted procedure was proposed by Drescher and Detournay [90] to consider nonassociated flow. The obtained solution is still guaranteed to represent a proper, unconservative bound of the true collapse load (e.g., it represents a lower bound of the active earth pressure).

3.2   Failure modes

As already seen in Section 2.2, multiple failure modes are possible for a geotechnical structure. They can be grouped into two categories: geotechnical failure modes and structural failure modes.
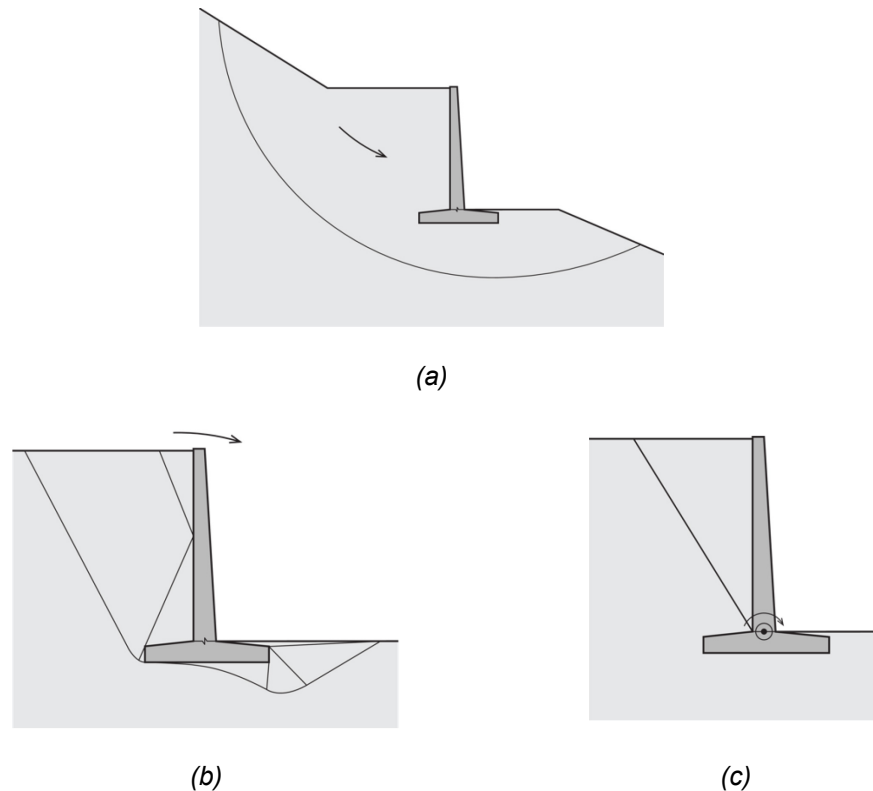
(a)

(b)

(c)

Fig. 20: *Types of failure: (a) global soil failure, (b) soil local failure, and (c) structural (bending) failure.*

Geotechnical failure can occur globally or locally. A global failure mechanism is depicted in Fig. 20a. In this case, a large portion of the slope fails due to the change in geometry. For granular materials, the failure line is represented by a logarithmic spiral. As the solution of this mechanism is not part of this work, the interested reader is referred to [31, pp. 399–446].

The local failure mechanism can instead occur in many different ways. Usually, pure sliding and bearing capacity failure are considered, as in Fig. 11b-c. The verification of the wall safety against those failure types is then carried out assuming decoupled systems, as in Fig. 13. Although supported by decades of use in engineering practice, decoupling the systems has a theoretical drawback. The kinematics is usually neglected by decoupling the systems (e.g., the earth pressure exerted by the backfill is derived from a translational mechanism and applied to a bearing capacity failure mechanism), and a kinematically admissible velocity field is not sought for the whole system. Consequently, the exact solution can not be bounded (see Section 3.1.1). Nevertheless, if it can be shown that a static admissible stress field can be found for the whole body, then a safe estimate of the safety factor can be made. A more rigorous solution based on the plasticity theory can otherwise be found considering, e.g., the mechanism depicted in Fig. 20b. In the depicted configuration, the wall is rotating about a point located below the foundation level. Note that this mechanism would turn into a pure sliding mechanism if the distance of the centre of rotation were assumed to be infinite. The solution to this failure type is not part of this work but can be derived based on the limit analysis theorems. Alternatively, nowadays, the Optum [105] software (or similar) can solve limit analysis problems numerically.

Structural failure can occur in a shear or bending mode, primarily on the wall stem. In this work, emphasis is put on structural failure led by corrosion of the reinforcement, in which bending failure is predominant (see, e.g., [106]). As corrosion of the reinforcement bars increases at the construction joint, a plastic hinge will develop. Therefore, the wall stem undergoes a rotation about the construction joint and the backfill fails (Fig. 20c). This failure mechanism will be analysed in the following sections.

3.3   Bending failure of cantilever retaining walls

3.3.1   Kinematic solution

Based on the kinematic principle, Section 3.1.1, a kinematic solution for the earth pressure problem shown in Fig. 20c will be formulated in this section. The most straightforward failure mechanism analysed in this section is depicted in Fig. 21 and considers a Coulomb-like failure plane. As a result of the increased steel stresses (due to the corrosion-driven cross-sectional loss of the reinforcement), a plastic hinge develops at the construction joint. The wall stem undergoes a (virtual) rotation increment ω causing active soil failure in the backfill (Fig. 21). The moment m_u is the unknown collapse load. In contrast to the case of a translational movement, where failure is assumed to occur only along a single failure line, in the case of a rotational movement, a shear zone must develop to meet the kinematic boundary conditions, as depicted in Fig. 21.
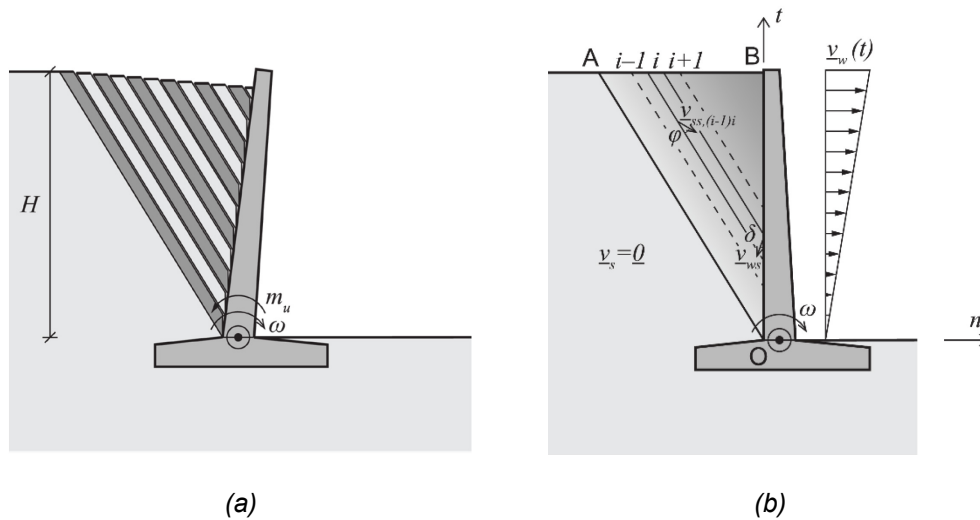

(a)   (b)

Fig. 21: *Kinematically admissible failure mechanism caused by corrosion-led bending failure of the wall. (a) Deformed configuration. (b) Velocity discontinuities for an infinitesimal slice of the shear zone and wall velocity.*

The shear zone consists of infinitely many slices (i.e. slices of infinitesimal thickness) that virtually move in compliance with the velocity boundary condition prescribed at the soil-wall interface and obeying the associated flow rule. Three such slices are depicted in Fig. 21b with a finite thickness for the reader's convenience. The relative velocities at the discontinuities between slice i and slice $(i - 1)$ and between slice i and the wall are shown. As a result of soil dilation and the associated flow rule, slice i moves away from slice $(i - 1)$. The relative velocity between two slices is inclined by φ with respect to their interface. The velocity at the soil-wall interface is assumed to be inclined by the interface friction angle δ, according to the friction Theorem 3, Section 3.1.2.

The virtual rotation around the construction joint imposed on the wall stem results in a linearly increasing velocity over its height $\underline{v}_w(t)$. The velocity $\underline{v}_w(t)$ is assumed to be perpendicular to the wall back face $\overline{OB}$. In other words, the wall stem thickness tends to zero.

The soil's virtual velocity outside the shear zone is zero, while inside the virtual velocity field is variable, as represented in Fig. 21b using a colour gradient. This vector field can be fully described using only the coordinate t of a soil slice at $n = 0$ (i.e., at the soil-wall interface):

$$\underline{v}_s(t) = \underline{\underline{C}}\, \underline{v}_w(t), \tag{3.14}$$

where $\underline{\underline{C}}$ is a constant diagonal matrix. Indeed, the slices are made of rigid material (Section 3.1), meaning the soil velocity is constant along the whole length of a slice.

The lowest slice of the shear zone (i.e., line $\overline{OA}$ in Fig. 21b), slice 0, is at rest: $\underline{v}_{s,0} \equiv \underline{v}_s(t = 0) = \underline{0}$ (since $\underline{v}_w(t = 0) = \underline{0}$). Slice 1's velocity therefore points in the same direction as the relative velocity between slice 0 and 1. Indeed,

$$\underline{v}_{s,1} = \underline{v}_{s,0} + \underline{v}_{ss,01} = \underline{v}_{ss,01}. \tag{3.15}$$

It follows that the velocity of all other slices $i > 1$ in the shear zone $\triangle\,OAB$ have the same direction, i.e. they are inclined by φ to the shear zone's boundary $\overline{OA}$, since the addition of two parallel vectors gives a vector with the same direction as the two summands. That is, if $\underline{v}_{s,i} \parallel \underline{v}_{ss,i(i+1)}$, then $\underline{v}_{s,i+1} \parallel \underline{v}_{ss,i(i+1)}$, where

$$\underline{v}_{s,i+1} = \underline{v}_{s,i} + \underline{v}_{ss,i(i+1)}. \tag{3.16}$$

Fig. 22 shows the velocity diagram for three adjacent slices inside the shear zone (as in Fig. 21b).
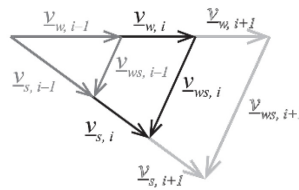

Fig. 22: *Velocity diagram for three adjacent slices $i - 1$, i, and $i + 1$.*

The kinematically admissible velocity field must also satisfy the prescribed wall velocity and comply with the soil-wall interface. The prescribed wall velocity is perpendicular to the wall back face, while the relative velocity at the interface is inclined by δ to the wall backface. Since the slice velocities in the shear zone and the wall velocity at the boundary always have the same direction, the velocity diagrams in Fig. 22 are similar. The length of their sides is therefore only given by the wall velocity $\underline{v}_w(t)$.

Failure mechanisms

Four kinematically admissible failure mechanisms, depicted in Fig. 23, are considered in this section. The one-wedge mechanism consists of a single triangular shear zone and can be fully described by one free parameter: the angle χ (Fig. 23a). The second and the third are both composed of two triangular shear zones separated by a velocity discontinuity. The two-wedges mechanism (1), Fig. 23b, is fully described by the three free parameters χ_{11}, χ_{12}, and χ_{21}, while the two-wedges mechanism (2), Fig. 23c, is described by two free parameters χ_{11}, and χ_{21}. The fourth mechanism is a logsandwich mechanism consisting of a logarithmic shear zone sandwiched between two triangular zones. The logarithmic spiral is centred at the wall top. The two-wedges (1) and the logsandwich mechanisms have first been introduced for a translational motion by Chen [31, p. 352]. In this work, they are re-visited by introducing a rotational motion of the wall.

The wall geometry is described by the height of the backfill H and the inclination of its back face α. The backfill's top edge is assumed to be a straight line inclined by β. All quantities drawn in Fig. 23 are positive.
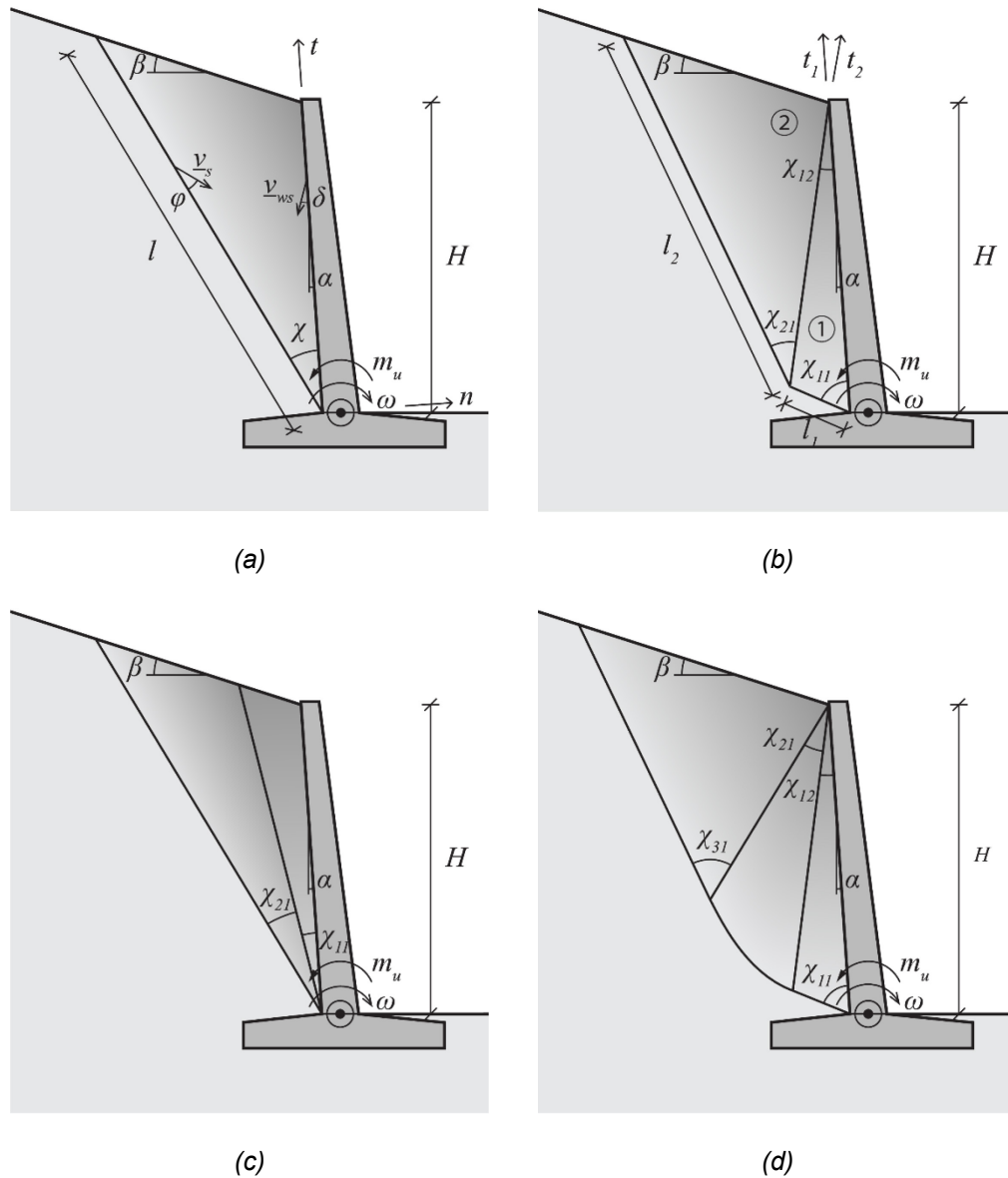
Fig. 23: (a) One-wedge mechanism; (b) two-wedges mechanism (1); (c) two-wedges mechanism (2); (d) logsandwich mechanism. All angles are drawn as positive.

One-wedge mechanism

The full analytical determination of the solution of the one-wedge mechanism can be found in [9] and is not restated here. The moment m_u that leads the soil to active failure for a given failure line inclination χ reads:

$$m_u(\chi) = \frac{\gamma H^3}{6} \cdot \frac{\sin\chi \cos(\alpha + \beta)\cos(\chi + \alpha + \varphi)\cos\bar{\delta}}{\cos^3\alpha \cos(\alpha + \beta + \chi)\sin(\bar{\delta} + \chi + \varphi)}. \tag{3.17}$$

Equation (3.17) must then be maximised to find the most critical failure mechanism:

$$\max \quad m_u(\chi)$$

$$\text{subject to} \quad \max\left\{0, -\frac{\pi}{2} - \alpha - \beta\right\} < \chi < \frac{\pi}{2} - \alpha - \beta \tag{3.18}$$

$$-\bar{\delta} - \varphi < \chi < \pi - \bar{\delta} - \varphi$$

Other mechanisms

Due to the presence of multiple velocity discontinuities, the other mechanisms shown in Fig. 23 can have multiple solutions, all of which must be independently optimised. Thus, it is impossible to find a single closed-form solution as for the one-wedge mechanism, and these solutions are not presented as part of this work for the sake of conciseness. Instead, the numerical solution of these mechanisms will be shown in Section 3.4.

3.3.2 Static solution

Based on the static principle, Section 3.1.1, a solution to the earth pressure problem in Fig. 20c will be formulated in this section. A solution based on the static principle of limit analysis was first proposed by Lancellotta [107] for the case of a horizontal backfill and a vertical wall. Later, the same author developed a static solution for the seismic passive earth resistance for a vertical wall and inclined backfill [108]. In the following, a static solution for the active earth pressure acting on an arbitrarily inclined wall with an inclined backfill is derived. The geometry and the static boundary conditions are depicted in Fig. 24.
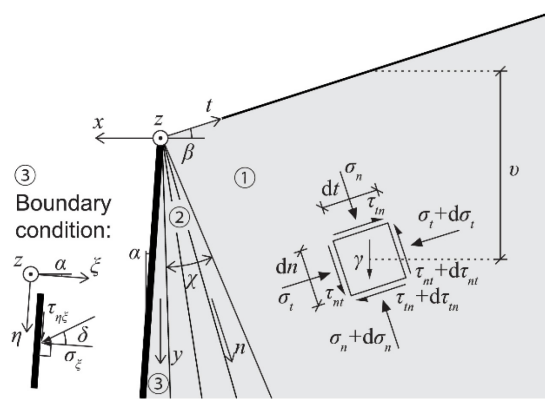

Fig. 24: Geometry and static boundary conditions.

The soil mass inclined by the angle β is subjected to its self-weight. In region ①, the soil surface must be stress-free. The equilibrium equations for the depicted soil element read:

$$\begin{cases} \sigma_{n,n} + \tau_{nt,t} = \gamma \cos \beta \\ \sigma_{t,t} + \tau_{tn,n} = -\gamma \sin \beta \\ \tau_{nt} = \tau_{tn} \end{cases} \tag{3.19}$$

where $_{,n} = \partial/\partial n$ and $_{,t} = \partial/\partial t$ denote partial derivatives. The extent of region ① is assumed to be infinite. Thus, the stress state cannot change in the t-direction, i.e.,

$$\begin{cases} \sigma_{n,t} = 0 \\ \sigma_{t,t} = 0 \\ \tau_{nt,t} = \tau_{tn,t} = 0 \end{cases} \tag{3.20}$$

Considering the boundary conditions at the soil surface

$$\begin{cases} \sigma_n(n = 0, t) = 0 \\ \sigma_t(n = 0, t) = 0 \\ \tau_{tn}(n = 0, t) = 0 \\ \tau_{nt}(n = 0, t) = 0 \end{cases} \tag{3.21}$$

and Equation (3.20) it is possible to integrate Equation (3.19):

$$\begin{cases} \sigma_n(n) = \gamma n \cos \beta \\ \tau_{tn}(n) = -\gamma n \sin \beta \end{cases} \tag{3.22}$$

Equation (3.22) defines the stress components acting on the element face with the normal vector corresponding to n. The stress resultant on the element face is inclined by the angle β with respect its normal vector, i.e. $\tau_{tn}/\sigma_n = -\tan\beta$. Because of the conditions Equation (3.20), the stress components are independent of the coordinate t and is hence omitted in Equation (3.22). The stress components can, therefore, also be written as a function of the vertical depth v of a material point. From Fig. 24 it can be deduced that $v = n/\cos\beta$. Thus,

$$\begin{cases} \sigma_n(v) = \gamma v \cos^2\beta \\ \tau_{tn}(v) = -\gamma v \sin\beta \cos\beta \end{cases} \tag{3.23}$$

By imposing failure everywhere in the stress region, the normal stress component σ_t can be computed. The Mohr-Coulomb failure criterion is assumed:

$$\tau = \sigma \tan\varphi. \tag{3.24}$$

Mohr's circles can be used to determine the remaining stress component and the stress states in the other regions. Fig. 25 depicts the stress states in the backfill of the wall drawn in Fig. 24.
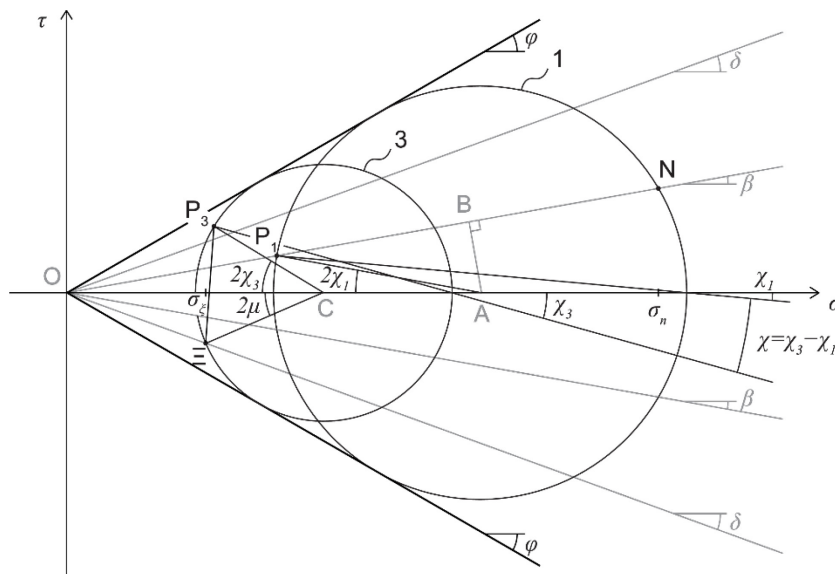

Fig. 25: *Mohr's circles for the stress regions in Fig. 24. The Point* N *represents the stress state in a soil element in region* ① *(σ_n, τ_{tn}) and* Ξ *the stress state on the wall ($\sigma_\xi, \tau_{\eta\xi}$). The letter* P *denotes the poles of the Mohr circles.*

In region ③, the stress resultant on the wall must be inclined by the interface friction angle δ (Fig. 24). The yield criterion must not be violated anywhere. In some exceptional cases, the stress state in region ③ already fulfils the boundary conditions at the wall interface. It is, for example, the case of Rankine's solution, i.e. when the backfill inclination corresponds to the interface friction angle, $\beta = \delta$. In general, however, the stress state must be rotated between region ① and ③ to satisfy all boundary conditions. In that case, the two regions are separated by a discontinuity region consisting of infinitely many discontinuity lines.

The full derivation of the static solution can be found in [9]. Here, only the solution is reported. The rotation of the stress state between the two regions reads

$$\chi = \chi_3 - \chi_1 = \frac{1}{2}\left[\arcsin\left(\frac{\sin\delta}{\sin\varphi}\right) - \arcsin\left(\frac{\sin\beta}{\sin\varphi}\right) + \beta - \delta\right] + \alpha. \tag{3.25}$$

The normal stress on the wall at active failure is

$$\sigma_{a,\xi}(\upsilon) = \gamma\upsilon\cos^2\beta\,\frac{1 - \sqrt{\sin^2\varphi - \cos^2\varphi\tan^2\beta}}{\cos^2\varphi}(1 - \sin\varphi\cos 2\mu)e^{-2\chi\tan\varphi} \qquad (3.26)$$

with

$$\mu = \frac{1}{2}\left[\arcsin\left(\frac{\overline{OC}\sin\delta}{\overline{OC}\sin\varphi}\right) - \delta\right] = \frac{1}{2}\left[\arcsin\left(\frac{\sin\delta}{\sin\varphi}\right) - \delta\right]. \qquad (3.27)$$

3.3.3 The coefficient of lateral earth pressure

In geomechanics, the coefficient of lateral earth pressure is often defined as the dimensionless ratio between the lateral stress σ_{lat} and the overburden stress σ_υ acting at a material point P (Fig. 26):

$$K = \frac{\sigma_{lat}}{\sigma_\upsilon}. \qquad (3.28)$$

In a soil half-space with no surcharge loads, the overburden stress is defined as the product of the soil weight and the vertical depth of the point:

$$\sigma_\upsilon = \gamma \cdot \upsilon. \qquad (3.29)$$

The Greek letter υ denotes the vertical depth of the material point P, as introduced in Fig. 24 and Fig. 26a.

<div align="center">(a)   (b)</div>

Fig. 26: (a) Geometry and coordinate systems centred at the wall top; (b) Normal and horizontal components of the earth pressure acting on an inclined wall.

If a linear stress distribution is assumed, the value of K is constant throughout the half-space and the lateral earth pressure is uniquely defined by the lateral earth pressure coefficient K and the overburden stress σ_υ.

When constructing the stress field of Section 3.3.2, a linear stress distribution was assumed. Therefore, according to Eqs. (3.26) and (3.28), the normal stress acting on the inclined wall segment $\overline{OP}$ can be written as:

$$\sigma_{a,\xi} = K_{a,\xi}\gamma\upsilon, \qquad (3.30)$$

with

$$K_{a,\xi} = \cos^2\beta\,\frac{1 - \sqrt{\sin^2\varphi - \cos^2\varphi\tan^2\beta}}{\cos^2\varphi}(1 - \sin\varphi\cos 2\mu)e^{-2\chi\tan\varphi}. \qquad (3.31)$$

To design or to verify a retaining wall, the main quantities of interest are the resultant forces on the wall (i.e., the earth pressure and the bending moment). These forces can be obtained by applying the kinematic method, as shown in Section 3.3.1, or by integrating the stresses obtained with the static method, Eqs. (3.26). For the latter option, the vertical depth v must first be expressed as a function of the variable η (Fig. 26a):

$$v = \eta \, \frac{\cos(\alpha + \beta)}{\cos \beta}. \tag{3.32}$$

The normal component of the resultant earth pressure can then be obtained by integrating Equation (3.31) along $\overline{OP}$:

$$E_{a,\xi} = \int_0^{\frac{h}{\cos \alpha}} K_{a,\xi} \gamma \eta \, \frac{\cos(\alpha + \beta)}{\cos \beta} \, \mathrm{d}\eta = \frac{\gamma h^2}{2} \frac{\cos(\alpha + \beta)}{\cos^2 \alpha \cos \beta} K_{a,\xi}. \tag{3.33}$$

The resultant earth pressure reads (Fig. 26b):

$$E_a = \frac{E_{a,\xi}}{\cos \delta} = \frac{\gamma h^2}{2} \frac{\cos(\alpha + \beta)}{\cos^2 \alpha \cos \beta \cos \delta} K_{a,\xi}, \tag{3.34}$$

and the horizontal earth pressure component:

$$E_{a,h} = E_a \cos(\alpha - \delta) = \frac{\gamma h^2}{2} \frac{\cos(\alpha + \beta) \cos(\alpha - \delta)}{\cos^2 \alpha \cos \beta \cos \delta} K_{a,\xi}. \tag{3.35}$$

The moment acting about the point P located on the wall reads:

$$M_a^P = \int_0^{\frac{h}{\cos \alpha}} K_{a,\xi} \gamma \eta \, \frac{\cos(\alpha + \beta)}{\cos \beta} \left(\frac{h}{\cos \alpha} - \eta \right) \mathrm{d}\eta = \frac{\gamma h^3}{6} \frac{\cos(\alpha + \beta)}{\cos^3 \alpha \cos \beta} K_{a,\xi}. \tag{3.36}$$

For the design of retaining walls, a modified formulation of the coefficient of lateral earth pressure that relates the integrated quantities (e.g., the horizontal earth pressure force E_h) to the soil weight and the wall height is often assumed:

$$\overline{K} = \frac{E_h}{\gamma h^2 / 2}. \tag{3.37}$$

This formulation is convenient as it encloses the stress integration for arbitrary wall and slope inclinations. However, it only relates the integrated quantity E_h to $\frac{\gamma h^2}{2}$, while the lateral stress $\sigma_{\text{lat}} = \overline{K} \gamma y$ acting on the normal projection onto the line $x = 0$ (Fig. 26a) has no physical meaning other than simplifying the integration of the forces acting on the wall. *By no means* does it represent a valid stress state in the soil. To calculate the soil stresses at the wall interface, $\overline{K}$ must be transformed back to K.

From Equation (3.36) and Eqs. (3.33), (3.34), and (3.35) the following coefficients can be defined:

$$\overline{K}_{a,\xi} = \frac{\cos(\alpha + \beta)}{\cos^2 \alpha \cos \beta} K_{a,\xi}, \tag{3.38}$$

$$\overline{K}_a = \frac{\overline{K}_{a,\xi}}{\cos \delta} = \frac{\cos(\alpha + \beta)}{\cos^2 \alpha \cos \beta \cos \delta} K_{a,\xi}, \tag{3.39}$$

$$\overline{K}_{a,h} = \overline{K}_a \cos(\alpha - \delta) = \frac{\cos(\alpha + \beta) \cos(\alpha - \delta)}{\cos^2 \alpha \cos \beta \cos \delta} K_{a,\xi}. \tag{3.40}$$

From Equation (3.36), it follows:

$$M_a^P = \frac{\gamma h^3}{6 \cos \alpha} \overline{K}_{a,\xi}.$$

(3.41)

Equation (3.41) allows a direct comparison of the moment acting on the plastic hinge resulting from the static and kinematic solutions. Comparing the moment resulting from Equations (3.38) and (3.41) (static solution) to the moment resulting from Equations (3.17) and (3.18) (kinematic solution) is the only correct method to compare static and kinematic solutions, as the outcome of the kinematic method is a total limit moment, not the stress distribution. However, in the following sections, the total moment will be normalised according to (3.41) for both the static and kinematic solutions by only considering the following unitless quantity:

$$\overline{K}_{a,\xi} = \frac{6 \cos \alpha}{\gamma h^3} M_a^P.$$

(3.42)

This implicitly assumes a linear stress distribution for the kinematic solution, although it may also just be regarded as an arbitrary normalisation of the moment that allows the comparison of the two limits of the limit analysis. In addition, the normalisation allows for a fast comparison with other solutions found in the literature (e.g. the Coulomb's solution).

3.4 Numerical results

3.4.1 Kinematic solution

The optimised solution of the one-wedge mechanism, Equation (3.17), is plotted in Fig. 27 for a vertical wall ($\alpha = 0°$) with variable backfill inclination β. The soil friction angle is $\varphi = 30°$ and the wall friction angle $\delta = 20°$. Two different kinematics are compared in the plot: a rotation about the toe (i.e., about the construction joint: the relevant kinematics in case of corrosion of the reinforcement at the construction joint; abbreviated in the following as ROT) and a translational mechanism (abbreviated in the following as T). These two solutions are compared to Coulomb's solution, which implicitly assumes a translation.
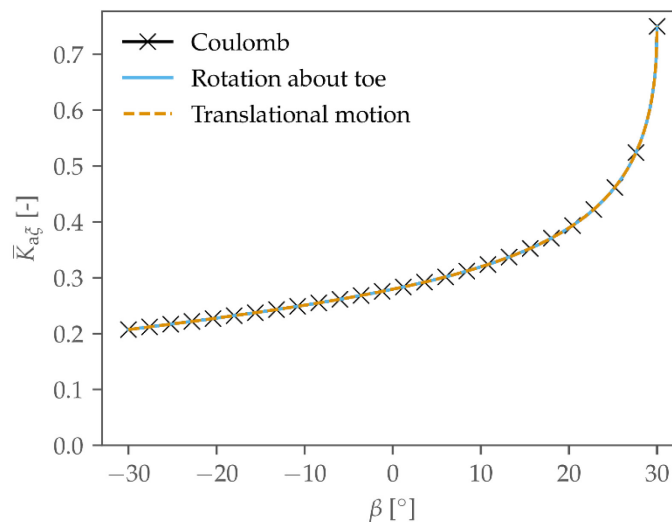

Fig. 27: *Optimised solution of the one-wedge mechanism for a vertical wall ($\alpha = 0°$) and variable backfill inclination. The soil strength is $\varphi = 30°$ and the wall friction angle $\delta = 20°$. Three solutions are plotted: the one-wedge mechanism for a translational wall movement, the one-wedge mechanism for a rotation about the wall toe (Equation (3.17)), and Coulomb's solution.*

For a vertical wall, the kinematic solution for the T and the ROT mechanism are equivalent. The reason is that the virtual velocity of the wall points in the same direction for both mechanisms: a horizontal velocity is prescribed in the translational mechanism, and the velocity resulting from a rotation about the wall toe is perpendicular to the wall (i.e., horizontal in the case of a vertical wall). Therefore, the kinematics of the soil and at the wall interface is the same for both mechanisms. Fig. 27 also shows that Coulomb's solution is equivalent to the kinematic solution of a one-wedge, translational mechanism. Indeed, it can be shown that a limit equilibrium solution is equivalent to a kinematic solution if the inclination of the forces applied on the blocks in the limit equilibrium solution satisfy the yield condition (i.e., $T = N \tan \varphi$) and is compatible with a kinematically admissible motion of the blocks [88], [98].

In general, the ROT mechanism and the T mechanism are equivalent if:

$$\chi_{\text{crit}}^{\text{T}} \leq \frac{\pi}{2} - \varphi, \tag{3.43}$$

where $\chi_{\text{crit}}^{\text{T}}$ is the critical angle that maximises the T mechanism. If Equation (3.43) holds, then the ROT mechanism, Fig. 23a, with $\chi^{\text{ROT}} = \chi_{\text{crit}}^{\text{T}}$ has the same kinematics at the wall interface as the translational mechanism. However, for negative wall inclinations α, this is not always the case. When Equation (3.43) does not hold anymore, the critical angle for the ROT mechanism $\chi_{\text{crit}}^{\text{ROT}}$ becomes smaller than $\chi_{\text{crit}}^{\text{T}}$, as shown in Fig. 28. The critical angle $\chi_{\text{crit}}^{\text{ROT}}$ is bounded above by $\chi_{\text{crit}}^{\text{ROT}} \leq \frac{\pi}{2} - \varphi$.
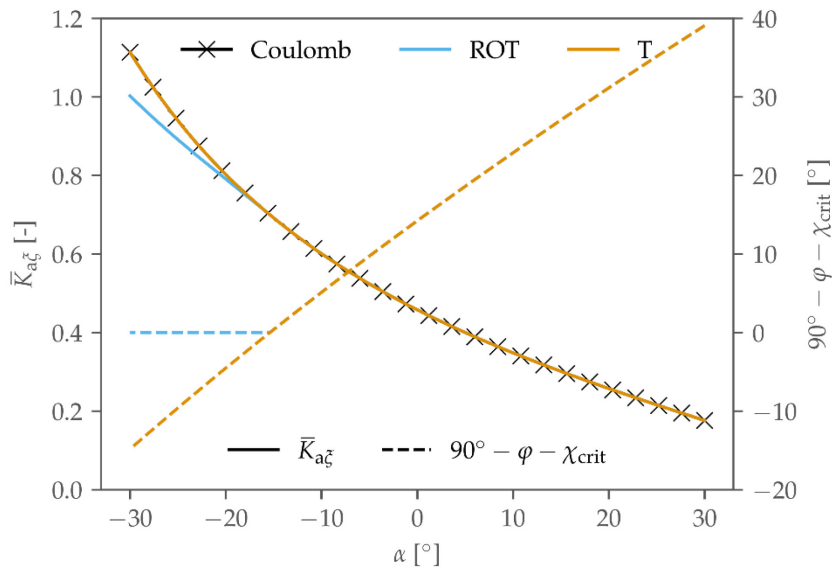

Fig. 28: *Optimised solution of the one-wedge mechanism for a wall with a variable inclination and backfill inclination $\beta = 25°$. The soil strength is $\varphi = 30°$ and the wall friction angle $\delta = 20°$. The coefficient of earth pressure is plotted for the T and ROT mechanisms and for Coulomb's solution. The critical angle is shown for the T and ROT mechanisms.*

For the configuration plotted in Fig. 28, the solution for the translational mechanism (and Coulomb's solution) corresponds to the rotation-about-wall-toe mechanism in the range $\alpha = [-15.5°, 30°]$. Outside this range, the solutions diverge. The different failure mechanisms are shown in Fig. 29. It can be seen that the failure line in the ROT mechanism for $\alpha = -25°$ is steeper than in the T mechanism so that $\chi_{\text{crit}}^{\text{ROT}} = \frac{\pi}{2} - \varphi$.
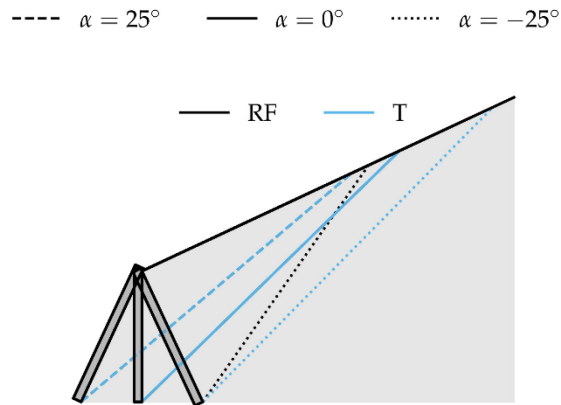
Fig. 29: *Optimised one-wedge mechanisms for different wall inclinations and backfill incli-nation* $\beta = 25°$. *The soil strength is* $\varphi = 30°$ *and the wall friction angle* $\delta = 20°$.

Outside the range $\alpha = [-15.5°, 30°]$, the two-wedges mechanism (2), Fig. 23c, becomes governing for the rotation about the wall toe, as shown in Fig. 30. In the translational case, however, the one-wedge mechanism remains governing.
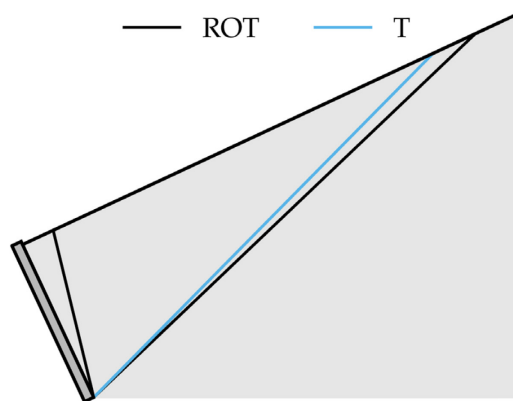

Fig. 30: *Optimised mechanisms for* $\alpha = -25°$, $\beta = 25°$, $\varphi = 30°$, *and* $\delta = 20°$. *For both kinematics (T and ROT), two different mechanisms were considered: the one-wedge mech-anism and the two-wedges mechanism (2).*

Considering the two-wedges mechanism (2), the earth pressure coefficient for the ROT mechanism is higher than the earth pressure coefficient for the T mechanism, as shown in Fig. 31.

This result can be confirmed numerically using, e.g., the OptumG2 software [105]. The failure mechanisms are shown in Fig. 32 through the rate of work of the deviatoric stress. A one-wedge mechanism develops when the wall moves horizontally, while a two-wedge mechanism arises in case of wall rotation about its toe.

Assuming a wall inclination of $\alpha = -25°$, the results summarised in *Tab. 3* are obtained.
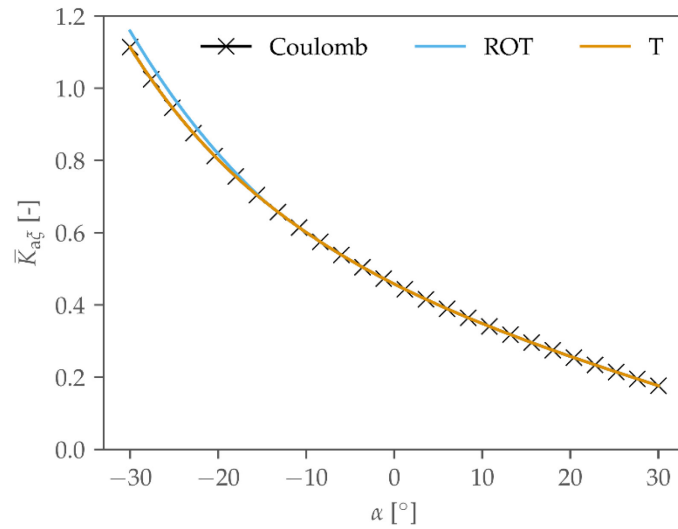
Fig. 31: *Optimised solution of the one-wedge and the two-wedges (2) mechanisms for a wall with a variable inclination and backfill inclination $\beta = 25°$. The soil strength is $\varphi = 30°$ and the wall friction angle $\delta = 20°$. The coefficient of earth pressure is plotted for the T and ROT mechanisms and for Coulomb's solution.*

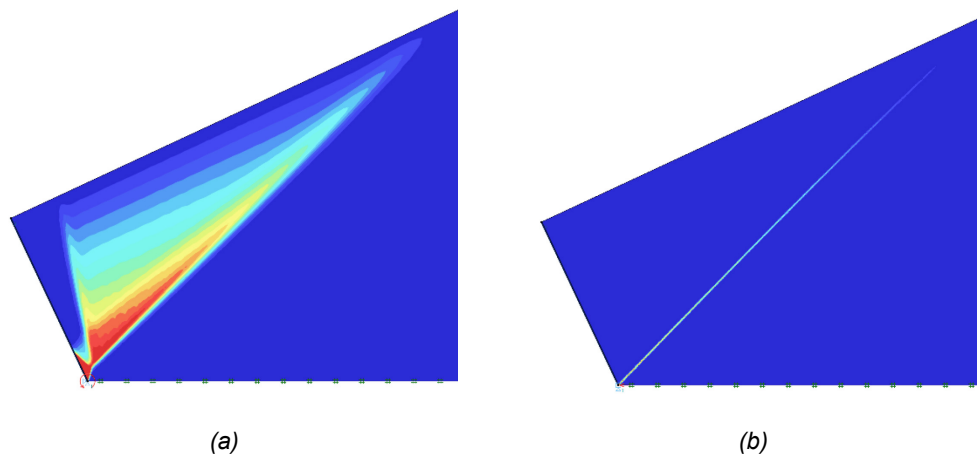| (a) | (b) |

Fig. 32: *Rate of work of the deviatoric stress resulting from the OptumG2 software [105] for a wall with inclination $\alpha = -25°$ and backfill inclination $\beta = 25°$ for two different kinematics: (a) rotation about the wall toe; (b) translational motion. The soil strength is $\varphi = 30°$ and the wall friction angle $\delta = 20°$. The analysis performed is "limit analysis" using the "upper" element type.*

Tab. 3: *Resulting coefficient of earth pressure $\overline{K}_{a\xi}$ for a wall with $\alpha = -25°$ backfill inclination $\beta = 25°$. The soil strength is $\varphi = 30°$ and the wall friction angle $\delta = 20°$.*

	Rotation about wall toe		Translational motion	
	Static solution	**Kinematic solution**	**Static solution**	**Kinematic solution**
This work	$\overline{K}_{a\xi} = 1.02$	$\overline{K}_{a\xi} = 0.97$	$\overline{K}_{a\xi} = 1.02$	$\overline{K}_{a\xi} = 0.94$
Optum G2	$\overline{K}_{a\xi} = 0.99$	$\overline{K}_{a\xi} = 0.99$	$\overline{K}_{a\xi} = 0.94$	$\overline{K}_{a\xi} = 0.93$

The Optum G2 results confirm that the different kinematics influence the earth pressure acting on the wall for this configuration. Therefore, applying Coulomb's solution to a rotation-about-the-wall-toe type of failure can sometimes lead to incorrect results. In this case,

assuming the exact solutions to be $\bar{K}_{a\xi}^{\mathrm{ROT}} \approx 0.99$ (Optum G2 provides the exact solution, although a tiny numerical error could be present) and $\bar{K}_{a\xi}^{\mathrm{T}} \approx 0.94$ (combining the kinematic solution of this work and Optum G2's static solution, assuming a tiny numerical error), the relative difference between T and ROT is close to 5%.

Nevertheless, the observed difference in results for different kinematics is usually of minor importance for the design and verification of cantilever retaining walls, whose stem is generally nearly vertical (or only slightly inclined).

For milder (or negative) slope inclinations and other wall inclinations, the other mechanisms, Fig. 23b and d, may become governing. The governing mechanisms for different parameter configurations and kinematics are shown in Fig. 33.

Fig. 33: Failure mechanisms for a vertical wall ($\alpha = 0°$) and variable backfill inclination β. The wall friction angle is $\delta = \frac{2}{3}\varphi$ and φ is variable: (a) $\varphi = 25°$; (b) $\varphi = 30°$; (c) $\varphi = 35°$.

For smaller backfill inclinations β, the most critical mechanism is the two-wedges mechanism (1). As it will be shown in the next section, when $\delta \neq \beta$, the stress distribution is not continuous over the whole soil mass. As a consequence, also the velocity field is discontinuous. Therefore, mechanisms considering velocity discontinuity interfaces and a polygonal or curved failure line may be used to improve the accuracy of the solution. For a vertical wall and $\delta > \beta$, the best solution is given by the two-wedges mechanism (1), among those shown in Fig. 23. In reality, the failure line is known to be curved (i.e., involving a logarithmic spiral). However, the logsandwich mechanism shown in Fig. 23d is too constrained to become governing. Indeed, the logsandwich mechanism always decayed to a two-wedges mechanism (1) for the analysis performed by the authors. This is because the assumption of a logarithmic spiral centred at the wall top is too strong for the case of the active earth pressure. The same is not true for the passive earth pressure.

The resulting earth pressure coefficients are shown in Fig. 34 for three different friction angles and a vertical wall.

Fig. 34: *Optimised solution of all mechanisms of Fig. 23 for a vertical wall with variable backfill inclination β. The soil strength is variable and the wall friction angle kept at $\delta = \frac{2}{3}\varphi$. The coefficient of earth pressure is plotted for the T and ROT mechanisms (only the value for the most critical mechanism is shown) and for Coulomb's solution.*

The results show again that in the case of a vertical wall, the T and ROT solutions are equivalent. The relative difference between the earth pressure for the ROT most critical mechanism and Coulomb's solution is also plotted in Fig. 34. This difference is zero for $\beta \geq \delta = \frac{2}{3}\varphi$, since the one-wedge mechanism is governing. The relative difference increases with decreasing β. The maximum difference between Coulomb's solution and the kinematic solution presented in this work for these configurations is around 2.2%. The plotted configurations (i.e., soil friction angle φ between 25° and 35°, vertical wall, and wall friction angle $\delta = \frac{2}{3}\varphi$) correspond to the most frequent parameter sets found in practice for cantilever retaining walls. In the range $\beta = [0°, \varphi]$, the relative difference between the kinematic solution for a wall rotation about the toe and Coulomb's solution is further reduced to approximately 0.7%.

Finally, the influence of the flow rule on the kinematic solution is investigated in Fig. 35 assuming Davis' reduced shear strength (Equation (3.24)). The ratio between the solution assuming nonassociated flow (NAFR) and associated flow (AFR) is plotted against the dilatancy angle. As the shear strength, characterised by φ^*, decreases with an increasing degree of nonassociativity, a lower dilatancy angle corresponds to a higher limit load. In addition, it is observed that the limit load increase is larger for higher soil friction angles at the same degree of nonassociativity. Indeed, the limit load ratio corresponding to $\psi = \varphi/2$ is higher for higher friction angles. For example, for $\varphi = 30°$ it is $\frac{K_{NAFR}}{K_{AFR}} \approx 1.05$, while for $\varphi = 40°$ it is $\frac{K_{NAFR}}{K_{AFR}} \approx 1.10$.
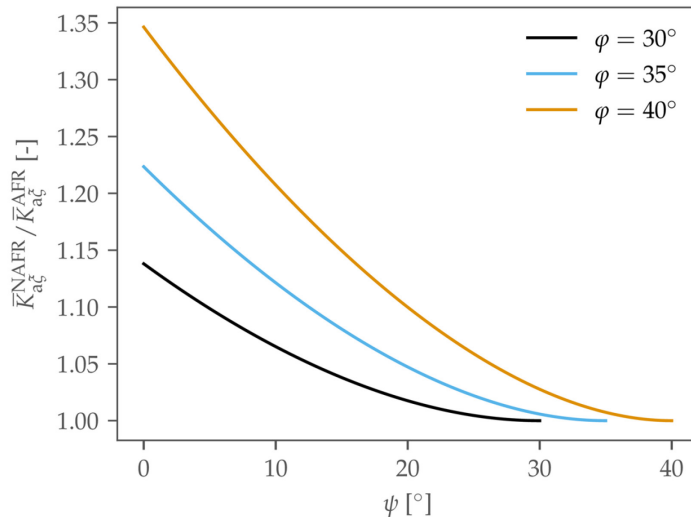
Fig. 35: *Influence of the flow rule on the active earth pressure coefficient: the ratio between the nonassociated and associated values as a function of the dilatancy angle for the ROT mechanisms.*

In this section, it was shown that for the most common cases, i.e. $\alpha \approx 0°$, $\beta = [0°, \varphi]$, $\varphi = [25°, 35°]$, and $\delta = \frac{2}{3}\varphi$, the Coulomb's solution corresponds to the one-wedge kinematic solution, Equation (3.17). These solutions are less conservative than those based on more complex mechanisms, but the difference is negligible in the said range of parameters.

In the case of special geometries and soil parameters, more complex failure mechanisms shall be considered. Moreover, all solutions presented here are lower bounds of the true value (see Section 3.1.1).

In the next sections, the static solution will be analysed and compared to the kinematic solution.

3.4.2 Static solution

The coefficient of earth pressure $\overline{K}_{a\xi}$ resulting from the static solution, Equation (3.26), is first compared to Rankine's solution in Fig. 36. Here, a vertical wall (i.e., $\alpha = 0°$) backfilled with soil having friction angle $\varphi = 30°$ are assumed. In Rankine's solution, the wall friction angle is implicitly assumed to be equivalent to the slope inclination, $\delta = \beta$. Instead, constant wall friction, $\delta = \frac{2}{3}\varphi = 20°$, is assumed for the static solution.

Rankine's solution is symmetrical about the vertical axis as a result of the assumption $\delta = \beta$. Rankine assumed a continuous failure stress state over the whole soil mass. This stress state is represented by Mohr's circle 1 in Fig. 25. He then considered a wall embedded in that soil mass and determined the earth pressure acting on the wall. In this case, it becomes clear that the earth pressure acting on a wall backfilled with a soil inclined by $-\beta$ must be the same as if the backfill would be inclined by $+\beta$. Indeed, both cases correspond to a wall embedded in an infinite slope with inclination β: if $-\beta$ is assumed, the stresses acting on the downhill wall face are considered; if $+\beta$ is assumed, the stresses acting on the uphill face are considered (Fig. 37). Clearly, due to equilibrium, $E_a^{downhill} = E_a^{uphill}$ must hold.

Therefore, for negative inclinations of the backfill, the earth pressure component tangential to the wall points upwards (Fig. 37), indicating an upward-directed slip of the soil mass relative to the wall. However, this does not correspond to the reality in the case of active failure. When a wall is moved horizontally away from the soil, a failing soil wedge moves downwards relative to the wall. Therefore, a kinematically admissible mechanism compatible with Rankine's solution for $\beta < 0$ cannot be found and the solution of Fig. 36 cannot be treated as a proper solution of the plasticity theory in that range. Instead, the static method provides a valid solution that satisfies all boundary conditions and for which a kinematically admissible mechanism can be found. The resulting stress states are shown in Fig. 39a.
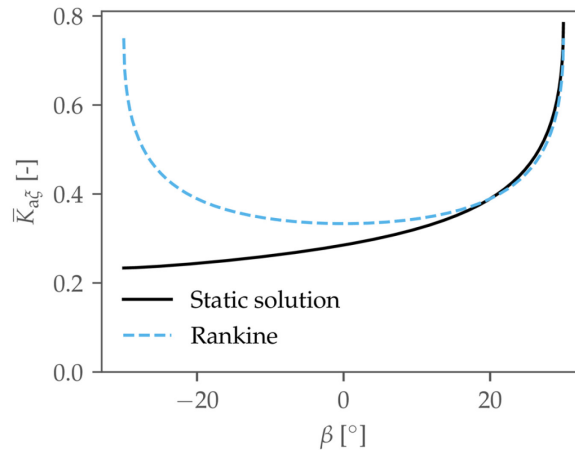
Fig. 36: *Comparison between the static solution Equation (3.26) and Rankine's solution for a vertical wall ($\alpha = 0°$) backfilled with a soil of strength $\varphi = 30°$. For the static solution, the wall friction is $\delta = 20°$, for Rankine's solution $\delta = \beta$ is implicitly assumed.*
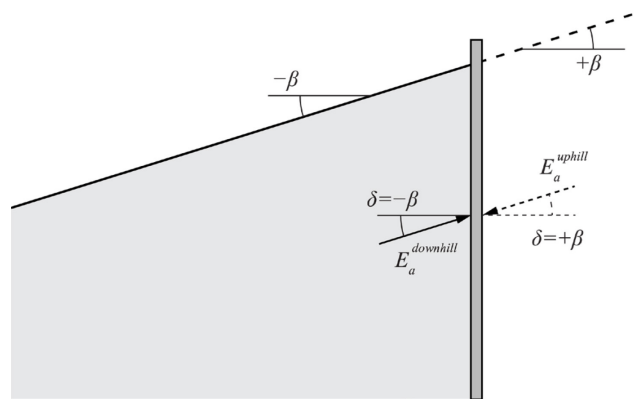

Fig. 37: *Earth pressure determination for a negative backfill inclination using Rankine's solution. A wall embedded in an infinite slope is considered, disregarding the kinematics and the boundary conditions.*

The static solution presented in Section 3.3.2 monotonically increases as the backfill inclination β increases. In a special case, $\beta = 20°$, it is equivalent to Rankine's solution. In that case, it is $\beta \equiv \delta$ and the stress state acting in the infinite slope is compatible with the boundary conditions at the wall interface. Therefore, the stress state must not be rotated, as illustrated in Fig. 38 and Fig. 39b (as opposed to the case $\beta = -20°$, which requires a stress rotation as shown in Fig. 39a).

It can be noted that in the case $\beta = 0°$ the earth pressure resulting from Rankine's solution is higher than the earth pressure resulting from Equation (3.26), as, in that case, Rankine assumes a frictionless wall (i.e., $\delta = 0°$). In the case $\beta = 30°$, Rankine's solution is instead lower than the solution from Equation (3.26). In that case, Rankine assumes a perfectly rough wall (i.e., $\delta = 30° = \varphi$). This result agrees with the frictional theorems presented in Section 3.1.2.
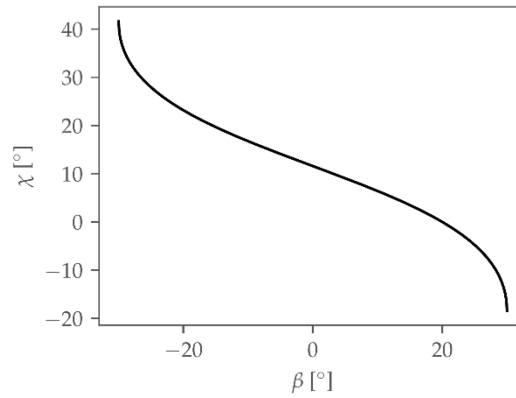
Fig. 38: *Rotation of the stress state χ (Equation (3.25)) between the stress regions ① and ③ (see Fig. 24) for a vertical wall ($\alpha = 0°$) with interface friction $\delta = 20°$ and backfilled with a soil of strength $\varphi = 30°$.*

(a)   (b)
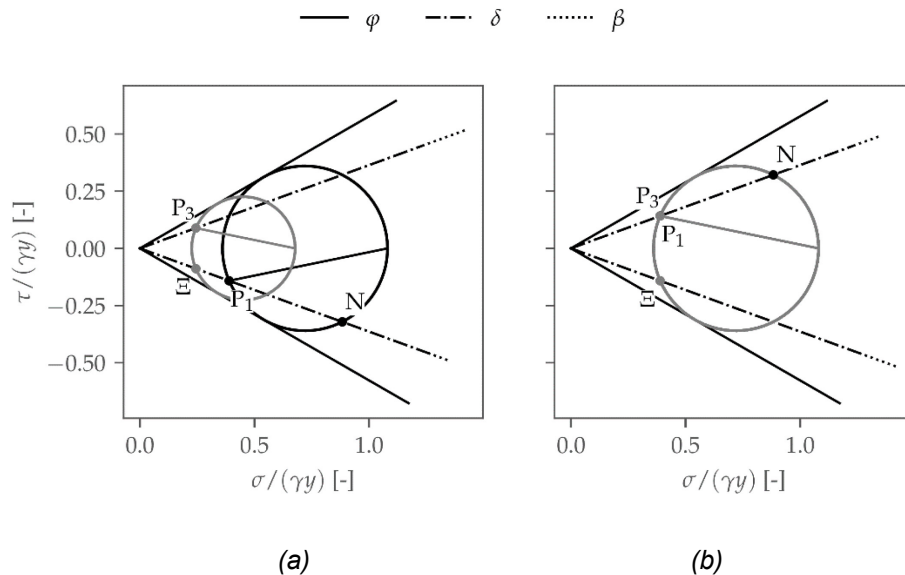
Fig. 39: *Mohr circles for a vertical wall ($\alpha = 0°$) with interface friction $\delta = 20°$ and backfilled with a soil of strength $\varphi = 30°$. (a) Backfill inclination $\beta = -20°$; (b) Backfill inclination $\beta = 20°$.*

3.4.3 Bounded solution

In this section, the bounded solution of the active earth pressure coefficient is shown and discussed. As shown in Section 3.1.1, the kinematic and the static solution define the bounds of the exact solution. All kinematic solutions in this section refer to the rotation-about-wall-toe (ROT) mechanisms in Fig. 23.

The bounds of the earth pressure coefficient acting on a vertical wall are plotted in Fig. 40. The relative difference

$$d_r = 2 \cdot \frac{\overline{K}_{a\xi}^{\text{stat}} - \overline{K}_{a\xi}^{\text{kin}}}{\overline{K}_{a\xi}^{\text{stat}} + \overline{K}_{a\xi}^{\text{kin}}}, \tag{3.44}$$

is plotted on the right axis to express the accuracy of the solution proposed in this work. The static solution corresponds to Equation (3.26), while the kinematic solution corresponds to the highest value given by the mechanisms in Fig. 23 (as it was done, e.g., in Fig. 34).
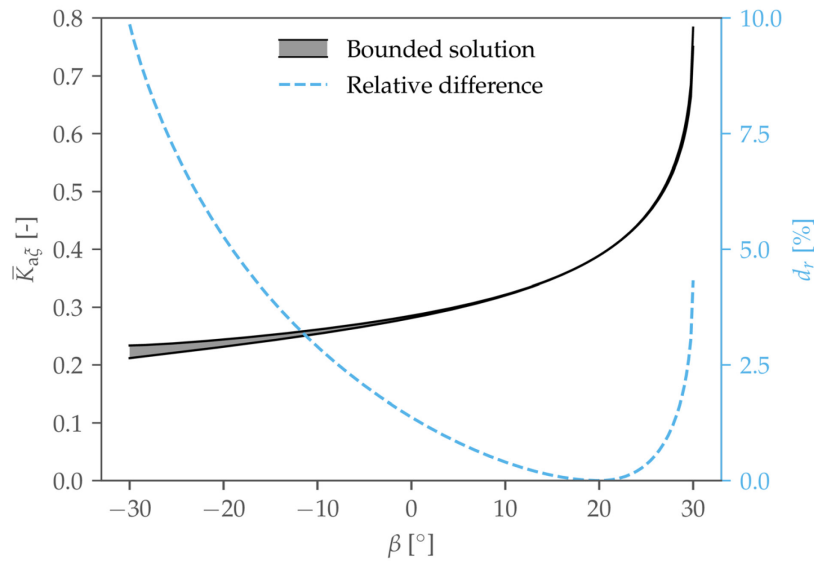
Fig. 40: *Static and kinematic solutions for a vertical wall ($\alpha = 0°$) and variable backfill inclination. The soil strength is $\varphi = 30°$ and the wall friction angle $\delta = 20°$. The difference between the two solutions relative to their average is shown to express the accuracy of the solution.*

At $\beta = 20°$ (i.e., $\beta = \delta$), the static and the kinematic solutions match exactly, meaning they represent the exact solution. In this case, the stress state corresponds to Rankine's solution everywhere in the soil as it must not be rotated to fulfil the boundary condition at the wall interface (see Fig. 38). It follows that failure occurs along straight lines, which are perfectly captured by the one-wedge mechanism. At lower and higher angles β, stress and velocity discontinuities occur in the soil (see Sections 3.4.1 and 3.4.2), and the proposed solutions cannot capture them perfectly. Therefore, the relative difference between the upper and the lower bound increases on both sides of $\beta = 20°$. At $\beta = -30°$, the needed rotation of the stress state reaches the highest value (see Fig. 38). Since this rotation can only be approximatively captured by the solutions proposed in this work, the accuracy decreases. However, it remains in an acceptable range. Especially in the range $\beta = [0°, 30°]$, the relative difference stays below 5%.

In Fig. 41, a numerical solution obtained with the OptumG2 software [105] is compared to the bounded solution of this work.

The difference between the numerical static and kinematic solutions is less than one permille over the whole range. Thus, it can be said that the numerical, exact solution has been found, and only the average between the two bounds can be plotted (the difference would not be visible in the plot). However, it is essential to clarify that the exact numerical solution depends on the discretisation of the problem. For example, suppose the mesh is too coarse. In that case, the numerical solution is likely not equivalent to the analytical, exact solution, even if both the static and kinematic solutions are the same. A discretisation and numerical error will be present in a numerical solution, as is the case in Fig. 41. Previously, it has been shown that the analytical, exact solution is obtained for $\beta = 20°$ (Fig. 40). Instead, the numerical solution in Fig. 41 underestimates the earth pressure coefficient for $\beta = 20°$ by 0.5% (compared to the analytical solution). Hence, a tiny numerical error is present. In general, it is important to benchmark numerical models against known analytical solutions.
Assuming the error of the numerical solution in Fig. 41 to stay approximately within the ±0.5% limit for all backfill inclinations β, it is possible to comment on the proposed analytical solutions. The kinematic solution is the closest to the numerical solution. The static and Coulomb's solutions have approximately the same relative difference to the numerical solution: the first lies on the conservative side, the latter on the unconservative side. Bearing in mind that a numerical error (of about 0.5%) may be present in the numerical solution, it

can be said that the static solution overestimates the exact solution by roughly the same amount that Coulomb's solution underestimates it. Therefore, the static solution should be preferred over Coulomb's solution.
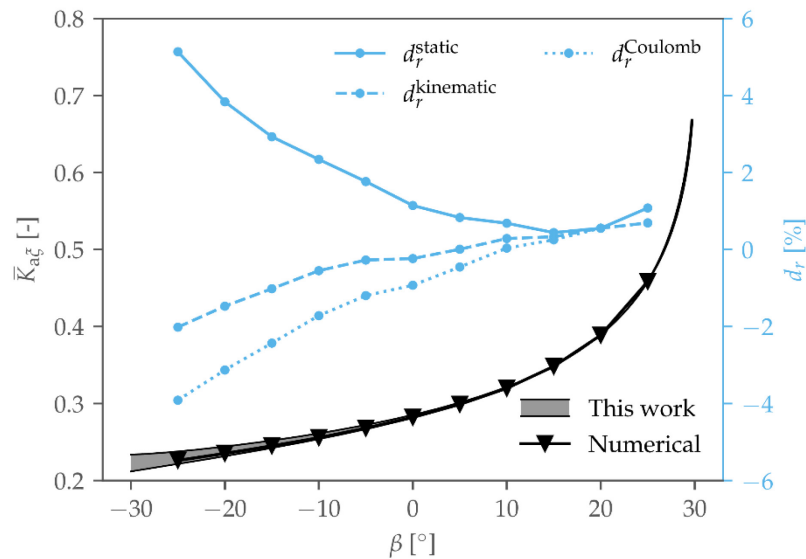

***Fig. 41:** Comparison of the analytical solution presented in this work and a numerical solution obtained using the OptumG2 software [105] for a vertical wall ($\alpha = 0°$) and variable backfill inclination. The soil strength is $\varphi = 30°$ and the wall friction angle $\delta = 20°$. The relative difference between the analytical solutions (static, kinematic, and Coulomb's solution) and the numerical solution is plotted on the right axis.*

3.5   Discussion

3.5.1   On the role of soil dilatancy

In plasticity theory, the solution of a boundary value problem can be significantly affected by the nonassociativity of flow. In Section 3.1.3, the consequences of the nonassociativity to the limit analysis theorems were explained. The effects of soil dilatancy on the soil behaviour and on the bounded solution to the boundary value problem presented in Section 3.3 were analysed in [9]. Here, the most important conclusions for the practical application of the limit analysis solutions are summarised.

The soil mechanical behaviour is affected in the following two ways by its nonassociativity:

1. During yielding, soil exhibit a lower volume change than if the flow were associative [109];
2. A strain localisation occurs [110]–[112].

While the first aspect is widely recognised in the geotechnical field, the second is often neglected. Indeed, it is commonly believed that dilatancy only affects the response of "kinematically constrained problems". Kinematically constrained are defined problems in which the soil expansion is hindered by surrounding soil or structures. Consider, for example, a frictionless pile pushed vertically into a soil half-space that obeys the associated flow rule. The soil surrounding the pile tip must be sheared to reach the limit state and, therefore, undergoes a volumetric expansion. However, any expansion is hindered by the surrounding soil, as the soil cannot easily flow to any free surface at the pile tip's depth. As a result, a pile's tip resistance depends (among other factors) on the soil dilatancy [109]. Intuitively, the limit load of a pile embedded in soil that obeys the associated flow rule is higher than in soil that obeys the nonassociated flow rule. However, many researchers argue that the nonassociated flow rule has additional effects on boundary value problems. In particular, it implies strain localisation, which leads to a nonuniqueness of the limit load [112], [113], and

a reduced limit load (increased, in the case of the active earth pressure) [99]. Therefore, the soil dilatancy would also affect the limit load on a corrosion-damaged cantilever wall, although it can be shown that it is a kinematically unconstrained problem (as the backfill can expand towards the wall, following its rotation, and towards the free surface).

This deduction was confirmed in [9] by solving the boundary value problem depicted in Fig. 42 using the finite element method.
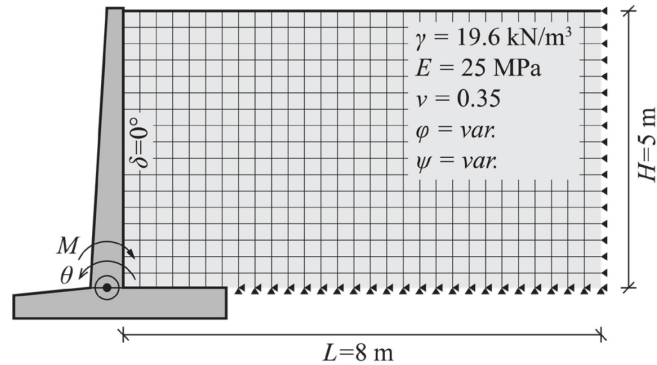

Fig. 42: Geometry and soil parameters considered in the parametric study.

A smooth, rigid cantilever retaining wall backfilled with a 5 m high and 8 m long soil layer is considered. Soil is modelled as an isotropic linear elastic, perfect plastic material obeying the Mohr-Coulomb failure criterion. Thus, the soil behaviour at the limit state corresponds to that assumed for limit analysis (Section 3.1) and allows for a direct comparison of the results. The wall is modelled as perfectly rigid and smooth to avoid additional influences on the stress-strain behaviour of the boundary value problem (e.g. curvature of the shear band due to wall friction). In addition, the two bounds of Section 3.3 deliver the exact solution in the case $\delta = 0°$ (and if associated plasticity is assumed). In a parametric study, the dilatancy angle ψ was varied between 5° and the value corresponding to associated flow, i.e. $\psi = \varphi$, with a step of 5°. A rotation is imposed at the base of the stem, and the moment caused by the earth pressure acting on the wall is evaluated.

The results for a soil friction angle $\varphi = 30°$ are plotted in Fig. 43. The moment-rotation relationship is shown for different dilatancy angles. As expected (see Section 3.1.3), the moment at the limit state increases with decreasing dilatancy angles. In the nonassociated case, a bifurcation is observed at a rotation of approximately 0.5 mrad. The localisation causes soil instabilities that result in an irregular moment-rotation line. These irregularities are shown by the black line, corresponding to $\psi = 5°$. The highest moment at the limit state is obtained for the highest degree of nonassociativity, $\psi = 5°$. Its value is almost 10% higher than the value corresponding to associated flow.
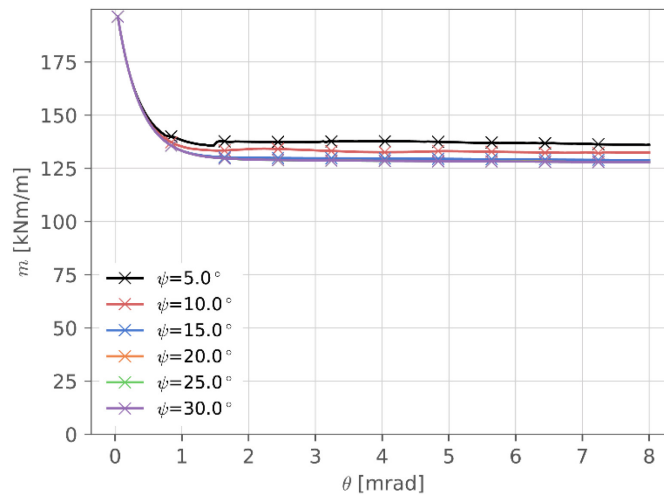
Fig. 43: *Moment as a function of the wall rotation for the soil friction angle $\varphi = 30°$ and the associated flow rule ($\psi = \varphi = 30°$).*

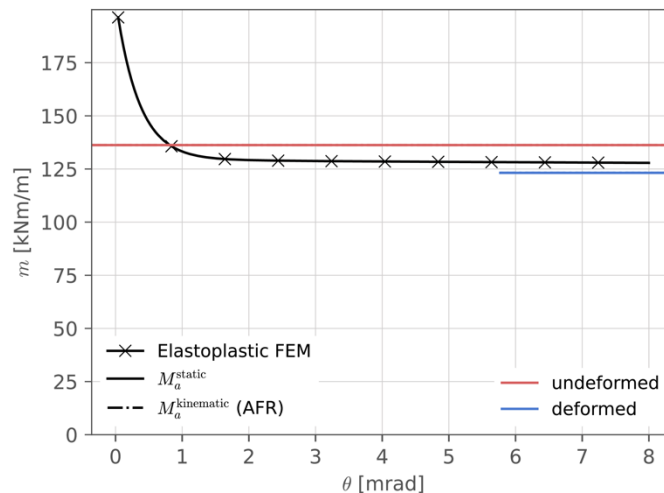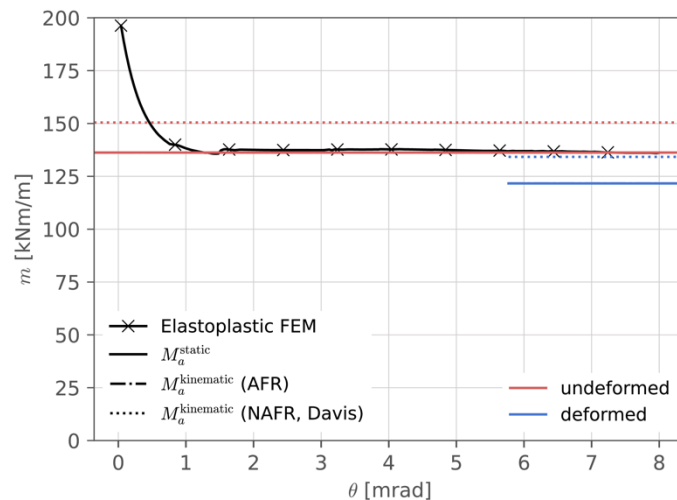**Fig. 44:** *Moment as a function of the wall rotation for the soil friction angle $\varphi = 30°$ and the associated flow rule ($\psi = \varphi = 30°$).*

Fig. 44 shows the resulting moment-rotation response assuming associated flow ($\psi = 30°$). The limit analysis solution, Equation (3.41), is represented by a red horizontal line. Since no wall friction is assumed, the static (solid line) and the kinematic solution (dash-dotted line) are equivalent and overlap (i.e., the exact solution is found). However, it is observed that the moment acting on the wall at the limit state in the elastoplastic FEM analysis is about 6% lower than the value given by limit analysis. The reason is that limit analysis assumes the undeformed configuration of the boundary value problem (i.e., the wall stays vertical, the soil is rigid, perfect plastic, and only a virtual rotation increment is considered). In the elastoplastic analysis, instead, deformations are considered. As the wall rotates, the backfill layer flows and fills the space created by the wall rotation. As a result, the soil surface settles, causing the resultant earth pressure to move down towards the wall's toe, thus reducing the moment acting at that point. An estimate of the limit load in the deformed configuration can be obtained from Equation (3.41) assuming the undeformed soil layer height. The obtained value is plotted in blue in Fig. 45 and is intended to be indicative, as limit analysis solutions cannot be used on deformed configurations. Nevertheless, it can be observed how the elastoplastic solution lies between the value for the undeformed configuration and the indicative value for the deformed configuration.

If the flow is nonassociated, a kinematic solution can be found using the procedure proposed by Drescher and Detournay [98], inserting Davis' reduced parameters [34], Eqs. (3.10)-(3.11). The elastoplastic solution is compared to the limit analysis solutions in Fig. 45. As for the associated case, it is observed that the limit analysis solution overestimates the moment at the limit state as it neglects deformations. Indeed, the moment at the limit state for $\psi = 5°$, represented by the dotted red line, overestimates the elastoplastic solution by approximately 9%. Instead, by pure coincidence, the limit analysis solution based on the associated flow rule corresponds very closely to the elastoplastic solution in this particular case. Again, it can be observed that the limit analysis solution represents a reasonable estimate of the true value if the height of the deformed backfill layer is inserted in Equation (3.41).

Furthermore, the accuracy of the kinematic solution proposed in the previous subsection has been proven for a range of dilatancies and friction angles of practical relevance in [9].
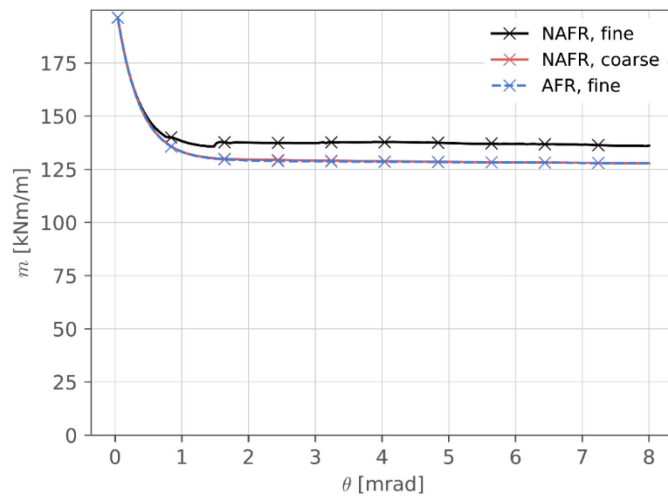

Fig. 45: *Moment as a function of the wall rotation for the soil friction angle $\varphi = 30°$ and the nonassociated flow rule with $\psi = 5°$.*

The cause of the observed increased limit load is ascribed to the plastic strain localisation caused by the nonassociated flow, depicted in Fig. 46.
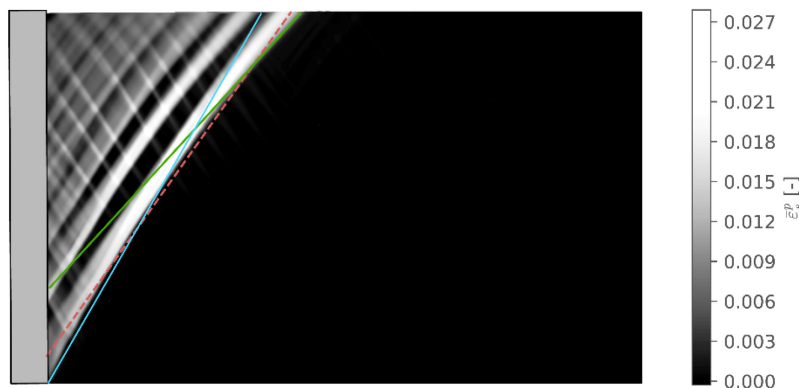
Fig. 46: *Cumulative deviatoric plastic strain for $\varphi = 30°$ and $\psi = 5°$.*

Nonuniqueness and mesh dependence

With nonassociated flow, the response of a boundary value problem is nonunique. Therefore, it becomes questionable whether speaking of *the* limit load rather than *a* limit load is

meaningful [99], as the limit load can take different values depending on the deformation pattern. In real soil samples, the configuration of a shear band (i.e., its position, shape, and orientation) depends on different factors. Among them, one can find material imperfections and boundary conditions (e.g., in a triaxial test, different failure modes can be observed if the top platen's rotation is hindered or not). In a FEM-based simulation, material imperfections do not exist (unless the user explicitly models an imperfection), as the material is assumed to be homogeneous. However, other factors can influence the development of deformation patterns: numerical errors and mesh-related factors. The former can be round-off errors or truncation errors and are, in a way, comparable to material imperfections due to their randomness. The latter can be the mesh orientation, mesh irregularities, or mesh size, to name the most important. While the boundary value problem of Fig. 42 does not suffer issues related to mesh orientation and irregularities (as the mesh is a regular grid aligned with the boundaries), the dependency of its response on the mesh size must be investigated.

Fig. 47: Moment as a function of the wall rotation for the soil friction angle $\varphi = 30°$ assuming the associated flow rule (AFR) and the nonassociated flow rule (NAFR, with $\psi = 5°$). A coarse mesh (element size = 0.1 m) and a fine mesh (element size = 0.02 m) are considered.

The moment acting exerted by nonassociated soil on the wall of Fig. 42 using a coarse and a fine mesh is depicted in Fig. 47. As a reference, the result for a fine mesh and the associated flow rule is plotted in the same figure. A coarse mesh combined with the nonassociated flow rule results in a smooth moment-rotation curve which overlaps almost perfectly the curve for associated flow. The reason is that if the mesh is too coarse, the strain can not localise in thin shear bands. Therefore, a diffused failure mechanism develops. The diffused failure mechanism is shown in Fig. 48.

However, it is noticed how the failure plane is more inclined than one would expect assuming the associated flow rule (i.e. $45° - \frac{\varphi}{2} = 30°$ to the vertical). Indeed, as was shown by Roscoe and other authors (e.g. [96], [114]), and explained in detail in [9], the inclination of the failure line is given by:

$$\chi^{\text{Roscoe}} = \frac{\pi}{4} - \frac{\psi}{2}, \tag{3.45}$$

Given the nonuniqueness of the limit state, the solution obtained using a coarse mesh is a valid solution that fulfils plasticity theory. The same value is obtained from the limit analysis solution, Equation (3.17), by assuming Roscoe's inclination of the failure line, Equation (3.45). However, the solution corresponding to a diffused failure mechanism is not the most critical. A finer mesh must be considered to get a localised failure mode, which leads to a higher moment at limit state.

The mesh dependency of the system response is also captured in the mesh convergence study shown in Fig. 49. A homogeneous failure mechanism develops with a mesh of less than 10'000 elements, and the resulting moment is equivalent to that of associated case. However, increasing the number of elements makes it possible to get localised failure modes, and the resulting moment increases.

Fig. 48: *Cumulative deviatoric plastic strain for $\varphi = 30°$ and $\psi = 5°$ using a coarse mesh (element size = 0.1 m).*
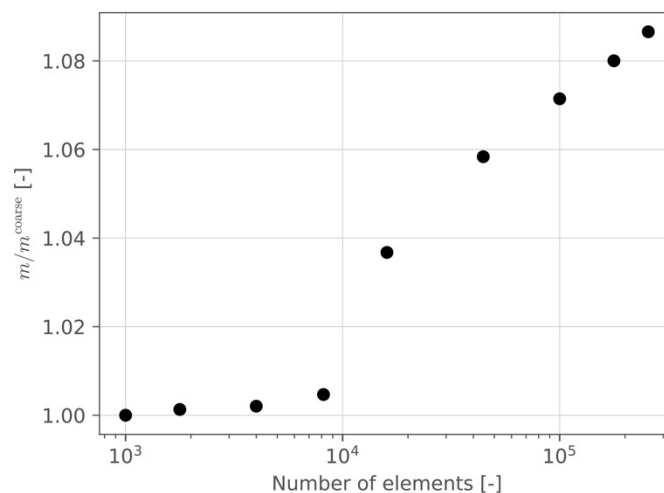
Fig. 49: *Mesh convergence study for $\varphi = 30°$ and $\psi = 5°$.*

Consequences for practical applications

The previous section showed that dilatancy can have a twofold influence on the limit state solution of a boundary value problem:

1. by affecting the volumetric soil behaviour, thus affecting the limit load of boundary value problems that are "kinematically constrained", that is, they have a geometry or boundary conditions that hinder the volume expansion; and/or

2. by causing localised deformation, leading to a nonunique and potentially lower limit load.

The results of this section showed how Item 1 does not concern the problem of a retaining wall rotating about its toe. Instead, its limit state can be affected by Item 2, as this follows directly by the definition of nonassociated flow. A sufficiently fine mesh is a prerequisite for

localisation in finite element calculations. If the mesh is too coarse, a homogeneous deformation field was observed, and the limit load corresponded to that obtained assuming the associated flow rule.

Based on the obtained results, the question immediately arises whether the reduced parameter φ^* (Equation (3.11)) should be considered to determine the earth pressure at the limit state and, in general, to simulate the soil behaviour. If the soil strength is determined using the conventional geotechnical method, that is, by performing triaxial tests and calculating the friction angle based on the measured stresses, the answer is *no*.
Indeed, the friction angle of a soil sample tested triaxially is usually back-calculated by assuming a solution to the boundary value problem based on the static principle of limit analysis, that is,

$$\varphi = \arcsin\left(\frac{\dfrac{\sigma_{max}}{\sigma_{min}} - 1}{\dfrac{\sigma_{max}}{\sigma_{min}} + 1}\right) \tag{3.46}$$

which corresponds to the exact solution to the problem, meaning that the kinematic solution is equivalent to Equation (3.46). The dilatancy angle is then computed based on the volumetric strain measured during the test in a fully decoupled fashion.

However, it is immediately clear that, as soil flow is nonassociated by nature, the friction angle in Equation (3.46) should be substituted by φ^*. In fact, the value φ in Equation (3.46) represents the mobilised strength of a real soil sample characterised by nonassociated flow. Therefore, further reducing the friction angle based on a dilatancy angle determined independently from the friction angle would be a mistake.

The following example better illustrates the meaning of the strength determined using Equation (3.46). Suppose that a biaxial test was run in the laboratory. The ratio between the axial stress and the applied lateral stress measured at the limit state is $\frac{\sigma_a}{\sigma_r} = 3.0$.
Assuming a homogeneous stress state over the whole sample, Equation (3.46) delivers the friction angle $\varphi = 30°$. The dilatancy is then determined based on the measured volumetric and deviatoric strain and corresponds to $\psi = 5°$.
An elastoplastic finite-element simulation of the biaxial test is run assuming a linear elastic, perfect plastic material behaviour, and the parameters $\varphi = 30°$, $\psi = 5°$. A fine mesh is applied to the problem. The obtained force-displacement response is plotted in Fig. 50 (blue line). It is observed how the assumed parameters underestimate the limit load.
Instead, assuming the associated flow rule (AFR; black line) leads to the same strength observed in the laboratory. Otherwise, the same result would be obtained by considering the nonassociated flow rule (NAFR) with $\varphi = 30°$, $\psi = 5°$ and a coarser mesh, as it would hinder the strain localisation.
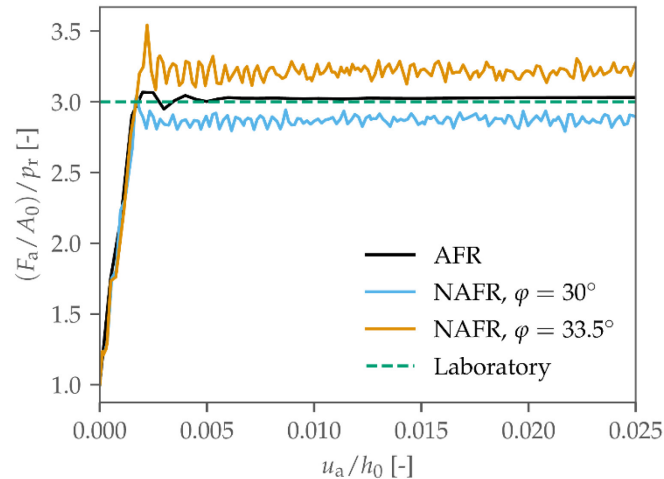
Fig. 50: *Simulation of a biaxial test with different flow rules and soil parameters.*

Instead, if a fine mesh is required, an iterative calibration of the friction and dilatancy angle is necessary to mobilise the correct strength. The first step of this calibration was carried out in Fig. 50, calculating φ^* from Equation (3.11). The friction angle $\varphi^* = 33.5°$ results if $\varphi = 30°$ and $\psi = 5°$ are assumed as a starting value. However, it is seen in the plot how this parameter set now overestimates the limit load, possibly because the mesh is not sufficiently fine to reach the same limit load as the real sample. Indeed, if a fine mesh is considered, the problem becomes mesh dependent, and the calibration must be tailored to the chosen mesh size.

For the verification or design of retaining walls, however, the suggested procedure for the determination of the material behaviour is the following:

1. Run conventional laboratory tests on a soil sample (e.g. triaxial test).
2. Based on the test results, determine the soil friction angle using Equation (3.46). The obtained φ-value implicitly considers nonassociated flow (i.e., it corresponds to φ^*), as the flow of a real triaxial sample is naturally nonassociated.
3. Determine the soil dilatancy angle based on the measured sample deformation.
4. Use the derived parameters without further reduction. In finite element calculations, perform a convergence analysis to ensure that the mesh is not too fine to avoid strain localisation (which would otherwise lead to a wrong limit load).

The last item is particularly relevant, although the obtained results would lie on the safe side in case of nonobservance. In Fig. 49, less than 10'000 elements should be considered if the proposed procedure is followed.

3.5.2 On the role of the frictional interfaces

As seen in Section 3.1.2, the validity of the limit analysis theorems is affected by the presence of (nondilatant) frictional interfaces. Therefore, additional theorems were introduced for problems involving frictional interfaces, such as the earth-pressure problem. It was seen that a solution could be obtained by assuming a dilatant frictional interface obeying the associated flow rule (i.e. with $\varphi = \delta$). That solution, however, only represents an unconservative bound of the exact solution for the real problem with nondilatant frictional interfaces. For the case of dilatant frictional interfaces, a kinematic and a static solution can be formulated to bound the solution. As shown in Fig. 51, the kinematic solution presented in Section 3.3.1 (grey dotted line) remains an unconservative estimate of the exact solution for nondilatant interfaces (solid black line). Instead, the static solution of Section 3.3.2 could either be conservative or unconservative.
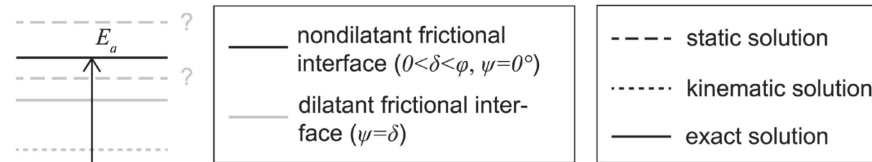
Fig. 51: Bounds of the active earth pressure for frictional interfaces problems.

In [9], a parametric study was carried out to study the validity of the bounded solution of Section 3.3 for problems involving frictional interfaces. The finite-element software is again used to run elastoplastic simulations of the model depicted in Fig. 42, assuming the frictional interface to be nondilatant, while soil flow was assumed to be associated.
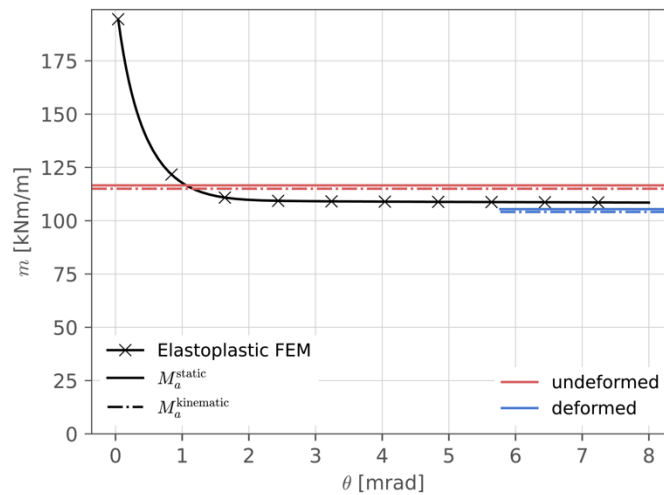

Fig. 52: Moment as a function of the wall rotation for the soil friction angle $\varphi = 30°$ and wall friction angle $\delta = \frac{2}{3}\varphi = 20°$.

Fig. 52 shows the moment-rotation curve for the case $\varphi = 30°$, $\delta = 20°$. Again, the limit analysis bounded solution (red lines) overpredicts the moment from the elastoplastic simulation, as it neglects soil deformations. The role of soil deformations is confirmed by plotting an estimate of the limit load for the deformed state based on the bounded limit analysis solution and the height of the deformed backfill layer (blue lines). It is observed that the dilatant interface assumed in limit analysis does not influence the moment value at the limit state for the analysed configuration since the problem is not kinematically constrained (as the wall moves away from the soil).

Contrary to soil dilatancy, dilatant frictional interfaces do not affect the limit state in any other appreciable manner. The failure mechanism, depicted in Fig. 53, also confirms this: a nondilatant frictional interface causes a curvature of the failure surface (as a dilatant interface does), but no strain localisation or other effects that could affect the limit load. Furthermore, the mechanism of Fig. 53 resembles the limit analysis mechanisms considered in Section 3.3.

Fig. 53: Cumulative deviatoric plastic strain for $\varphi = 30°$ and $\delta = 20°$.

3.5.3 Review of conventional methods

In Section 2.2.5, two methods used in the engineering practice to verify the safety against the structural failure of cantilever retaining walls were shown. These methods differ in how the earth pressure acting on the wall is calculated. In this section, the moment acting at the construction joint of a reference wall is determined using both methods. The results will be compared to the bounded solution presented in Section 3.3 and discussed.
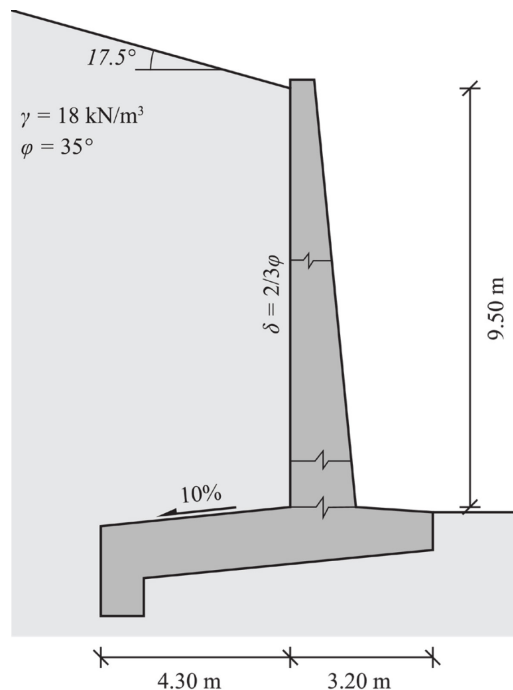
Fig. 54: Reference wall used to compare different state-of-the-art methods, Section 2.2.5, and the bounded solution of Section 3.3 (adapted from [26]).

The reference wall is shown in Fig. 54: the backfill is inclined at an angle $\beta = 17.5°$, and the soil parameters are $\gamma = 18 \text{ kN/m}^3$, $\varphi = 35°$, and $c = 0 \text{ kPa}$.

The first method presented in Section 2.2.5 followed Mörsch's procedure to determine the earth pressure on a cantilever retaining wall. From the graphical construction in Fig. 55, the earth pressure acting on the failure line $\overline{AF}$ is calculated as

$$E_a = \gamma \frac{e \cdot f}{2} = 593.4 \frac{kN}{m}.$$ (3.47)

The resulting earth pressure coefficient reads

$$\overline{K}_a = \frac{e \cdot f}{h_f^2} = 0.646.$$ (3.48)

The inclination of $\overline{AF}$ can be read graphically using a CAD software. It is

$$\chi = 69.6°.$$ (3.49)

The earth pressure is assumed to be linearly distributed on the line $\overline{AF}$. Thus, the resultant force acts at the point one-third of the way along $\overline{AF}$ starting from F (see Fig. 56).
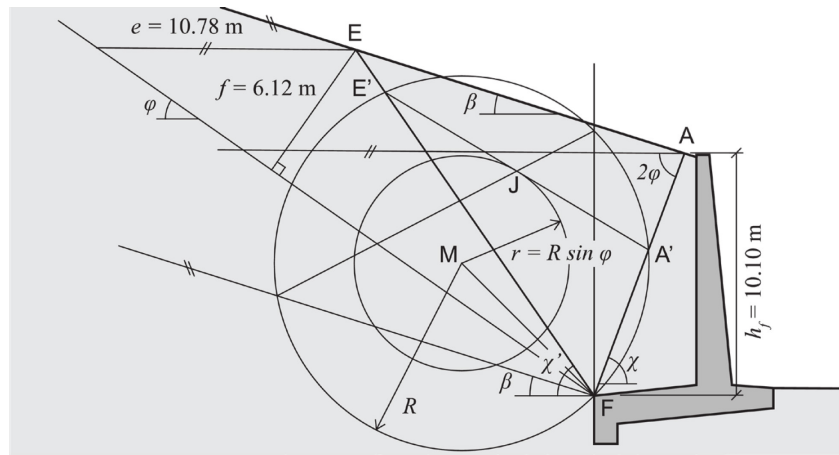

Fig. 55: Determination of the earth pressure with Mörsch's method (Section 2.1.2).
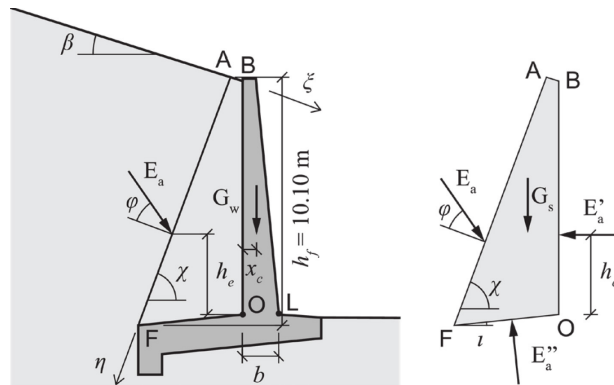
Fig. 56: Earth pressure acting on the failure line according to Mörsch's theory and free body diagram of the soil quadrilateral resting on the wall base.

The same result can be obtained following the analytical procedure based on Mörsch's method described in Section 2.1.2. The inclination of the failure line $\overline{AF}$ results from Rankine's theory, Equation (2.7):

$$\chi = 45° + \frac{\varphi - \beta}{2} + \frac{1}{2}\arcsin\left(\frac{\sin\beta}{\sin\varphi}\right) = 69.6°.$$ (3.50)

The earth pressure coefficient results from Coulomb's theory, Equation (2.2). It is calculated on the inclined failure line $\overline{AF}$:

$$\overline{K}_a = \frac{\cos^2(\varphi + \alpha)}{\cos^2 \alpha \cos(\delta - \alpha)\left[1 + \sqrt{\dfrac{\sin(\varphi + \delta)\sin(\varphi - \beta)}{\cos(\delta - \alpha)\cos(\alpha + \beta)}}\right]^2} = 0.646, \tag{3.51}$$

where $\alpha = \chi - \pi/2$ and $\delta = \varphi$. The resulting earth pressure acting on the soil body resting on the wall base is therefore given by:

$$E_a = \overline{K}_a \frac{\gamma h_f^2}{2} = 593.1 \frac{\text{kN}}{\text{m}}. \tag{3.52}$$

As expected, the two forces in Eqs. (3.47) and (3.52) are equivalent (except for a tiny approximation error).

The moment acting at the bottom of the wall stem can then be calculated. The free-body diagram in Fig. 56 is considered: the earth pressure is transferred from the body resting on the wall base to the wall stem. Assuming no relative motion occurs at the soil-wall interface, E_a' and E_a'' have no tangential components. Thus, the following equilibrium equations can be formulated:

$$\begin{cases} E_a \sin(\chi - \varphi) = E_a' + E_a'' \sin \iota \\ E_a \cos(\chi - \varphi) + G = E_a'' \cos \iota \end{cases}. \tag{3.53}$$

Equation (3.53) would apply if the soil quadrilateral OBAF (Fig. 56) were rigid. However, although it does not reach failure, the soil block OBAF will undergo deformations. Thus, tangential stresses can develop on the soil-wall interface, and Equation (3.53) lose its validity. In engineering practice, it is instead usually assumed that the force E_a'' has no horizontal component. This leads to the more conservative solution:

$$\begin{cases} E_a \sin(\chi - \varphi) = E_a' \\ E_a \cos(\chi - \varphi) + G = E_a'' \end{cases}. \tag{3.54}$$

Indeed, in Equation (3.54), it is assumed that the earth pressure is fully resisted by the wall stem. The moment acting at the construction joint therefore reads:

$$M_a = h_e' E_a \sin(\chi - \varphi) = \frac{9.5}{3} \cdot 336.6 = 1066.0 \frac{\text{kNm}}{\text{m}}. \tag{3.55}$$

The lever arm $l_e' = 9.50\,\text{m}/3$ is determined assuming that the load acting on the wall stem is linearly distributed over the wall height.

The second method described in Section 2.2.5 assumes Coulomb's active earth pressure to act on the wall stem. The wall friction angle is assumed to be $\delta = \frac{2}{3}\varphi$. The resulting moment is therefore given by:

$$M_a = \overline{K}_{ah} \frac{\gamma h^3}{6} = 0.2827 \cdot \frac{18 \cdot 9.5^3}{6} = 727.1 \frac{\text{kNm}}{\text{m}}. \tag{3.56}$$

The resulting moments are summarised in Tab. 4. Additionally, the moment acting at the construction joint obtained using the Stützmauer software (see Section 2.2) [80] and the kinematic and static solutions of limit analysis are listed.

Tab. 4: Moment acting at the construction joint $\overline{OL}$ calculated using different methods. The relative difference refers to the static solution (limit analysis).

Method	Moment	Relative difference
Based on Mörsch	1066.0 kNm/m	46.3%
Based on Coulomb	727.1 kNm/m	-0.2%
Static method (limit analysis)	728.6 kNm/m	0.0%
Kinematic method (limit analysis)	727.8 kNm/m	-0.1%
Stützmauer software	1208.9 kNm/m	65.9%

It can be noted that, for this specific case, the moment resulting from the method based on Mörsch's earth pressure calculation is 46.3% higher than the moment calculated assuming Coulomb's earth pressure acting on the wall stem. The reason is that Mörsch's earth pressure calculation assumes a rigid body translational motion of the cantilever wall. As a result, a Rankine's failure zone develops in the backfill, and the stress acting on the rigid block resting on the wall base is transferred to the wall. In the case of a translational motion of the cantilever wall, the wall friction angle only plays a marginal role (if any) on the earth pressure magnitude, as failure at the soil-wall interface can only occur on the upper portion of the wall (i.e., if the failure line $\overline{AF}$, Fig. 56, intersects the wall stem). Instead, the method that considers Coulomb's earth pressure implies that the soil-stem interface fails. This leads to a lower moment acting at the construction joint. The value based on Coulomb's theory is very close to the bounded limit analysis solution. It has been shown in Section 3.4.1 that for the most common wall and backfill geometries, the moment obtained by integrating Coulomb's earth pressure corresponds to the kinematic solution for a wall rotating about its toe.

It is also observed that the moment calculated using the Stützmauer software is 13.4% higher than that resulting from Equation (3.55), although both are calculated following Mörsch's method. In the software, the moment is calculated as:

$$M_\mathrm{a} = h_e E_\mathrm{ah} = 2.99 \cdot 404.3 = 1208.9 \, \frac{\mathrm{kNm}}{\mathrm{m}}. \tag{3.57}$$

The first difference relative to Equation (3.55) is that the lever arm h_e is assumed to be the distance between wall section $\overline{OL}$ and the acting point of the earth pressure along the failure line $\overline{AF}$ (Fig. 56): the resultant earth pressure is not transferred to the wall prior to the moment calculation. The second difference is the earth pressure value. The software gives the horizontal and vertical earth pressure components as $E_\mathrm{ah} = 404.3 \, \mathrm{kN/m}$ and $E_\mathrm{av} = 571.0 \, \mathrm{kN/m}$. The resultant earth pressure is therefore

$$E_\mathrm{a} = \sqrt{404.3^2 + 571.0^2} = 699.6 \, \frac{\mathrm{kN}}{\mathrm{m}}. \tag{3.58}$$

Knowing that the earth pressure is inclined by φ on the normal to the failure line, the inclination of the latter can be deduced from the direction of the earth pressure:

$$\chi = 90° + \varphi - \arctan \frac{571.0}{404.3} = 70.3°. \tag{3.59}$$

The inclination of the failure line is very close to the result based on Rankine's theory, Equation (3.50). Assuming $\alpha = 70.3° - 90° = -19.7°$, the earth pressure coefficient results in

$$\overline{K}_\mathrm{a} = \frac{\cos^2(\varphi + \alpha)}{\cos^2 \alpha \cos(\delta - \alpha) \left[1 + \sqrt{\frac{\sin(\varphi + \delta)\sin(\varphi - \beta)}{\cos(\delta - \alpha)\cos(\alpha + \beta)}} \right]^2} = 0.629. \tag{3.60}$$

It can then be shown that the earth pressure in the Stuetzmauer software is calculated as

$$E_a = \int_0^{\frac{h_f}{\cos\alpha}} \bar{K}_a \gamma \eta \frac{\cos(\alpha + \beta)}{\cos\beta} \, d\eta = 688.0 \frac{\text{kN}}{\text{m}}. \tag{3.61}$$

Where $h_f = 10.14$ m is the height of the failure line $\overline{AF}$ given $\chi = 70.3°$. Equation (3.61) shows that the earth pressure is integrated along the coordinate η, parallel to the wall (see Fig. 56). However, in the software, the earth pressure coefficient $\bar{K}_a$, normalised by $\gamma h_f^2/2$ as described in Section 3.3.3 is erroneously assumed, leading to an overestimation of the earth pressure acting on the wall. The values in Eqs. (3.58) and (3.61) still differ by less than 2%. The reason for this difference cannot be explained precisely without access to the source code and is likely to be caused by different numerical approximations.

The two methods described in Section 2.2.5 are further compared through a parametric study. The simplified wall section depicted in Fig. 57 is considered. The reference parameters are listed in the same figure. The parameters are varied one at a time, keeping all others constant as in the reference configuration. [6]

$\beta = 0°$

$\gamma = 18$ kN/m³
$\varphi = 35°$

$\alpha = 0°, \delta = 2/3\varphi$

$H = 9.50$ m

$B = 4.30$ m   3.20 m
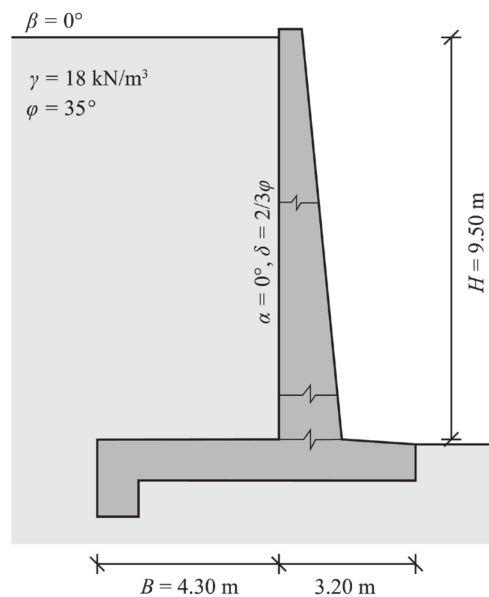
Fig. 57: Wall section and reference parameters considered in the parametric study.

In Fig. 58, the wall base width is varied. The bounded solution has a constant value over the whole range. Unlike the case of a translational motion, in the case of a structural failure at the construction joint, the failure mechanism is independent of the geometry of the wall base. Instead, in the case of a translational motion, the geometry of the failure mechanism is affected by the wall base width, as the failure line $\overline{AF}$ defining the soil block resting on the base can either intersect the soil surface or the wall stem. For large ratios B/H, that failure line intersects the soil surface (Fig. 59a). In that case, no failure occurs at the soil-wall interface, and Rankine's earth pressure acts on the soil quadrilateral resting on the wall base. For a vertical wall with horizontal backfill, the moment calculated assuming Mörsch's earth pressure is equivalent to the moment calculated assuming Rankine's earth pressure acting on the wall:

$$M_a^{\text{Rankine}} = \bar{K}_{ah} \frac{\gamma h^3}{6} = \frac{1 - \sin\varphi}{1 + \sin\varphi} \frac{\gamma h^3}{6} = 697.0 \frac{\text{kN}}{\text{m}}. \tag{3.62}$$

However, if the ratio B/H is lower than a specific value (about 0.5 in the example of Fig. 58), the failure line $\overline{AF}$ intersects the wall stem, and failure partially occurs on the soil-wall interface (Fig. 59b). Then, the moment calculated applying Mörsch's method decreases

---

[6] To note is that the wall friction is defined as a fraction of the soil friction angle. That is, the absolute value of the wall friction does vary when the soil friction angle is varied.

and approaches the bounded solution. At $B/H = 0$, Mörsch's failure mechanism corresponds to Coulomb's, and the moment calculated assuming Mörsch's earth pressure is very close to the lower bound delivered by the kinematic solution of Section 3.4.1 (because the kinematic solution considers more complex failure mechanisms).
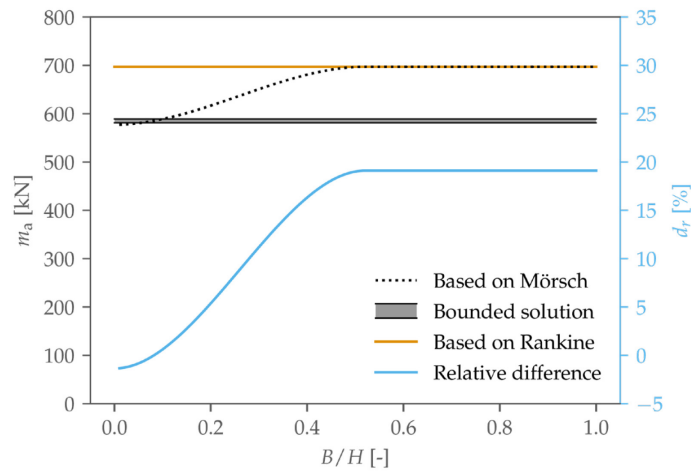

Fig. 58: Moment at the construction joint of the wall shown in Fig. 57 for the reference values and a variable base width B.
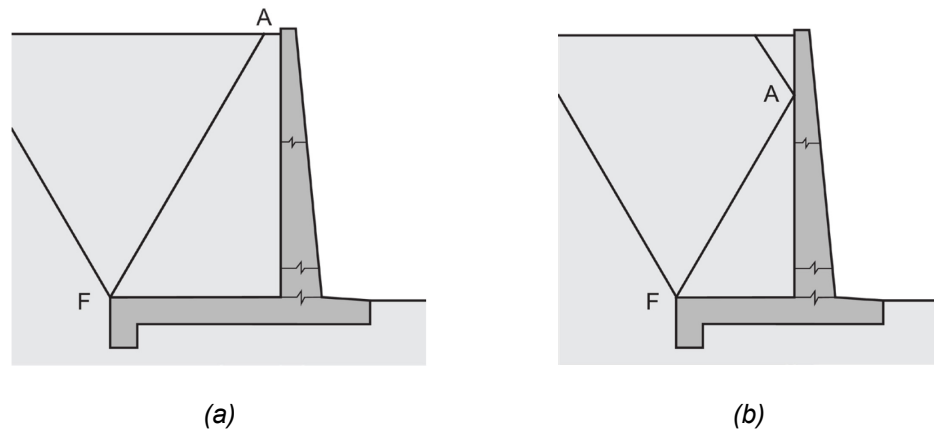

*Fig. 59: Kinematically admissible failure mechanisms for a translational motion: (a) for a long wall base; (b) for a short wall base.*
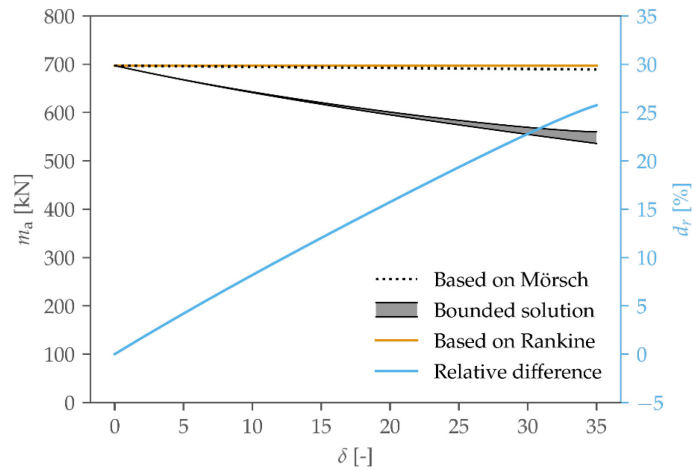
Fig. 60: *Moment at the construction joint of the wall shown in Fig. 57 for the reference values and a variable wall friction angle δ.*

Fig. 60 shows the influence of the wall friction angle. The solution based on Mörsch's earth pressure shows a minimal variation. The reason is that the reference wall has a ratio $B/H \cong 0.45$. Thus, the failure line $\overline{AF}$ intersects the wall stem at a high position (i.e. close to the soil surface), and the wall friction angle is almost irrelevant. At $\delta = 0°$, the two solution correspond to the solution based on Rankine's earth pressure. As the wall friction angle increases, the relative difference between the bounded solution for structural failure and the solution based on Mörsch's earth pressure increases.
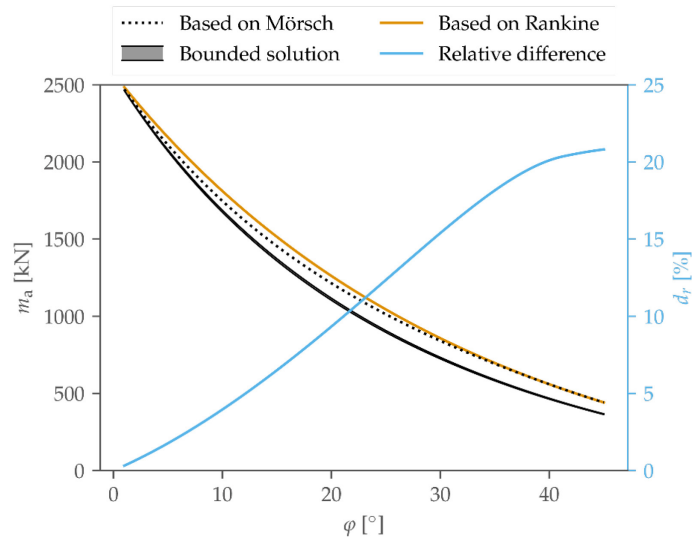
Fig. 61: *Moment at the construction joint of the wall shown in Fig. 57 for the reference values and a variable soil friction angle φ. The reference wall friction angle is defined as $\delta = 2/3\,\varphi$ and therefore also varies.*

The influence of the soil friction angle is shown in Fig. 61. At $\varphi = 0°$, both solutions correspond to the solution based on Rankine's earth pressure. As the soil friction angle increases, the two solutions start deviating. The solution based on Mörsch's earth pressure overestimates the moment acting at the construction joint in the case of a structural failure. It is interesting to note that, as φ increases, the solution based on Mörsch's earth pressure first deviates from the solution based on Rankine's earth pressure and then converges back to it. This is because the inclination of the failure line $\overline{AF}$ increases with higher soil friction angles and intersects the soil surface instead of the wall stem.
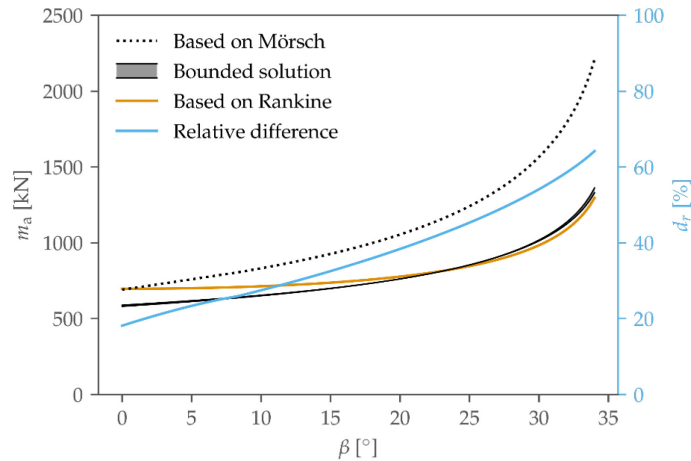
Fig. 62: *Moment at the construction joint of the wall shown in Fig. 57 for the reference values and a variable backfill inclination β.*

Fig. 62 shows the influence of the backfill inclination. In the case of a horizontal backfill, the solution based on Mörsch's earth pressure is very close to that based on Rankine's, as already discussed. However, for higher inclinations, the two solutions diverge since Rankine assumes $\delta = \beta$, while Mörsch's limit-equilibrium solution assumes no relative motion at the wall interface, which is equivalent to assuming $\delta = 0°$. In general, the solution based on Mörsch's earth pressure overestimates the moment at structural failure for the whole considered range.

3.5.4 On the role of the soil cohesion

In this work, no soil cohesion was assumed. Soil cohesion has a stabilising effect on the backfill that would cause lower stresses on the wall at the limit state.
The limit analysis solution proposed in this section could be extended to consider soil cohesion. However, for the reasons listed in Section 1.1, assuming cohesion for wall backfills is generally unsafe.

3.5.5 On the role of groundwater

Groundwater has a destabilising effect on soil, causing higher pressures on retaining walls. Therefore, proper drainage is usually required for retaining walls [5], [6]. However, in some situations, the effects of groundwater are unavoidable. This is the case of a continuous water flow in a slope or drainage damage. In the first case, flow forces act on the backfill, potentially affecting the geometry of the failure mechanism, while the latter represents the case of water accumulation characterised by hydrostatic water pressures.
In each case, neglecting groundwater pressures in the design or verification of retaining walls can potentially lead to catastrophic failure (e.g. [115, p. 148]).

The presented solution can be directly used in the case of hydrostatic groundwater pressures by conducting the analysis using effective stresses. Instead, the case of water flow is better carried out using total stresses, following, for example, the procedure proposed by Lambe and Whitman [116]. Following their procedure, the presented kinematic solution can be adapted to consider the flow forces. Alternatively, numerical limit state solutions can be obtained, e.g., using the OptumG2 software [105].

3.6 Conclusions and recommendations for the practice

This section first presented and discussed various failure modes of cantilever retaining walls. Then, the structural failure in bending was identified as the relevant failure mode potentially threatening corrosion-damaged cantilever walls and was further investigated in the rest of the section.

A bounded solution, based on limit analysis, was proposed. The solution provides the engineer with an excellent tool to benchmark numerical solutions and assess the safety and the design of existing structures. It was then shown that the problem of a rotation about the wall toe corresponds to a wall translation for the most relevant parameter ranges. In addition, the one-wedge mechanism often delivered a sufficiently accurate solution, meaning that walls designed assuming the Coulomb's active earth pressure were correctly designed. The proposed solution was generally shown to bound the true solution accurately. The static solution is not more cumbersome than Coulomb's and can be easily employed in practice. Its advantage is that it lies closer to the safe side.

The effects of dilatancy were then discussed. Nonassociated flow leads to strain localisation and a higher limit load. In addition, the inclination of the shear bands was also observed to depend on the dilatancy angle. In finite element calculations, the higher limit load was only achieved for sufficiently fine meshes, while coarser meshes reached the same limit state as assuming the associated flow rule. On the other hand, the problem was shown to be "kinematically unconstrained". Indeed, the dilatancy angle does not influence further the magnitude of the limit load, as the yielding soil is free to "flow" following the wall movement and in the direction of the soil surface. Therefore, no kinematic constraint hinders any volume expansion.

For practical purposes, it was shown how the strength derived following conventional geotechnical procedures can be directly employed in the limit analysis solutions or for finite element calculations. For the latter, care is required when choosing the mesh size.

Similarly, the implications of wall friction on the limit analysis solutions were investigated. Although the limit analysis solution models the interface as dilatant, its accuracy was demonstrated by running elastoplastic finite-element simulations.

Finally, the conventional methods were reviewed based on the newly gained knowledge. It was shown how different assumptions often led to more conservative forces than the more accurate limit analysis solution, leading to higher safety margins against bending failure.

Recommendations for the practice

A plastic hinge in the structure must be considered to design and verify the structural safety of cantilever retaining walls. The moment acting at the plastic hinge at the limit state can be computed following this procedure:

1. Determine the wall geometry, soil parameters, and wall interface friction.
2. Determine the moment acting at the limit state using Equation (3.17) (kinematic solution), or Equations (3.31) and (3.41) (static solution).
   Alternatively, integrate Coulomb's active earth pressure along the wall height. The kinematic solution corresponds to Coulomb's solution and lies on the unsafe side (although with negligible error).

The obtained value can be used to assess the safety of cantilever retaining walls or to benchmark finite element calculations. In finite element calculations, the mesh size must be determined to avoid strain localisation due to the associated flow.

4   Corrosion-driven wall unloading

4.1   Soil-wall interaction in the case of incremental wall corrosion

Localised corrosion of the main reinforcement bars of a cantilever retaining wall causes a decrease in its strength and ductility [117]. Consequently, the equilibrium state of the wall can be altered.

The actions and reactions of a fictitious cantilever retaining wall are plotted in Fig. 63, where m_r represents the bending resistance, and m_s the acting moment due to the earth pressure. The earth-pressure induced moment m_s is expressed as a function of the wall rotation θ, while the structural resistance m_r additionally depends on the corrosion degree ζ. Throughout this work, the rotation θ and moment m are referred to as the respective quantities measured about the construction joint between the stem and the wall base (i.e. at the stem toe), where corrosion damages are usually located (as reported in [1], [2]).

During the wall's service timespan, the actions and resistance do not necessarily (in fact, never) stay constant but rather change over time due to different factors, such as the type of use of the structure, meteorological influences, time effects, and damages. The present work mainly focuses on corrosion-driven damage. The corrosion process is illustrated in Fig. 63, starting from the undamaged state of a newly constructed wall.
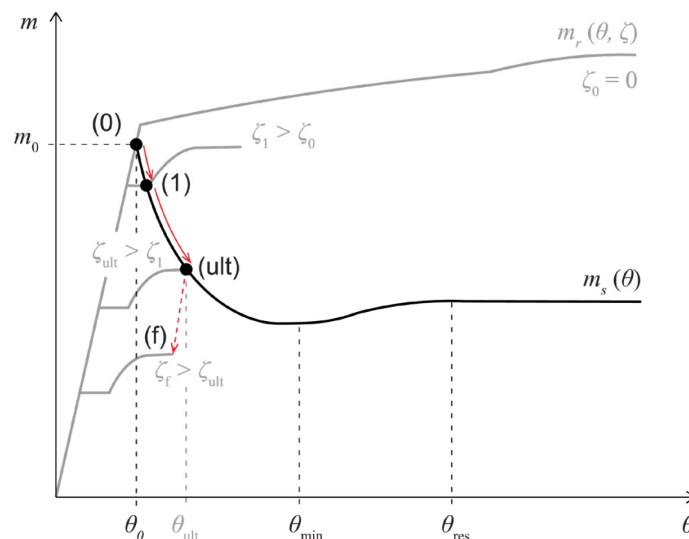

Fig. 63: Moment-rotation behaviour of a cantilever retaining wall and earth pressure-induced moment about the construction joint (picture drawn in collaboration with S. Häfliger, Institute of Structural Engineering, ETH Zurich).

The value of the moment acting at the construction joint at the onset of corrosion is the result of the full loading history, starting from the wall construction. As the backfill is deposited in multiple lays and (possibly) compacted, the moment m_s gradually increases until the value m_0 (called *initial moment* throughout this work and resulting from the *initial stress state*) is reached. As a result, the wall deforms to mobilise the strength m_r required for equilibrium and the rotation θ_0 arises. Over the lifespan of the wall, the moment acting at the construction joint fluctuates around the value m_0 due to external influences, such as surcharge loads, meteorological influences, or time effects. At the same time, the structural resistance can vary due to, e.g., time effects or damages. The present work focuses mainly on corrosion-related damages.

Later in the lifetime of the wall, as the degree of corrosion slowly increases and reaches the degree ζ_1, both the strength and the rotation capacity of the wall are reduced [117], as shown in Fig. 63. At this stage, it is the decrease in strength that causes the previously safe equilibrium state at $m_0 \equiv m_r(\theta_0, \zeta = 0)$ to become unstable. While the wall would fail immediately under constant load m_0, it does not necessarily fail as the earth pressure depends on the wall displacement. Indeed, as equilibrium is lost, the wall undergoes additional displacement, localised at the damaged region (in this case, at the construction joint), until a new equilibrium state is found. If no admissible equilibrium state is found, failure occurs. The effects of the additional displacement of the wall are twofold. First, it causes the soil to unload, reducing the earth pressure on the wall. Second, it (possibly) mobilises additional wall strength. At a given corrosion degree, the rotation capacity and strength of the wall are just sufficient to ensure stability. This point is denoted (ult) in Fig. 63 and represents the ultimate state: if the corrosion degree further increases, $\zeta_\mathrm{f} > \zeta_\mathrm{ult}$, the wall collapses.

While it is generally safe to assume that the stress state in the backfill of undamaged walls can be fully unloaded to the active state before the wall fails, failure of a corroded retaining wall can occur before complete unloading of the backfill to the active state. That is, the wall rotation capacity θ_ult is too small to allow complete unloading of the backfill, and the wall collapses under higher loads than the active earth pressure: $\theta_\mathrm{ult} < \theta_\mathrm{res}$. Therefore, it becomes questionable whether it is safe to assess the stability of corroded retaining walls assuming the limit state as in Section 3.3. In the following chapters, the corrosion-driven unloading of the backfill of retaining walls will be investigated in controlled laboratory experiments and numerical models. Instead, the structural behaviour of corrosion-damaged cantilever retaining walls is investigated in [3].

4.2 Qualitative analysis of the wall unloading

This section presents a preliminary, qualitative analysis of the corrosion-driven wall unloading through a simplified numerical analysis. The numerical analysis is carried out using the Abaqus finite element software [118]. Simplified assumptions are made to study the essence of the wall unloading process and isolate irrelevant external influences at this stage. Thus, a rigid wall is modelled, and the backfill is assumed as an isotropic linear elastic, perfect plastic material obeying the Mohr-Coulomb failure criterion. The Abaqus implementation of the failure criterion was written by Clausen et al. [119]–[121]. The soil-wall interface is frictional ($\delta > 0°$).
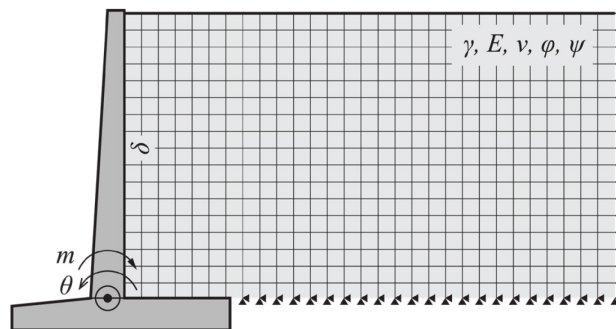

Fig. 64: *Finite element model for the boundary value problem of a corrosion-driven wall rotation.*

The modelled boundary value problem is sketched in Fig. 64. As already discussed in the previous section, a rotation is imposed at the toe of the wall stem to simulate a corrosion-driven rotation caused by a loss of structural resistance. Initially, the earth pressure is assumed to be linearly distributed:

$$e_{0n} = K_0 \gamma y. \tag{4.1}$$

The salient stages of the wall unloading process are shown in Fig. 65-Fig. 67, which show the normalised contact pressure and mobilised friction angle at the wall interface, and the deviatoric plastic strain in the backfill.
The normalised contact pressure is defined as

$$\bar{\sigma}_n = \frac{\sigma_n}{\gamma h}, \tag{4.2}$$

where σ_n is the pressure exerted by the soil on the wall, and h is the wall height. The normalised mobilised friction angle is defined as

$$\bar{\delta}_{\text{mob}} = \frac{\sigma_t / \sigma_n}{\tan \delta_{\text{wall}}}, \tag{4.3}$$

where σ_t is the tangential stress acting on the soil-wall interface. Failure occurs at the soil-wall interface when $\bar{\delta}_{\text{mob}} = 1$ (i.e. the wall friction is fully mobilised). The resulting quantities are plotted as a function of the normalised vertical depth

$$\bar{y} = \frac{y}{h}. \tag{4.4}$$

As the wall starts rotating, a plastic region develops in the upper backfill, where the most significant wall displacement occurs. In this region, plastic deviatoric deformations are developed, and the pressure on the wall decreases from its initial value $\bar{e}_0$ to the active value $\bar{e}_{\text{an}}$ (in the plot, the kinematic solution $\bar{e}_{\text{an}}^{\text{kin, AFR}}$ is drawn). At the same time, failure occurs at the soil-wall interface, as confirmed by the high plastic strain intensity measured along the upper portion of the interface and by the value of the mobilised friction angle that already reaches the wall friction angle, $\bar{\delta}_{\text{mob}} = 1$.
In Fig. 65, it is noted that failure in the soil has already reached a depth of about $\bar{y} \cong 0.4$, while the interface failure only took place in the range between the soil surface and $\bar{y} \cong 0.2$. This is reflected in the earth pressure: in the range $\bar{y} \in [0,0.2]$, the active value $\bar{e}_{\text{an}}$ is fully reached, while in the range $\bar{y} \in [0.2,0.5]$ the earth pressure is still marginally higher than $\bar{e}_{\text{an}}$. In that depth range, the wall provides support to the soil, which does not slip along the interface. Thus, the weight of the failing soil is partially redistributed by fictitious arches to the wall and the intact soil outside the formed failure mechanism.
This phenomenon can be observed by looking at the deviatoric plastic strain in Fig. 65, where three main failure lines are observed. Two of them are parallel to each other. The lowest one separates the yielding soil from the intact soil (i.e. the soil below yield). The upper failure line delimits the soil that has fully reached failure (i.e. the active state) and the soil that is yielding but is still partially supported by the aforementioned arching effect. Finally, the third failure line intersects the other two and represents the region where the arching effect occurs.

As the rotation further increases, the failure region grows (Fig. 66), and the failure along the soil-wall interface propagates until it reaches the wall toe (Fig. 67). At that point, slip occurs over the entire height of the soil-wall interface, and the arching effect that partially contributed to supporting the soil weight by redistributing it to the wall and the intact soil is lost. Thus, the *limit state* is reached and the earth pressure is ultimately reduced to its active value over the entire wall height. The stress distribution is linear over the depth, and the limit analysis solution of Section 3.3 is valid.
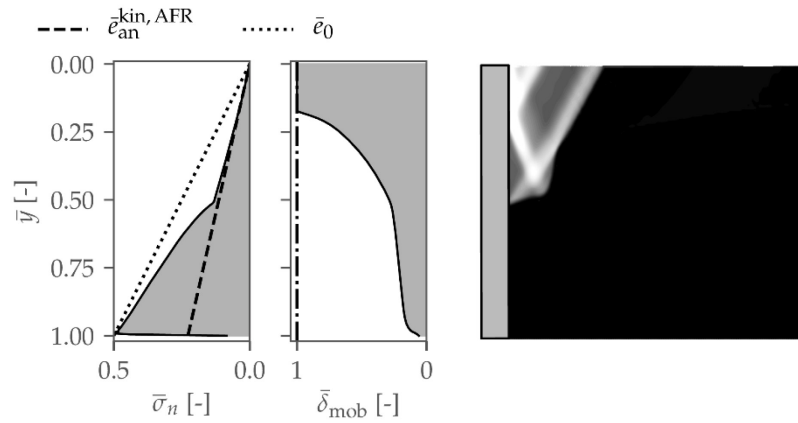
Fig. 65: *Contact pressure and mobilised friction angle at the wall interface and cumulative deviatoric plastic strain after a rotation of 0.7 mrad.*
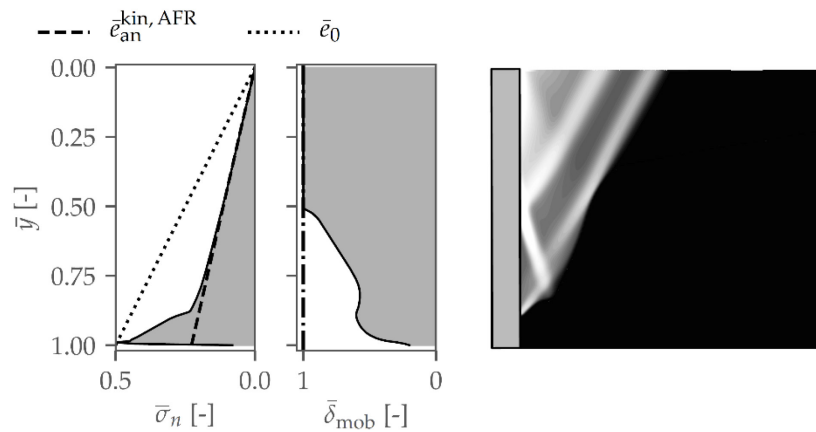

Fig. 66: *Contact pressure and mobilised friction angle at the wall interface and cumulative deviatoric plastic strain after a rotation of 2.3 mrad.*
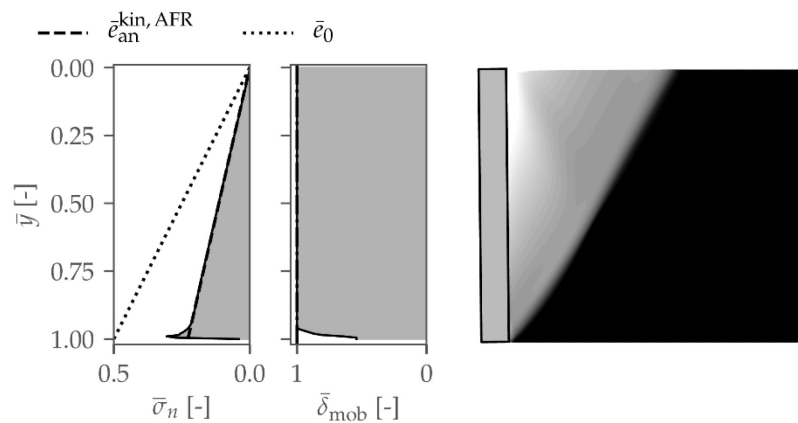

Fig. 67: *Contact pressure and mobilised friction angle at the wall interface and cumulative deviatoric plastic strain after a rotation of 10 mrad.*

4.3   Investigation into the controlling parameters

The results of a limited parametric study are presented here to identify the most influential parameters on the wall unloading process. These results were considered to design a proper experimental setup capable of capturing the most important aspects of the unloading behaviour and as a starting point for further numerical analyses. The rotation of a rigid wall backfilled with linear elastic, perfect plastic soil was considered as in the previous section. The study is conducted by varying one parameter at a time and keeping the remaining ones constant. Only the dilatancy angle is changed together with the friction angle to simulate associated flow.

Fig. 68a shows the moment-rotation response resulting from two configurations only differing by their Young's modulus E. The results confirm the intuition that stiffer soil requires smaller wall displacements to reach the limit state, as yielding is reached at smaller soil strains than in softer soil. It is also observed that the limit load is not influenced by the Young's modulus as failure is governed by plastic parameters only.

The influence of the soil friction angle is shown in Fig. 68b. Higher strength means that lower stress values are admissible. To reach plastic failure, therefore, larger displacements are needed (provided that the soil stiffness is the same). Consequently, the limit state is lower in the case of soil with higher strength, but larger wall rotations are required to reach it. However, it must be noted that stiffer soil often has higher strength, thus compensating for the stiff moment-rotation response.
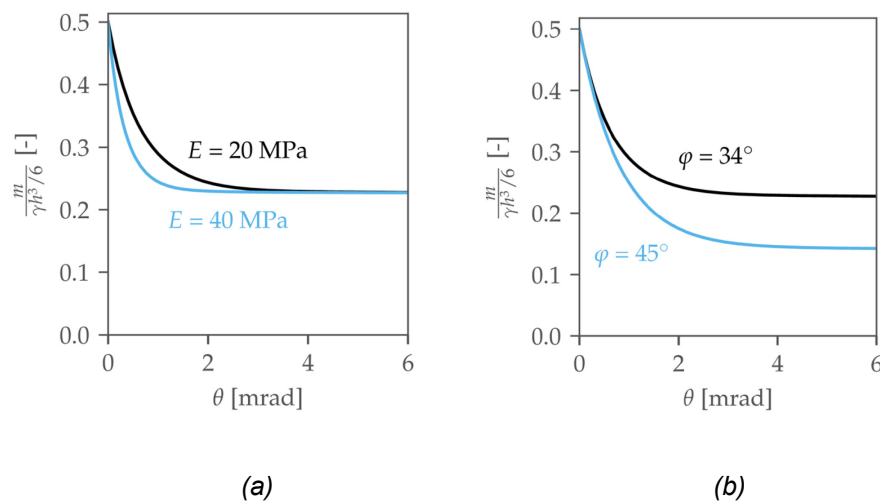

(a)   (b)

Fig. 68: *Normalised moment as a function of the wall rotation for two different values of Young's modulus (a) and soil friction angle (b).*

The effects of increased initial soil stresses are shown in Fig. 69. A higher stress state means that it is further away from the failure surface, which means that larger deformations are needed to reach failure and the limit state. However, also in this case, it must be noted again that increased stresses usually lead to stiffer soil, thus decreasing the needed wall rotation to reach the active limit state.

The influence of soil dilatancy was discussed in detail in the previous section, where it was concluded that the problem of a wall rotating about its toe is not affected by the volumetric behaviour of soil. Also the variation of the Poisson's ratio showed no influence on the wall unloading process.

This simple parametric study identified the most relevant influence parameters and showed how the elastoplastic soil behaviour and the initial stress state influence the wall unloading.
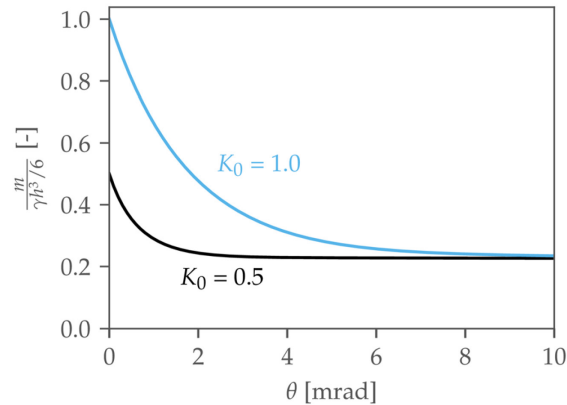
Fig. 69: *Normalised moment as a function of the wall rotation for two different values of the initial earth pressure.*

4.4   Conclusions

This section qualitatively described the corrosion-driven unloading process of cantilever retaining walls. It was shown how the earth pressure evolves from the wall's construction to its end of life, considering corrosion damages. Corrosion leads to a loss of strength and a decrease in the rotation capability of the walls. For this reason, the wall may fail before the backfill can be fully unloaded to the active state, highlighting the importance of investigating the complete unloading process between the initial state and soil failure.

A qualitative analysis of the soil-wall interaction showed how soil failure propagates from top to bottom in a backfill with an initial linear stress distribution. In the first phases of the unloading, the wall supports the yielding soil, generating an arching effect, which later disappears as the limit state is reached. The stress distribution at failure is linear, as predicted by the limit analysis solution in Section 3.

Finally, a limited parametric study showed the most influential parameters on the wall unloading process. The most relevant parameters are the soil stiffness and strength (more generally, the elastoplastic soil behaviour) and the initial stress state. These results will be considered in the following section for the experimental setup design.

5 Experimental study of the corrosion-driven wall unloading process: setup and program

As part of this work, an experimental setup has been designed and built to study the soil unloading caused by corrosion-driven wall displacement. The experimental campaign aims to study the development of the earth pressure acting on damaged retaining walls under different conditions. The location of the damage is assumed to be at the wall toe. In particular, the parameters influence of the preliminarily studied in Section 4.3 must be investigated under controlled, repeatable conditions. Furthermore, the experimental setup must also allow precise measurements, reducing any bias caused by external factors (e. g. boundary effects) to a minimum.

5.1 Design of the test walls

As a result of an optimising process, a scaled and fully instrumented wall was designed. The test wall is 150 cm long, its stem is 50 cm high, and the foundation is 30 cm wide. The tests will be carried out in a glass box having dimensions BxLxH 150 cm x 150 cm x 110 cm. The box size was chosen so that no boundary effects affect the results in the central wall segment. A sketch of the experimental setup is shown in Fig. 70.
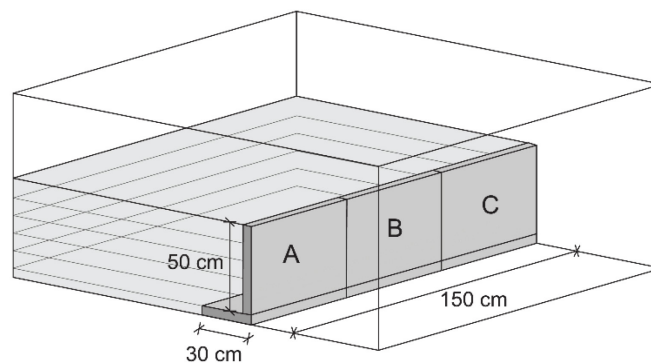

Fig. 70: Isometric view of the test setup. The cantilever wall (Section 5.1.1) is placed in a glass box and backfilled. The three wall sections are named "A", "B", and "C".

Two different walls have been built. The first wall allows a controlled differential rotation between its stem and foundation and behaves similarly to a full-scale concrete wall (in terms of deformation). This wall consists of three identical, disconnected sections, each 50 cm long (Fig. 70). It is used to investigate the initial earth pressure acting on cantilever retaining walls and the unloading behaviour in the event of corrosion-driven wall rotations. This wall will be referred to as the *cantilever retaining wall* in the following. The second wall is 150 cm long and is very stiff. It undergoes infinitesimal deformation when subjected to the lateral earth pressure exerted by the backfill. Therefore, it is used to study the initial earth pressure at rest, i.e. the earth pressure acting on rigid structures. This wall will be referred to as the *rigid wall* in the following.

The design of the two wall types is presented in the following sections.

5.1.1 Cantilever retaining wall

The test cantilever retaining wall consists of the foundation plate and the stem. These two parts are connected by a hinge that allows a differential rotation. A detailed section of the test walls and two isometric views are shown in Fig. 71 and Fig. 72.
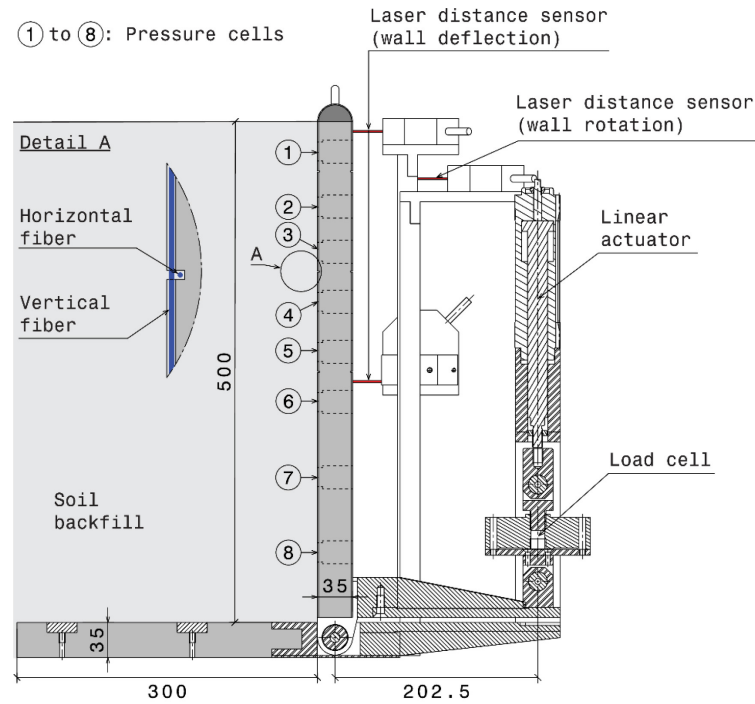
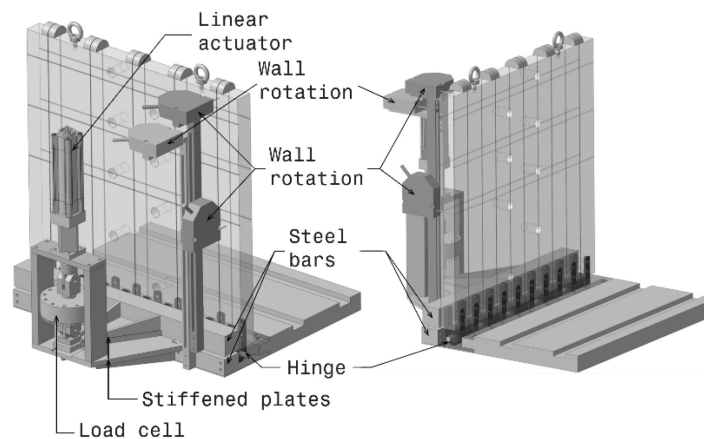*Fig. 71: Section of the test wall. Dimensions are given in millimetres.*

Fig. 72: Isometric views of the test wall.

The stem and the foundation consist of 35 mm thick PVC plates, chosen to match the ratio between the wall deflection at the wall top and the wall height of a 10 times larger reinforced concrete wall. In this way, it is ensured that there are similar initial stress conditions in the soil.

The stem rotation is controlled by an off-centre linear actuator mounted on a stiffened steel plate connected to the foundation by controlling the position of another steel plate connected to the stem. Two square steel bars fastened to the stem and the foundation ensure a uniform wall rotation over its length.

Two off-axis measuring devices are used to determine the moment acting about the hinge and the stem rotation. The moment is calculated from the force transferred by the actuator from the stem to the foundation, measured by the load cell shown in Fig. 71 (i.e. by multiplying it by the lever arm $l_e = 202.5\,\text{mm}$). Similarly, the wall rotation is obtained from the off-axis linear distance between two bars fastened to the wall foundation and stem, respectively, measured by a laser sensor. The measurement of a linear off-axis distance ensures higher accuracy and reliability than using a rotational position sensor, as the influence of systematic error induced by the noise in the digital signal is minimised by increasing the distance between the sensor and hinge.

Furthermore, two laser sensors measure the stem deflection at the top and the middle of the wall. These sensors are connected to the bar fastened to the stem and measure pure deflections of the wall (i.e. the measured displacement does not include any rotational part). In addition, the wall strain can be measured spatially using distributed fibre optic strain sensing on a raster of glass fibres embedded in the wall (see Fig. 71 and Fig. 73). These fibres are glued in notches on both sides of the stem.

In the middle wall section, the normal stress exerted by the soil backfill on the wall is additionally measured by eight pressure cells distributed over the wall height.
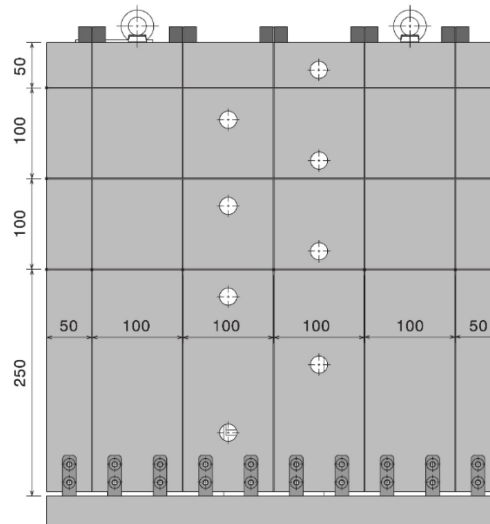
Fig. 73: *Longitudinal view of the test wall and raster of glass fibres. Dimensions are given in millimetres.*

In the designed test setup, independent devices measure each quantity of interest redundantly. In this way, every measurement can be checked for plausibility. Thus, the wall rotation can be checked using the position of the actuator, the moment by integrating the measured contact stresses, and the wall deflections by integrating the strain or by calculating the deflections of an elastic wall subjected to the measured earth pressure.

During a test, the three wall sections are placed in the box next to each other. A soft felt strip is glued to one side of the wall to avoid a transfer of forces between neighbouring sections (i.e. to minimise the contact pressure) and prevent the sand from flowing through the gap. Teflon tape is applied on the adjacent side to obtain a very low friction coefficient. The efficacy of these measures has been proven by applying a force or imposing a rotation on one segment and checking that no force was transmitted to the adjacent wall(s).

5.1.2   Rigid wall

The rigid wall consists of a stiffened, 15 mm thick, 510 mm high, and 1480 mm long steel plate welded to a base plate instrumented with ten pressure cells distributed over its height (Fig. 74). Eight stiffener plates are welded to the wall with a spacing of 187 mm.

During a rigid wall, the wall is backfilled in different layers and the lateral earth pressure acting on the wall is measured.

The wall has been designed to undergo negligible displacement when subjected to the lateral earth pressure exerted by the backfill during the tests. The Abaqus finite element software was used to simulate a very conservative design situation by assuming a uniformly distributed pressure (i.e. constant over the wall height and length) of 5 kPa. The resulting maximal displacement was 4.8 µm. Under more realistic loads, the expected displacement is in the range of 0.1-1 µm.
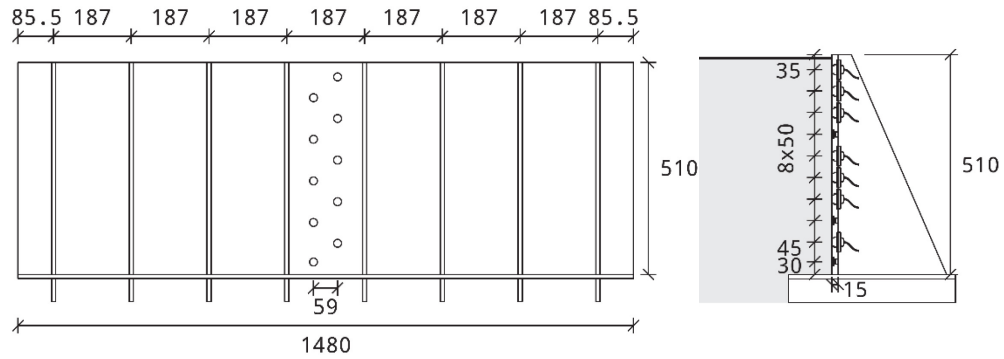
Fig. 74: Longitudinal view and section of the rigid wall. Dimensions are given in millimetres.

5.2 Materials

5.2.1 Cantilever retaining wall

The wall material is primarily unplasticised polyvinyl chloride, often called uPVC or rigid PVC. uPVC has been chosen because its mechanical properties allow the construction of a test wall that meets all requirements discussed at the beginning of the previous section. In particular, it allows one to get a similar wall behaviour to that of a full-scale wall. The only drawback of uPVC is its high coefficient of thermal expansion, meaning that the temperature change during the execution of the tests must be minimised.

The relevant mechanical and thermal properties of uPVC are listed in the following table. No source is given for the Young's modulus of uPVC, as it was determined in the lab using the fibre optic measuring system. The hinge and connectors that connect the wall stem and the foundation are made of aluminium and steel, as they are subjected to higher stresses.

Tab. 5: Properties of uPVC.

Property	Value	Source
Density	1.4 g/cm^3	[122]
Young's modulus	3500 MPa	
Poisson's ratio	0.4	[123]
Coefficient of thermal expansion	$7 \cdot 10^{-5}$/K	[123], [124]

5.2.2 Rigid wall

The rigid wall is entirely built of steel. The relevant mechanical properties are listed in the following table:

Tab. 6: Properties of steel.

Property	Value	Source
Density	7.85 g/cm^3	[125]
Young's modulus	210 GPa	[125]
Poisson's ratio	0.3	[125]

5.2.3 Soil backfill

The soil used as backfill is *Perth Sand:* pure silica sand (also known as quartz sand) [126] won on the Australian coast south of Perth. The sand has been used in many research projects at ETH Zurich (e.g. [126], [127]). Also, a very similar sand type (with a sieve curve slightly shifted to the left, i.e. having smaller grains) has been extensively studied at the Centre for Offshore Foundation Systems of the University of Western Australia.

In this work, the test soil and its mechanical behaviour were characterised in the laboratory and by numerical experiments using the level set discrete element method (LS-DEM). While laboratory tests build the link with reality, LS-DEM simulations were performed to gain a deeper understanding of the soil mechanical behaviour under ideal conditions, i.e., studying the behaviour in actual element tests having no boundary effects (e.g. no wall friction). LS-DEM was developed and implemented by Kawamoto et al. [128] and allows the modelling of each sand grain and the transmission of intergranular force, giving access to information unavailable in laboratory tests. Furthermore, unlike the classic discrete element method (DEM), which assumes grains as spheres or clumps of spheres, the actual shape of the grains is considered by LS-DEM, ensuring highly reliable results [114]. The theory and the methodology followed in this work were briefly introduced in [9].

The most relevant test results are reported in Appendix II. For a complete description, the reader should refer to [9].

5.3   Testing procedure

Tests carried out on the cantilever retaining wall consist of two phases: the backfilling and the rotation phase. In the backfilling phase, the soil is deposited layer after layer by air pluviation. Subsequently, a rotation is imposed at the stem's toe, and the evolution of the earth pressure acting on the wall is monitored.

Only the backfilling phase is carried out on the rigid wall. During that phase, the lateral pressure acting on the wall is monitored.

In the following, each test phase is explained briefly.

5.3.1   Backfilling phase

The backfill soil is deposited by air pluviation using the ad hoc automated system shown in Fig. 75. The system consists of a crane and a hopper. The automated crane system drives the hopper back and forth over the glass box with a specific horizontal velocity. Sand is poured into the box through the hopper's discharge opening, whose width can be adjusted depending on the target soil density that must be achieved. The combination of the horizontal velocity v_h, the falling height h, and the aperture width a influence the relative density of the deposited soil sample (e.g. [129], [130]).

Careful calibration was needed to quantify the achieved densities for different parameters. Twelve bins of known volume were distributed over the box area and filled using the newly constructed system with multiple parameter combinations in the ranges $a \in [2\,\text{mm}, 8\,\text{mm}]$, $v_h \in [1.8\,\text{m/s}, 16.0\,\text{m/s}]$, and $h \in [127\,\text{cm}, 155\,\text{cm}]$. The relative density and its spatial distribution have thus been determined over the whole box area. The aggregated results are plotted in Fig. 76, where each dot represents one test run (i.e., the average relative density of all bins). It can be observed that the relative density has an approximately linear relationship with the aperture width of the hopper.

Although a homogeneous discharge is guaranteed by the stiff construction of the hopper (Fig. 77), the soil density measured in the bins located at the box's boundaries deviated slightly from the values measured in the other bins, as air turbulence occurs close to the box walls disturbing the laminar sand flow. Nevertheless, the observed absolute deviation never exceeded a difference in relative density of 0.05: a very low value considering the sand uniformity (indeed, a difference of 0.05 in relative density corresponds to a difference of 0.01 in void ratio). Therefore, it is confirmed that the constructed crane and hopper system allows preparing soil samples with a relative density (as defined by Equation (II.4)) between 13% and 104% [7] in a controlled, reliable manner.

---

[7] A relative density greater than 100% means that the achieved density is greater than the maximum density obtained following ASTM Standard D4253-16 [131].

During the tests, the walls will be backfilled in layers of 6 to 8 cm thickness using the pluviation system. The falling height is kept constant for each layer.
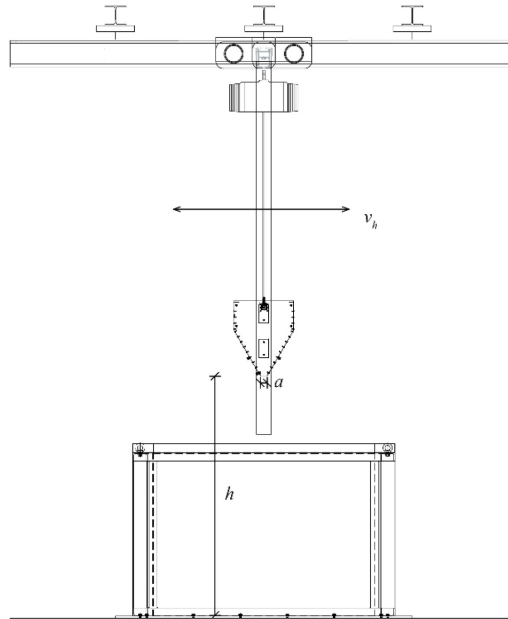

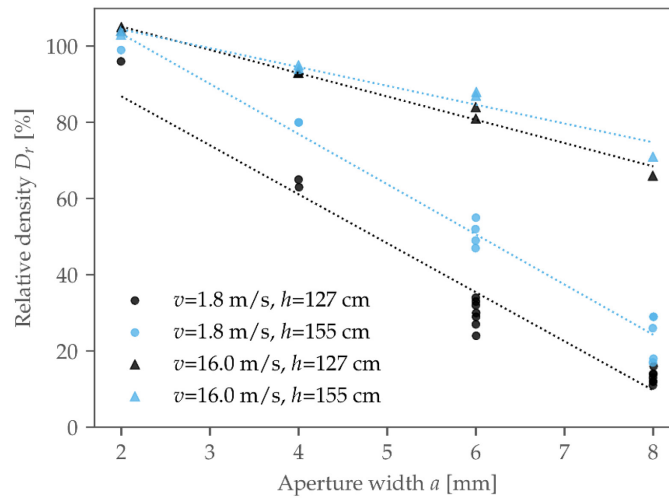**Fig. 75:** *The crane and hopper system used to deposit sand in the test box.*

Fig. 76: *Relative density as a function of horizontal speed, falling height, and aperture width.*

Fig. 77: *Hopper discharge during a calibration test.*

The relative density and void ratio for the configurations used in the wall tests are summarised in Tab. 7.

Tab. 7: *Configurations of the pluviator system used in the wall tests and achieved density.*

v [m/s]	h [cm]	a [mm]	Relative density	Void ratio
1.8	127	8	D_d=13% 95% CI [12%, 15%]	e=0.76 95% CI [0.75, 0.76]
1.8	127	6	D_d=30% 95% CI [27%, 33%]	e=0.72 95% CI [0.71, 0.72]
16.0	155	4	D_d=95% 95% CI [95%, 95%]	e=0.57 95% CI [0.57, 0.57]
16.0	155	2	D_d=104% 95% CI [104%, 104%]	D_d=0.55 95% CI [0.55, 0.55]

5.3.2 Soil compaction

The effects of soil compaction (e.g., increased initial soil lateral stress and increased soil stiffness) are studied by compacting each layer right after deposition.

In engineering practice, soil is mainly compacted using roller compactors, often fitted with a vibrating device to improve its performance. The effect of these machines on the soil density is twofold: soil gets compacted by a constant moving load and by vibration. The first applies irreversible stresses to the soil similar to a static load; the second causes a rearrangement of soil particles, causing a decrease in void ratio, leading to increased stiffness.

In this work, the purpose of simulating soil compaction is to *study the effects of increased lateral stresses and stiffer soil* on the corrosion-driven wall unloading process. For further numerical analysis, it is essential to quantify the effects of the compaction. For this reason, the possibility of compacting by vibration has been immediately discarded, as it is not possible to quantify precisely the effects of vibration using conventional engineering tools (i.e. conventional constitutive laws and the finite element method). Instead, a static load was used to compact the soil layers in this work. In fact, a static load is easy to quantify, and the correlation between compaction stress and an increase in lateral earth pressure is straightforward. Furthermore, static compaction only marginally influences the soil relative

density, allowing to test purely contractive (low relative density) and contractive-dilative (high relative density) soil samples.

After deposition of each layer, the backfill is compacted by applying a vertical load distributed over a 10x10 cm stiff plate, as shown in Fig. 78. The applied vertical stress corresponds to 20 kPa.

Fig. 78: Compaction of the backfill by applying a static load.

5.3.3   Rotation-driven wall unloading

After the deposition of the wall backfill, a rotation of the stem about its toe is imposed by moving the linear actuator down at a speed of 0.06 mm/min. The resulting rotational speed is about 0.3 mrad/min. The constant, low rotational speed guarantees a good temporal resolution of the results and eliminates possible dynamic, inertial effects because of a fast rotation. A total rotation of about 35 mrad has been reached at the end of each test.
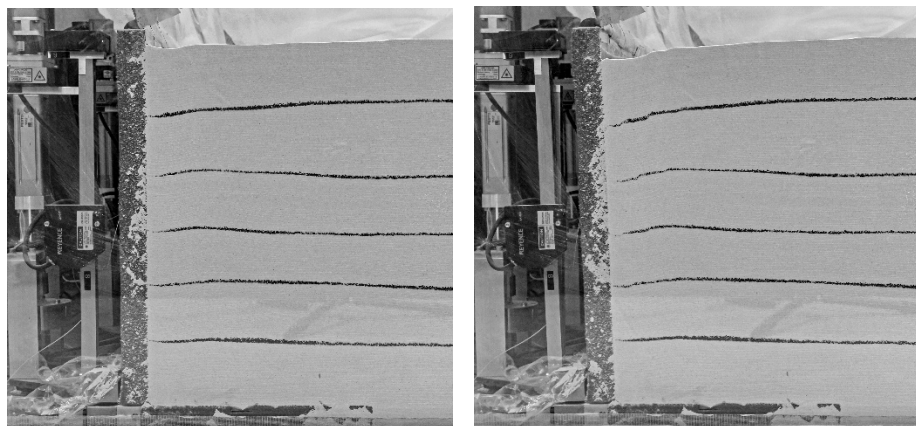
Fig. 79: Backfilled wall at the beginning and the end of the rotation phase (dense soil specimen).

5.4   Experimental program

The goals of the experimental campaign are to study the corrosion-driven unloading of the backfill under different conditions:

1. different soil behaviours (hardening, softening, stiffer soil, etc.);
2. initial earth pressure;
3. inhomogeneous corrosion over the wall length (e.g. some sections are more severely damaged than others).

The conditions listed above are simulated by:

1. varying the soil's relative density (leading to different stiffnesses and behaviours; e.g. a softening regime);
2. compacting the soil;
3. rotating only the middle wall section.

Additionally, being the initial earth pressure a critical factor, the earth pressure at rest is studied on the rigid wall.

In total, twelve tests have been carried out. As one of the goals of the test series is to study the unloading process for different soil behaviours (i.e. dense, contractive-dilative, and loose, contractive soil), the tested soil densities were chosen close to the extremal values to emphasise the different behaviours better. The behaviour of medium-density soil can be deduced from the results of the present series. A summary of the most relevant information about each test is given in the following table.

Tab. 8: Summary of wall tests.

Identifier	Relative density	Static compaction	Observations
C1L	D_{d0}=10%	No	On the cantilever retaining wall.
C2D	D_{d0}=95%	No	On the cantilever retaining wall.
C3L	D_{d0}=30%	No	On the cantilever retaining wall.
C4D	D_{d0}=105%	No	On the cantilever retaining wall.
C5Lc	D_{d0}=30%	Yes	On the cantilever retaining wall.
C6Dc	D_{d0}=95%	Yes	On the cantilever retaining wall.
C7D3d	D_{d0}=95%	No	On the cantilever retaining wall. Only the middle wall section is rotated.
C8L3d	D_{d0}=30%	No	On the cantilever retaining wall. Only the middle wall section is rotated.
R9L	D_{d0}=30%	No	On the rigid wall.
R10Lc	D_{d0}=30%	Yes	On the rigid wall.
R11D	D_{d0}=95%	No	On the rigid wall.
R12Dc	D_{d0}=95%	Yes	On the rigid wall.

The test identifier is composed of a letter indicating on which wall it was carried out (C: cantilever retaining wall; R: rigid wall), a unique number, a letter indicating if the soil is dense (D; a soil that exhibits softening behaviour) or loose (L; a soil which only hardens before reaching a constant volume state), and possibly an indication that the soil has been compacted (c) or that the test has been carried out only rotating the middle wall segment (3d). The relative density D_{d0} corresponds to the density of a single layer after deposition. The relative density after compaction is not given.

5.5   Conclusions

The design of the experimental setup and the experimental program were presented in this section.

First, the features of the testing devices were presented, showing which requirements led to the chosen design. Two types of walls were built and used: a flexible cantilever retaining wall and a very stiff steel wall.

Then, the material parameters were listed. The chosen model soil is known at the Institute as Perth Sand. Its material behaviour and descriptive parameters were determined in the laboratory. The experimental results are summarised in Appendix II.

Finally, the testing procedure was shown. The walls will first be backfilled; then, a rotation of the wall stem is enforced. The resulting moment-rotation response will be monitored, along with other quantities. In some tests, the wall backfill is compacted statically. Additionally, the distribution of the earth pressure on the steel wall will be investigated.

6 Experimental study of the corrosion-driven wall unloading process: results

The results of the wall tests are presented and discussed in this section. In the following, it will be referred to as "plane strain conditions" when all three wall sections are rotated simultaneously and "3D conditions" when only the central wall section is rotated while keeping the outer sections fixed at their initial position. Strictly speaking, plane strain conditions are never satisfied, as the friction of the glass box causes boundary effects. However, preliminary numerical analyses showed that boundary effects are limited to the outer 15 cm of the external wall and do not influence the results of the central section. The observed deformation pattern in Fig. 86 also confirms this.

6.1 Cantilever retaining wall

Backfilling

As the soil is backfilled, the earth pressure on the wall varies continuously. During soil deposition, the vertical stress at a material point in the backfill increases due to the increase in soil cover. The vertical stress increase causes increased lateral stresses and, thus, a higher pressure on the wall. However, at the same time, the wall deflects because of the additional load. Consequently, a partial unload of the backfill is observed. In addition, shear stresses develop at the soil--wall interface, causing a further change in the soil stress state and the resulting earth pressure. This complex interaction results in the earth pressure distributions shown in Fig. 80, where the earth pressure acting on wall B (see Fig. 70) and measured after the deposition of each layer in the C2D test is plotted.
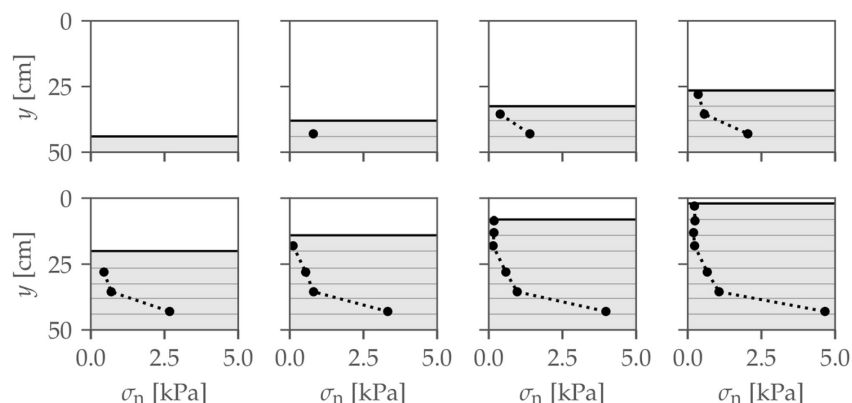

Fig. 80: *Earth pressure acting on wall B measured after the deposition of each layer in test C2D.*

An approximately bilinear distribution is observed at all stages, starting from the fourth stage (when at least three pressure cells were covered). In the upper part of the wall, where the most significant deflection occurs, the soil undergoes partial unloading and is in a stress state between the "rest" condition and failure. In the lower part, the wall deflection is minimal and the earth pressure increases with depth at a higher rate (i.e. the coefficient of lateral earth pressure increases).

Rotation

The simultaneous rotation of the three wall sections A, B, and C causes elastoplastic soil unloading leading to active failure. The different moment-rotation responses of a loose and dense sample are shown in Fig. 81 and Fig. 82.
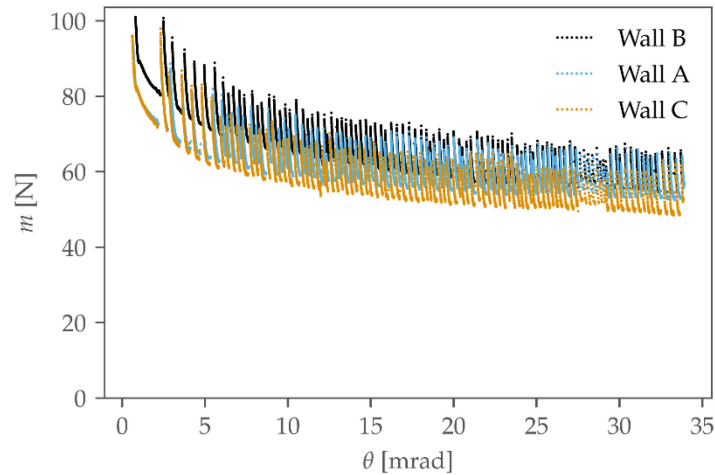
Fig. 81: Moment versus wall rotation measured during the rotation phase of test C1L.
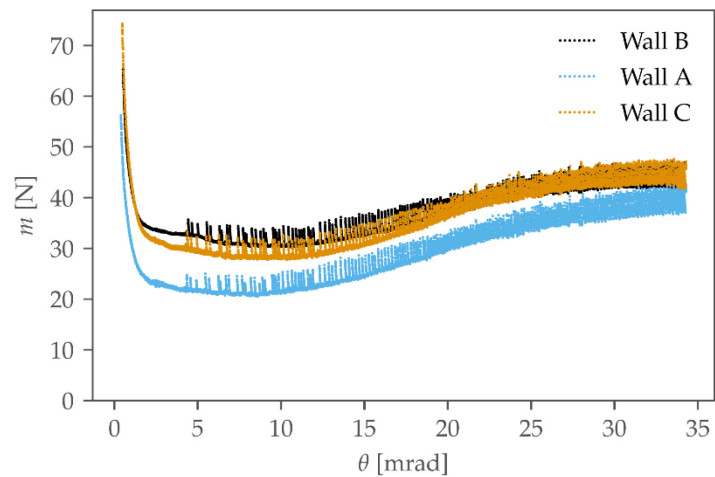

Fig. 82: Moment versus wall rotation measured during the rotation phase of test C2D.

The lower envelopes of the moment-rotation curves (ignoring the sudden increases) correspond to the typical behaviour of loose and dense soil. The moment decreases monotonically in the loose, contractive sample (Fig. 81). On the other hand, a moment increase due to softening is observed in the dense, contractive-dilative sample after peak strength is reached (Fig. 82). Both samples show sudden jumps of the moment, which represent stick-slip events. Stick-slip is a common phenomenon observed in granular materials (see, e.g., [116, p. 65], [132], [133]) and will be discussed later in this section.

A higher moment was measured on the central wall section (wall B) than on the lateral sections (A and C; Fig. 81 and Fig. 82). This difference is expected and was the main reason for building three separate sections. It is caused by boundary effects (i.e. the frictional interface between the glass wall and the soil). Different initial conditions explain the difference between the results of walls A and C in Fig. 82 (i.e. a slightly different backfill height and, possibly, some friction between the rotating wall and the box).

The evolution of the normalised earth pressure in a loose and dense sample is plotted in Fig. 83 for different wall rotations. The results of the C4D test are shown to represent the dense sample, as a technical issue affected the pressure measurements in test C2D after reaching a rotation of about 15 mrad.
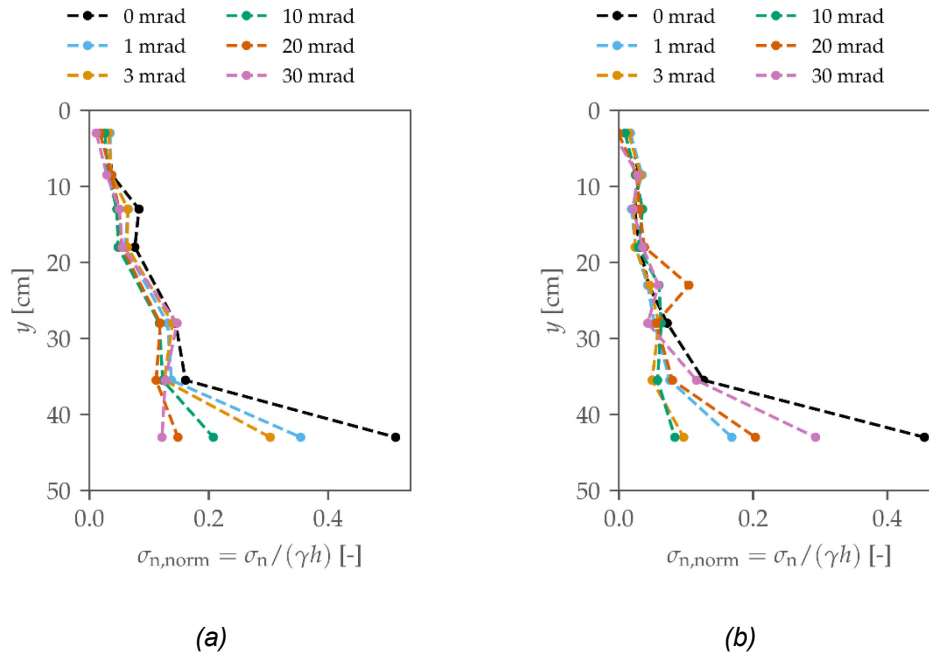
(a) *(b)*

Fig. 83: *Normalised earth pressure during the rotation phase in (a) test C1L; and (b) test C4D. The rotation indicated in the legend corresponds to the applied rotation net of the initial value measured after the backfill.*

The initially increased pressure in the bottom region of the wall is reduced in both samples as soon as the rotation starts. In the loose sample, unloading is also observed on the upper part of the wall, as the maximum shear strength could not be fully mobilised during the backfilling phase. In contrast, it seems that the peak shear strength was already mobilised during backfilling in the upper part of the dense sample, as no further decrease is observed with increasing rotation. In fact, dense sand needs smaller deformations than loose sand to mobilise a higher strength, as seen, for example, in Fig. 6 in Appendix II.

In light of the slower strength mobilisation of the loose sample, the earth pressure reached a linear distribution after a rotation of about 10 mrad, while only 3 mrad were needed by the dense sample. After reaching a plateau at peak strength, the dense sample softens with increasing rotation, leading to increased stress in the lower part of the wall (see the red and pink lines in Fig. 83b).

An advantage of the experimental setup developed is the redundancy of the measurements that allows double-checking every measurement with an independent measurement. For example, stress measurements can be integrated to estimate the moment that acts on the wall hinge. The integrated moment is plotted in Fig. 84. A good match with the direct measurement of the moment is observed: the qualitative trend is the same, and only a minor deviation is observed between the two quantities. In particular, the direct measurement is more accurate, as stress measurements have a low spatial resolution (i.e. only eight measurements over the wall height) and are more affected by noise (as the measured quantities are small).

Dividing the integrated moment by the resulting integrated force, the location of the stress resultant $\hat{y}$ can be deduced. The ratio $\hat{y}/h_{soil}$, where h_{soil} is the height of the soil backfill, is plotted in Fig. 85. This measure gives an indication of the earth pressure distribution. Observing how the location of the stress resultant moves over the continuous rotation domain, it is possible to confirm the results observed in Fig. 83. The stress resultant in the loose sample moves from $0.25h_{soil}$ to about $0.35h_{soil}$ showing a continuous increasing trend, as the earth pressure distribution transitions from bilinear to approximately linear. However, the earth pressure resultant force seems to be slightly more shifted towards the middle of the wall. Instead, the dense sample reaches a local maximum after about 10 mrad

before decreasing again as the pressure distribution goes from bilinear to linear and back to bilinear due to softening.
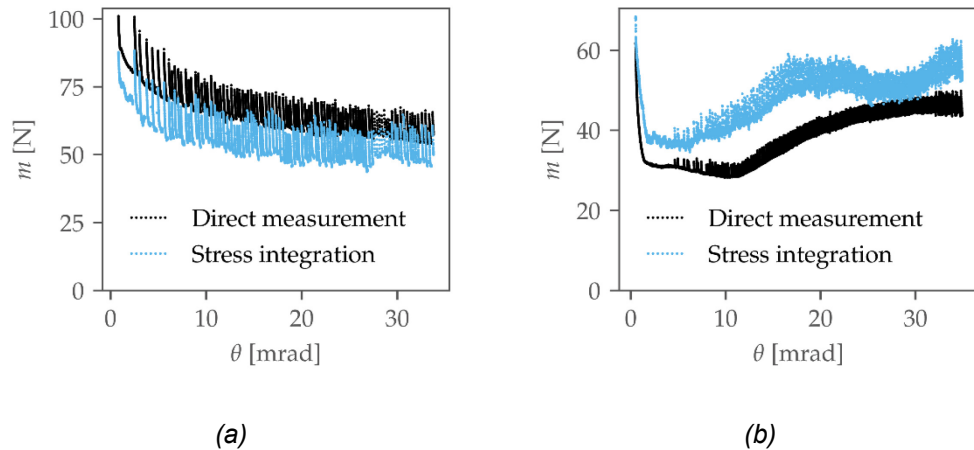

(a)

(b)

Fig. 84: Comparison of the moment determined from the direct measurement of the force acting on the linear actuator and from the integration of the lateral earth pressure measured by the pressure sensors: (a) test C1L; and (b) test C4D.
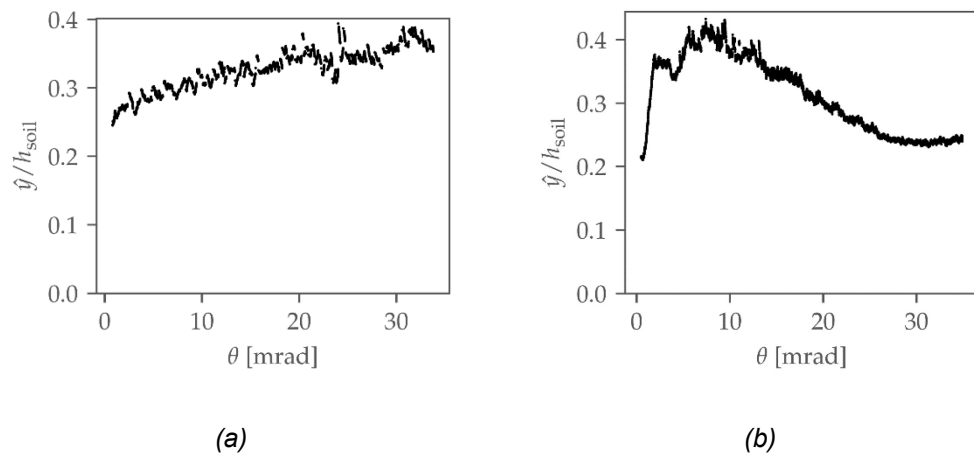

(a)

(b)

Fig. 85: Location of the earth pressure resultant $\hat{y}$ normalised by the height of the backfill h_{soil} as a function of the wall rotation: (a) test C1L; and (b) test C4D.

Failure mechanism

The formed failure mechanism can be qualitatively assessed by looking at the soil defor-mation on the surface and at the sides through the glass walls. Fig. 86 shows the shear bands observed from the top at the end of the C2D test. The plastic soil deformation is strongly localised in dense samples, mainly due to the softening behaviour. Consequently, clear shear bands are observed. In Fig. 86 (left), the entire width of the model is shown. At the two extremities, the shear bands curve due to boundary effects. This picture clearly shows how the frictional boundaries only influence the soil behaviour in the outer 15 cm of the outer wall sections, thus not affecting the results outside that range. The picture to the right shows a closeup behind the central wall section. The upper side of the region where the most significant plastic strain occurs measures approximately 17-18 cm.

Fig. 87 and Fig. 88 show the failure mechanism developed in a dense and looser sample. The deformation viewed from the side has only qualitative value, as boundary effects influ-ence the soil strain at the boundary. It is shown that a straight line can approximate the failure mechanism and that the size of the region where the most significant plastic strain occurs depends on the soil relative density (i.e. on the hardening behaviour).

Fig. 86: *Shear bands observed from the top after the conclusion of test C2D.*
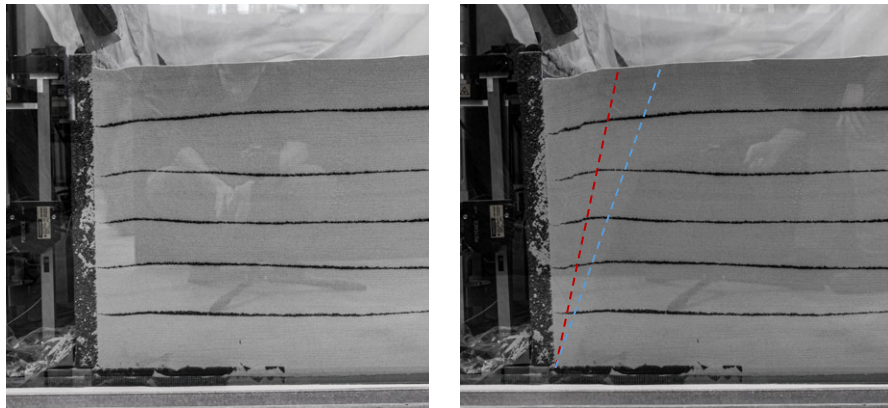

Fig. 87: *Side view of the backfill at the beginning (left) and the end (right) of the rotation phase in test C6Dc. The red line marks approximately the rightmost strongly localised shear band, and the blue line delimits the region where displacement occurs. The observed displacement only has a qualitative character, as boundary effects influence it.*
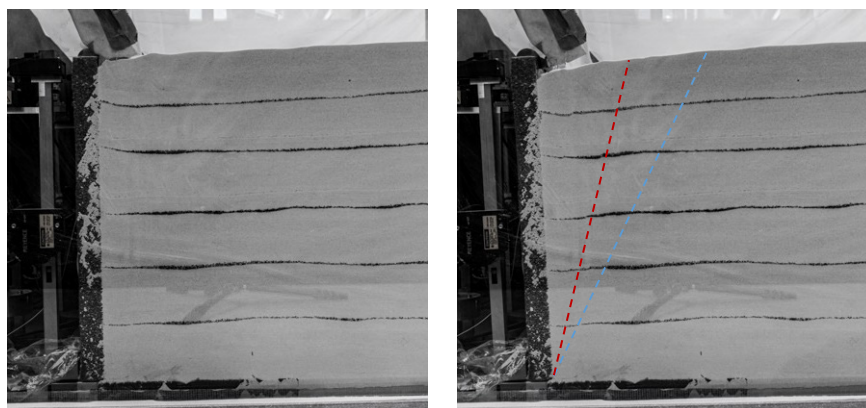

Fig. 88: *Side view of the backfill at the beginning (left) and the end (right) of the rotation phase in test C5Lc. The red line marks approximately the rightmost strongly localised shear band, and the blue line delimits the region where displacement occurs. The observed displacement only has a qualitative character, as boundary effects influence it.*

Stick-slip behaviour

Stick-slip behaviour is observed in granular materials ([132]–[134]), rock [135], and in a variety of solid materials. Furthermore, it describes the motion of geological faults [132], [136].

Stick-slip behaviour is caused by the transition between static and dynamic friction, resulting in a periodic movement at the frictional interface. Let us assume a spring-slider system, as depicted in Fig. 89a. The spring is assumed to have a linear behaviour (Fig. 89c), and the slider's static friction is higher than the kinematic. When a displacement x is applied to the spring (at a constant rate), its internal force increases and is transmitted to the slider. Subjected to the force F, the slider does not move until the static friction is fully mobilised. As soon as the maximal static frictional force is reached, the slider transitions to a kinetic regime and starts moving (slip phase). As it starts moving, its friction coefficient decreases (i.e. it enters the kinetic regime, Fig. 89d). Thus, the slider accelerates, causing a reduction in the spring elongation and, consequently, in the internal force F to a value lower than the kinetic friction. The slider therefore transitions back to a static regime (stick phase). In the stick phase, the internal spring force ramps up again until the static friction is mobilised on the slider and a new slip occurs. As long as the displacement x is increased, this behaviour occurs indefinitely, giving raise to the oscillatory system response depicted in Fig. 89b.
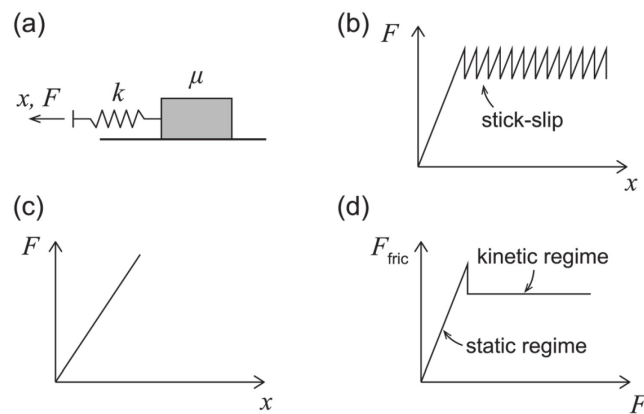

Fig. 89: Stick-slip behaviour: (a) spring-slider model representing the material behaviour; (b) force-displacement diagram for the slider; (c) response of the linear spring; (d) frictional force mobilised by the slider as a function of the applied force.

The nature of stick-slip in granular materials has been studied extensively. The instability of the granular structure (i.e. the collapse of force chains; e.g. [133], [137]) and contact ageing [133] are often cited as causes of stick-slip behaviour in granular solids. Doanh et al. [133] studied stick-slip in a loose granular assembly tested triaxially. They show that a slip event corresponds to a drop in the deviatoric stress, accompanied by a sudden contraction (i.e. an increase in compressive volumetric strain). After the drop, the soil enters the stick phase and hardens (and dilates) slowly until the next slip event. It is shown that the upper envelope of the deviatoric stress conforms with the typical soil behaviour. The same study shows an indirect proportionality between the stress drop (during the slip phase) and the strain rate and a direct proportionality of the stress drop with the confining pressure. Similar results were obtained, e.g., by Ozbay and Cabalar [134]. While the previously mentioned studies did not show a significant velocity weakening of soil, Adjemian and Evesque [132] observed a velocity weakening leading to a difference in friction angle of about 4% (i.e., less than 2°) by changing the axial strain rate from 0.18 mm/min to 0.5 mm/min. Adjemian and Evesque also conducted tests on a dense specimen and did not observe stick-slip.

In Fig. 81 and Fig. 82, stick-slip behaviour is observed. Since a slip event decreases the soil strength and the tests involve active unloading of the wall, a slip causes an increase in moment. The moment increase is higher for the loose sample than for the dense sample, and slip events occur earlier in loose samples: stick-slip events are first observed in the

dense sample when peak strength is reached. A closer view of the stick-slip events occurring in tests C1L and C2D is plotted in Fig. 90 when the wall rotation of both tests was at around 17 mrad. The position of the linear actuator shows that the wall rotation was applied at a constant rate, i.e. the jumps in the other measured quantities were not mistakenly imposed by the test setup. The moment and the stress measurements show that the stress state in the soil increases at regular intervals. Three slip events were registered over 200 s in the loose sample, while the dense sample had six such events in the same timespan. Slip events cause an increase in moment of about 20% in the loose specimens, about 10% in the dense specimens.

Because the stress is measured at a single location, the amplitude of the stress jumps can vary between different events. Indeed, slip events are discrete in space and not always the stress at a specific location is affected the same way. Instead, the amplitude of the moment jumps is much less variable.

The stress increase is confirmed by the measurements of wall deflection and rotation (at the axle). The jumps in the wall deflection and wall rotation are explained by the earth pressure increase on the flexible wall. Indeed, the wall rotation is dependent on the pressure applied to the wall because of the finite stiffness of the construction (see Section 5.1.1).
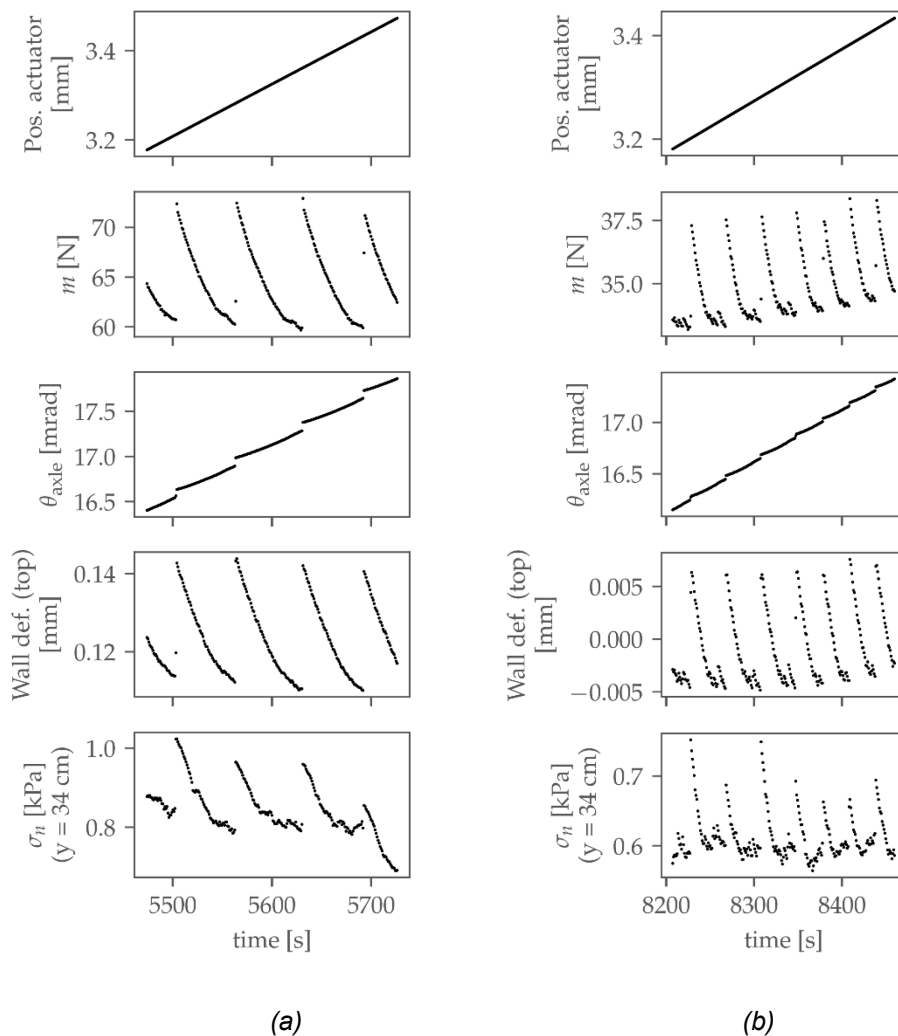

(a) (b)

Fig. 90: *Stick-slip events in test C1L (a) and C2D (b). Measurements on the central wall section as a function of time. From top to bottom: position of the linear actuator, moment at the wall toe, axle rotation, wall deflection measured by the top laser device, and stress measured at the second lowest pressure cell.*

6.1.1 Uncompacted soil specimens

The uncompacted soil samples are deposited in multiple lays with the pluviator. During the backfill procedure, the stress state at a material point in the backfill continuously changes and depends on the soil weight and mechanical properties, the flexibility of the wall, and the properties of the frictional soil-wall interface as no additional stresses or irreversible strains are applied by external devices

The earth pressure measured after the complete deposition of the backfill is plotted in Fig. 91 for all tests on uncompacted soil, C1L to C4D. Good agreement is observed between the two samples having similar densities (i.e. C1L and C3L, and C2D and C4D), indicating that the tests are reliable and repeatable. The earth pressure distribution is bilinear due to soil yielding induced by the wall deflection and the frictional interface. From Fig. 91, it can be deduced that yielding occurs at least in the range $y \in [10\,\text{cm}, 37\,\text{cm}]$ for all samples, where low, almost constant lateral earth pressure coefficients were measured. The reason is that the wall displacement causes the highest horizontal strain in the soil in that range. Fig. 93 shows the cumulative horizontal displacement $w - w_0$ at the wall interface for each deposited layer. The value w indicates the total wall displacement measured at the end of each backfill stage and w_0 the wall displacement measured at the beginning of the deposition of the given layer (i.e. $w - w_0$ indicates the net cumulative displacement of the n-th layer measured from the moment it was first deposited). It can be clearly seen that the highest displacement is measured in the range $y \in [10\,\text{cm}, 37\,\text{cm}]$.

It is further observed that the lateral earth pressure measured in loose samples is higher than in dense samples. Consequently, the wall displacement is higher for lower relative densities (see Fig. 92). The reason is that dense soil mobilises a higher strength than loose soil at low strains (see Fig. 6 in Appendix II). Therefore, equilibrium in dense soil is reached at lower wall displacement and lower earth pressure values than in loose soil.
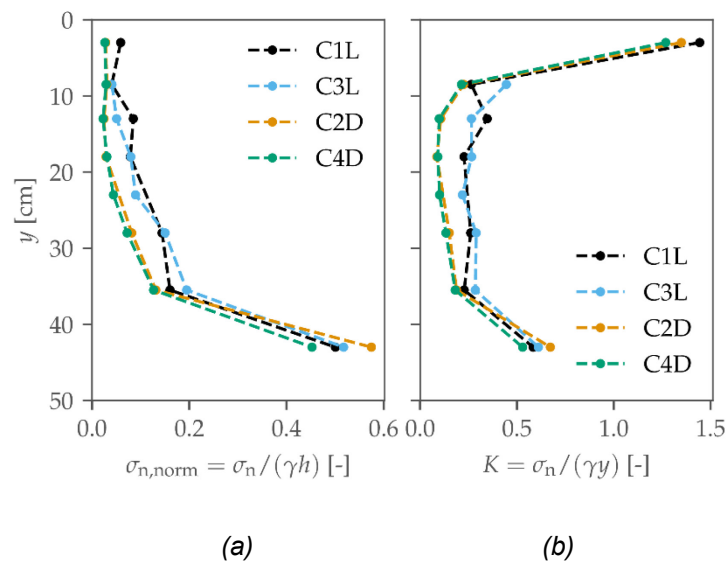

Fig. 91: Horizontal earth pressure acting on the wall measured after the deposition of the backfill in the uncompacted tests: (a) horizontal earth pressure normalised by γh; (b) horizontal earth pressure coefficient $\overline{K} = \sigma_n/\gamma y$.
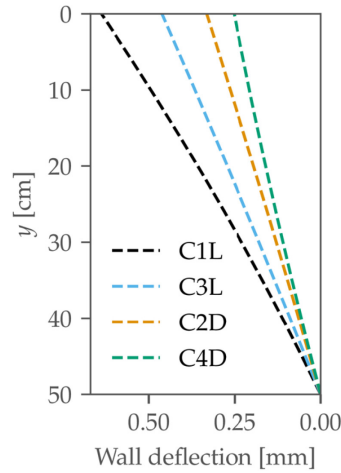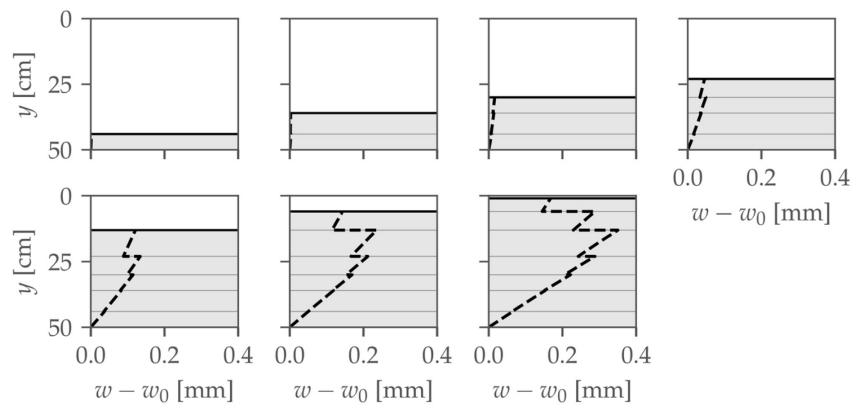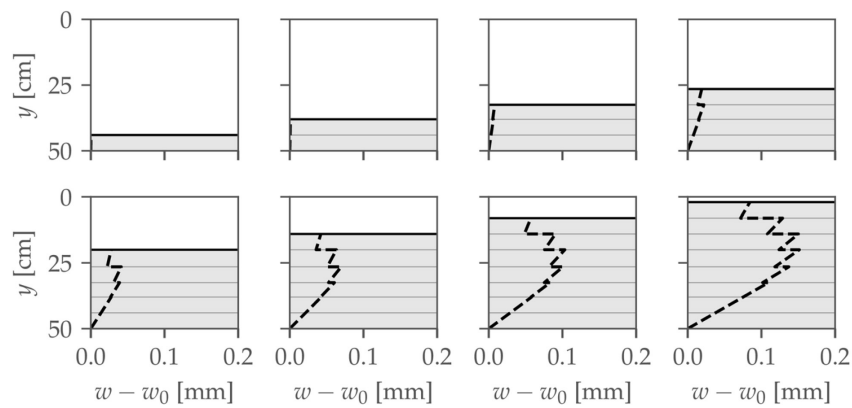
Fig. 92: *Wall displacement measured at the end of the backfilling phase.*

(a) Test C1L

(b) Test C2D

Fig. 93: *Cumulative horizontal displacement of each backfill layer measured at the wall interface after the deposition of each layer.*

The evolution of the normalised moment during the rotation phase is plotted in Fig. 94 as a function of the imposed wall rotation. The measure $m/(\gamma h^3/6)$ corresponds to the earth pressure coefficient defined in Section 3.3.3. However, it should be kept in mind that the values in Fig. 94 generally correspond to a nonlinear pressure distribution.

In agreement with the earth pressure measurements, the initial moment is higher in the loose samples than in the dense ones. Due to the initial moment, a rotation of approximately 0.5 mrad was measured in all tests at the end of the backfill phase. Initially, a steep moment decrease is observed in the test on dense specimens: after a rotation of 2 mrad, the moment is close to its minimum value. At that point, part of the backfill begins to soften, leading to a lower mobilised strength, while the rest is still undergoing hardening. This results in a relatively long plateau in the moment-rotation curve. Then, after a rotation of about 10 to 15 mrad, softening dominates the soil behaviour, causing the moment to increase again.

The moment in the tests on loose samples exhibits a slower decrease as higher strains are needed for the soil to harden until the critical state is reached. The lower envelope of the curve decreases monotonically as loose soil does not soften. At large rotations, the normalised moment measured in the loose samples tends to the same residual state of about 0.18. A slightly lower residual state is observed in the dense sample. In addition, dense soil reaches a local minimum at a value of approximately 0.1. Both values are relatively low compared to those generally assumed in practice, ranging between 0.2 and 0.3 (corresponding to a soil friction angle between 30° and 40°). In fact, the coefficient of lateral earth pressure of 0.1 is obtained for a friction angle higher than 50°, which disagrees with the values determined in Appendix II.1. However, such a low earth pressure can be confirmed by every independent measurement (i.e. the stress, the moment, the wall deflection, the wall strain, and the dimensions of the failure mechanism in Fig. 87 and Fig. 88). The reason for such high strength is explained in Appendix II.2.2.
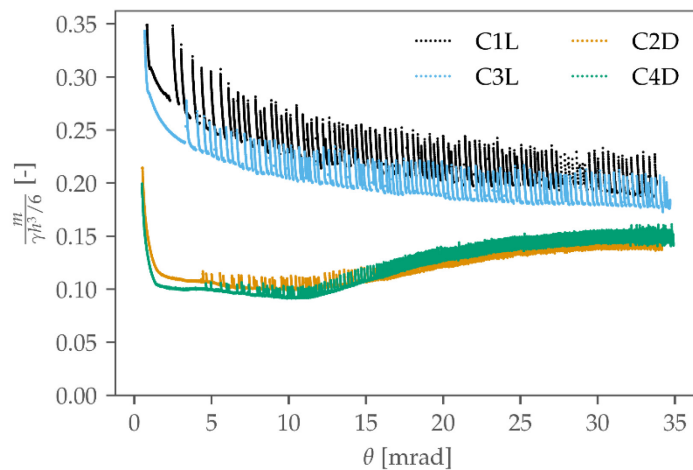

Fig. 94: *Normalised moment as a function of the wall rotation for the uncompacted samples.*

Fig. 95 shows the location of the earth pressure resultant as a function of the wall rotation. The loose samples are shown to transition from a bilinear to an approximately linear earth pressure distribution as the wall rotation increases. Instead, dense samples go from a bilinear distribution to a roughly linear one and back to a bilinear distribution. It follows that the lower region of the backfill is mainly affected by softening, as the lowering of the location of the resultant earth pressure indicates an increase in stress in that region. This stress increase could be due to arching, as observed by Nadukuru and Michalowski [74]. However, in the limit state, all force chains that contribute to the arching effect are expected to collapse and the earth pressure could become linearly distributed again.
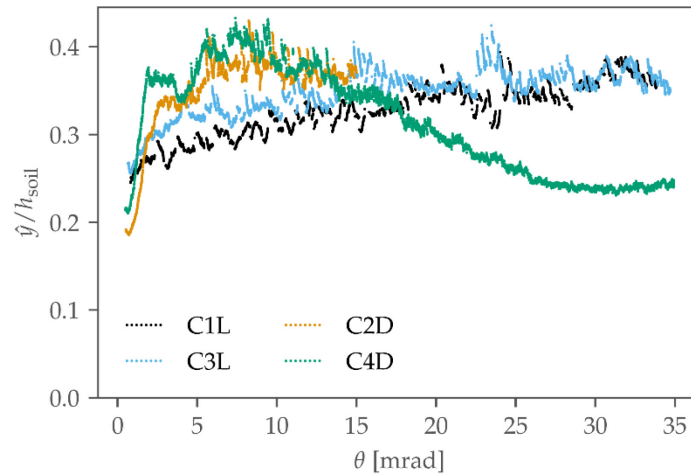
Fig. 95: *Location of the earth pressure resultant* $\hat{y}$ *normalised by the height of the backfill* h_{soil} *as a function of the wall rotation.*

6.1.2 Compacted soil specimens

Compacted soil specimens are created by depositing 8 cm thick layers in an initial loose (test C5Lc) or dense (test C6Dc) packing and compacting them by applying a static load following the procedure described in Section 5.3.2. When the compaction load is applied, the stress state in a confined region of the backfill changes and the soil undergoes plastic deformations. Thus, irreversible strains and increased lateral stress remain in the soil when the load is removed. During the compaction procedure, the soil density changes only minimally, as compaction by a static load is not as effective as compaction by vibration in rearranging the soil particles. Proper quantifying the change in soil density is not possible in the test setup. However, visual and tactile perception confirmed that none of the samples underwent a drastic change in density after compaction, and the behaviour of both samples still matches that of the deposited soil (i.e. contractive for C5Lc and contractive-dilative for C6Dc). Therefore, the effect of increased stresses could be investigated on two different soil behaviours.

The earth pressure measured after the compaction of each layer in tests C5Lc and C6Dc is shown in Fig. 96a. Fig. 96b shows the cumulative horizontal displacement $w - w_0$ at the wall interface for each deposited layer. w indicates the total wall displacement measured at the end of each backfill stage and w_0 the wall displacement measured at the beginning of the deposition of the given layer (i.e. $w - w_0$ indicates the net cumulative displacement of the *n*-th layer measured from the moment it was first deposited). In the first backfilling steps, the wall displacement is very small and the horizontal stress high. As additional layers are deposited, the wall displacement increases and a partial soil unload is observed. Unloading causes a horizontal stress reduction, especially in the lower part of the backfill.

In the initial backfill phases, the lateral stress measured in the test on the contractive-dilative soil (test C6Dc) is higher than in the contractive soil (test C5Lc). As explained in the previous section, the reason is the different hardening behaviour of the two soil types. In fact, higher strength is mobilised at lower deviatoric plastic strain levels in dense soil. Consequently, since compaction causes the horizontal stress to increase and approach passive failure, higher stresses result. On the contrary, when active unloading takes place in the lower part of the backfill due to the increasing wall displacement, higher strength leads to lower stresses, as observed in step 6 of the backfilling procedure depicted in Fig. 96.
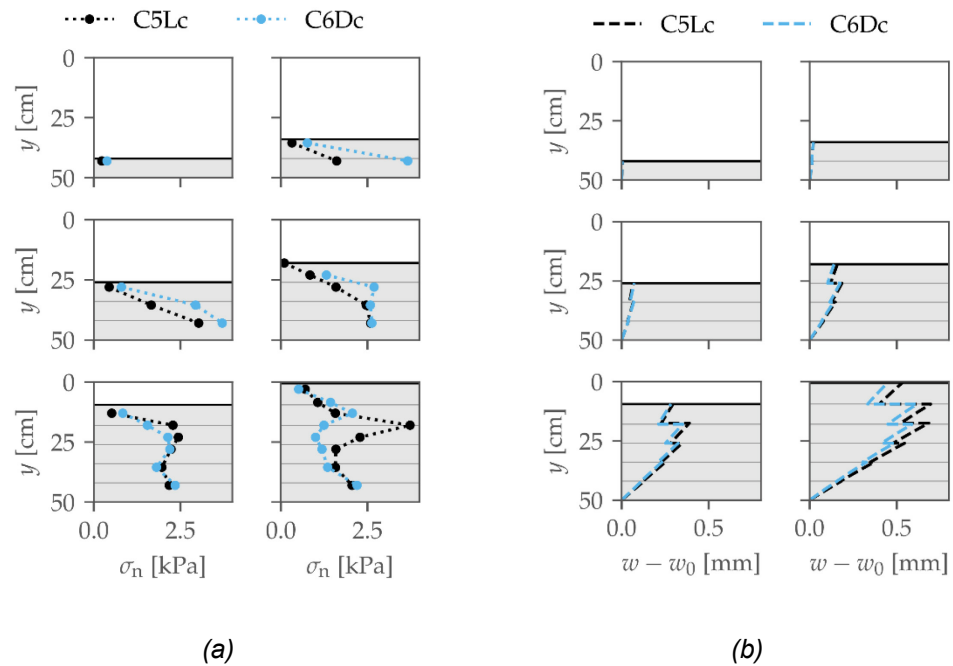
Fig. 96: *Stress distribution and cumulative wall deflection in tests C5Lc and C6Dc: (a) earth pressure acting on wall B measured after the compaction of each layer; (b) cumulative horizontal displacement of each backfill layer measured at the wall interface after deposition. Consecutive steps are shown from left to right, top to bottom.*

Fig. 97 shows the earth pressure measured right after the deposition of a layer (i.e. before compaction; blue), after the compaction of that same layer (black), and after deposition of the next layer (orange) for tests C5Lc and C6Dc. These plots allow a direct assessment of the influence of the compaction (leading to a stress increase) and the deposition of a new layer (leading to higher vertical stresses and wall displacement) on the soil lateral stress. Initially, both the compaction procedure and the deposition of the following layer cause an increase in the lateral stress, although only the former lead to an increase in the lateral earth pressure coefficient. However, after the half backfill height is reached, the deposition of additional layers causes a net decrease in stress. Indeed, the wall displacement, a cubic function of the distance between pivot and stress resultant, fully compensates and overcomes the positive effect of the increased vertical stress on the lateral stress. The stress decrease is especially pronounced in dense soil, characterised by a steeper hardening curve. On the other hand, the compaction of newly deposited layers causes a stress increase, although only to a limited depth (i.e. the effective depth of compaction as observed, e.g., in [11, p. 48]). For example, between steps 4 and 5 in Fig. 97, the horizontal stress in the lowest part of the backfill barely changes.

The magnitude of the compaction-induced stresses decreases in the dense specimen after reaching a certain backfill level. While a maximum stress increase of about 2 kPa is measured in the initial backfill phases, about 1.2 kPa is measured in the last two steps. The loose sample shows the opposite trend, where the maximum stress increase is initially about 0.8 kPa and increases to 1.6 kPa in the last steps. The effective depth of the compaction is also different in dense and loose soil: about 15 cm in dense soil and 20 cm in loose soil (see Fig. 97). This difference arises from the different soil behaviour and wall deflections.
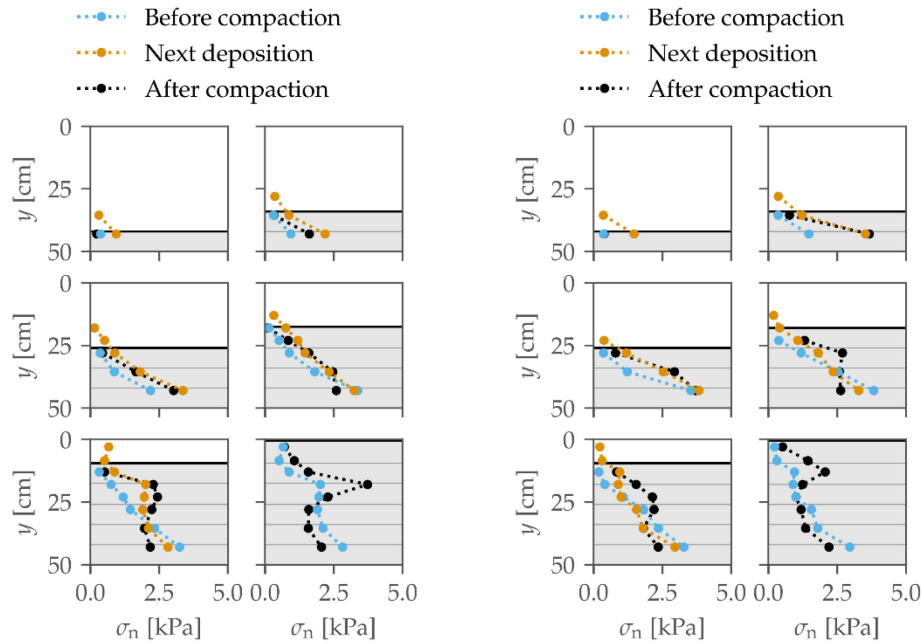
Fig. 97: *Earth pressure acting on wall B after the deposition of a layer (blue), after its static compaction (black), and after the deposition of the next layer (orange) in tests C5Lc (left) and C6Dc (right).*

The evolution of the normalised moment during the wall rotation phase is plotted in Fig. 98. It is observed that the initial moment of the compacted samples is about twice as high as in the uncompacted tests with the same relative density due to the increased pressure and the higher location of the resultant force. Consistently with the results of the uncompacted samples, the specimen deposited in a loose configuration (i.e. test C5Lc) shows a higher initial moment.

In the compacted specimens, the wall rotation caused by the initial earth pressure on the wall structure is approximately 1.4 mrad. When the wall rotation is induced, the moment quickly decreases in both tests. The unloading curve's first steep portion is followed after an imposed rotation of about 3 mrad by a relatively flat plateau. In the case of compacted soil, the contractive soil of test C5Lc also shows a steeper initial unload than in the corresponding uncompacted test C3L. The cause is the particular earth pressure distribution shown in Fig. 96 (i.e. the resultant force is located further away from the pivot) and the kinematics of the wall, resulting in larger displacements at the wall top, where the highest initial pressure is observed. This is further confirmed by the evolution of the earth pressure plotted in Fig. 99 at different stages of the wall rotation. It can be seen how the stress peak initially measured close to the wall top is decreased to about half its value after just 1 mrad in both samples.

When a normalised moment of about 0.22 is reached in test C5Lc, the moment-rotation curve enters a new regime of slight decrease. In this phase, stick-slip events are observed. The lower envelope of the curve shows a monotonic decrease, which confirms that the soil of test C5Lc is relatively loose even after static compaction. Instead, test C6Dc enters a regime of slighter decrease at a normalised moment of about 0.15 and exhibits softening starting from a rotation of about 15 mrad. If the lower envelope is considered, the moment in both samples tends to the value of about 0.18 at large rotations. The dense specimen reaches a minimum of 0.11. These values correspond well with the values from the uncompacted tests. Confirming that the soil in test C5Lc is looser than in C6Dc, the jumps due to slip events are higher in test C5Lc, although they are lower than in the uncompacted tests C1L and C3L. In soil compacted by vibration, it can be expected that the initial deposition density of the backfill does not influence the soil behaviour, as the densification caused by the vibration leads to a contractive-dilative behaviour in any case.
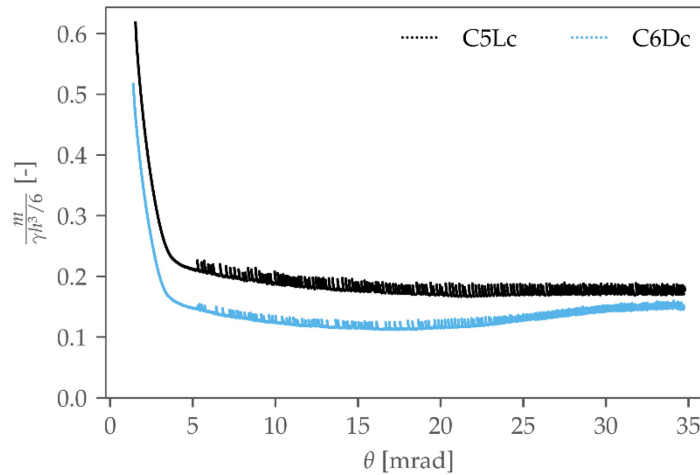
Fig. 98: *Normalised moment as a function of the wall rotation for the compacted samples.*

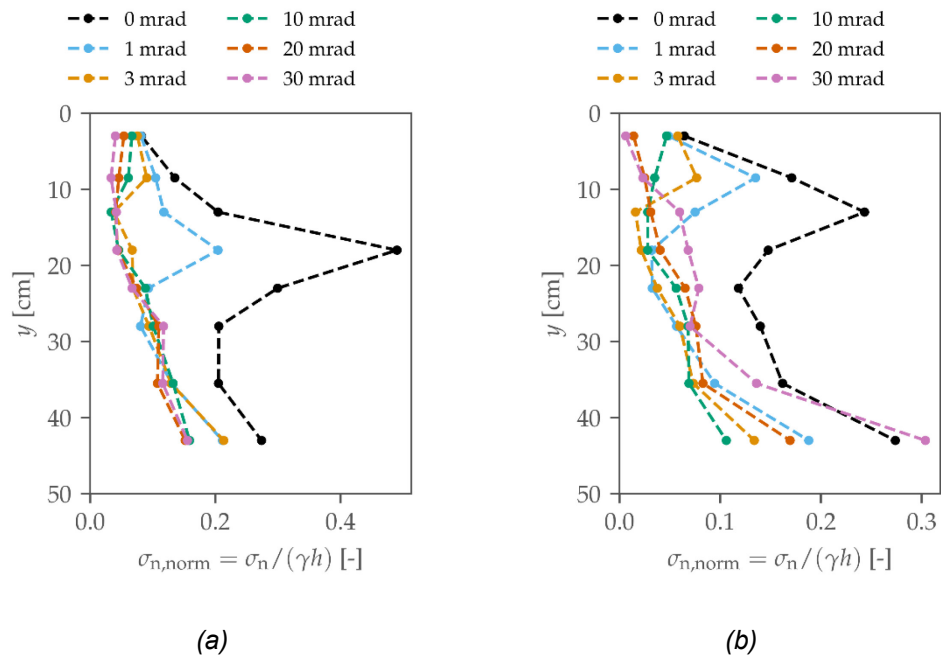*(a)*   *(b)*

Fig. 99: *Normalised earth pressure during the rotation phase in (a) test C5Lc; and (b) test C6Dc. The rotation indicated in the legend corresponds to the applied rotation net of the initial value measured after the backfill.*

Fig. 99 shows further differences between the loose and dense samples, as observed in the uncompacted samples. While the loose sample shows an approximately linear distribution after a rotation of 30 mrad, the dense sample does not. In fact, the earth pressure starts increasing in some parts of the backfill after a rotation of 10 mrad due to softening. While the stress increase was confined in the lower part of the backfill in the uncompacted tests, Fig. 99 shows a stress increase in the upper part as well, confirming the intuition that at a larger rotation (i.e. at the critical state) a linear distribution could be reached.

The earth pressure distribution can be deduced from Fig. 100 for the compacted and uncompacted tests having similar deposition densities. While the location of the earth pressure resultant initially diverges between compacted and uncompacted specimens, very similar results are obtained in the rotation phase for samples having similar density.
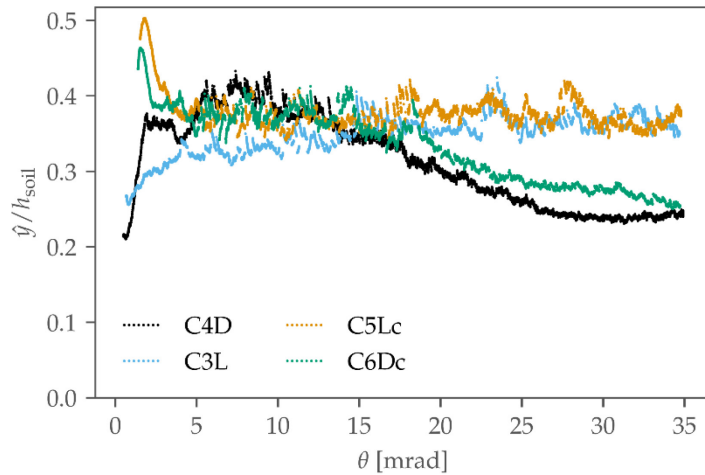
Fig. 100: *Location of the earth pressure resultant $\hat{y}$ normalised by the height of the backfill h_{soil} as a function of the wall rotation.*

Fig. 101 compares the moment-rotation relationship of compacted and uncompacted samples having the same deposition density. It is observed that as soon as the moment-rotation curve of the loose, compacted sample C5Lc meets that of the loose, uncompacted sample C3L, it becomes parallel to it, with just a slight offset likely caused by the slightly higher relative density achieved by compaction. Instead, the densely deposited samples diverge more in the initial phase, probably because of a reduced relative density caused by the soil dilation that occurs during the application of the static compaction load. At a wall rotation of 5 mrad, the dense, compacted specimen showed a 50% higher moment than its uncompacted counterpart. After a rotation of 20 mrad, a good match is observed. All samples show good agreement on the moment at the residual state and at peak strength.

In general, it is observed how the increased stresses cause a relatively fast unloading because of the higher soil stiffness and, more importantly, of the different stress distribution, with higher stresses farther away from the wall toe, where the highest rotation-induced wall displacement occurs.
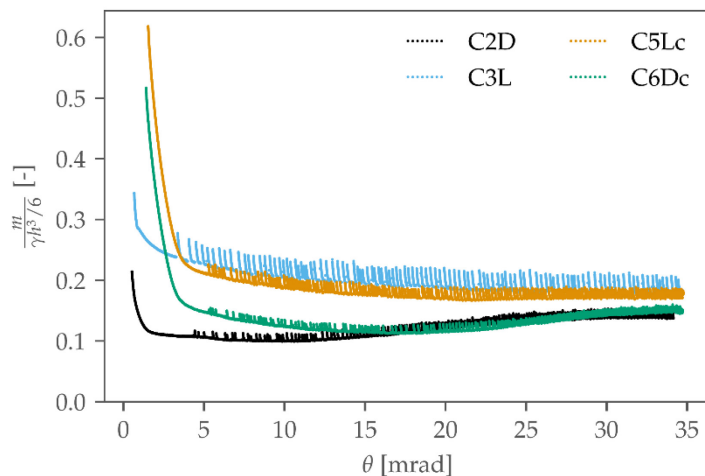

Fig. 101: *Normalised moment as a function of the wall rotation for the compacted and uncompacted samples with corresponding deposition density.*

6.1.3   3D conditions

Tests under 3D conditions were conducted by imposing a rotation to the central wall section while keeping the outer sections fixed at their initial position. The goal is to simulate the

situation where the corrosion degree along the wall length is inhomogeneous (or only one wall section is corroded), causing the most damaged wall sections to undergo a higher rotation than the others.

The backfill was deposited following the same procedure as in the tests carried out under plane strain conditions (Section 6.1.1). Due to the proven reliability and repeatability of the tests, practically identical initial earth pressure distributions were obtained. The results are therefore not reported here for the sake of conciseness. After the backfill deposition, the central wall section was rotated while keeping the outer sections fixed. The resulting moment on the central and outer sections is plotted in Fig. 102 for dense and loose sand specimens.
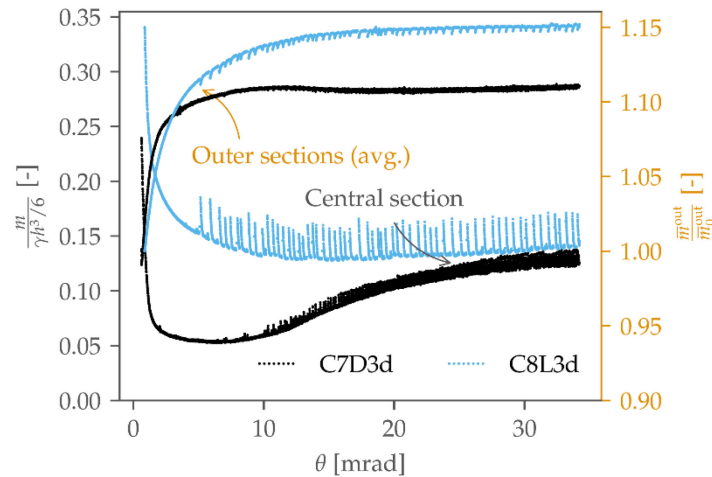

Fig. 102: *Moment as a function of the rotation of the central wall section under 3D conditions. On the left y-axis: normalised moment acting on the central section; on the right y-axis: moment increase on the outer sections as a function of the rotation of the central section. The moment increase is expressed in terms of the ratio between the current moment $\bar{m}^{out}$ and the moment $\bar{m}_0^{out}$ acting at the beginning of the rotation phase. The bar on $\bar{m}$ indicates that the moment of the outer sections was averaged.*

The observed soil behaviour compares well to the tests presented in the previous sections. The lower envelopes of the moment show the expected behaviour for dense (contractive-dilative) and loose (contractive) soil, and stick-slip is more pronounced in loose than in dense soil. The normalised moment on the central wall section reaches a minimum of about 0.05 in the dense sample, followed by an increase due to softening. At larger rotations, the moment for both samples tends to the value of about 0.13. These values are lower than those of the previous tests (see the comparison in Fig. 104 and Fig. 105 discussed later) as a three-dimensional failure mechanism defined by a curved line in the horizontal plane develops.

A top view of the curved failure mechanism is shown in Fig. 103 for the loose and dense sample. The dense soil shows again strongly localised deformations. In the middle of the central section, the distance of the outer shear band from the wall measures approximately 18 cm: about the same distance as in test C2D (Fig. 86). In the test carried out under 3D conditions, slightly more localised deformations occurred in the loose sample, so a failure mechanism is recognised. The outer shear band is highlighted in red in Fig. 103b. It is noted that the failure mechanism in the loose sample covers a larger surface than in the dense sample. The distance of the outer shear band in the middle of the central wall section is about 28 cm.
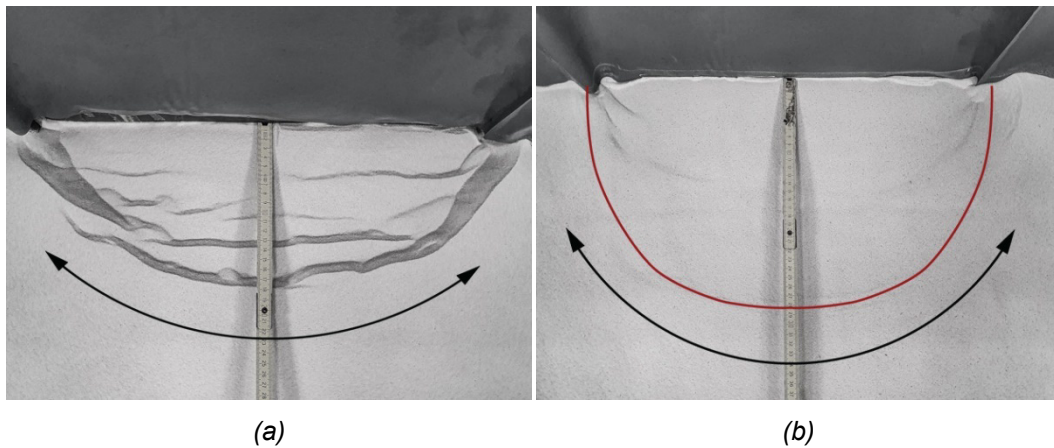
(a)   *(b)*

Fig. 103: *Top view of the failure mechanism observed after the conclusion of tests C7D3d (left) and C8L3d (right). The outer shear band is highlighted in red to improve visibility in test C8L3d.*

In the case of a three-dimensional failure mechanism, a stress redistribution occurs due to arching (idealised by black arrows in Fig. 103), resulting in a lower limit load acting on the failing wall section and a higher load on the neighbouring sections. As a result, the neighbouring sections must sustain an 11% increase in moment in the dense sample and 15% in the loose sample (Fig. 102). These results are barely affected by boundary effects, as the outer walls are kept in their initial position (i.e. there is no relative displacement between the soil and the glass walls), and the width of the fictitious arches responsible for the stress redistribution are narrower than the outer wall sections. In fact, tom Wörden [45] observed increased stresses on only half of the width of the neighbouring walls.

A lower increase is observed in the dense sample, as the curvature of the failure mechanism (i.e. the curvature of the "arch") is lower than in loose soil, which has a lower ability to carry the load. Further, it is observed that softening occurring inside the failure mechanism does not influence the moment acting on the outer sections in the dense sample. Indeed, a plateau is observed after the maximum increase value is reached. The reason is that softening is a local behaviour and only influences the soil inside the failure mechanism, where significant plastic strains develop. On the other hand, the results in Fig. 102 show that stick-slip also affects the moment acting on the outer wall sections, although only minimally. Indeed, arching causes a stress redistribution in the form of force chains that can collapse, causing slip events.

Fig. 104 and Fig. 105 compare the tests carried out under 3D conditions to those carried out under plane strain conditions on samples with the same relative density.

Under 3D conditions, the loose sample shows a faster unload to the residual value of the moment when only the central wall section is rotated than under plane strain conditions. Indeed, the limit state is reached after a rotation of about 10 mrad, whereas it was not fully reached after 35 mrad under plane strain conditions. Furthermore, the limit load reached in test C8L3d is about 30% lower than in test C3L.
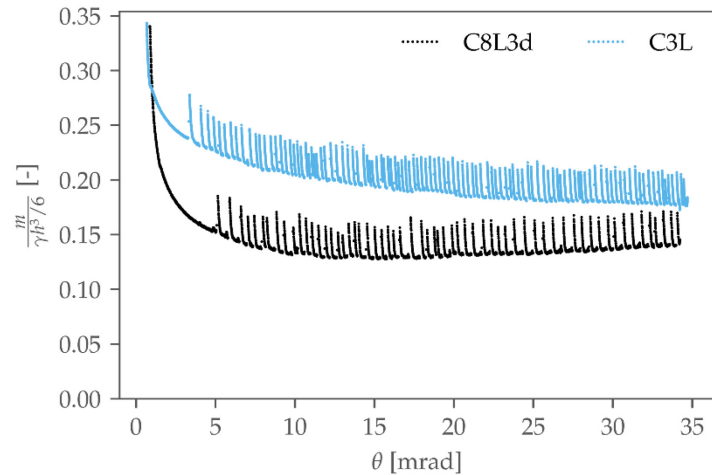
Fig. 104: Comparison of the moment on the central section as a function of its rotation for the tests carried out under 2D (blue) and 3D (black) conditions in loose sand.

Similarly, the moment-rotation curve of test C7D3d is characterised by faster unloading and quicker moment increase due to softening, as the local mechanism is smaller (on the sides) than the plane strain mechanism and needs lower displacements to mobilise the soil strength. While the limit load in test C7D3d is about 30% lower than in C2D (as for the loose samples), the limit load acting when the soil peak shear strength is mobilised is 50% lower.
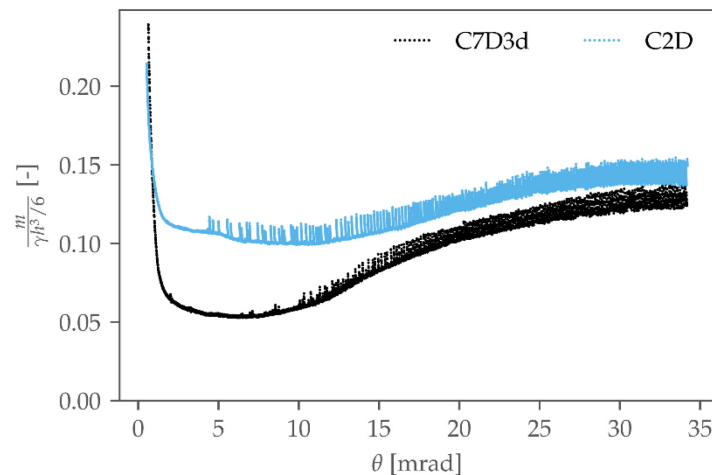

Fig. 105: Comparison of the moment on the central section as a function of its rotation for the tests carried out under 2D (blue) and 3D (black) conditions in dense sand.

The presented test results show that the active limit load on walls with an inhomogeneous distribution of the corrosion degree along their length is lower than on walls with equally corroded sections, provided that the less damaged sections can carry the additional load caused by the stress redistribution. More precisely, the less damaged wall sections must have a sufficient safety margin to carry the increased load undergoing smaller displacement than the damaged section. Instead, if the neighbouring sections do not have a sufficient safety margin to carry additional load, they will yield and be unloaded to the limit state. This limit state depends on the width of the yielding wall sections and tends to value obtained under plane strain conditions (Section 6.1.1) with increasing width. Under all circumstances, the proper limit load of a retaining wall must consider the failure of the complete wall (i.e. of all wall sections), as the failure of a single section could always trigger a domino effect leading to the failure of the whole wall.

6.2 Rigid wall

The tests on the cantilever wall (Section 6.1) revealed an approximately bilinear distribution of the earth pressure acting on the wall. This section studies the earth pressure acting on a nearly rigid, frictional wall to study whether wall displacement is the only factor causing a bilinear distribution of the earth pressure on flexible cantilever walls. Four tests were conducted on loose and dense soil. In two tests, the soil was deposited in a loose or dense state without additional compaction; the other two tests were compacted statically. The following testing procedure was described in Section 5.3.1-5.3.2.

6.2.1 Uncompacted soil specimens

Uncompacted soil samples were deposited using the pluviator in different lays without compacting them. The resulting earth pressure after each deposition step in the dense and loose sample is shown in Fig. 106.
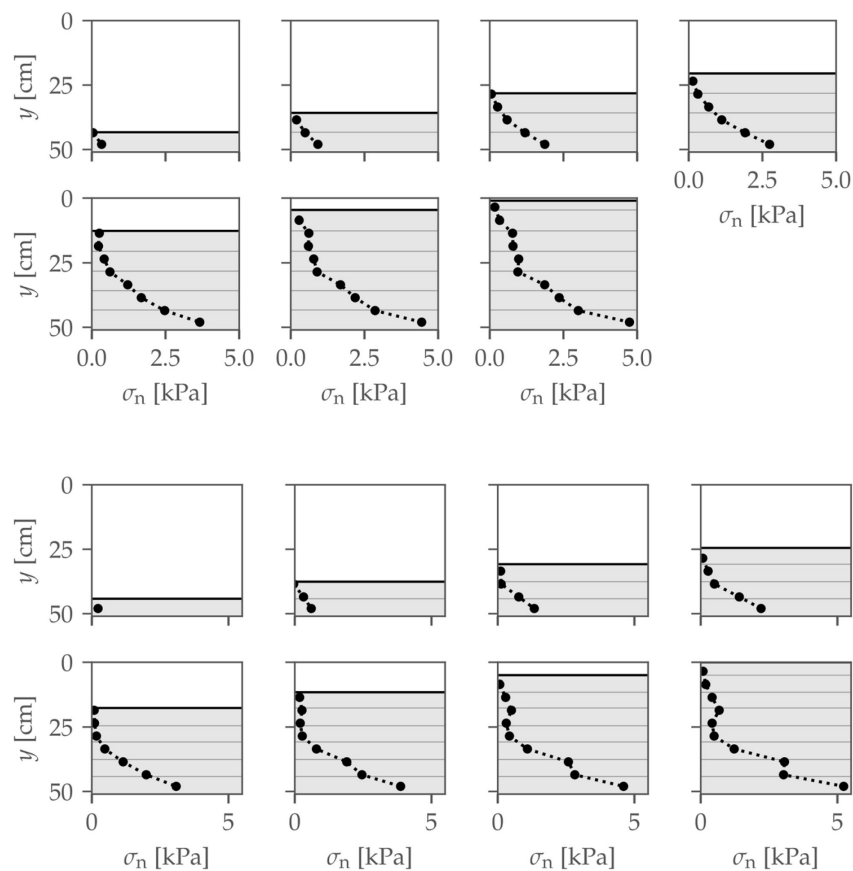

Fig. 106: *Earth pressure acting in the middle of the wall measured after the deposition of each layer in tests R9L (top) and R11D (bottom). Consecutive steps are shown from left to right, top to bottom.*

Both samples show qualitatively the same evolution of the earth pressure distribution. Initially, the earth pressure grows nearly linearly with depth. Then, as additional layers are deposited, the earth pressure transitions to an approximately bilinear distribution: on the higher part of the backfill, the lateral earth pressure coefficient is lower than in the bottom part. The presented results clearly show that the frictional soil-wall interface affects the stress distribution in the wall backfill.

As a soil layer is deposited, the overburden stress acting at a material point P in the underlying soil is increased by $\Delta\sigma_v = \gamma\Delta y$ (Fig. 107). If the rigid wall were frictionless ($\delta = 0°$),

the backfill would settle everywhere by the same amount. The strain path would correspond to a one-dimensional compression, and the increase in the vertical strain would be

$$\Delta\varepsilon = \frac{\Delta\sigma}{M},$$ (6.1)
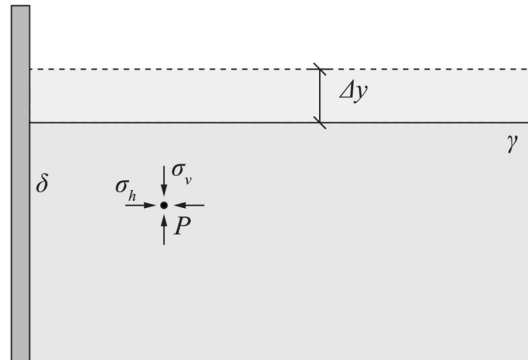
where $M = f(\sigma)$ is the constrained modulus.

Fig. 107: *Deposition of a soil layer of thickness Δy behind a rigid wall with interface friction angle δ.*

However, behind real walls (i.e. characterised by finite wall friction, $\delta > 0°$), the soil deformation is partially resisted by friction, leading to a nonhomogeneous deformation field and stress distribution. For this reason, the earth pressure "at rest" should be treated as a two-dimensional boundary value problem rather than a one-dimensional (consolidation) problem. This behaviour will be further investigated in Section 8.

Fig. 108 and Fig. 109 compare the earth pressure on the rigid walls with that on the flexible cantilever wall backfilled with soil deposited with the same relative density. The coefficient of lateral earth pressure is shown to be higher behind the rigid wall in the upper backfill, while in the bottom part of the backfill, higher values are measured behind the cantilever wall. This shows that the wall flexibility contributes to the bilinearity of the earth pressure distribution by further increasing the difference in the coefficient $\bar{K}$ with depth.
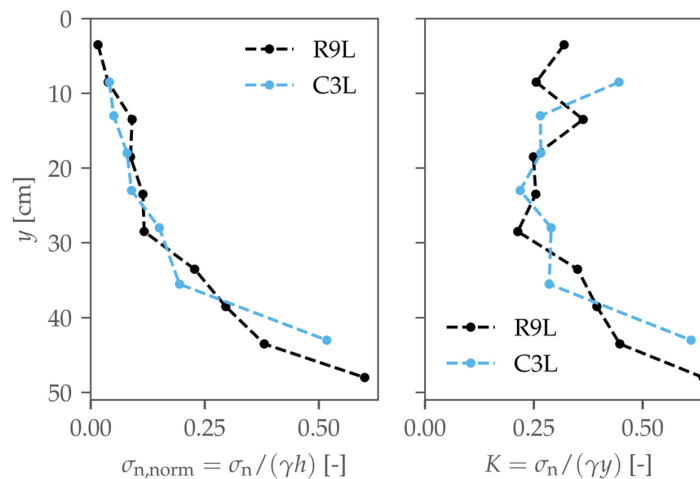

Fig. 108: *Earth pressure acting in test R9L (rigid wall, loose sand) and in test C3L (cantilever wall, loose sand). Left: normalised earth pressure acting on the wall; right: coefficient of lateral earth pressure $\bar{K}$.*
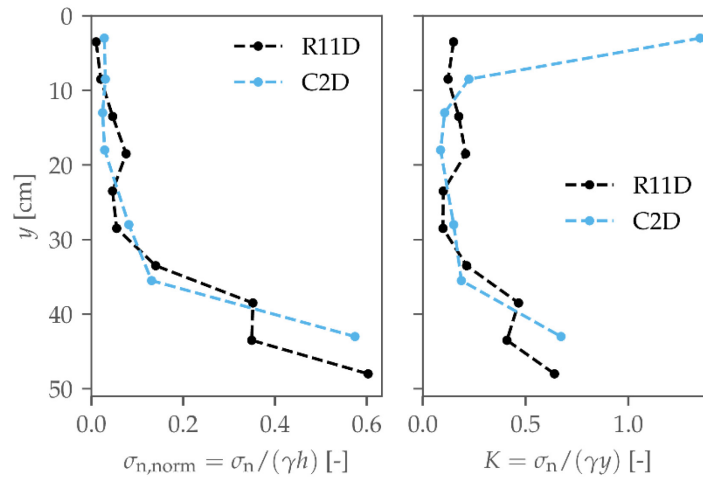
Fig. 109: *Earth pressure acting in test R11D (rigid wall, dense sand) and in test C2D (cantilever wall, dense sand). Left: normalised earth pressure acting on the wall; right: coefficient of lateral earth pressure $\bar{K}$.*

6.2.2 Compacted soil specimens

Two additional tests were carried out to study the effects of compaction behind rigid walls. The backfilling and compaction procedure is the same as in the tests presented in Section 6.1.2. The development of the earth pressure is plotted for both tests in Fig. 110. Qualitatively, similar results as in the cantilever retaining wall tests are observed. In the first stages, the earth pressure increases over the entire deposited depth in both samples. The earth pressure in the dense sample is slightly higher as a higher strength can be mobilised in the horizontal loading process. The bottom layers get partially unloaded in later stages, as in the cantilever retaining wall tests. However, while this unloading caused lower earth pressures in the dense sample than in the loose sample in the cantilever wall tests, very similar pressure levels are observed here. A possible explanation is that, in this case, the unloading is not caused by a wall deflection but rather by the interaction with the frictional wall interface. On the other hand, the location of the local peak in horizontal stress is higher in the dense sample than in the loose, as in the cantilever wall tests.
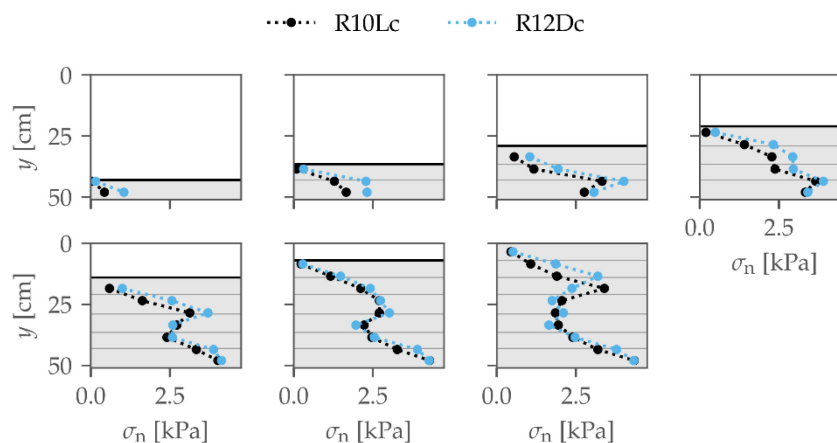

Fig. 110: *Earth pressure acting in the middle of the wall measured after the deposition of each layer in tests R10Lc and R12Dc. Consecutive steps are shown from left to right, top to bottom.*

Fig. 111 and Fig. 112 compare the earth pressure after backfilling the cantilever retaining wall and the rigid wall with soil having the same deposition density. The dense sample

consistently showed lower pressures on the cantilever wall than on the rigid wall due to the wall deflection. Instead, the loose soil exerted a lower pressure on the bottom part of the cantilever wall but slightly higher or similar pressures on the top part.
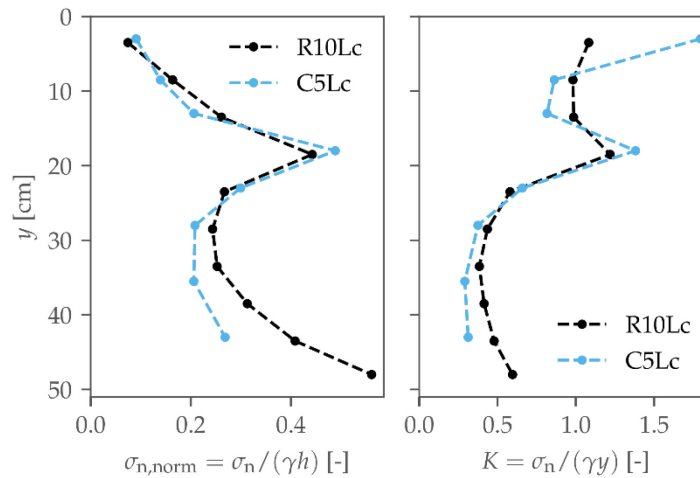
Fig. 111: Earth pressure acting in test R10Lc (rigid wall, loose sand, static compaction) and in test C5Lc (cantilever wall, loose sand, static compaction). Left: normalised earth pressure acting on the wall; right: coefficient of lateral earth pressure $\overline{K}$.
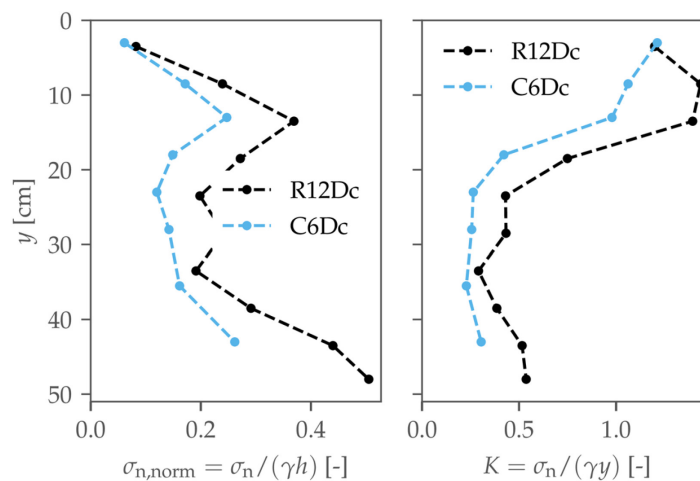
Fig. 112: Earth pressure acting in test R12Dc (rigid wall, dense sand, static compaction) and in test C6Dc (cantilever wall, dense sand, static compaction). Left: normalised earth pressure acting on the wall; right: coefficient of lateral earth pressure $\overline{K}$.

6.2.3 Discussion

To verify that the minimal displacement of the steel wall did not influence the earth pressure measurements, a test in which both sides of the wall were simultaneously filled with dense sand was additionally performed. The results are presented in [9] and did not show relevant differences. On the contrary, the measured pressure was slightly lower than in test R11D. Furthermore, the influence of the deflection of the pressure sensors should also be negligible, as shown through independent measurements in Fig. 84. The suitability of the pressure cells to measure soil stresses in the range of this work had previously been confirmed by Hauswirth [138].

Despite the evidence, a certain degree of uncertainty about fulfilling "at rest" conditions remains, as it is practically impossible to simulate a rigid structure in the laboratory. Nevertheless, the presented results show that a bilinear earth pressure distribution is also observed behind very stiff constructions, confirming previous experimental evidence obtained by Chen and Fang [64] and by Arnold [139].

6.3   Conclusions

This section presented the results of an experimental study of the evolution of the earth pressure acting on corrosion-damaged cantilever retaining walls. The most influential parameters, namely, the initial stress state and the elastoplastic soil behaviour, were investigated in a scaled test setup. The reliability and repeatability of the results obtained were demonstrated in different ways.

First, the complete evolution of the pressure of the earth during the lifetime of a wall was investigated, from its construction to structural failure due to corrosion damage. When the soil was deposited without compaction, a bilinear earth pressure distribution was observed at the end of the backfilling phase. Higher pressures were measured in loosely than in densely deposited soils because of the slower strength mobilisation in loose packings. Imposing a wall rotation on its toe led to the unloading of the wall, caused by the stress redistribution that occurred in the soil mass. The typical behaviour of loose, contractive and dense, contractive-dilative soil was observed, with the moment in the dense specimen reaching a minimum at a rotation of about 5-10 mrad before increasing due to soil softening. Instead, the moment in the loose specimen decreased monotonically, at a slower pace.

Furthermore, stick-slip events were observed in both samples; they were described, and their origin was explained. The earth pressure coefficients at active failure are pretty low, indicating a high strength that cannot be explained by triaxial tests carried out in the laboratory.

Then, compacted specimens were prepared by applying a static load to the surface of the soil after the deposition of each layer. Compared to the uncompacted samples, a higher stress state was observed at the end of the backfill. In particular, a different earth pressure distribution was obtained, characterised by a maximum value located in the upper part of the backfill. As a result, the earth pressure resultant force had a higher location. Because of that and the increased soil stiffness, the moment--rotation relationship of the compacted samples was characterised by a steep unloading, although only slightly larger rotations than in uncompacted samples are needed to reach active failure. In general, the behaviour of the compacted samples was similar to that of the uncompacted samples.

Additionally, the unloading behaviour of uncompacted samples was investigated under three-dimensional conditions. A single corroded wall section was simulated by rotating only the middle wall section. A stress redistribution occurred in the backfill, leading to a lower limit state and a curved failure mechanism. Consequently, a moment increase was measured in the adjacent wall sections.

Lastly, the earth pressure was measured on a nearly rigid wall during filling and compaction. The frictional interface was shown to contribute to the bilinear distribution of the earth pressure acting on real walls.

7   Numerical analysis: wall unloading process

This section presents and validates a numerical procedure to model the unloading process of cantilever retaining walls when damage occurs at the stem's toe. The goal is to propose and validate an appropriate constitutive law and a numerical model of the boundary value problem that allows a reliable simulation of the stress evolution in the soil during a corrosion-driven rotation of the wall stem. The numerical model will provide insight from a different perspective into the soil behaviour and the soil-structure interaction by evaluating quantities of difficult access in experimental setups and will allow further analyses of the problem at a larger scale than in the physical experiments.

First, the assumed constitutive law and model parameters are presented. Then, static, implicit finite element analyses are carried out to validate the numerical models against the experimental results presented in the previous section. At this stage, the initial soil stress state is treated as a known quantity (based on the experimental results), as this section only aims to study the unloading phase. Based on the gained knowledge, the model will be extended to model the initial state in the next section.

7.1   Constitutive modelling

7.1.1   Constitutive law

Granular soil is a complex material consisting of solid particles and voids. Its deformation behaviour is nonlinear, irreversible and stress-dependent. Despite its discrete nature, granular soil is commonly modelled as a continuous medium to analyse large-scale field problems. For this reason, many constitutive laws have been proposed by different authors in the last decades. Among the most used in the field are the linear elastic, perfect plastic model with the Mohr-Coulomb failure criterion [140] and the hardening soil model [141], as they are often implemented and readily available in commercial finite element programs. While the first leads to inaccurate predictions of the soil deformation field and should only be used for simple predictions of the limit load, the second can capture many features of granular soil, such as yielding and nonlinear elasticity but involves a more detailed calibration. Other constitutive laws include von Wolffersdorff's hypoplastic model [142] and SANI-SAND [143], [144]. Hypoplastic models describe the inelastic soil response without defining a yield surface and a plastic potential and without decomposing the strains in elastic and plastic parts [145]. This leads, in general, to simpler mathematical formulations that allow more straightforward implementations in numerical codes that lead to fewer computational instabilities. SANISAND is a very sophisticated elastoplastic model that accurately models soil behaviour in element tests.

A preliminary analysis of the performance of the above-mentioned constitutive laws applied to the problem of the unloading of damaged cantilever retaining walls was conducted in [146]. The results showed rather bad agreement with experimental data using von Wolffersdorff's hypoplastic model, while SANISAND was abandoned in the early stages because its implementation did not provide the required stability needed to solve boundary value problems involving contacts. In addition, this work aims at validating and suggesting a modelling procedure to be used in the geotechnical field, where SANISAND is still mostly unknown and out of reach because of the rather complicated calibration procedure. The following model was proposed.

Elastic response

The elastic response is modelled assuming isotropic hypoelasticity. The governing parameters are the Poisson's ratio and the pressure-dependent Young's modulus. The Young's modulus is defined as

$$E = E_{\text{ref}} \left(\frac{p'}{p'_{\text{ref}}} \right)^n , \tag{7.1}$$

and the Poisson's ratio is constant. It is worth noting that hypoelasticity violates the First Law of thermodynamics [147]. Nevertheless, it is assumed here as it has a proven agreement with experimental data and is of good practical use. Hypoelasticity is also used in the hardening soil model to model the elastic response [141], [148].

Plastic response

The soil plastic response is modelled by assuming a Mohr-Coulomb yield surface. In the general stress space, its formulation reads

$$Y : \sqrt{J_{2D}} - \sqrt{3} \, \frac{p \sin \varphi + c \cos \varphi}{\sqrt{3} \cos \theta + \sin \varphi \sin \theta} = 0, \tag{7.2}$$

where J_{2D} is the second invariant of the deviatoric stress tensor, p is the mean effective stress, θ the Lode angle, c the cohesion, and φ the friction angle. In a granular soil, the cohesion is usually zero, while the friction angle is a function of a hardening parameter χ

$$\varphi := f(\chi). \tag{7.3}$$

Equation (7.3) is often termed as the hardening law. In geotechnical engineering, the hardening parameter is commonly assumed as the cumulative plastic deviatoric strain:

$$\chi := \bar{\varepsilon}^p_{\text{dev}} = \int d\varepsilon^p_{\text{dev}} . \tag{7.4}$$

The plastic deviatoric strain increment is defined as:

$$d\varepsilon^p_{\text{dev}} = \frac{2}{3} \sqrt{3 I^p_{2D}} , \tag{7.5}$$

where I^p_{2D} is the second invariant of the plastic deviatoric incremental strain tensor

$$I^p_{2D} = I^p_2 - \frac{\left(I^p_1 \right)^2}{6} , \tag{7.6}$$

with

$$I^p_1 = \text{tr} \left(d\underline{\underline{\varepsilon}}^p \right) , \tag{7.7}$$

and

$$I^p_2 = d\underline{\underline{\varepsilon}}^p : d\underline{\underline{\varepsilon}}^p , \tag{7.8}$$

where $\text{tr}(\cdot)$ indicates the trace operator and : double contraction.

The plastic potential is modelled as a Mohr-Coulomb surface affine to the yield surface, Equation (7.2). The plastic potential is described by the soil dilation angle ψ, which, similarly to the friction angle, depends on the hardening parameter $\bar{\varepsilon}^p_{\text{dev}}$.

The plastic response is modelled similarly in the hardening soil model, where a mathematical function is used to approximate the hardening law. Instead, in this work, tabular data extracted from experimental evidence is used. This allows to model strain softening and hardening, whereas the hardening soil model only allows the modelling of strain hardening.

7.1.2 Strain regularisation and mesh dependency

Because of the strain softening response of the used constitutive law, the numerical results are affected by mesh dependency. Therefore, a simple regularisation technique first proposed by Pietruszczak and Mróz [149] is applied. This technique was successfully applied in various studies in the past (e.g., [150], [151]) and consists of scaling the hardening parameter after the onset of strain softening as follows:

$$d\varepsilon^p_{\mathrm{dev,el}} = d\varepsilon^p_{\mathrm{dev,SB}} \frac{d_{\mathrm{SB}}}{l_{\mathrm{el}} \cdot \cos \alpha} \,, \tag{7.9}$$

where $d\varepsilon^p_{dev,el}$ and $d\varepsilon^p_{dev,SB}$ are the plastic deviatoric strain increment in the element and in the shear band, respectively, d_{SB} is the shear band thickness, α its inclination, and l_{el} the element size. The shear band thickness is assumed to be $d_{\mathrm{SB}} \approx 15 \cdot d_{50}$ with d_{50} as the average grain size (e.g. [114], [152]–[154]). By applying the regularisation, the results are insensitive to the mesh size (see Appendix III.1).

7.1.3 Calibration of the constitutive law

Based on the results obtained in the previous section, the hardening curve for Perth Sand was derived and plotted in Appendix II.2. The conventional geotechnical procedure described in Section 3.5.1 was applied, meaning that the mesh should not be too fine to avoid an undesired strain localisation due to nonassociativity. The strength obtained in the virtual biaxial tests was assumed. Due to strain localisation, however, its mobilisation as a function of the deviatoric strain is not very accurate. Therefore, the shape of the hardening curve resulting from the triaxial test was also considered.
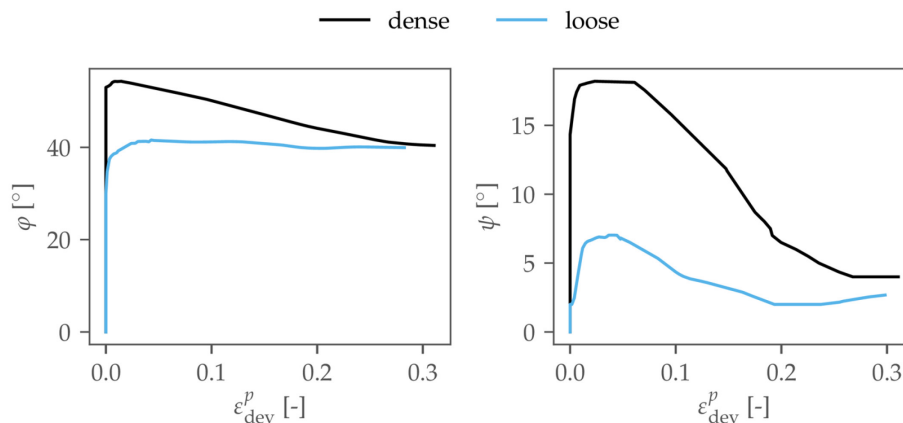
Fig. 113: *Hardening curves for the dense and loose samples employed in the finite element simulations.*

7.2 Unloading behaviour under plane strain conditions

In this section, the numerical model is validated during the wall unloading (i.e. rotation) phase. The material model presented in Section 7.1 is employed using the Abaqus user material model implemented by Clausen et al. [119]–[121] and modified to include all needed features. It is important to remark that state-dependent variables, such as hardening parameters, are only updated at the end of a computation increment. Therefore, although equilibrium iterations are performed, the solution scheme cannot be defined as purely implicit.

7.2.1   Finite element model

The finite element model employed for the simulation of the unloading process of the wall tests is shown in Fig. 114. Plane strain conditions are assumed. The wall and backfill dimensions are the same as in the laboratory tests. The wall friction was determined in the laboratory and corresponded to $\delta = 21.8°$ for all sand densities.

The simulation procedure is the following: first, the stresses measured in the experiment are initialised throughout the whole backfill. Then, a wall rotation is imposed at its toe, and the evolution of the bending moment at the same point is measured and compared to the test results.
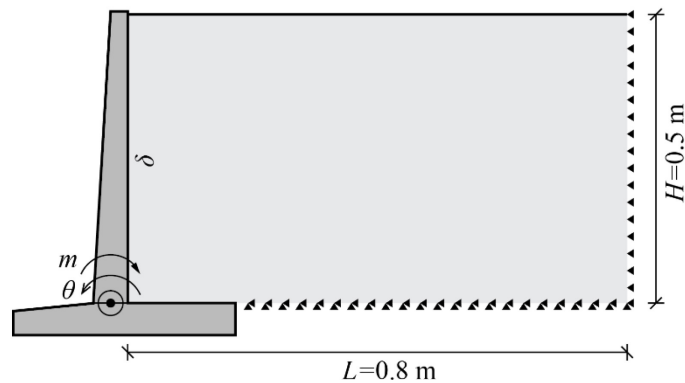

Fig. 114: Numerical model employed for the simulation of the wall experiments.

7.2.2   Results and discussion

Fig. 115 compares the numerical model response to test C2D (dense, uncompacted sample). In the initial phase, a very close match is observed between the two curves. After the steep moment decrease, the experimental curve shows a first plateau, followed by an additional slight decrease. The same behaviour is observed in the numerical model, albeit in a less perceptible form, as the first plateau has a higher inclination. Slight variations of the hardening curve showed that this inclination is very sensitive to the strength's mobilisation at small strains. This could indicate a slight inaccuracy in the calibration or the importance of correctly modelling the plastic strains occurring in the backfilling phase.
Nevertheless, it can be safely stated that the observed differences are irrelevant for practical use (e.g. for verifying existing walls). In general, the results show excellent agreement with the experimental evidence. Only at relatively large rotations, when the soil behaviour is dominated by softening, do the two curves start diverging.

Fig. 115 additionally shows the moment at the limit state, assuming the friction angle's peak and residual value. The solutions presented in Section 3.3 are considered. For the kinematic solution, both the associated and a nonassociated flow rule are considered. The results show that estimating the limit state by assuming the maximum resistance leads to underestimating the minimum moment value. The underlying reason is that the maximum soil resistance is not mobilised simultaneously over the entire height of the backfill. On the other hand, the limit state value calculated assuming the soil's residual shear strength yields a reliable upper bound of the numerical solution and, thus, a safe estimate of the moment measured in the experiment. It is also shown that the limit state estimates assuming Davis' reduced parameters provide very conservative estimates.
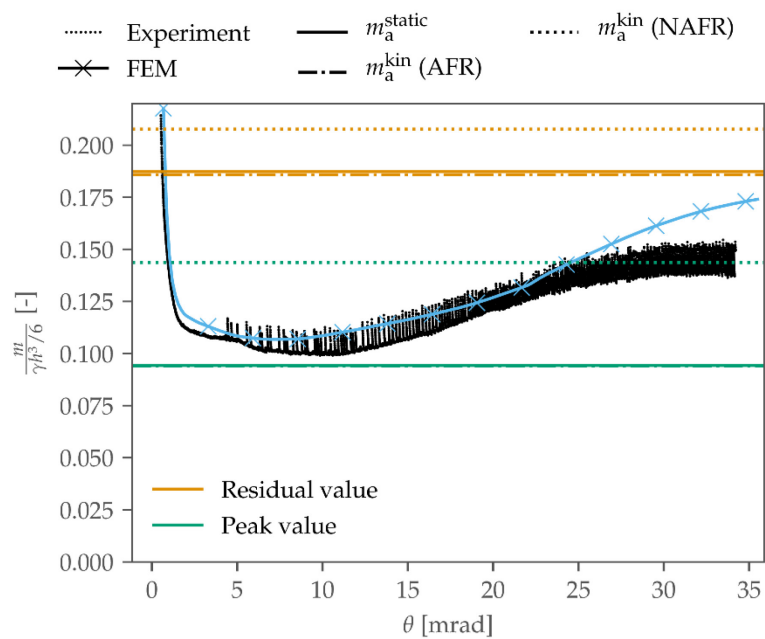
Fig. 115: *Moment vs rotation measured at the stem's toe in the numerical model and physical test C2D. Additionally, the analytical solutions for the limit state are plotted.*

The good agreement between numerical and experimental results is confirmed by the contact stress measured at the soil-wall interface, plotted in Fig. 116. Before the wall rotation is induced, the stress in the upper part of the wall is close to the active value at peak strength, while it is higher in the lower part. A rotation of 1.5 mrad suffices to cause a mobilisation of the peak shear strength almost over the entire depth of the backfill, as evidenced by the practically linear stress distribution observed in the numerical simulation. Only in the vicinity of the wall heel, the stress deviates from $e_{ah,peak}^{kin,MC}$. There, the numerical results are influenced by the stress singularity induced by the contact with two different surfaces at the corner between the stem and heel. However, it is clear that unloading has not yet occurred.
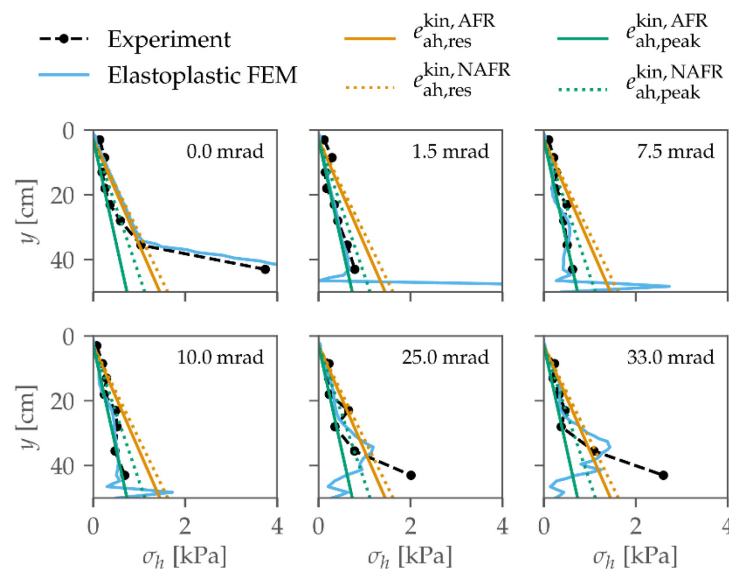

Fig. 116: *Contact pressure distribution along the soil-wall interface during the rotation phase. The rotation is expressed as the total induced rotation after the backfilling phase (i.e. the rotation induced by the backfilling is subtracted from the value given in each plot).*

The experimental results show very similar results, with one subtle difference. Indeed, the experimental stress shows a slightly nonlinear distribution in the upper 20 cm of the backfill. This likely indicates the onset of softening in that region. On the other hand, the stress towards the bottom of the stem is slightly higher than its minimum value $e_{ah,peak}^{kin,MC}$, indicating that the peak strength has not yet been reached there. The rotation of 1.5 mrad also marks the beginning of the first plateau in Fig. 115, and the previous observations show how minute the differences that influence the plateau's inclination are. Indeed, the flat plateau observed in the experiment is the result of the unload at the bottom compensated by the stress increase at the top. Instead, the numerical results are dominated by the unload at the bottom, leading to a higher inclination.

(a)

(b)
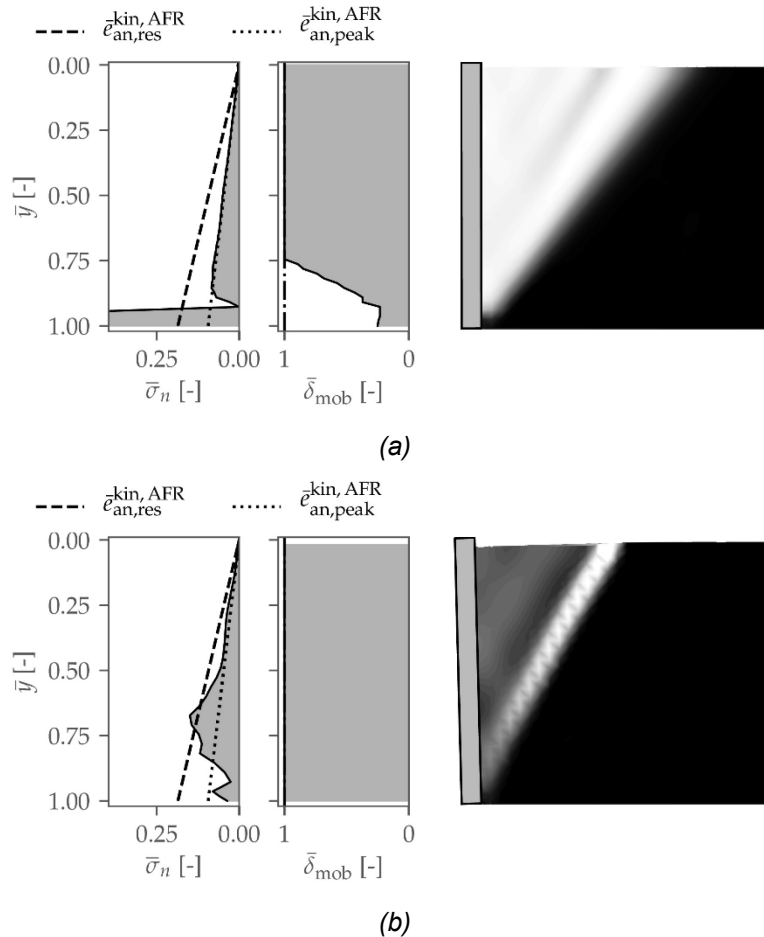
Fig. 117: *Contact pressure (left), mobilised interface friction expressed as the ratio of the mobilised friction over the interface friction, $\bar{\delta}_{mob} = tan \frac{\delta_{mob}}{\delta_{wall}}$ (centre), and deviatoric plastic strain increment at the rotation of 1.5 mrad (a) and 25 mrad (b). The normalised depth $\bar{y} = h_{wall}$ is adopted in the plots.*

Fig. 117a shows the contact pressure, the mobilised friction at the soil-wall interface, and the plastic deviatoric strain increment at an induced rotation of 1.5 mrad. The plastic strain increments indicate the formation of a diffused failure wedge with very little localisation of the deformation, meaning that the soil did not soften, in agreement with previous observations. In addition, the plot of the friction mobilisation along the soil-wall interface indicates that failure has only occurred in the upper 80% of the interface. It is to be noted that, in reality, the wall friction is at least partially mobilised during the backfilling phase, while the shear stress at the interface was initialised as $\tau_{int} = 0$ kPa in these simulations. However, this difference does not influence the results to a noticeable degree.

Starting at an induced rotation of about 7.5 mrad, softening influences the soil behaviour significantly. The soil deformation localises in shear bands, which is reflected by the non-linear distribution of the earth pressure. As the rotation progresses, the stress increases and tends to its residual active value in the top region of the backfill while it keeps a non-linear distribution in the wall's middle and bottom parts. A region of increased stresses (above the limit state given by the residual strength) in the lower part of the backfill is observed in both the experimental and numerical results, although it is more shifted to the bottom in the experimental results (see, e.g., Fig. 116 at $\theta = 25\ \mathrm{mrad}$).

Fig. 117b shows that failure has occurred along the whole soil-wall interface and that the deformation is strongly localised, resulting in a nonlinear distribution. The strain is mainly localised in two shear bands: the first intersects the wall at its toe and is experiencing the most shearing deformation, while the second intersects the wall close to its middle point. Over the wall height, the presence of a shear band corresponds to a region of reduced earth pressure. Between them, the pressure acting on the wall is increased. The two shear bands intersect the soil surface at a distance of about 11 and 20 cm from the stem's top corner. In experiment C2D, two shear bands intersected the soil surface at a distance of 9 and 18 cm (Fig. 86). Good agreement is therefore also observed in terms of deformations.

Fig. 118 compares the numerical model response to test C3L (loose, uncompacted sample). Overall, the numerical results show excellent agreement with the experimental data. The same figure also shows the limit state solution assuming the residual shear strength. As in the case of the dense sample, it provides a reliable, conservative estimate of the numerical and experimental moment. Again, the value estimated assuming the nonassociated flow rule is very conservative.

Fig. 118: *Moment vs rotation measured at the stem's toe in the numerical model and physical test C3L. Additionally, the analytical solutions for the limit state are plotted.*

The evolution of the contact pressure on the wall is plotted in Fig. 119. As for the bending moment, great agreement with the experimental data is observed, confirming the suitability of the proposed constitutive law to model the corrosion-driven unloading of cantilever retaining walls.

Fig. 120 shows the contact pressure, the mobilised friction at the soil-wall interface, and the plastic deviatoric strain increment at an induced rotation of 25 mrad. Compared with the corresponding figures for the dense sample, it is immediately noted that no localisation of the deformation occurs in loose sand. Here, yielding occurs in a diffuse wedge, leading to a linear distribution of the earth pressure. The upper width of the wedge is about 30 cm.

No such measurement could be done in the laboratory, as no clear delimitation could be observed in the loose, uncompacted sample.
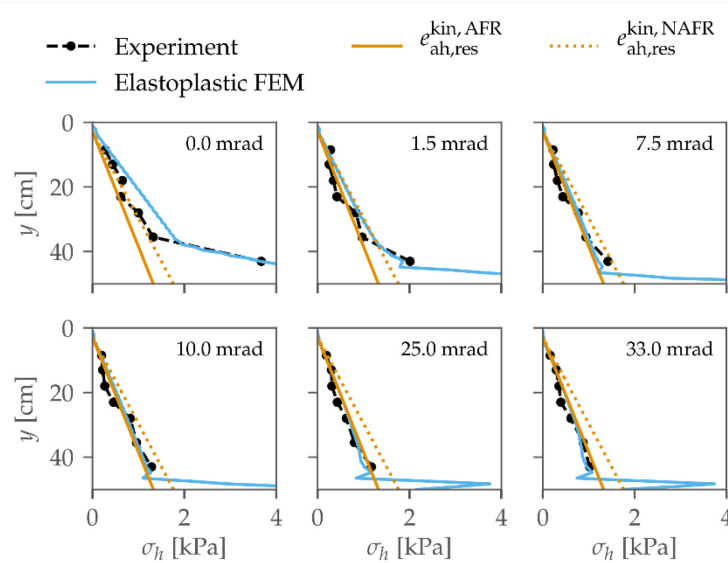
Fig. 119: Contact pressure distribution along the soil-wall interface during the rotation phase. The rotation is expressed as the total induced rotation after the backfilling phase (i.e. the rotation induced by the backfilling is subtracted from the value given in each plot).

Fig. 120: Contact pressure (left), mobilised interface friction expressed as the ratio of the mobilised friction over the interface friction, $\bar{\delta}_{mob} = tan\frac{\delta_{mob}}{\delta_{wall}}$ (centre), and deviatoric plastic strain increment at the rotation of 25 mrad. The normalised depth $\bar{y} = h_{wall}$ is adopted in the plots.

Fig. 121 compares the numerical model response to test C6Dc (dense, compacted sample). While the numerical model successfully predicts the initial steep unloading and the minimum value of the moment, it underpredicts the moment in the rotation range between 4 and 15 mrad. This underprediction is caused by the fast unloading in the upper backfill observed in Fig. 122, which depicts the earth pressure distribution. It is observed how the increased initial lateral pressure in the upper region almost immediately disappears while the pressure in the central part remains higher than in the experiment. Only when softening becomes dominant does the numerical earth pressure match the experimental measurements reliably. This initial divergence is possibly caused by the decrease in soil density due to shearing caused by compaction of the soil deposited at its maximum density. Another possible cause is an inaccuracy of the chosen constitutive law in modelling the cyclic behaviour of soil.

However, the achieved accuracy suffices for practical purposes, keeping in mind that the

response obtained after the first steep unloading and before softening becomes dominant may be underpredicted.
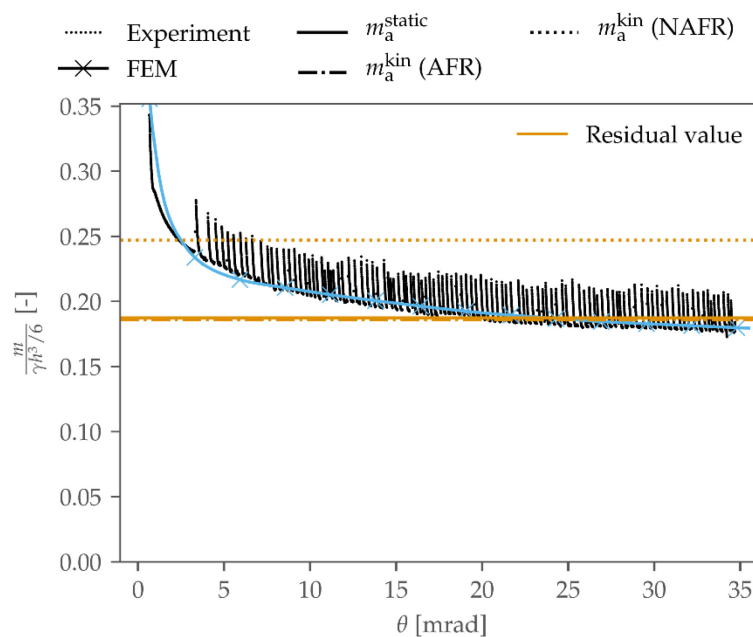

Fig. 121: *Moment vs rotation measured at the stem's toe in the numerical model and physical test C6Dc. Additionally, the analytical solutions for the limit state are plotted.*
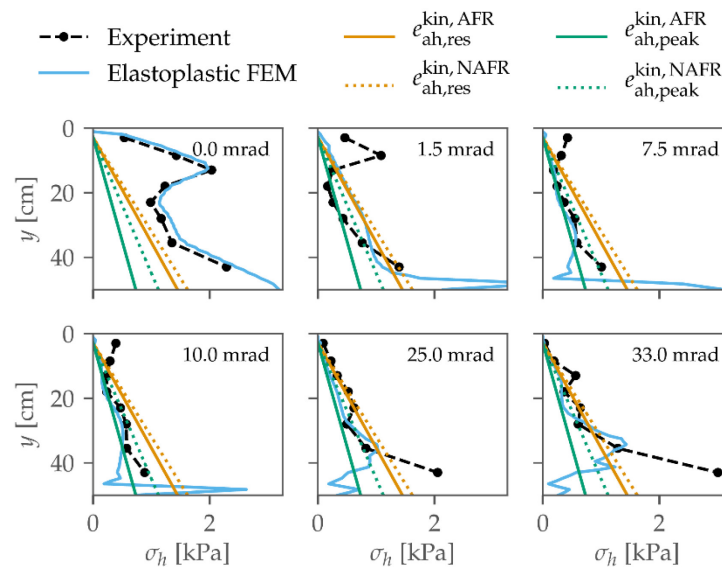
Fig. 122: *Contact pressure distribution along the soil-wall interface during the rotation phase. The rotation is expressed as the total induced rotation after the backfilling phase (i.e. the rotation induced by the backfilling is subtracted from the value given in each plot).*
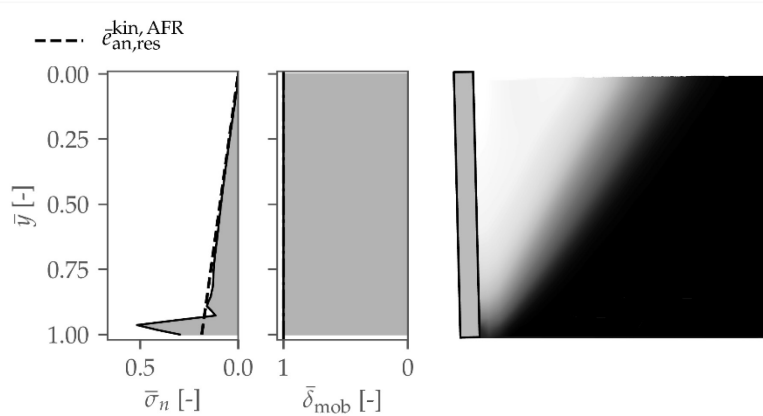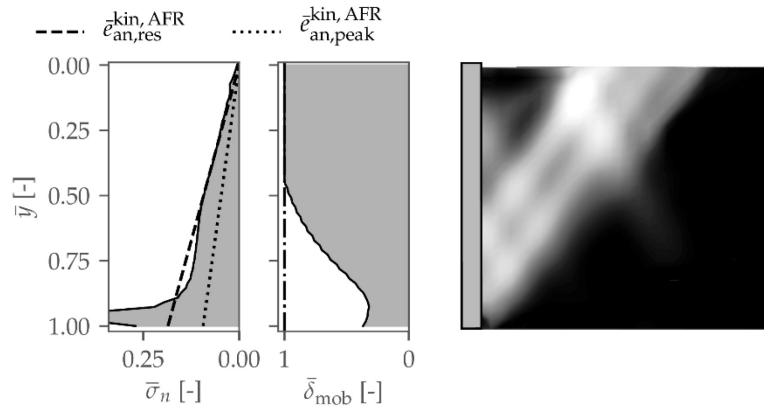
Fig. 123: Contact pressure (left), mobilised interface friction expressed as the ratio of the mobilised friction over the interface friction, $\bar{\delta}_{mob} = tan\frac{\delta_{mob}}{\delta_{wall}}$ (centre), and deviatoric plastic strain increment at the rotation of 1.5 mrad. The normalised depth $\bar{y} = h_{wall}$ is adopted in the plots.

Fig. 123 shows localised yielding in the bottom part of the backfill at small wall rotations. In the beginning, the stress state in that region is namely closer to yielding as the lateral earth pressure coefficient is lower. This behaviour contrasts with uncompacted samples, where yielding propagates from top to bottom.
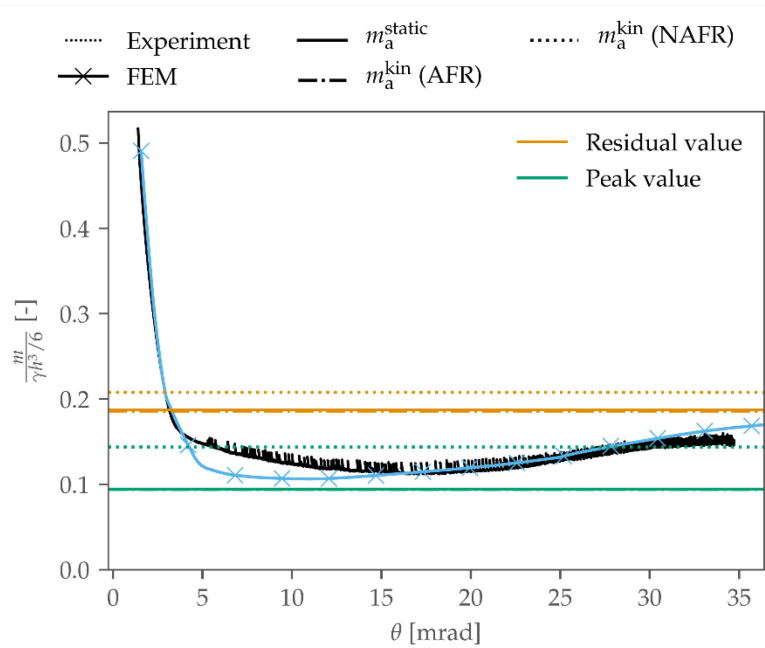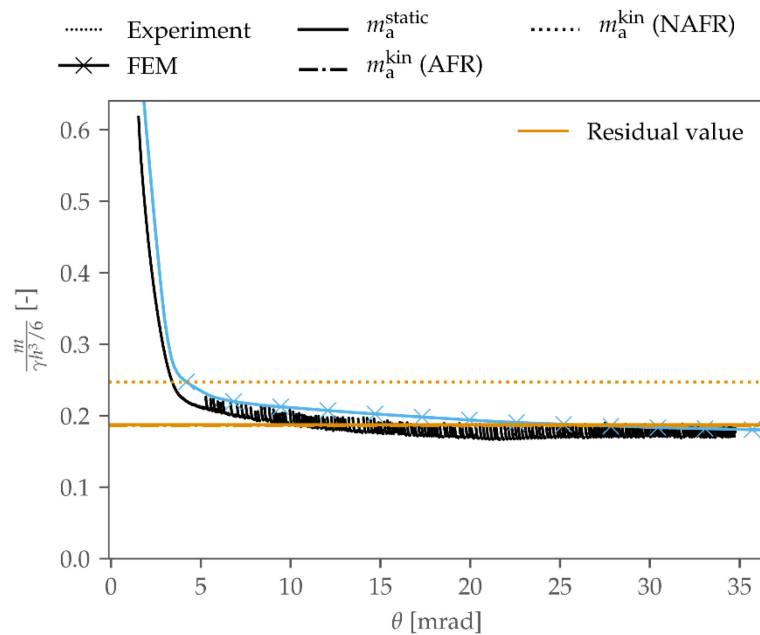

Fig. 124: Moment vs rotation measured at the stem's toe in the numerical model and physical test C5Lc. Additionally, the analytical solutions for the limit state are plotted.

Fig. 124 depicts the moment-rotation response of a loose, compacted sample. The numerical response agrees very well with the experimental measurements. First, a stiff response is observed, followed by a slightly inclined plateau.

The good match of the loose specimen with the experimental results leads to the rejection of the assumption made earlier for the dense sample that the constitutive model cannot accurately model the cyclic soil response.
Again, the limit analysis solution (assuming the associated flow rule) provides a reasonable and safe estimate of the limit load. On the other hand, the kinematic solution calculated

assuming a nonassociated flow rule overpredicts the moment, as the soil hardening curve was calibrated in the conventional way (Section 3.5.1).
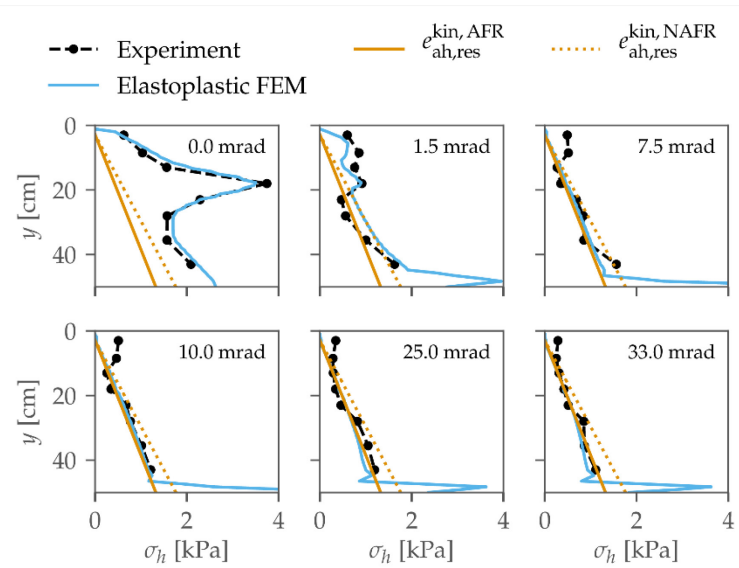
Fig. 125: *Contact pressure distribution along the soil-wall interface during the rotation phase. The rotation is expressed as the total induced rotation after the backfilling phase (i.e. the rotation induced by the backfilling is subtracted from the value given in each plot).*

The good agreement is confirmed by the earth pressure distribution in Fig. 125. Here, very reliable numerical results are obtained over the whole rotation range, even where the numerical model failed to predict the earth pressure distribution for the dense sample.

Therefore, this result generally refutes the previous hypothesis on the necessity of modelling the initial plastic deviatoric strain and the possible inability of the constitutive model to reproduce consecutive loading and unloading cycles correctly. Nevertheless, these aspects may have a more significant influence on denser samples. To verify that, additional tests should be performed.

7.3 Three-dimensional numerical limit state

Determining the limit load acting on a single wall section constitutes a three-dimensional problem, as the stress is partially redistributed on neighbouring, intact sections when the damaged section collapses. While no reason should prevent the numerical model presented in the previous sections from correctly capturing the wall unloading process of a single damaged section, emphasis is put here on the limit state solution since the possible reduction of the limit load for three-dimensional unloading conditions is one of the objectives of interest of the present work. The Optum G3 [155] computer program is employed to pursue that objective. The geometry and kinematics of tests C7D3d and C8L3d are simulated assuming the peak and residual shear strength of Perth Sand.
The obtained values are compared to the experimental results in Tab. 9. The residual value measured in the test on the loose sample (C8L3d) is assumed as the residual value in the table. Numerical and experimental values agree well. In this case, the limit analysis solution provides a safe estimate of the limit state of the dense sample at peak resistance. However, as it was noted earlier, it is generally not safe to assume that the whole backfill mobilises the peak shear strength $\varphi = \varphi_{\text{peak}}$ simultaneously.

Tab. 9: *Moment at limit state assuming peak and residual friction angle of Perth Sand.*

	$\varphi = \varphi_{\text{peak}}$	$\varphi = \varphi_{\text{res}}$
Experiment	0.05	0.13
Numerical	0.07	0.13

The numerical failure mechanisms are shown in Fig. 126 and Fig. 127. As expected, the failure mechanism formed in the dense specimen has a smaller volume than in the loose specimen. In the vertical plane cutting the mechanism in the middle perpendicular to the longitudinal wall direction, the failure mechanism is very close in form to the wedge considered for the plane strain case. However, close to the damaged wall section's sides, the mechanism shows a pronounced curvature, especially in the horizontal plane (see Fig. 126b and Fig. 127b).

The extension in the middle of the mechanism measured at the soil surface (see Fig. 126b and Fig. 127b) is comparatively smaller in the numerical results than in the experiments (Fig. 103), especially for the loose sample. This discrepancy arises because the numerical, limit-analysis-based solution assumes the associated flow rule.

| (a) | (b) |
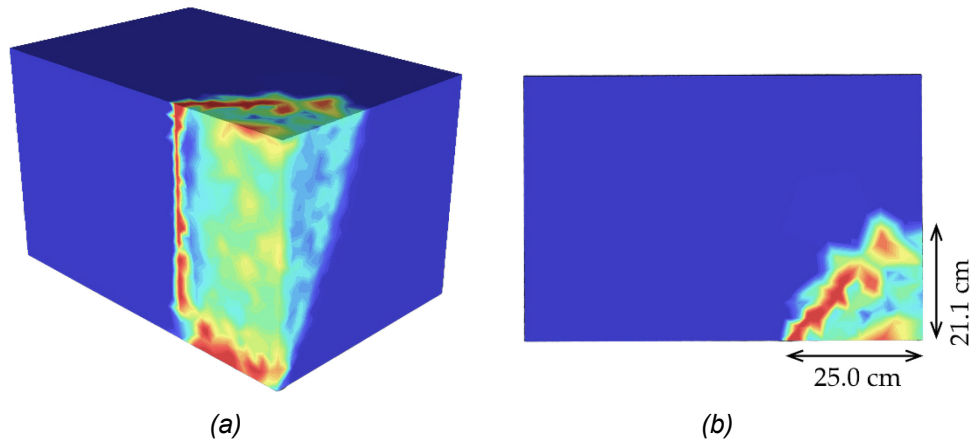
Fig. 126: *Three-dimensional failure mechanism in loose sand represented by the rate of work of the deviatoric stress: (a) isometric view; (b) top view.*

| (a) | (b) |
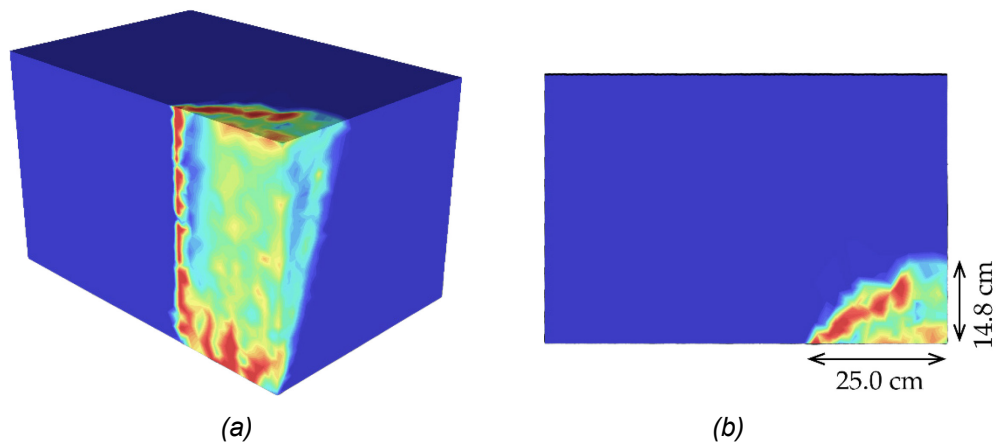
Fig. 127: *Three-dimensional failure mechanism in dense sand represented by the rate of work of the deviatoric stress: (a) isometric view; (b) top view.*

The influence of the flow associativity on the three-dimensional limit state can be investigated by running finite-element-based elastoplastic simulations.

A fictitious, rigid wall is considered in the following. Narrow sections with a height-to-width ratio of two ($h/b = 2$) are modelled to emphasise the possible effects of flow associativity. The backfill is assumed to be a weak frictional soil, characterised by $\varphi = 30°$. The soil is modelled as linear elastic, perfect plastic, as only the limit load is sought. When assuming nonassociated flow, the dilatancy is set to $\psi = \varphi/2$. The wall friction is $\delta = 20°$.

Modelling the three-dimensional boundary value problem using a Lagrangian mesh poses additional challenges. Indeed, if the backfill is modelled as a single body, the mesh gets distorted in correspondence with the edges of the damaged and intact wall sections because of the abrupt difference in the kinematic boundary conditions. Furthermore, and even more importantly for the accuracy of the results, the contact between the soil and wall is partially lost, as observed in Fig. 128a (highlighted by a white rectangle). This inaccurate

deformation further leads to unrealistic high stresses developed on the edge of the undamaged wall section. These problems can be overcome by separating the backfill into two parts by a vertical plane passing through the point of union of the two walls and perpendicular to the longitudinal wall direction. The two bodies created are successively tied along the entire contact plane except for the two rows of elements immediately behind the retaining wall. There, instead, a frictional interface is modelled that has friction coefficient $\mu = \tan \varphi_{\text{soil}}$ and allowing a relative displacement between nodes. Fig. 128b shows that this approach mitigates the problems observed in Fig. 128a and allows employing a Lagrangian mesh to solve the boundary value problem considered in this section.

(a)   (b)
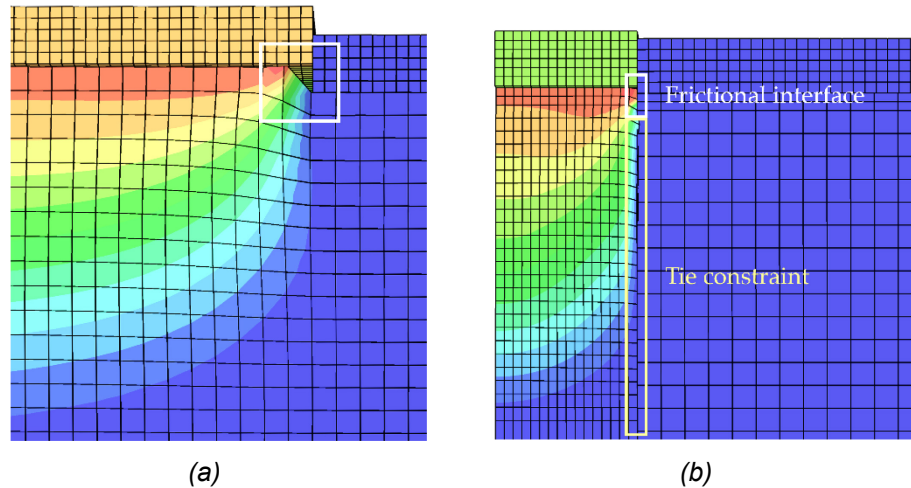
Fig. 128: *Top view of the finite-element model illustrating the mesh deformation for two different modelling techniques of the backfill. (a) Modelling of the whole backfill as a single body; (b) modelling of the backfill as two entities tied together along the vertical contact plane except for the last two elements close to the wall, where a frictional interface is modelled.*

The normalised, resulting moment-rotation response is plotted in Fig. 129. The limit analysis solution (computed using the Optum G3 software [155]) is 0.18. It is observed how both solutions based on the associated (AFR) and nonassociated flow rule (NAFR) are slightly lower than the limit analysis solution. Only a tiny difference is observed between the AFR and NAFR solutions, with the latter being marginally higher. The moment increase on the undamaged, neighbouring sections is plotted in the same graph. An increase of about 25% is measured; no significant difference is observed between the NAFR and AFR. This value is consistent with the values measured in the experiments, considering that narrow wall sections and a lower soil strength are considered here.
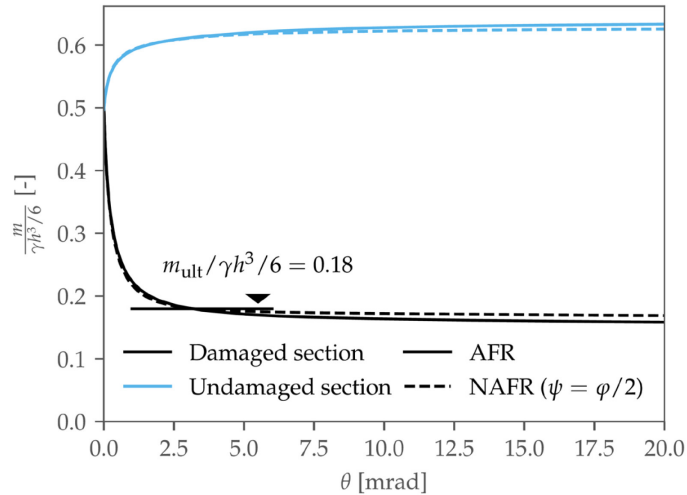
Fig. 129: *Moment-rotation response of a single damaged wall section and its neighbouring sections.*

The obtained failure mechanisms are depicted in Fig. 130. The soil forming the failure mechanism is isolated by the rest of the backfill (shown in transparency) by setting a lower threshold for the deviatoric plastic strain. It is observed how the nonassociated flow rule generates a failure mechanism having a larger volume. This is only possible as the considered boundary value problem does not impose any constraint on the extension of the failure mechanism. As a result, the limit load is not sensitive to the dilatancy angle. Therefore, as in Section 3, the limit analysis solution produces a reasonable estimate of the actual limit load, provided that the soil strength is determined correctly.

(a)   (b)
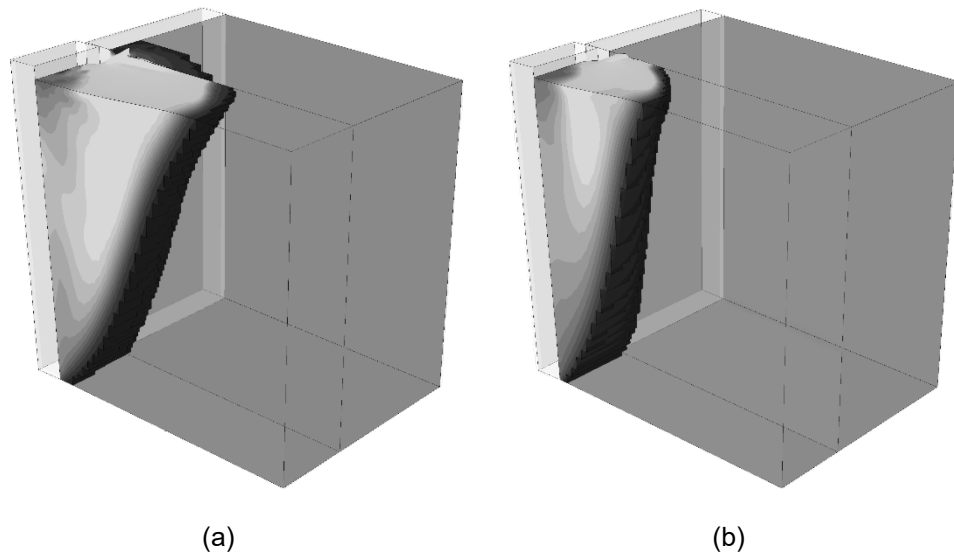
Fig. 130: *Three-dimensional failure developed behind a fictitious wall assuming: (a) the nonassociated flow rule and (b) the associated flow rule: (a) $\varphi = 30°$, $\psi = 15°$; (b) $\varphi = 30°$, $\psi = 30°$.*

7.4   Conclusions and recommendations for the practice

A procedure for simulating the earth pressure exerted on damaged cantilever retaining walls was presented. It is based on a finite-element model of the wall and its backfill and requires knowledge of the stress state of the soil under service conditions. The latter can be obtained through numerical analyses (as in the following section) or assumptions based

on experience. Direct measurements (as were available in this work) are usually unavailable and, in general, difficult to obtain in the field. The employed constitutive law is based on pressure-dependent isotropic elasticity and the Mohr-Coulomb failure criterion. A custom hardening rule was employed based on experimental data from Appendix II.2. Alternatively, the hardening rule of the Hardening Soil model [141] could be assumed for approximate results. In addition, a simple regularisation rule is applied in the samples that exhibit softening behaviour showing good results.

The obtained numerical soil response was compared to the experimental results. The uncompacted samples showed excellent agreement, both in terms of stress and deformations. In the uncompacted samples, soil failure propagates from top to bottom. The accuracy of the limit analysis solution was also confirmed in this section by comparing it to the experimental and numerical results. It was observed that the limit load obtained by the solutions proposed in Section 3.3 provides a good, conservative estimate of the limit load at the residual state. Instead, a slightly unconservative result was obtained when estimating the minimal bending moment induced by earth pressure assuming the peak friction angle. Indeed, the state where the whole backfill mobilises the peak strength contemporarily does not exist. On the other hand, it was confirmed that the limit load obtained assuming the nonassociated flow rule overestimates the moment, as the friction angle was calibrated using the conventional geotechnical method (see Section 3.5.1).

The numerical simulation of the compacted tests also showed good agreement with the experimental data. Only in the dense sample a slight underestimation of the moment and earth pressure in the hardening regime was observed. The reason is presumably that the test soil was deposited at (almost) its maximum density, which decreased due to shearing during the compaction procedure. However, the proposed constitutive model only considers the soil density as a constant throughout the analysis.

Therefore, it is concluded that the proposed numerical model can be employed for reliable estimations of the earth pressure exerted on damaged walls. A rate-and-state model could be assumed to reproduce the stick-slip effect observed in the experiments. However, the wall should always be able to find an equilibrium state along the lower envelope of the moment-rotation curve, as the period of the oscillations is small.

In the second part of the section, the three-dimensional limit state was analysed using the OptumG3 software. Good agreement with the experimental results was shown, although the dimensions of the failure mechanism did not match perfectly due to the implicit assumption of the associated flow rule in limit analysis. The influence of the flow associativity was then investigated by using the finite element method and a simple linear elastic, perfect plastic constitutive law. It was shown that the associativity of flow does not influence the results as the shear strength of the soil was backcalculated assuming a limit analysis solution to the limit load measured in an element test. The reason is that the problem is not kinematically constrained. However, if the mesh in a finite element simulation is fine enough, the deformation would be localised in thin shear bands, leading to an increased limit load. In this case, however, the soil strength calibration should also consider strain localisation.
Furthermore, the challenges encountered in modelling three-dimensional conditions were shown, and possible countermeasures were proposed.

Recommendations for the practice

The unloading response of a wall backfill can be quantified using commercial finite-element codes, such as Abaqus or Plaxis. While a custom material model is needed for Abaqus, Plaxis' implementation of the hardening soil model can be easily used. The hardening soil model [141] allows pretty accurate modelling of soil hardening behaviour, while it does not allow modelling soil softening, commonly observed in dense soil. However, to verify cantilever retaining walls, the accurate modelling of the hardening phase is much more critical, as corroded walls generally do not have sufficient rotation capacity [3] for the soil to reach the softening phase. Also, as shown in this work, softening always implies mesh dependency, which, if not addressed correctly, can lead to erroneous results.
Consequently, the engineer should neglect the peak strength of dense soil and calibrate

the constitutive law only considering the residual state, as in Fig. 131a, which shows the calibration of the stress-strain response of a dense and loose granular material truncated at the residual strength. It is noted that the different compliance of the two probes is considered (the sand sample being stiffer) before reaching the residual state. Fig. 131a represents the most conservative calibration.

However, in particular cases, a higher strength than the residual can be considered, provided that the stress state at *each* point stays below the peak strength of the material. The calibration of Fig. 131b would result. In that case, the engineer must verify and demonstrate that the peak deviatoric stress is reached nowhere in the model. Otherwise, the model delivers incorrect results, and the engineer obtains an unsafe estimate.

The calibration procedure consists of fitting the hardening rule to the triaxial data, as shown in Appendix III.2.

(a)   (b)
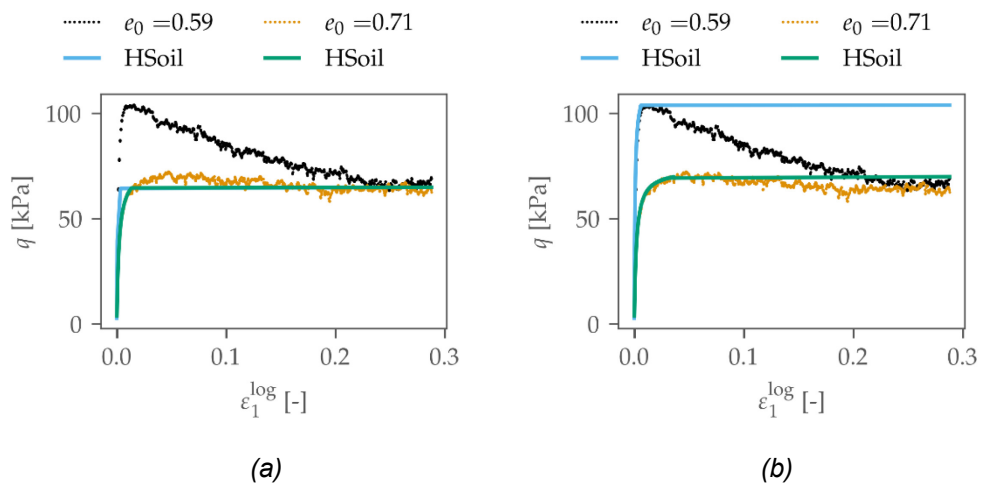
Fig. 131: *Calibration of the Hardening Soil model implemented in Plaxis [148]: (a) considering the residual strength; (b) considering the peak strength.*

After correctly calibrating the constitutive law, the backfill unloading response can be simulated using a model similar to that presented in Section 7.2.1. the initial stress state is either initialised in the model (based on some assumptions) or is directly computed by simulating the construction stages (as in Section 8).

Possibly, the model of Section 7.2.1 could be extended by adding a foundation layer, although its influence on the unloading process is negligible.

Lastly, it is worth noting that the constitutive model was calibrated through biaxial tests in this work. It was shown in Appendix II.2.2 that the soil strength is higher under plane strain conditions, meaning that a calibration through triaxial tests potentially leads to a more conservative moment-rotation response.

8   Numerical analysis: initial stress conditions

The initial stress state in a wall backfill depends on multiple factors, such as the soil properties, the filling procedure, and the wall's properties (e.g. its bending stiffness and interface friction).

In analysing the problem of walls deteriorated by corrosion, the *initial stress state* denotes the stress state acting in the backfill when the wall integrity starts worsening, which is assumed to take place a long time after the construction and backfilling of the wall. During the wall lifetime, therefore, this stress state could be modified by external actions (e.g. because of traffic loads). However, the consideration of additional external influences is not part of this work and will be neglected. It would be possible to include additional effects based on the results obtained in this section.

This section is divided into three parts. First, a study of the earth pressure at rest at a particle level is carried out. Then, the obtained results are integrated into the previous section's constitutive model. Finally, finite element simulations are performed using the improved constitutive model and validated against the wall test results.

8.1   Particle-scale study of the earth pressure at rest

This section summarises the results of the particle-scale study conducted in [9]. Virtual oedometer tests were performed using the LS-DEM to study the earth pressure at rest. LS-DEM has established itself as an extremely valuable tool to perform element tests on real soil, thanks to its formulation that allows consideration of real grain shapes.

Fig. 132 shows the evolution of K_0 in two Perth sand samples as a function of the applied vertical stress. Both samples show a similar trend. Only a slight decrease in K_0 is observed during virgin loading, especially at lower stress values, while a greater increase is observed during unloading. Reloading causes an almost immediate drop to lower values, followed by a slower convergence to the value recorded before unloading. For practical purposes, it is generally safe to assume K_0 to be constant for a normally consolidated granular material, as was observed by Gao and Wang [156].
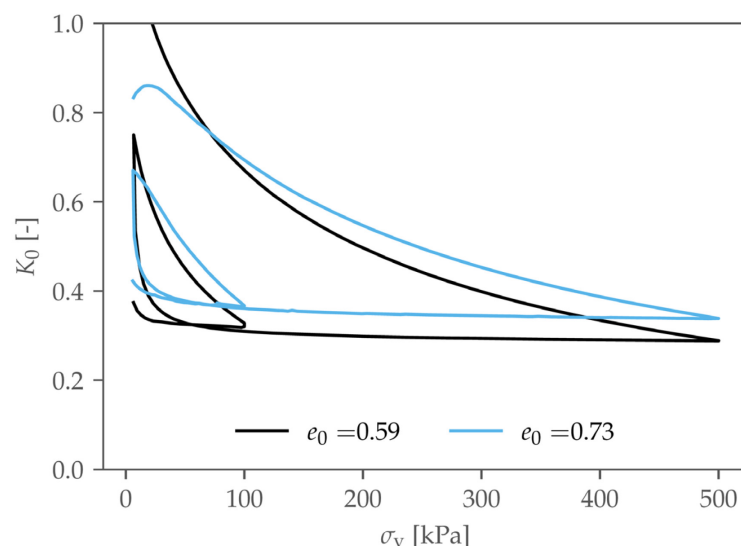

Fig. 132: *Coefficient of lateral earth pressure at rest K_0 as a function of the applied axial stress for a dense and loose sample.*

It is observed that $K_{0,\mathrm{nc}}$, the value measured during virgin loading, is lower in the dense sample than in the loose one. Gu et al. [59] explained this difference by the different number

of contacts per particle (i.e. the coordination number) of the two samples. In Fig. 133a, K_0 is plotted as a function of the coordination number. The roots of this explanation are both probabilistic and geometric: having a higher coordination number means a denser contact network, making it more likely to have stronger vertical force chains carrying the applied load resulting in lower lateral pressure. It follows that the orientation of the contacts is also a governing factor for K_0, which depends on the grain shape and the loading direction. On the other hand, the dense sample shows a steeper increase of K_0 during unloading.
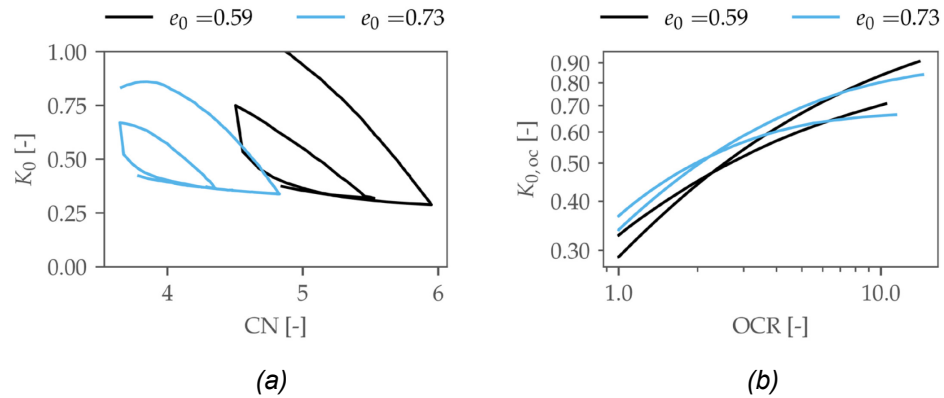
Fig. 133: *Coefficient of lateral earth pressure at rest K_0 measured in: (a) the loading and unloading phase, plotted as a function of the coordination number; (b) the unloading phase, plotted as a function of the overconsolidation ratio using a double logarithmic scale.*

A power law is often assumed to approximate the coefficient of earth pressure at rest of an overconsolidated material as a function of the overconsolidation ratio (OCR) (Equation (2.23)). Fig. 133b shows K_0 for the two tests in Fig. 132 during the two unloading phases in a double logarithmic scale. The dataset is truncated at $\mathrm{OCR} = 15$, as the fitted function diverges for higher values. It is observed that the plotted data does not precisely follow a power law (in fact, the lines are curved). However, a power law can provide a satisfactory approximation of K_0, especially at lower OCR values. It is further observed that the inclination, i.e. the exponent in Equation (2.23), of the K_0-OCR lines depends on the maximum vertical stress (i.e. the stress measured at the beginning of the unloading phase).
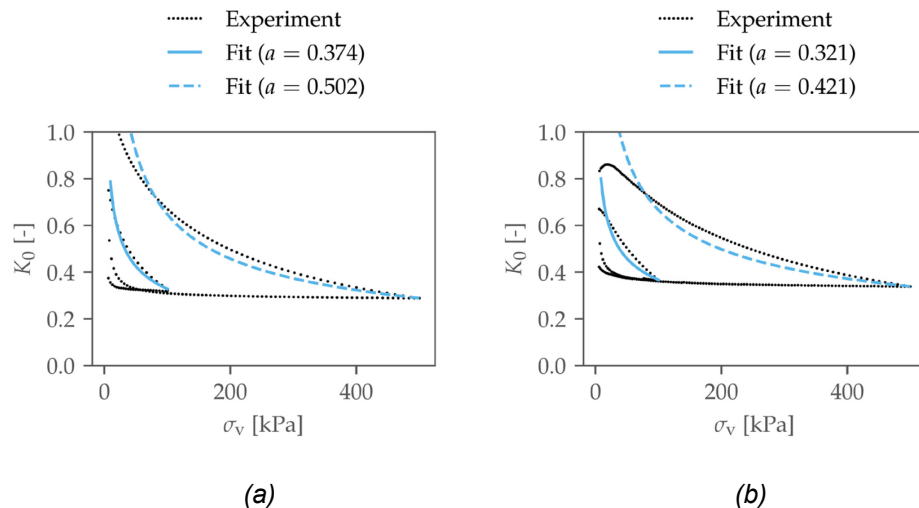
Fig. 134: *Coefficient of lateral earth pressure at rest K_0 as a function of the applied axial stress for a dense (a) and loose (b) sample and power law fit.*

The fitted $K_{0,oc}$-OCR lines are plotted for the two samples in Fig. 134. The fitted exponent for each unloading is given in the legend. It is again observed that the exponent depends

on the stress level at which unloading occurs. A difference of about 0.1 is observed between the exponent fitting the unloading starting at 100 kPa and the one starting at 500 kPa. In the remaining of this section, the average of the two exponents will be considered.

The coefficient of earth pressure at rest during virgin compression, $K_{0,\mathrm{nc}}$, and exponent a are summarised in Tab. 10 for a dense and loose initial configuration. These values are averaged over the whole stress range. Additionally, $K_{0,\mathrm{nc}}$ at a stress level $p = 4\,\mathrm{kPa}$ is given in the same table. This value should be close to that observed in the laboratory wall experiments.

Tab. 10: *Characterisation of the earth pressure at rest for Perth Sand.*

	$K_{0,\mathrm{nc}}$ [-]		a [-]
	average	at $p = 4\,\mathrm{kPa}$	average
Dense	0.307	0.374	0.438
Loose	0.356	0.422	0.371

The fitted exponents agree well with the value indicated by Talesnick et al. [57]. Instead, Mayne and Kulhawy's [54] empirical formula assuming $a \approx \sin\varphi$ would fit the data poorly. Assuming $\varphi_{\mathrm{res}} \approx 34°$, the exponent would be $a = 0.56$. If $\varphi_{\mathrm{max}} \approx 42°$ would be assumed instead for the dense sample, the exponent would be $a = 0.67$. Both possibilities clearly overestimate the exponent.

Nevertheless, the experimental data shows a qualitative inverse correlation between the peak friction angle of a sample and the K_0 related quantities. From the viewpoint of the plasticity theory, it is incorrect to relate the stress state at rest (i.e. a stress state below yielding in shearing) to the material strength. However, the same micromechanical parameters may be tied to both the soil strength and the stress state at rest. This is investigated in a parametric study in the next section.

8.1.1   Investigation into the controlling parameters

Virtual oedometer tests were run on the same Perth sand specimens, varying the contact parameters one at a time, i.e. the normal contact stiffness and the interparticle friction coefficient. The tangential stiffness is varied together with the normal stiffness by keeping a constant ratio $k_t/k_n = 0.9$. The variation of the contact stiffness within a meaningful range (i.e. $k_t/k_n \in [0.7, 0.9]$) showed a negligible influence on both the stress-strain response and on K_0.

At the same time, triaxial tests can be run to determine the influence of the micromechanical properties on the soil bulk stiffness, strength, and Poisson's ratio. By combining the results of oedometer and triaxial tests, it is possible to investigate correlations between the earth pressure at rest and elastoplastic macroscopic quantities.

All triaxial tests are run on isotropically consolidated samples at a mean stress level of $p_0 = 25\,\mathrm{kPa}$. It must be noted that the elastic parameters (i.e. the Young's modulus and the Poisson's ratio) are pressure-dependent [9]. However, this does not impede the observation of possible trends, as all triaxial tests were performed at the same stress level (i.e. normalisation would just scale the data).

The obtained results are plotted in Fig. 135-Fig. 138. Circular markers represent the results obtained by varying the interparticle friction, while triangles represent different contact stiffnesses. Black represents dense and blue loose samples.
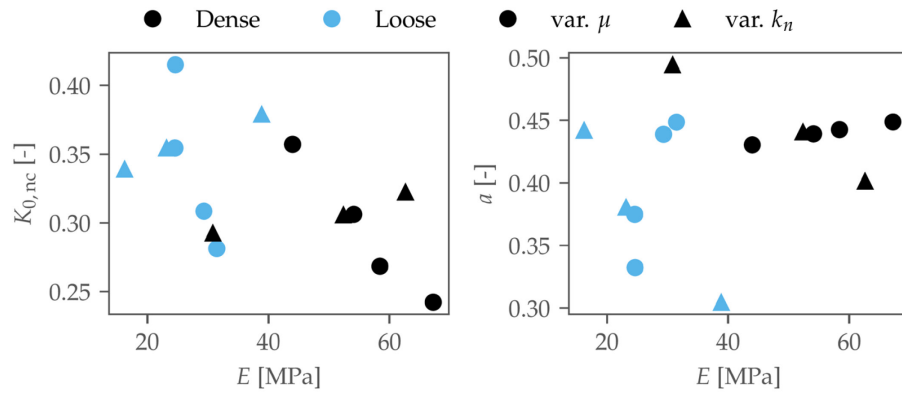
Fig. 135: *Earth pressure at rest's parameters $K_{0,\text{nc}}$ and a as a function of the sample's Young's modulus.*

No trend is observed between $K_{0,\text{nc}}$ and a and the Young's modulus (Fig. 135). Indeed, the two sets of results {var. μ, var. k_n} representing the dense and loose samples intersect almost perpendicularly (especially in the case of $K_{0,\text{nc}}$). In fact, as μ increases, $K_{0,\text{nc}}$ decreases, but the Young's modulus barely changes. The same conclusion holds for a.
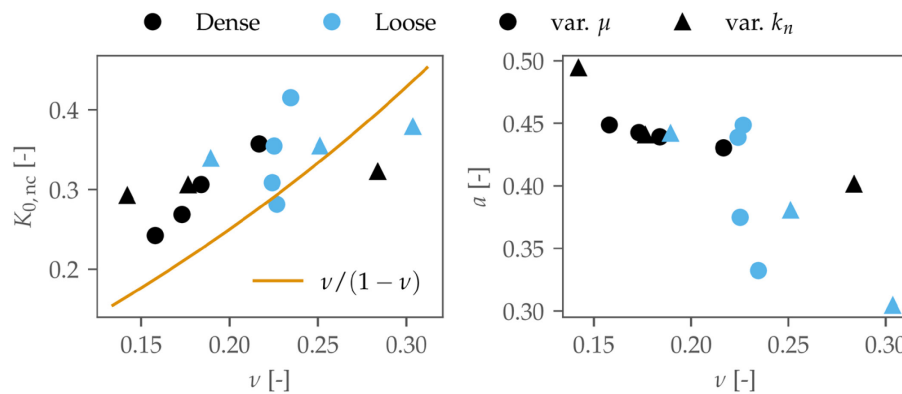
Fig. 136: *Earth pressure at rest's parameters $K_{0,\text{nc}}$ and a as a function of the sample's Poisson's ratio.*

A similar observation is made in Fig. 136, where the dependence on the Poisson's ratio is shown. Also in this case, a change in μ in the loose sample does not influence the resulting Poisson's ratio, while it has an inverse correlation with $K_{0,\text{nc}}$. The elastic solution (2.20) is plotted in Fig. 136. It can be seen how it provides an unsafe estimate for K_0 during virgin loading. Therefore, its use for estimating K_0 of normally consolidated granular soil should be discouraged, also because of the previous observation.
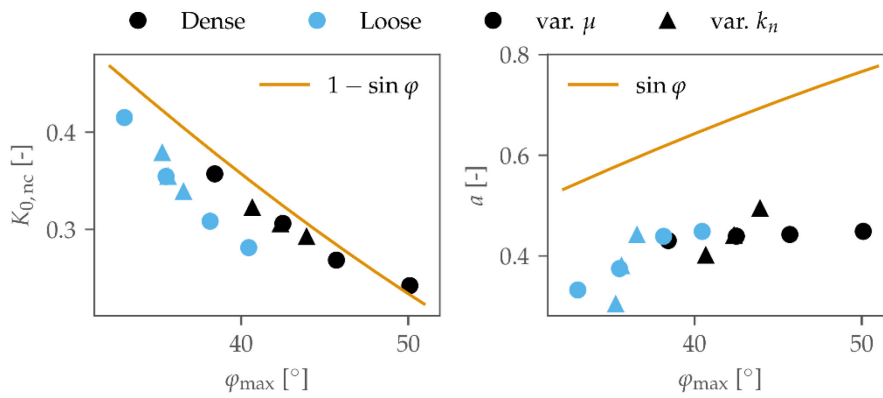
Fig. 137: *Earth pressure at rest's parameters $K_{0,nc}$ and a as a function of the sample's peak shear strength.*

Fig. 137 shows that the $K_{0,nc}$ data sets for the loose and dense sample lie on a line if plotted against the peak shear strength, implying a good correlation. It must be immediately noted that this does not imply causation but rather that the same micromechanical parameters influence both $K_{0,nc}$ and φ_{max}. Indeed, causation has been disproved in theory [52]. Nevertheless, Jáky's modified Equation (2.22) is plotted assuming $\varphi = \varphi_{max}$ in Fig. 137. It is observed that it provides a reasonable safe estimate of $K_{0,nc}$ for the dense sample, while it overpredicts with a larger margin the data on the loose specimen.

The exponent a, instead, shows a slightly more chaotic trend. Mayne and Kulhawy's [54] prediction is plotted as well, confirming the overprediction of the exponent.
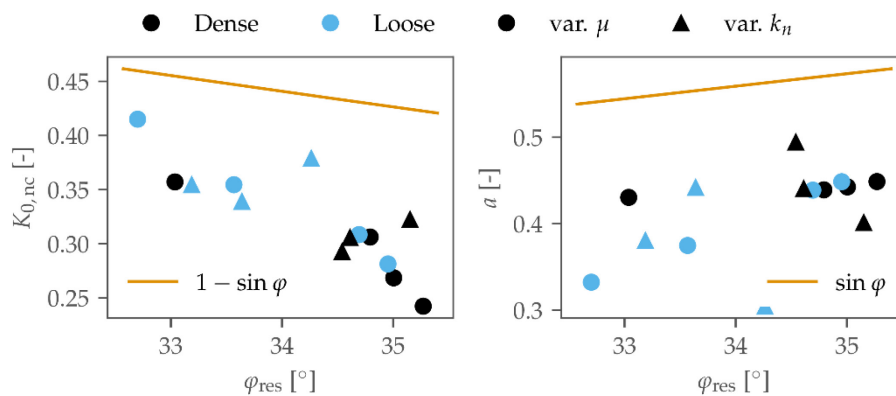
Fig. 138: *Earth pressure at rest's parameters $K_{0,nc}$ and a as a function of the sample's residual shear strength.*

$K_{0,nc}$ is then plotted against φ_{res} in Fig. 138. Here, it must be noted that the residual strength of a sample is not very sensitive to the varied parameters (i.e. the contact stiffness and friction), as the obtained values of φ_{res} are contained in the tiny range [32.5°, 35°]. This reason alone discards φ_{res} as a good parameter to correlate with $K_{0,nc}$ and a, as they have shown a good sensitivity on those two micromechanical parameters.

Nevertheless, Jáky's and Mayne and Kulhawy's solutions are plotted, showing an overprediction of both parameters.

8.2 Constitutive modelling

8.2.1 Constitutive law

The constitutive model presented in Section 7.1.1 is extended here to include a so-called "cap", allowing the accurate modelling of soil consolidation. Among the most famous cap models are the Modified Cam Clay [157] and the Hardening Soil model [158]. Two requirements must be satisfied by a good cap model:

1. it must not develop deviatoric strain in a material loaded isotropically, and
2. it should provide an accurate prediction of K_0 in a one-dimensional consolidation.

While item 1 is satisfied by both cited cap models, only the cap of the Hardening Soil model satisfies item 2. Indeed, Modified Cam Clay's K_0-coefficient is given by the yield surface formulation and is a function of the soil residual shear strength (see, e.g., [147]). Instead, K_0 is a free parameter in the Hardening Soil model.

The present work adopts a cap satisfying both requirements but having a slightly simpler formulation than Hardening Soil's. In the triaxial stress space, the yield surface is described by the vertical line

$$Y_{\text{cap}}: \quad p - p_c(\varepsilon_{\text{vol}}^p) = 0. \tag{8.1}$$

The hardening rule is based on observations made in the laboratory (oedometer tests, see Appendix II.1) and reads:

$$p_c(\varepsilon_{\text{vol}}^p) = \left[\frac{1 + e_0}{\lambda - \kappa}\varepsilon_{\text{vol}}^p\right]^{1/\alpha}. \tag{8.2}$$

The full derivation can be found in [9]. It is noted that the parameters κ and λ must be determined under the same assumption $p_{\text{ref}} = 1$. Otherwise, p_{ref} must also be considered in the hardening rule.
The flow on the cap is nonassociated. The plastic strain increments are defined as:

$$\begin{Bmatrix} \mathrm{d}\varepsilon_{\text{vol}}^p \\ \mathrm{d}\varepsilon_{\text{dev}}^p \end{Bmatrix} = \begin{Bmatrix} \dfrac{\mathrm{d}p}{K^{\text{p}}(p)} \\ \dfrac{\mathrm{d}q}{3G^{\text{p}}(p)} \end{Bmatrix} \tag{8.3}$$

where K^{p} and G^{p} are material parameters defined based on Equations (II.19) and (II.20) in Appendix II and are denoted by the exponent p to distinguish them from the elastic properties. Assuming $p_{\text{ref}} = 1$, it is

$$K^{\text{p}}(p) = \frac{1 + e_0}{\alpha(\lambda - \kappa)}(\text{p})^{1-\alpha} \tag{8.4}$$

where the exponent α, λ, and κ were defined in Equations (II.17) and (II.19) in Appendix II. The parameter $G^{\text{p}}(p)$ can be expressed as a function of $K^{\text{p}}(p)$ and the coefficient of earth pressure at rest, as shown later.
Noting that during plastic loading $p = p_c$, the consistency condition is satisfied by the cap model:

$$\begin{aligned} \mathrm{d}Y &= \mathrm{d}p - \frac{\partial p_c}{\partial \varepsilon_{\text{vol}}^{\text{p}}}\mathrm{d}\varepsilon_{\text{vol}}^{\text{p}} \\ &= \mathrm{d}p - \frac{1}{\alpha}\frac{1 + e_0}{\lambda - \kappa}p_c^{1-\alpha} \cdot \alpha\frac{\lambda - \kappa}{1 + e_0}p_c^{\alpha-1}\,\mathrm{d}p = 0 \end{aligned} \tag{8.5}$$

The advantage of the presented cap is that it is straightforward to implement for numerical computations. In the triaxial stress space, its elastoplastic response is given by

$$\begin{Bmatrix} d\varepsilon_{\text{vol}} \\ d\varepsilon_{\text{dev}} \end{Bmatrix} = \begin{bmatrix} \dfrac{1}{K^{\text{ep}}(p)} & 0 \\ 0 & \dfrac{1}{3G^{\text{ep}}(p)} \end{bmatrix} \begin{Bmatrix} dp \\ dq \end{Bmatrix} \tag{8.6}$$

This formulation is similar to that of isotropic elastic material.

The elastoplastic bulk modulus is defined as

$$K^{\text{ep}}(p) = \frac{1 + e_0}{\lambda\alpha}(p)^{1-\alpha} \tag{8.7}$$

and the elastoplastic shear modulus

$$G^{\text{ep}}(p) = \frac{3}{2}\frac{1 - K_0}{1 + 2K_0}K^{\text{ep}}(p), \tag{8.8}$$

where the exponent α, λ, and κ were defined in Equations (II.17) and (II.19) in Appendix II, and K_0 is the coefficient of earth pressure at rest during normal consolidation. Equation (8.8) ensure the fulfilment of the second requirement listed above.

The implementation of the constitutive law presented in Section 7.1.1 for the Abaqus finite element software is extended to consider the cap. A similar cap implementation was first used by Lampach [159].

8.2.2 Calibration of the constitutive law

The cap model is calibrated using the results of the oedometer tests presented in Appendices II.1 and II.2. The parameters are summarised in Tab. 11.

Tab. 11: *Constitutive parameters used to model volumetric yielding with the cap model. The given values are reference values calculated at* $p = 25\,kPa$.

	K^{ep}	G^{ep}	K_0	E^{e}	ν^{e}
Dense	17.3 MPa	11.1 MPa	0.307	53.8 MPa	0.18
Loose	16.1 MPa	9.1 MPa	0.356	43.2 MPa	0.21

Comparing the elastic Young's moduli to those determined in the triaxial tests and given in Tab. 5 in Appendix II.2, it is noted that the values obtained for the dense sample agree well. At the same time, a divergence is observed in the loose specimen, with the modulus based on the triaxial test being lower than that based on the oedometer. As explained in [9], the stiffness obtained from the triaxial test refers to the initial phase of the virgin loading of a normally consolidated sample. Therefore, the stiffness derived from the triaxial test can be interpreted as the stiffness for primary loading, while that derived from the oedometer test as the proper elastic stiffness for unloading and reloading. Both parameters were defined by Schanz et al. [141]. If the stiffness derived in the triaxial test is considered, the hardening curve must take the same value into account, as was correctly done in Section 7.1.3.

The cap model described in the previous section and calibrated as in Tab. 11 is validated against experimental data in Fig. 139 and Fig. 140. The void ratio vs vertical stress data is taken from the laboratory tests, while the coefficient of lateral earth pressure K_0 was determined in LS-DEM simulations. Both samples show good agreement with experimental data. The stiffness of a normally consolidated and an overconsolidated sample can be modelled reasonably well, as well as the coefficient of earth pressure at rest for a normally consolidated soil. In the case of an overconsolidated sample, the cap model gives a good prediction of K_0 for dense soil. The loose sample shows a worse match with experimental data, although for OCR values less than 5, the prediction of the cap model is sufficiently precise.

Additionally, the fitted power law (Equation (2.23)) is plotted in Fig. 139 and Fig. 140 using the parameters summarised in Tab. 10. It is observed how the FEM results and the power law fit give similar predictions of K_0, suggesting that the exponent a in Equation (2.23) may be related to the Poisson's ratio ν.

(a) (b)
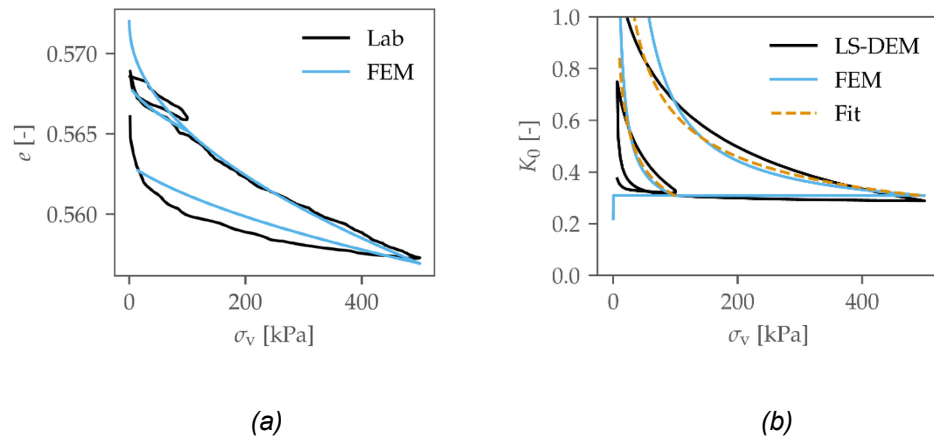
Fig. 139: *Validation of the constitutive law calibrated for dense Perth Sand against experimental data. (a) Void ratio plotted against the applied vertical stress (experimental results based on the laboratory tests), and (b) K_0 plotted against the applied vertical stress (experimental data based on the LS-DEM simulations).*

(a) (b)
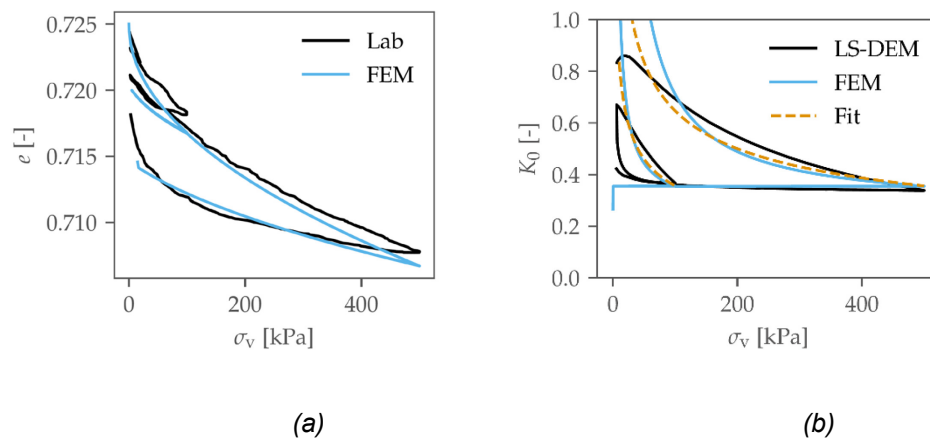
Fig. 140: *Validation of the constitutive law calibrated for loose Perth Sand against experimental data. (a) Void ratio plotted against the applied vertical stress (experimental results based on the laboratory tests), and (b) K_0 plotted against the applied vertical stress (experimental data based on the LS-DEM simulations).*

8.3 Study of the initial stress state in wall backfills

This section employs the developed finite element model to simulate the earth pressure in the staged backfill of the laboratory tests. The obtained results will be compared to the experimental results to validate the constitutive model proposed in the previous subsection.

8.3.1 Finite element model

The finite element model employed in this section is depicted in Fig. 141 and is similar to the model employed in the previous section. First, the soil is deposited layer by layer (the number of deposited layers varies to reflect the filling steps in the laboratory). In compacted tests, each layer is compacted after deposition by applying a static load to a steel, 10 cm wide plate lying on the soil. After the deposition and compaction of each layer, the pressure

acting on the wall is measured. Finally, a wall rotation is imposed at the stem toe and the evolution of the bending moment is monitored.
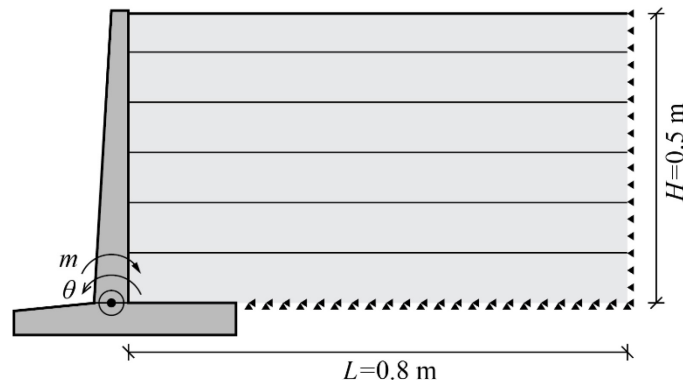
Fig. 141: *Numerical model employed for the simulation of the wall experiments.*

8.3.2 Results and discussions

Fig. 142 depicts the earth pressure measured after the deposition of each layer of the backfill in the experiment and the numerical simulation of a dense, uncompacted sample (test C2D). It is seen that the parameters in Tab. 11 lead to an underestimation of the earth pressure. The observed difference is likely caused by the deposition by pluviation carried out in the lab, as opposed to the static deposition simulated numerically (where gravity is ramped up in the activated layer). As was described by Cresswell et al. [130], the soil gets slightly compacted during pluviation, as an *energetic layer* forms close to the surface where the grain movement is predominantly horizontal. Unlike the compaction performed by applying a static load in tests C5Lc and C6Dc, the pluviation-induced compaction is homogeneous over the backfill surface and can therefore be simulated by an increased K_0. The effects of this compaction are also observed in Fig. 91, which shows an increased earth pressure coefficient close to the soil surface.

Further evidence of compaction is provided by the earth pressure measured in the second and third deposition layer Fig. 142, where the soil and wall deformation should be small enough to guarantee conditions close to those in a one-dimensional consolidation. Instead, the measured stress values are higher than e_0 calculated using the assumed K_0.
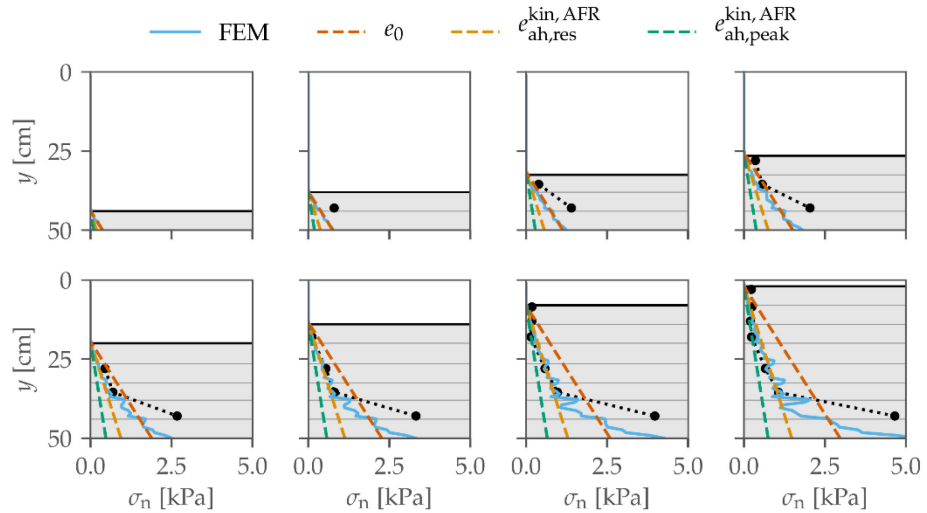
Fig. 142: *Earth pressure distribution on the wall during the backfilling phase in a dense uncompacted sample assuming K_0 from Tab. 11.*

Therefore, increased K_0-values are assumed for the loose and dense samples in the following. Specifically, $K_0^{\text{dense}} = 0.48$ is assumed for the dense sample, and $K_0^{\text{loose}} = 0.56$ for the loose sample. Those values are estimated from the experimental observations.

The resulting earth pressure for the dense sample is shown in Fig. 143. With the increased K_0-value, the model can reliably predict the experimentally observed stresses, although an even higher K_0 could have been assumed. Indeed, in the first three deposition steps, the experimental value is slightly higher than the numerical one.

Fig. 143: *Earth pressure distribution on the wall during the backfilling phase in a dense uncompacted sample assuming $K_0^{\text{dense}} = 0.48$.*

It is observed that the earth pressure is linearly distributed until the fourth deposition step. From that point on, the earth pressure assumes a bilinear distribution caused by the wall deflection and the soil deformation induced by the frictional interface. So, in the upper portion of the backfill, the earth pressure approaches the active value, although the wall displacement is insufficient to cause a mobilisation of the soil's peak strength. Instead, close to the wall toe, the earth pressure can exceed the earth pressure at rest.

While the effect of the wall displacement on the earth pressure distribution is intuitive, as it causes unloading, the impact of the frictional interface is less obvious.

The following analysis is performed to investigate the effects of the frictional interface on the stress distribution: a rigid wall is backfilled in six equally thick layers with a linear elastic (i.e. not plastic) material. The wall-backfill interface is frictional. These assumptions are made to avoid external influences on the observed behaviour and to investigate only the role of the frictional interface. Fig. 144 shows the displacement field observed at the end of the analysis. A nonsymmetric deformation is noticed by neglecting the displacement field for a moment and watching the backfill's outline. Close to the wall, the soil experiences less settlement than further away, where far-field conditions (characterised by a one-dimensional strain path) are approached. This happens as the frictional interface partially resists the backfill settlement caused by its self-weight and is shown by the vertical displacement field in Fig. 144a. In the horizontal direction, the upper portion of the backfill moves away from the wall (thus decreasing the horizontal stress). At the same time, the bottom part is pushed towards the wall, causing a stress increase (Fig. 144b). Therefore, this behaviour contributes to the nonlinear earth pressure distribution observed in Fig. 143.

(a)   *(b)*
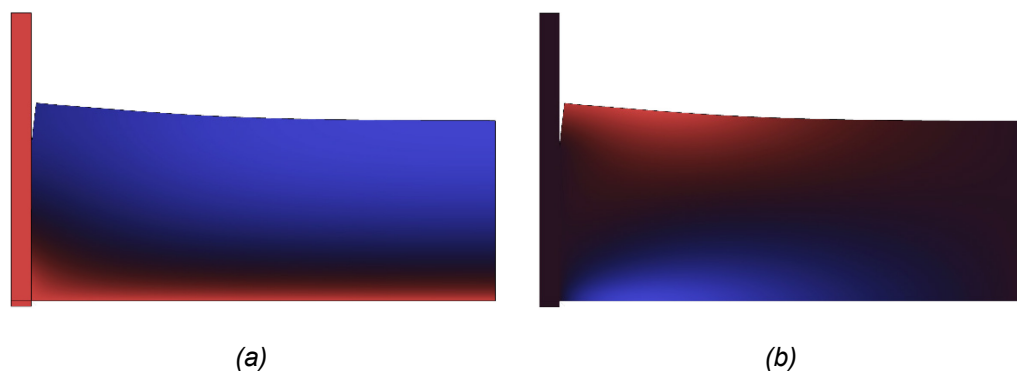
Fig. 144: *Displacement field of a (linear elastic) backfill deposited behind a rigid wall in 6 lays: (a) vertical displacement (red indicates zero, blue negative displacement); (b) horizontal displacement (red indicates positive, blue negative displacement). The rendered displacements are exaggerated by 500.*

The earth pressure coefficient obtained in test C2D and in the numerical simulation is plotted in Fig. 145. The blue curve represents the true ratio of the horizontal and vertical stress measured in the soil along the soil-wall interface. In contrast, the orange curve is the ratio between the horizontal stress and the overburden stress $\gamma \cdot y$. It is not necessarily the case that the two values coincide, as the vertical stress in the backfill is influenced by the wall friction (as was observed in [57]). However, the results show only a very small deviation between the two values, confirming that the earth pressure coefficient increases considerably in the lower part of the backfill. The plots further show that the earth pressure coefficient varies over the wall width starting from the first filling steps, although the earth pressure seemed to be nearly linearly distributed in Fig. 143. The behaviour explained with Fig. 144 is observed here. Indeed, starting from the first filling step, the earth pressure coefficient increases with depth and exceeds K_0 at the bottom. Interestingly, the earth pressure coefficient measured in the three bottom layers barely changes in the last four deposition steps.

Moreover, the experimental results show a high coefficient close to the surface. This is caused by the pluviation-induced compaction and possibly by an experimental error amplified at such low stress levels.

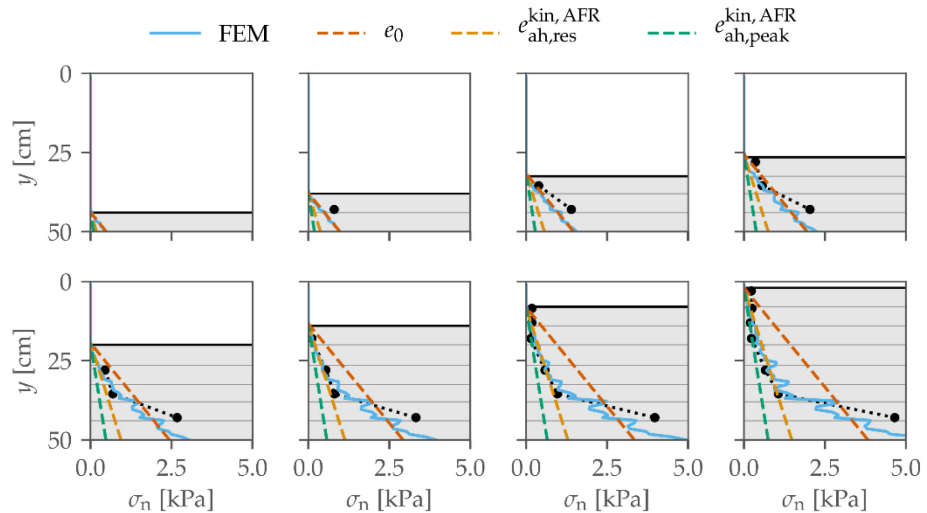***Fig. 145:*** *Coefficient of earth pressure measured during the backfilling phase in a dense uncompacted sample assuming $K_0^{\text{dense}} = 0.48$.*

It was remarked in Section 7.2.2 that plastic strain develops in the soil during backfilling due to the wall displacement, and the wall friction is mobilised as a result of the soil settlement caused by the incremental layer deposition. This is confirmed by Fig. 146, representing the normalised earth pressure and mobilised interface friction, as well as the cumulative deviatoric plastic strain at the end of the backfilling. Indeed, it is observed how the soil yields in the upper two thirds while the stress state in the lower region remains below yield, being more constrained by the wall and influenced by the behaviour of the whole backfill explained in Fig. 144.

Failure along the soil-wall interface occurs in the same region, except close to the soil surface, where the freshly deposited soil did not deform sufficiently to mobilise the friction fully.

However, by imposing a wall rotation at the end of the backfilling, it can be shown that after 1.5 mrad the deviatoric plastic strain and the mobilised wall friction angle are practically the same as for the simulation run in Section 7.2.2. Therefore, it is confirmed that the lack of initialisation of these two quantities hardly affects the results for an uncompacted sample.

In general, the results obtained in the unloading phase are very similar to those obtained in the previous section and are therefore not shown here.
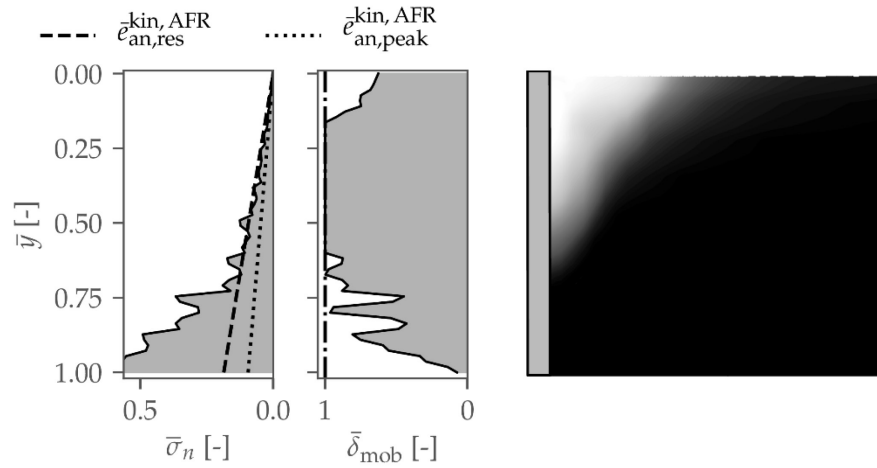
Fig. 146: *Qualitative representation of the contact pressure (left), the mobilised interface friction $\bar{\delta}_{\mathrm{mob}} = \tan \delta_{\mathrm{mob}} / \tan \delta_{\mathrm{wall}}$ (centre), and the cumulative deviatoric plastic strain at the end of the backfilling. The vertical coordinate is the normalised depth $\bar{y} = y/h_{\mathrm{wall}}$.*

The earth pressure and earth pressure coefficient obtained for a loose sample are plotted in Fig. 147 and Fig. 148 and compared to test C3L. The increased $K_0^{\mathrm{loose}} = 0.56$ was considered. The numerical data shows good agreement with the experiment. Similar observations as for the dense sample are made, leading to the same interpretations.

Initially, the horizontal pressure on the wall follows the earth pressure at rest quite closely. Then, as more material is deposited, the wall is deflected, and the soil deforms, resulting in partial unloading in the upper backfill. Due to the slower shear strength mobilisation of the looser soil, the earth pressure acting on the wall at the end of the backfilling phase is higher than in the dense sample.
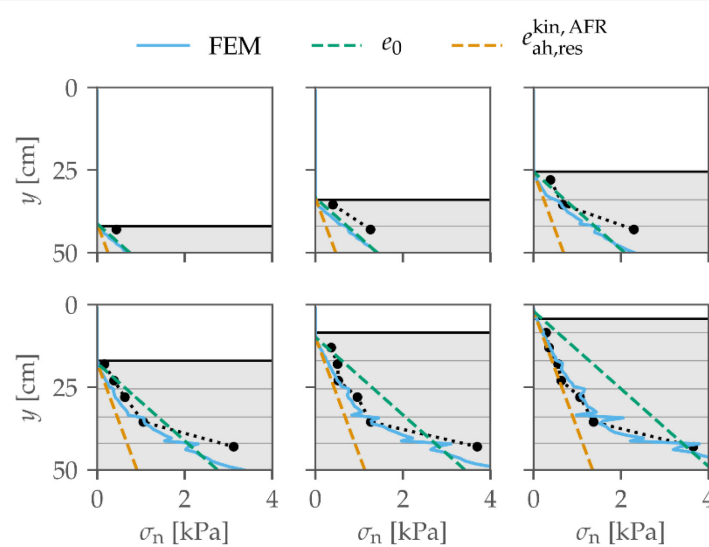
Fig. 147: *Earth pressure distribution on the wall during the backfilling phase in a loose uncompacted sample assuming $K_0^{\mathrm{loose}} = 0.56$.*
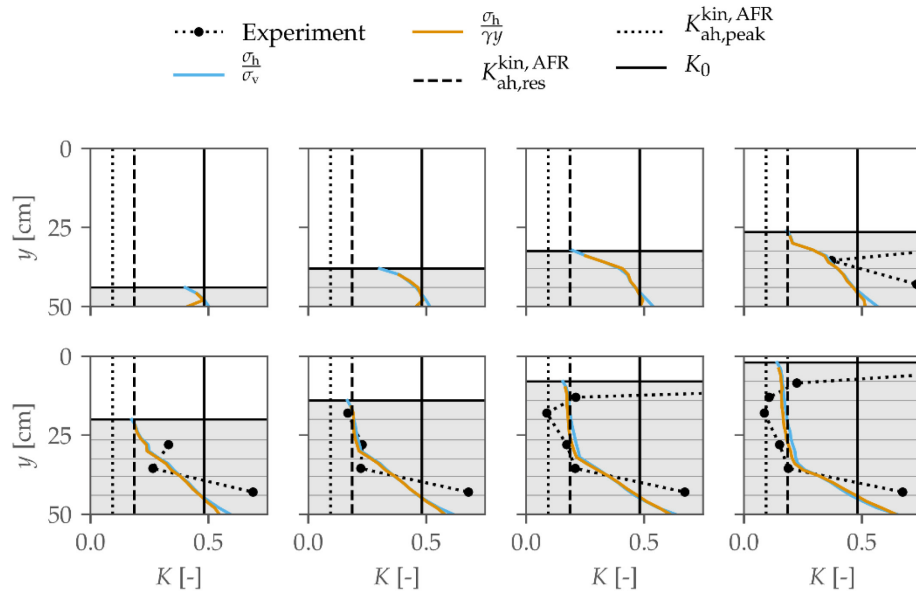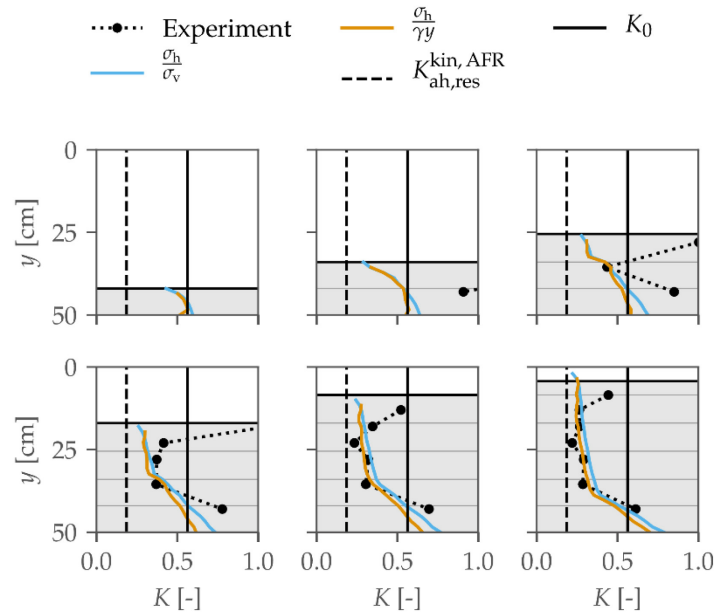
Fig. 148: *Coefficient of earth pressure measured during the backfilling phase in a loose uncompacted sample assuming $K_0^{\text{loose}} = 0.56$.*

The numerical earth pressure of the dense, compacted sample is plotted and compared to the experimental results in Fig. 149. Overall, a satisfactory agreement, although not perfect, is obtained. In the loose sample, the moment obtained by the estimated pressures is about 10% higher than the value observed in the laboratory, while an underestimation of about 12% is observed in the dense sample.

Very high horizontal stresses, close to the passive state, are developed during compaction in the vicinity of the compactor. When the compaction load is removed, a partial unloading occurs, leading to the pressure plotted in Fig. 149. For this reason, the highest pressures developed in the dense sample could be higher than in the loose one, as the peak strength of the former is higher than that of the latter. However, higher pressures also lead to higher deflections, causing the soil to unload. Because the unloading response of loose soil is more compliant, higher final stresses are measured than in dense soil.
After the first deposition phases, high earth pressures are measured, as the wall displacement is small. The steepest horizontal stress increase is observed near the surface, as the compactor has a vanishing influence with increasing depth. As more layers are deposited and compacted, the wall deflection increases, causing the unloading of the underlying layers. The experimental results illustrate this process very well, while the numerical data only shows little stress decrease. This leads to an overestimation of the earth pressure in the middle of the wall at the end of the backfilling. Instead, in the upper backfill part, the earth pressure is slightly underestimated. Similar observations are made in the loose sample, Fig. 150.
The reason for these inaccuracies is mainly to be ascribed to the FE model. Indeed, the layers are reactivated during the analysis according to the initial, undeformed geometry. However, due to the relatively high loads involved, the already deposited layers settle and deform, and the wall deflects, leading to inaccuracies. While the modelling choices made are common for solving static problems with the finite element method, a meshless method could be advantageous to model compaction-induced earth pressures.
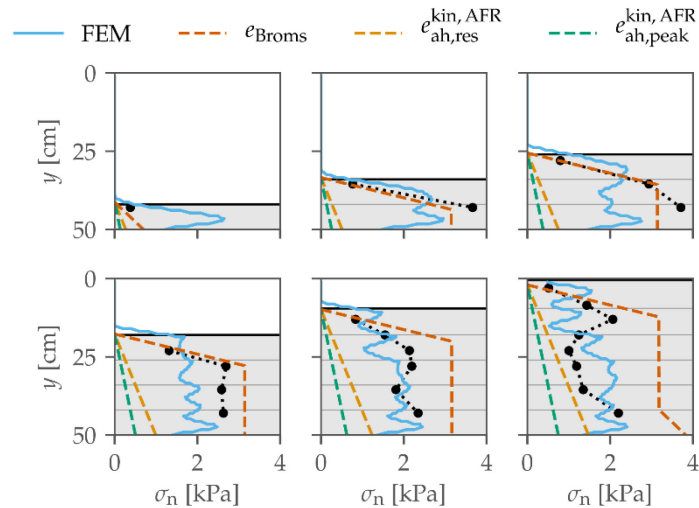
Fig. 149: *Earth pressure distribution on the wall during the backfilling phase in a dense compacted sample.*
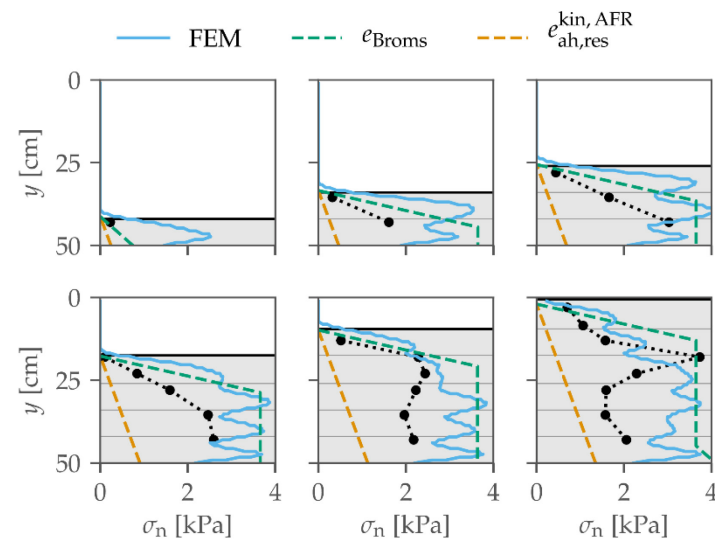
Fig. 150: *Earth pressure distribution on the wall during the backfilling phase in a loose compacted sample.*

The earth pressure distribution after Broms [65] is additionally plotted in Fig. 149 and Fig. 150. It is obtained assuming the K_0-coefficient of Perth Sand, the a exponents in Tab. 10, and a constant OCR of 30. This solution consistently overestimates the truly measured earth pressure in the experiments. Although the theory proposed by Broms is not mechanically absolutely correct (as was explained in Section 2.1.5), it is based on a soil half-space. For this reason, the obtained horizontal stresses tend to be higher than those acting in the backfill of a cantilever retaining wall (i.e. a flexible structure). However, it is not guaranteed that the solution always delivers conservative results.

8.4   Conclusions and recommendations for the practice

In the first part of the section, a particle-scale study of the earth pressure at rest was conducted. A good understanding of the earth pressure in the case of one-dimensional strain conditions is a prerequisite for understanding the earth pressure exerted on retaining walls in the service state (i.e. not at the limit state). The numerical model of Appendix II.2 was used to run oedometric tests.

It was shown that the coefficient of earth pressure at rest K_0 is inversely proportional to the averaged coordination number of the sample, leading to higher values in loose specimens. On the other hand, the K_0 coefficient during unloading shows a steeper increase with an increasing overconsolidation ratio (OCR) in denser samples. During unloading, the empirical power-law function relating the K_0 coefficient of overconsolidated soil to the OCR often assumed in the literature was demonstrated to provide a reasonable estimate for practical purposes, although not very precise. Subsequently, the controlling parameters of the earth pressure at rest were investigated. No correlation between K_0 and the elastic parameters were shown for normally consolidated soil, while a good correlation with the interparticle friction was found. Consequently, the earth pressure coefficient at rest correlates well with the soil peak strength, although no causality is implied. Although founded on fragile theoretical foundations, Jáky's formula was found to give a reasonable, conservative estimate of K_0 for dense Perth Sand. The values estimated by the formula overestimate the numerical data for the loose sample but remain conservative. However, additional research on other grain shapes is needed.

In the second part of the section, the numerical model introduced in Section 7 was extended to consider volumetric yielding and to model soil compaction. Numerical simulations of the wall tests were carried out, and the obtained results were compared to the experimental results. The simulations of the uncompacted samples showed good agreement with the test results. The earth pressure distribution in these samples is bilinear, characterised by a higher earth pressure coefficient in the lowest part of the backfill, and influenced by the wall deflections and the frictional interface.
The simulation of the compacted specimens resulted in a somewhat less accurate prediction of the initial stress, mainly because of some difficulties in modelling the considered problem using the finite element method. As a result, the estimated pressures led to underestimating the moment acting at the wall toe in the dense specimen and overestimating it in the loose one. Improved results could be achieved by employing a mesh-free method. Furthermore, Broms' analytical solution was verified. It was shown that conservative results are obtained, although a too high safety would probably result from its use, especially for dense soil.

Recommendations for the practice

The recommendations in Section 7.4 also apply to this section. However, since this section determines the initial stress conditions through the modelling of the construction stages, modelling the elastoplastic soil foundation layer beneath the wall can affect the resulting initial stress on the wall. In fact, during backfilling, the wall will settle under soil weight and move horizontally due to the applied horizontal earth pressure, causing a wall displacement that results in partial unloading of the already deposited backfill. Therefore, neglecting the foundation layer leads to conservative results.

Undoubtedly, the proposed constitutive model can be employed to simulate more complex construction phases, e.g., involving a slope cut, construction of the wall, and backfill. In fact, the mechanical processes involved in a more detailed simulation of the construction stages are the same as those that were investigated in the present experimental and numerical analysis (i.e. consolidation, compaction, and unloading). The suitability of the proposed constitutive law for simulating these processes has therefore already been demonstrated.

Two different models for the construction phases of a wall are shown in Figs. 151 and 152. In Fig. 151, the wall is constructed on flat ground and subsequently backfilled. That is, the entire backfill is deposited in eleven lays in the same way as it was done in the laboratory for the tests described in Section 6. Instead, Fig. 152 models a more common practical situation, in which a soil cut is made and the ground is temporarily stabilised by a soil nail wall. Subsequently, the wall is built and backfilled in multiple layers. The Optum G2 software [105] was used for a qualitative analysis, assuming pressure-dependent isotropic elasticity and perfect plasticity.

The resulting total displacement (i.e. the absolute value of the displacement vector at each material point) is shown in Figs. 151 and 152. The results show the influence of the different

modelling assumptions on the wall and soil displacement. In fact, if the deposition of the backfill is modelled without consideration of the soil cut, as in Fig. 151, the entire backfill causes an additional load of the soil beneath it, resulting in a significant settlement depression that extends from the left edge of the wall heel to the right edge of the model. As a result, the wall rotates clockwise. Consequently, this wall rotation counteracts (at least partially) the counterclockwise rotation that arises due to the pressure increase on the wall resulting in lower wall displacement and, therefore, to a smaller horizontal stress decrease.
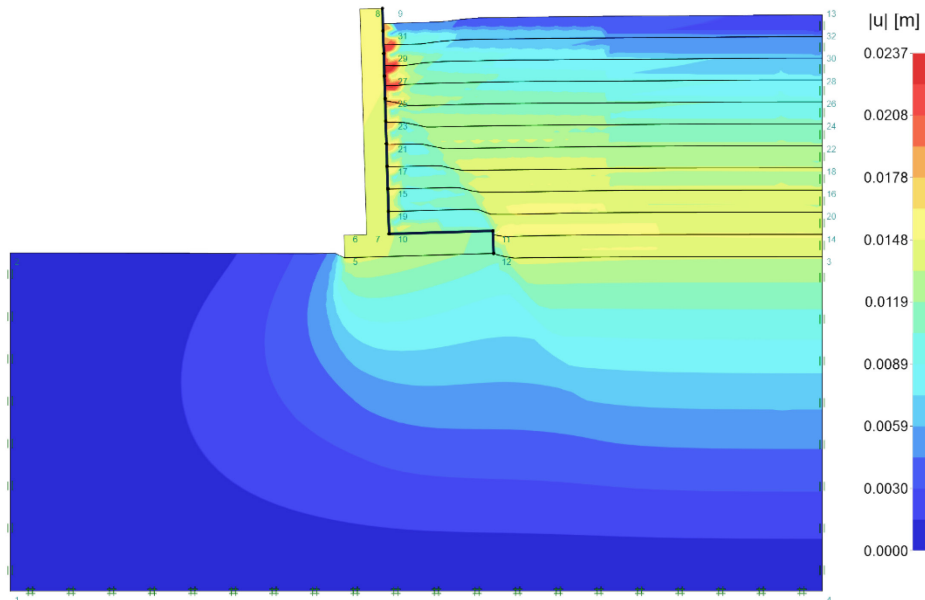
Fig. 151: *Simulation of the deposition of the whole backfill of a cantilever retaining wall in multiple layers. The resulting total displacement is shown.*

On the other hand, by modelling a soil cut, as in Fig. 152, the settlement of the foundation layer is limited to a smaller area right below the wall heel. This results in a more pronounced wall tilt, leading to a larger stress decrease than in Fig. 151. In fact, the wall displacement in Fig. 152 is approximately 33% higher than in Fig. 151.
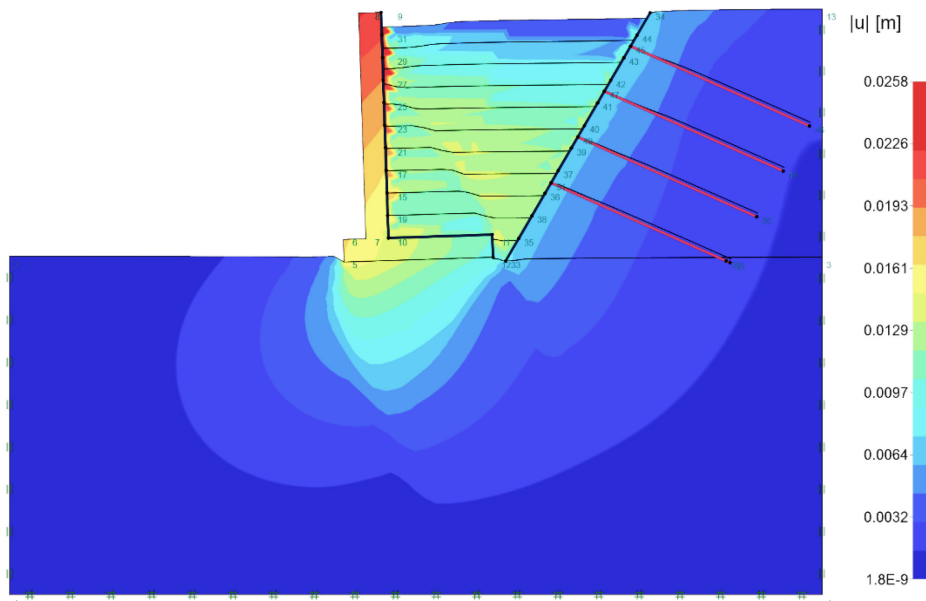

Fig. 152: *Simulation of the deposition of the backfill between a soil nail wall and a cantilever retaining wall in multiple layers. The resulting total displacement is shown.*

9 Further investigations

9.1 Soil-structure interaction considering an improved structural model

So far, the structural behaviour of the wall stem above the construction joint has been assumed to be linear elastic, and a rotation has been enforced at the construction joint, assuming that all plastic deformation localises at one point. In reality, the behaviour of a concrete wall is linear elastic only below a certain stress level, which is likely to be exceeded close to the stem's toe. This leads to cracking and mobilisation of the concrete's plastic strength, resulting in a nonlinear, irreversible material response. Additionally, the wall response can be strongly affected by local corrosion of the reinforcement [117].

This section investigates the influence of the structural response on the soil-structure interaction through more accurate modelling of the structural behaviour.

The numerical model presented in Section 7 and further refined in Section 8 is adapted to consider a more accurate structural response. For this reason, the wall is not modelled as an elastic element anymore but rather by rigid beams connected by nonlinear torsional springs, as depicted in Fig. 153. Each spring in Fig. 153 is characterised by a unique moment-rotation response depending on the wall properties and the corrosion degree ζ, defined as the ratio between the loss in cross-section over the initial cross-sectional area of the reinforcement bars [117] (i.e. $\zeta = 0$ for an intact bar).
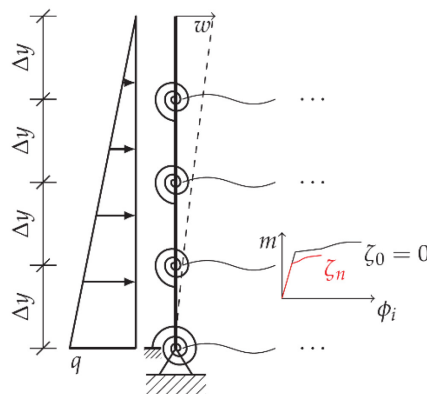
Fig. 153: Assumed structural model under a linear distributed load q.

The nonlinear torsional springs govern the relative rotation ϕ_i between two consecutive rigid beams, $(i + 1)$ and i, when subjected to the moment m. If $\Delta y \rightarrow 0$, ϕ represents the twist of the wall:

$$\phi = \frac{dw}{dy}. \tag{9.1}$$

Here, an approximation is obtained by assuming a spacing of $\Delta y = 0.1\,m$, resulting in 45 rigid beams connected by torsional springs. The load-deformation response of every second spring among the first 24 (counting from the wall toe) is illustrated in Fig. 154. The data concerning the structural model was kindly provided by S. Häfliger based on preliminary results of the newly developed corroded tension chord model [117]. It is referred to the representative 4.6 m high cantilever retaining wall described in [106] and the moment resulting from a linearly distributed force was assumed.
The most pronounced plastic behaviour is observed close to the construction joint, namely in the first metre of the wall (i.e. in the first ten springs). Starting from the height of 2 m, a linear behaviour is observed.

It must be emphasised that ϕ represents the local twist of the wall and is not directly comparable to the wall rotation θ that was considered in the previous sections. In fact, θ is rather interpreted as a measure of the total wall rotation resulting from the plastic deformation in the zone close to the construction joint.
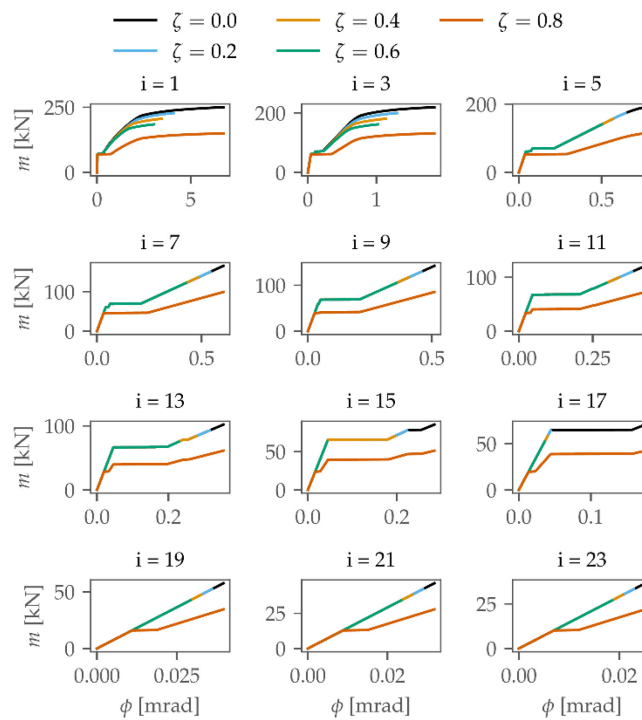
Fig. 154: *Moment-(relative) rotation behaviour of every second torsional springs among the first 24 starting from the wall toe for an increasing corrosion degree ζ. Preliminary data provided by S. Häfliger, ETH Zurich, based on [117].*

Fig. 155 shows the modelled soil behaviour. A soft soil was assumed to conform to the wall design assumed for the wall in [106] and based on existing walls. A relatively high value was chosen for the soil weight, i.e. $\gamma = 20 \text{ kN/m}^3$. No compaction was assumed.
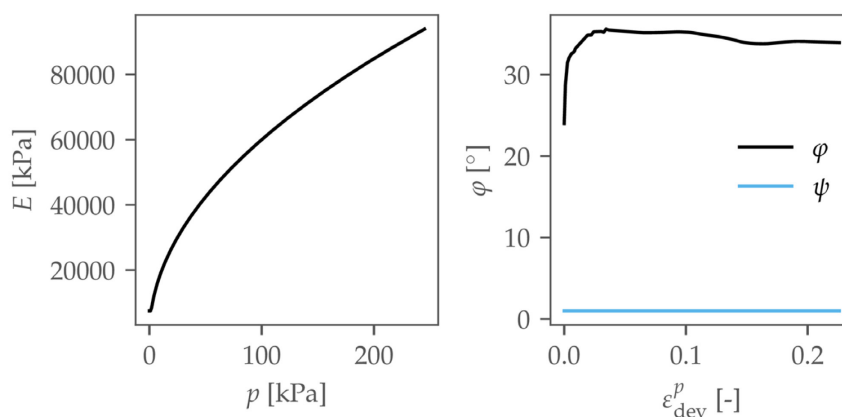
Fig. 155: *Assumed soil behaviour.*

The following situation is simulated: first, the intact wall (i.e. $\zeta = 0$) is backfilled by depositing the soil in different layers. This procedure estimates the earth pressure acting on the wall under service conditions. Then, the wall corrosion is initiated by increasing the corro-

sion degree, thus changing the wall behaviour. In the finite element simulations, the corrosion degree is increased in steps of $\Delta\zeta = 0.1$ up to $\zeta = 0.9$, and the wall behaviour in between is interpolated linearly.

Fig. 156 shows the earth pressure and the wall deflection measured at different simulation stages. It is observed how, for this specific configuration, soil unloading starts occurring at a corrosion degree greater than $\zeta = 0.7$. However, it must be emphasised that the present results are based on preliminary data from [106]. They are presented here with the sole purpose of discussing the modelling of the soil-wall interaction, not to draw general conclusions on the state of existing walls. The results are therefore discussed qualitatively.
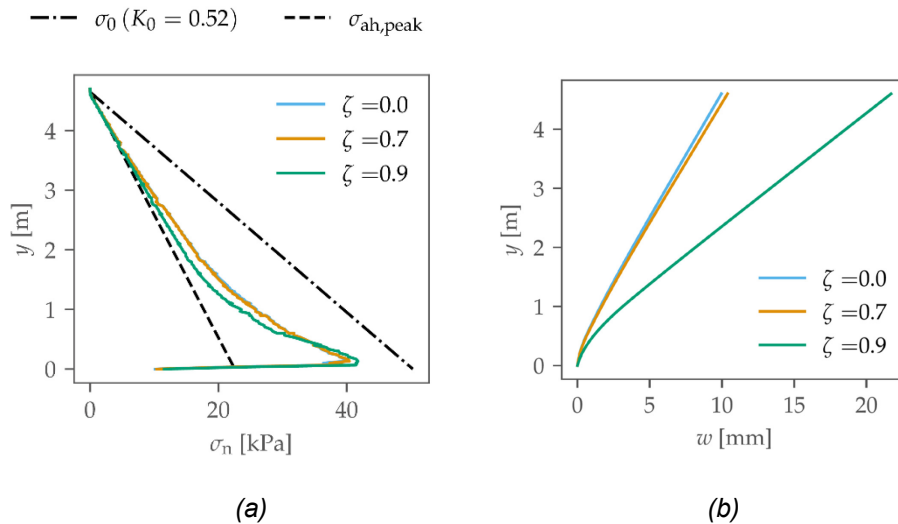
Fig. 156: Simulated earth pressure distribution (a) and wall deflection (b) for different corrosion degrees.

The initial insensitivity of the soil pressure on the wall corrosion is due to the relatively high safety margin that the intact wall had. Fig. 157 shows the input behaviour for the lowest spring of the wall in Fig. 153 compared with the moment-rotation response in the finite element model. It is seen how the same equilibrium position is practically valid for the corrosion degrees between 0 and 0.7. Soil unloading is, therefore, only initiated by a corrosion degree of 0.8 when the previous equilibrium state is lost. At that point, the wall undergoes additional displacement (Fig. 156b) until a new equilibrium is found. The new equilibrium is reached due to a combination of earth pressure reduction and increased wall strength caused by the additional displacement.
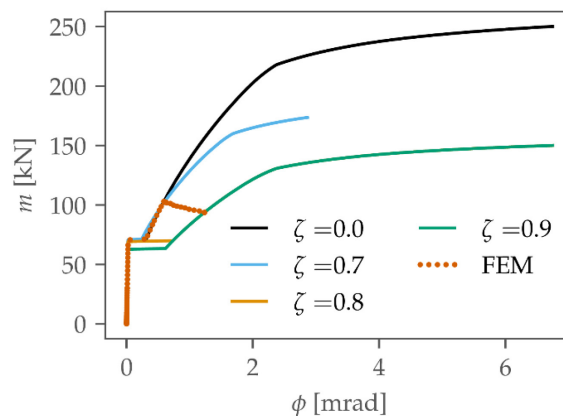
Fig. 157: Constitutive response and moment-rotation response in FEM at the bottom spring. The constitutive wall response is based on preliminary data provided by S. Häfliger, ETH Zurich [117].

The moment measured during the simulation is plotted in Fig. 158a against the wall deflection measured at h=1.7 m above the construction joint. The black curve represents the intact wall, $\zeta = 0$. The blue curve represents an initially intact wall, increasingly damaged up to a corrosion degree of $\zeta = 0.9$. In both cases, the intact wall is first backfilled, and the moment increases to a value slightly above 100 kN. Then, the intact wall (black curve) is immediately subjected to a rotation imposed at its toe, causing soil unloading. The other wall (blue curve), instead, is progressively damaged by increasing its corrosion degree. In the end, a new equilibrium state has been found and is represented in Fig. 158a by a blue dot. After that point, a rotation is imposed at the stem's toe. The resulting response is represented by a dashed line. The moment-displacement response of the wall is practically the same in both cases, highlighting how the modelling of the wall damage is superfluous for modelling the earth pressure evolution. Therefore, the problem can be decoupled, and the earth pressure can be determined on an intact wall imposing a rotation at the toe, as shown in the previous sections.

This result is further corroborated by Fig. 158b, where the wall twist (i.e. the relative rotation of the beams in Fig. 153) is plotted. It is noted how the lowest portion of the wall contributes almost exclusively to the total wall displacement. In particular, the highest value is observed at the construction joint, while at the height of $h = 1\,\mathrm{m}$ the twist is practically zero (indicating that the wall remains elastic) even at an advanced corrosion state ($\zeta = 0.9$). This means, therefore, that the wall displacement of a damaged wall can be modelled with sufficient accuracy by assuming a localised rotation at its toe (and modelling the stem as an elastic body).

(a) (b)
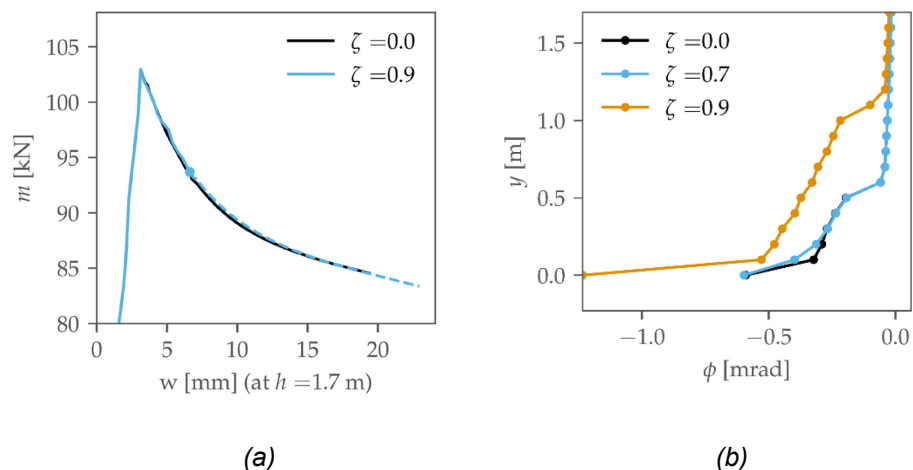
Fig. 158: *(a) Simulated moment versus wall deflection measured at $h = 1.7\,m$ above the construction joint. (b) Wall twist ϕ along the wall for different corrosion degrees.*

9.2 Investigation of thermal actions

In civil engineering, thermal actions are defined as stresses induced by temperature changes in a structure. While they are always considered for the design of hyperstatic structures, such as integral bridges [160] or dams [161], they are usually neglected in isostatic structures, which can accommodate temperature-induced strains with no stress increase. However, thermal actions can not be ignored for the subclass of isostatic systems subjected to displacement-dependent forces, such as cantilever retaining walls. Although unanchored cantilever retaining walls can be considered isostatic from a purely structural point of view, they are embedded in soil on the backfill side, which will resist temperature-induced deformations.
Therefore, temperature changes can lead to increased stresses in the wall. For corrosion-damaged walls, the stress increase will lead to additional displacement localised at the damaged point.

Temperature actions can have two more profound implications on damaged cantilever retaining walls. First, they can make monitoring more challenging, as most displacements

are due to temperature changes rather than an increase in the degree of corrosion [4]. Second, the cyclic nature of the temperature action can lead to a build-up of irreversible strain, leading to higher lateral stresses in the backfill and, thus, higher structural stresses of damaged walls. In this section, a model to consider thermal actions is presented and applied to a case study.

9.2.1   Heat transfer in a retaining wall

During the day and throughout the year, the temperature of a wall changes as a result of heat diffusion through its cross-section and heat exchange with the external environment. Fig. 159 illustrates the different heat sources at the outer wall surface and the heat diffusion through conduction.

The solar and atmospheric radiations, $\dot{q}_{\text{sun}}$ and $\dot{q}_{\text{atm}}$, constitute heat influxes, while the wall releases heat to the environment through radiation $\dot{q}_{\text{rad}}$. Depending on the wall surface and air temperatures, heat is gained or lost by convection, $\dot{q}_{\text{conv}}$. A comprehensive review of all these heat sources is found, e.g., in [162]. Here, only a short description and the relevant mathematical formulations are given.
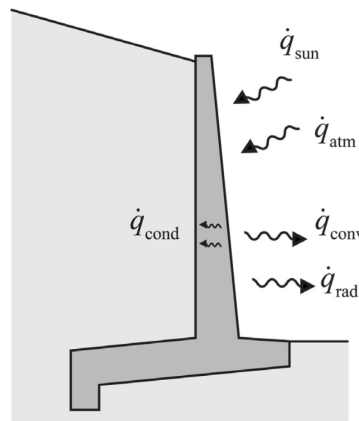
Fig. 159: *Heat exchange at the outer wall surface and conduction across the wall.*

Inside a body, heat is transferred from the hotter regions to the colder ones through *conduction*. Conduction is governed by Fourier's law, which reads [162]

$$\underline{\dot{q}}_{\text{cond}} = -k\nabla T, \tag{9.2}$$

where $\underline{\dot{q}}_{\text{cond}}$ is the heat flux density, k the material's conductivity, and ∇T the temperature gradient.
On the other hand, heat is transferred between different bodies in the form of electromagnetic waves by radiation. The rate of radiation by a body is given by [162]

$$\underline{\dot{q}}_{\text{rad}} = \varepsilon\sigma T_s^4, \tag{9.3}$$

where ε is the emissivity of the surface, $\sigma = 5.67 \cdot 10^{-8}\,\text{W/(m}^2\text{K}^4)$ is the Stefan-Boltzmann constant, and T_s the surface temperature. The wall in Fig. 159 emits radiation and is radiated by the gas molecules present in the earth's atmosphere. Therefore, $\underline{\dot{q}}_{\text{atm}}$ is calculated from Equation (9.3) with $T_{\text{sky}} \approx 230 - 285\,\text{K}$ [162].
Furthermore, heat is provided to the wall by solar radiation. Solar radiation is usually separated into a direct and a diffuse component [162]. The direct component represents the part of the solar radiation that directly reaches the earth's surface without being scattered or absorbed by the atmosphere. The scattered radiation builds the diffuse component. The total solar radiation on a surface is, therefore, given by:

$$G_{\text{solar}} = G_{\text{direct}} \cos \theta_s + G_{\text{diffuse}}, \tag{9.4}$$

where θ_s is the angle of incidence of direct solar radiation. It is described in [163] for the solar radiation on a wall as:

$$\cos \theta_s = \cos \beta \cos \gamma \sin \epsilon + \sin \beta \cos \epsilon, \tag{9.5}$$

where β is the solar altitude, γ the wall-solar azimuth, and ϵ the wall tilt ($\epsilon = 0°$ if the wall is horizontal, $\epsilon = 90°$ if it is vertical). Finally, the total solar radiation absorbed by the wall is

$$\dot{q}_{\text{sun}} = \alpha_s G_{\text{solar}}. \tag{9.6}$$

α_s is the solar absorptivity.

The wall in Fig. 159 additionally exchanges heat with the surrounding air by *convection*. Convection describes the heat transfer between a solid surface and a liquid or gas and is expressed as [162]

$$\dot{q}_{\text{conv}} = h(T_s - T_{\text{air}}), \tag{9.7}$$

where h is the convection heat transfer coefficient, T_s is the surface temperature, and T_{air} is the air temperature. The convection heat transfer coefficient h is an experimentally determined parameter and depends on factors such as fluid motion and surface geometry.

9.2.2 Case study: Winkelstützmauer Wirüti Widerlager Süd, Steinen, Switzerland

The *Winkelstützmauer Wirüti Widerlager Süd* wall, located in Steinen, Switzerland was instrumented in 2017 by Marmota Engineering AG as part of a pilot test aiming at monitoring the state cantilever retaining walls. A representative section of the wall is depicted in Fig. 160. The indicative geometry of the drill holes B1-B3, B5, B7, and B8 is sketched in the same section, although their longitudinal position differs.
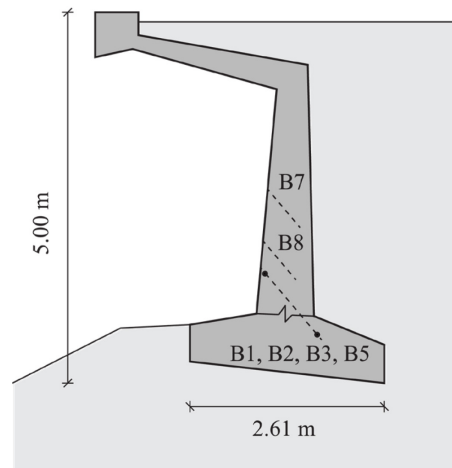
Fig. 160: Cantilever retaining wall in Steinen, Switzerland, instrumented by Marmota Engineering AG [4]. The location of the drilled holes is only indicative and not to scale. For more precise details, see [4].

The measuring system consists of glass-fibre-based sensors installed in drill holes, as shown (only qualitatively) by the dashed lines in Fig. 160. In drill holes B1-B3, and B5, a sensor is installed to measure the strain between the two dots in Fig. 160. The underlying idea is to monitor the displacement at the construction joint due to damaged reinforcement. However, to detect anomalies, the temperature-caused displacement must be filtered out. For this reason, a second sensor measuring the temperature over the wall thickness was

installed in the same holes. Additionally, temperature measurements were carried out in holes B7 and B8. A full description of the monitoring system is found in [4].

The strain measurements in the drill holes B1 and B3 and the wall temperature measured at two depths in B1 over the period from January to September 2019 are shown in Fig. 161. The temperature measurements are distinguished as outer and inner temperature, where outer denotes the temperature measured close to the wall surface and inner close to the soil-wall interface. The exact location of the temperature measurements is found in [4].
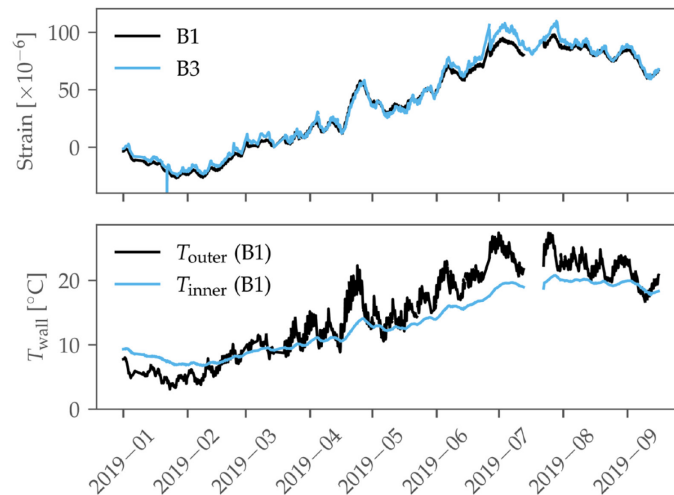
Fig. 161: *Strain and temperature measurements at the wall pictured in Fig. 160. Data were kindly provided by M. Iten and F. Fischli (Marmota Engineering AG) and published in [4].*

A strong correlation is observed between the measured strain and the wall temperature. The implications are twofold. First, the successful implementation of a displacement-based monitoring system depends on the ability to reproduce and filter the temperature-caused strain. Second, the wall is subjected to continuous unloading and reloading, which can increase the damage of already damaged structures.

In this section, the instrumented model will be modelled and solved with the FEM using knowledge gained in previous sections. The obtained results will be validated against the field data collected by Marmota Engineering AG. Finally, the evolution of the moment acting at the construction joint will be evaluated.

The modelling parameters for the wall are summarised in Tab. 12. The wall is modelled as linear elastic, and a reduced stiffness is assumed to partially compensate for the lack of cracking. Heat transfer is not modelled in the soil and a constant temperature $T_{\text{soil}} = 15°C$ assumed. The soil was modelled as in Sections 7.1.3 and 8.2.2. A preliminary study on the influence of the soil parameters showed little sensitivity to the quantities of interest.

The analysis will be restricted to daily temperature fluctuations by simulating four days at the beginning of June 2019. The data measured in the selected period is plotted in the upper two graphs in Fig. 162. The lower two graphs show the meteorological data recorded during the same period at nearby locations and based on data available through Agroscope's *Agrometeo* [164]. The air temperature is measured at the height of 2 m from the ground, while the solar radiation is given as global radiation, i.e. the total radiation that reaches the (horizontal) earth's surface [165]. In Fig. 162, the total solar radiation Equation (9.6) is given. The radiation on the wall is obtained by assuming the diffuse radiation to amount 50% of the total radiation [166], considering the position of the sun (e.g. from [167]) and the orientation of the wall, and assuming the solar absorptivity of concrete to be $\alpha_s = 0.6$ [162]. It is assumed that if the total radiation is less than 250 W/m², then it is entirely

diffuse radiation (e.g. in case of cloudy weather). Furthermore, the shade of the wall itself has to be considered.

Tab. 12: *Material properties for the thermal analysis of the wall in Fig. 160.*

Parameter	Value	Source
Thermal conductivity k	0.8 W/(m²K)	[162]
Specific heat c_p	9·10⁵ J/(tK)	[162]
Convection coefficient h	15 W/(m²K)	[162]
Solar absorptivity α_s	0.6	[162]
Emissivity ϵ	0.88	[162]
Expansion coefficient α_T	10⁻⁵ 1/K	[125]
Young's modulus E	20 Gpa	
Poisson's ratio ν	0.2	
Soil temperature T_{soil}	15°C	
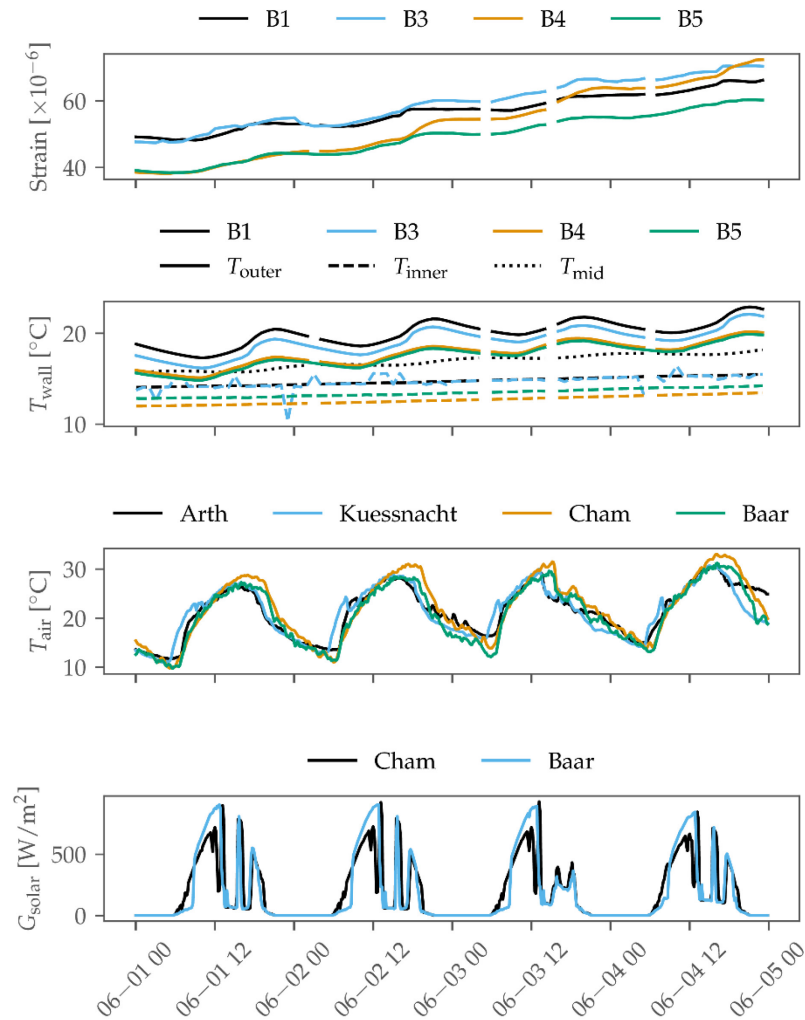
Fig. 162: *Cantilever retaining wall in Steinen, Switzerland, instrumented by Marmota Engineering AG [4]. The location of the drilled holes is only indicative and not to scale. For more precise details, see [4].*

It is observed that the considered four days were mostly sunny. Because of that, and the fact that the chosen period is in late spring, the 24h-average air temperature increased monotonically. These two factors contributed to the temperature rise of the wall, shown in

the second plot from above in Fig. 162. While the outer temperature measurement shows daily fluctuations, the inner temperature increases monotonically but at a slower rate. Although the strain measured in the drill holes is influenced by the difference between outer and inner wall temperature, no fluctuations are observed in the measured data. Instead, an increase was only measured during the day.

The simulated wall temperature distribution in the morning and evening of June 3 is depicted in Fig. 163. The temperature over the drill holes is shown in Fig. 164 at the same times and compared to the measured data, showing very good agreement. It is seen how the temperature distribution in the first 20 cm (measured along the drill holes) radically changes in different periods of the day. For this reason, it is critical for any analytical approach aimed at compensating the measured temperature-induced strain (as proposed, e.g., in [4]) to be supported by multiple data points, in particular close to the wall surface.

(a)   *(b)*
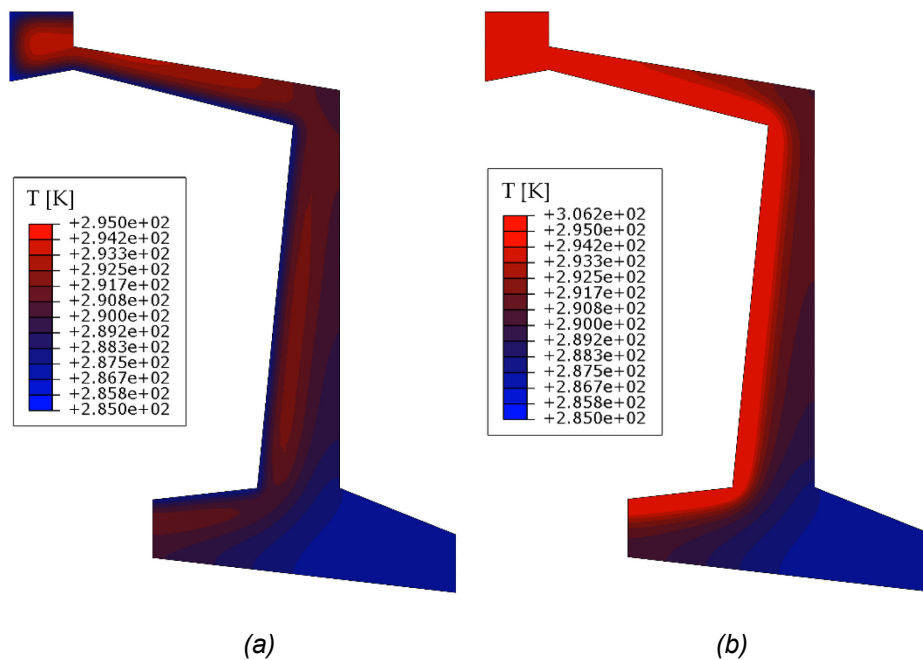
Fig. 163: *Simulated temperature distribution of the wall on June 3, 2019, at 6:00 (a) and at 19:00 (b).*

(a)   *(b)*
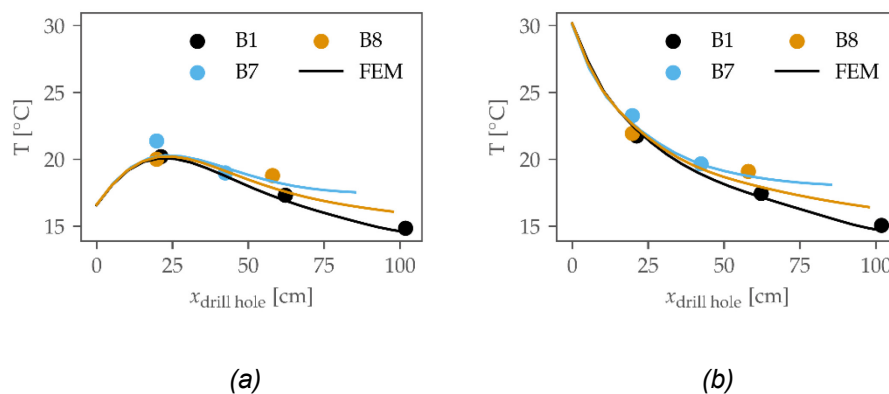
Fig. 164: *Simulated temperature in the drill holes on June 3, 2019, at 6:00 (a) and at 19:00 (b) compared with field data.*

During the day, the temperature gradient over the wall thickness reaches a maximum, causing a curvature of the wall cross-section leading the stem to push against the soil, which exerts resistance against any wall displacement. As a result, the pressure on the wall increases, resulting in a stress and strain increase at the stem toe. During the night, the outer temperature decreases and reaches values lower than the inner temperature,

causing a change in sign in the temperature-induced cross-sectional curvature. In this case, a wall unloading would be expected, followed by a strain decrease. Instead, the measured data shows no decrease.

Fig. 165 compares the measured data with the simulated data. The lower two graphs plot the inner and outer temperature in the drill holes, showing a good agreement between numerical and field data. The strain is plotted in the upper graph. It is set to zero at the beginning of the considered time interval. It is immediately noted that the simulated strain shows daily oscillations, which were not recorded in the field. Plastic displacements could cause the absence of negative strain increments overnight, although the full data series, Fig. 161, shows that strain indeed decreases in colder months. Interestingly, it is noted that the 24-h average agrees very well with the measured data, indicating what could be defined as a "latency" problem, with the simulation being more "reactive" to temperature changes (e.g. due to modelling assumptions) than the monitoring system or the wall itself. To fully understand the difference, additional analysis is needed.
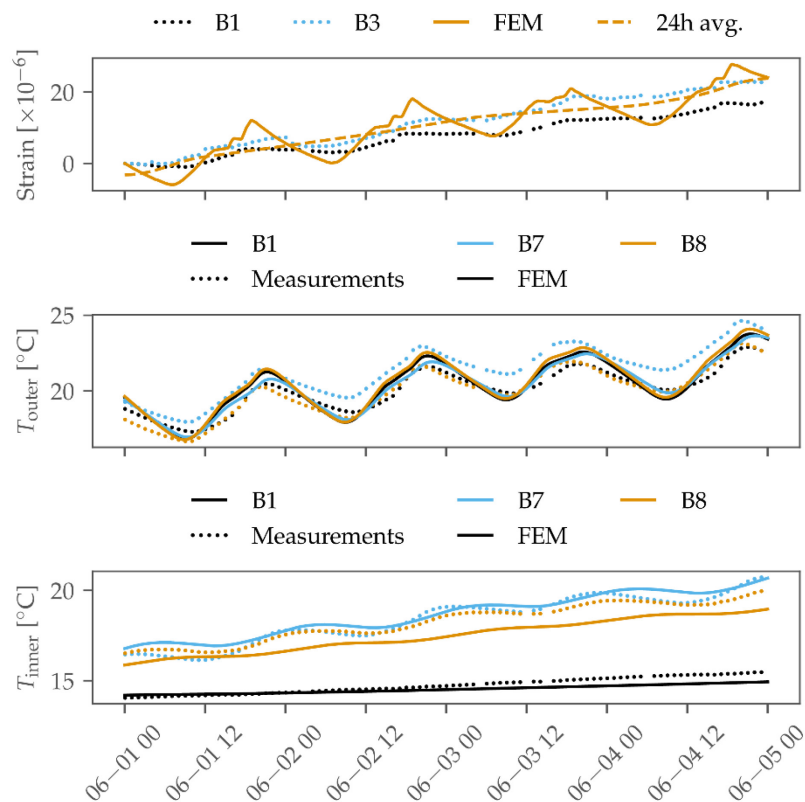
Fig. 165: *Comparison of field and simulated data from June 1, 2019 and June 5, 2019. From top to bottom: strain measured in the drill holes crossing the construction joint, outer temperature, and inner temperature.*

Fig. 166 shows the moment as a function of the measured strain in the FEM simulation. Again, a cyclic action is observed. The moment oscillates daily in approximately the same range while a strain accumulation is observed. The maximum moment reached, $m \approx 100\,\mathrm{kN}$, is likely well below the design capacity [8], justifying in this case the assumption of the wall elastic behaviour. In addition, it is noted that no traffic loads were considered, although the retaining wall supports a road.

The moment is plotted in Fig. 167 against the normalised horizontal displacement of the wall measured at the height $H = 2.35\,\mathrm{m}$ above the construction joint. An approximately

---

[8] The reinforcement layout at the construction joint is $\emptyset = 26\,\mathrm{mm}$, $s = 400\,\mathrm{mm}$, the static height is about 65 cm.

linear relationship is observed between the two quantities. Instead, a strain accumulation was observed in Fig. 166, which is likely caused by the wall expansion caused by the increasing temperature gradient over the sensor length during the considered time period (compare, for example, the outer and inner temperatures measured in the B1 hole in Fig. 165, which show an increasing difference with time). In fact, the measured strain includes the temperature-induced deformation of the wall cross section throughout the sensor length, including the horizontal wall expansion that is not resisted by the backfill and thus does not contribute to increased wall stresses. By reducing the sensor length, the influence of this irrelevant strain component would be significantly reduced, allowing a better estimation of the wall displacement localised at the construction joint. However, installing a short sensor would require very accurate knowledge of the location of the construction joint walls, which is usually difficult to have, so a shorter sensor may completely miss it. Therefore, a possible alternative to excluding unwanted wall deformation is to install a reference sensor (e.g. shifted vertically or horizontally with respect to the primary sensor) that does not cross the construction joint. By subtracting the deformation measured by the reference sensor from that measured by the primary sensor, a more accurate measurement of the displacement at the construction joint can be obtained.
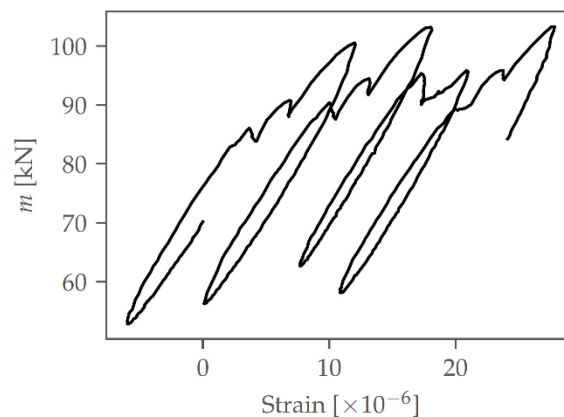
Fig. 166: *Moment versus strain at the construction joint measured in the FEM simulation.*
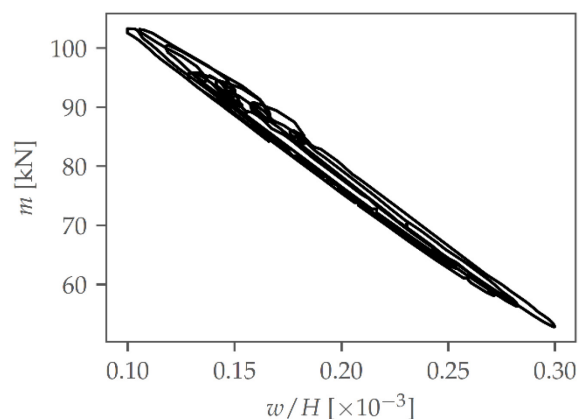
Fig. 167: *Moment at the construction joint versus normalised horizontal wall displacement* ($H = 2.35\,m$) *measured in the FEM simulation.*

In general, cyclic temperature changes can lead to a cyclic evolution of the moment acting at the construction joint of cantilever retaining walls. For example, during the short period considered in this analysis, a moment increase of $40\,\mathrm{kN}$ was observed. However, this can surely increase by considering a more prolonged time range due to higher fluctuations in the temperature. Additionally, the cyclic action of the temperature can induce irreversible stress increase in the soil (and consequently in the wall). In fact, if a large portion of the

backfill has already reached its maximum shear strength (because of the high plastic deformation), any wall displacement will cause additional soil deformation, which leads to the mobilisation of lower strength due to softening. Consequently, the moment acting on the wall can slowly increase.

9.3 Investigation into the scale effects

The previous sections considered the scaled model wall described in Section 5. The influence of the wall behaviour and the initial stress state were investigated. However, the effects of the wall dimensions could not be investigated. In geotechnics, the direct applicability of scaled test results to larger structures is often debated, primarily because of the pressure-dependent soil behaviour.

While Appendix II.2.1 showed that the soil strength is not sensitive to the stress level, the soil-structure interaction has not been tested on larger structures. For this reason, a limited parametric study is carried out in this section. The behaviour of Perth sand, described in Appendix II, is considered. No soil compaction is modelled. The wall height is varied in the range $[3\,\text{m}, 4\,\text{m}, 5\,\text{m}, 7\,\text{m}]$. The FE model described in Sections 7.2.1 and 8.3.1 is assumed. The wall thickness and stiffness are varied to keep a realistic slenderness and to reflect the stiffness of a cracked concrete wall with adequate reinforcement given the wall height.

Assuming dense sand, the results in Fig. 168 are obtained. The left plot shows the moment-rotation response. It is observed how the wall height does not influence the wall unloading process, provided that a reasonable thickness and wall reinforcement are assumed. Also, the results are very similar to those obtained in the wall tests. Indeed, as in the wall tests, the residual value of the moment is reached at a rotation of about 20 mrad and a similar value of 0.15 is obtained.
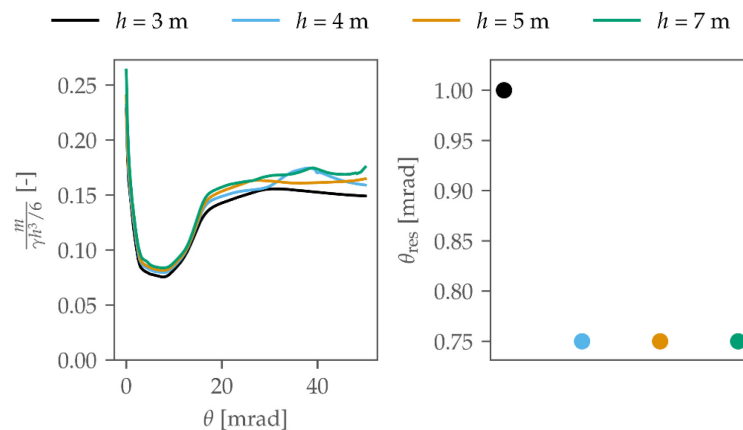
Fig. 168: Left: Moment-rotation response of a wall of variable height backfilled with dense soil; right: wall rotation required to reach the residual value of the moment.

The rotation required to reach the residual state is plotted in the right graph in Fig. 168. Due to the stiff response of the dense sample, a rotation of 0.75-1 mrad is sufficient to reach a value less or equal to the moment measured at the residual state.

Fig. 169 shows the results for loose soil. Also in this case, similar results as in the laboratory were obtained. Considerably larger rotations are needed to reach the residual state in this case. Indeed, it is only reached after a rotation of about 30-50 mrad. The limit state value is the same as for the dense sample.
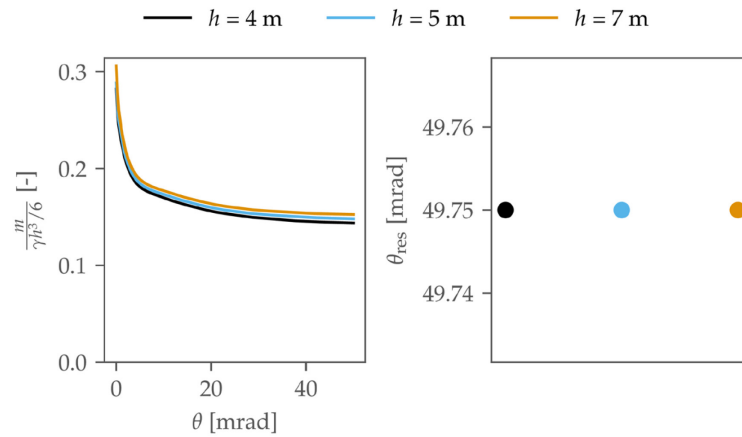
Fig. 169: *Left: Moment-rotation response of a wall of variable height backfilled with loose soil; right: wall rotation required to reach the residual value of the moment.*

These results confirm the validity of the conclusions drawn in the previous sections, even when considering larger structures. Indeed, no scale effects were observed at the level of the soil-structure interaction. On the other hand, it was shown previously how the material strength is not affected by scale effects.

9.4   Investigation into the backfill inclination

Another parameter that was not considered in the experimental and numerical study of the previous sections is the backfill inclination. Therefore, the influence of the backfill inclination on the wall unloading process is investigated in this section using the developed numerical model. The procedure is the same as in the previous section, where the height was varied. The backfill inclination β is varied in the range [0°, 5°, 10°]. Again, uncompacted loose and dense sand are considered. The wall height is assumed to be $h = 5\,\text{m}$.

The results for dense sand are shown in Fig. 170. While the initial and residual moment increase with the backfill inclination, its variation does not heavily affect the unloading behaviour. The rotation required to reach the residual value only slightly increases with increasing inclination because of the higher initial value. Again, a value of 0.75-1 mrad is obtained.
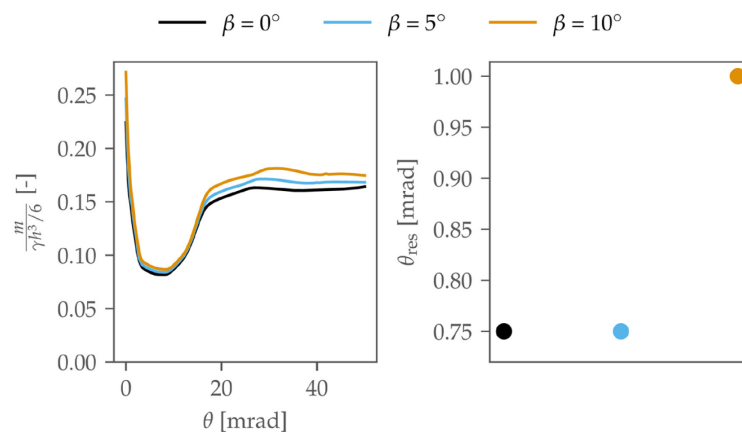
Fig. 170: *Left: Moment-rotation response of a wall backfilled with dense soil and a variable backfill inclination; right: wall rotation required to reach the residual value of the moment.*

Fig. 171 shows the results for loose soil. Also in this case, the backfill inclination mainly affects the initial moment and its residual value, but the unloading behaviour is not much affected. The residual value of the moment is reached after a rotation of about 30-50 mrad.
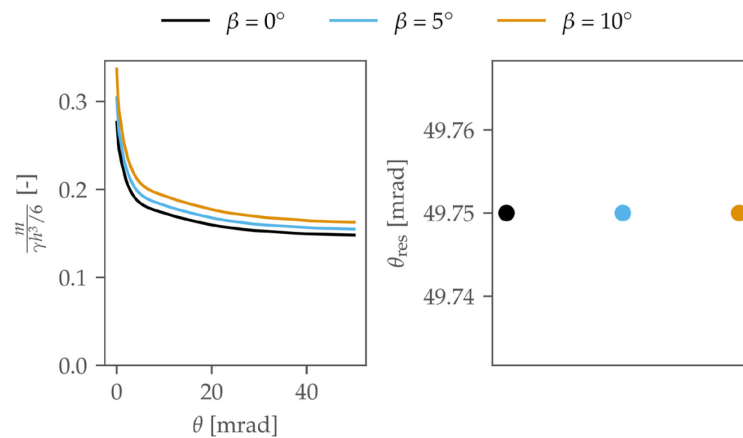
Fig. 171: *Left: Moment-rotation response of a wall backfilled with loose soil and a variable backfill inclination; right: wall rotation required to reach the residual value of the moment.*

Although additional tests on different soil types should be carried out, these results indicate that it is possible to define ranges for the rotation required to reach the residual value of the moment. Although the range proposed by the Eurocode 7 [13] (see Tab. 1) for dense sand seems plausible, the values given for loose soil are too low, based on the results of this work, especially in case of higher initial stresses.
Based on the model developed in this work and a larger database of soil types, a more comprehensive parametric study can be carried out.

9.5 Investigation into the controlling parameters of the soil unloading under 3D conditions

Based on the models developed in Section 7.3, a limited parametric study is carried out to investigate the controlling parameters of the soil unloading when only a limited number of wall sections are corroded.

The ratio between the three-dimensional and the two-dimensional limit state of the moment for different friction angles and height-to-width ratios, h/b of the wall sections is plotted in Fig. 172. Both the ratio h/b and the friction angle have a positive effect on the three-dimensional limit state, allowing a higher stress redistribution and thus reducing the value of the moment on the failing section.
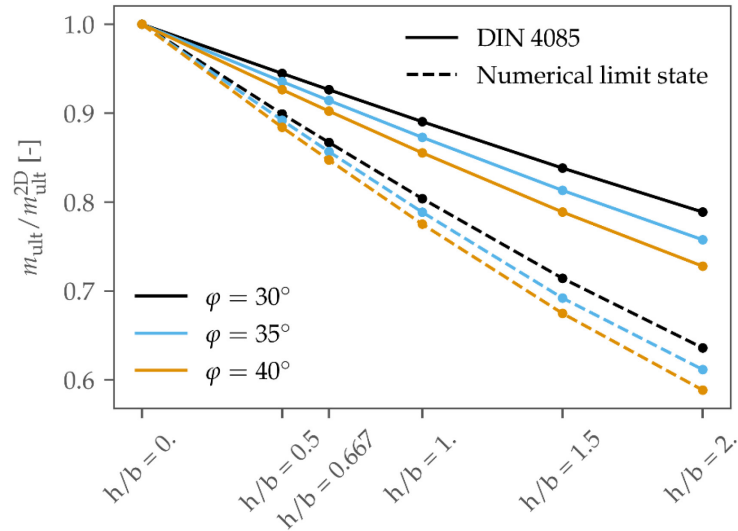
Fig. 172: Ratio between the three-dimensional and the two-dimensional limit state of the moment for different friction angles and height-to-width ratios of the wall sections.

In addition, the solution proposed in the DIN 4085, Equation (2.17), is plotted. Although conservative, the solution provides a bad fit of the numerical limit state solution, potentially leading to a considerable overestimation of the moment.

The moment increase on the neighbouring wall sections is plotted in Fig. 173. Because a higher friction and h/b ratio led to a reduction of the moment acting on the damaged wall, the moment acting on the neighbouring sections shows a larger increase under the same circumstances, as a higher stress redistribution occurs in the backfill.
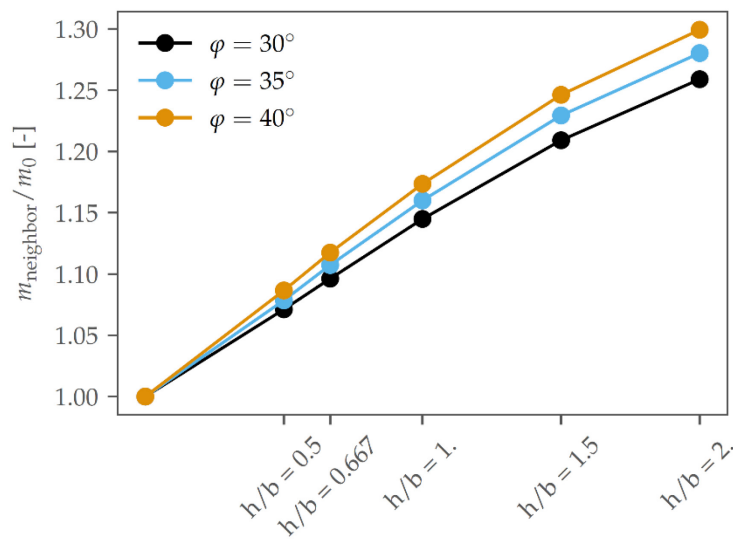
Fig. 173: Ratio between the moment acting on the neighbouring, intact wall sections when the damaged wall section fails and the initial moment.

9.6 Conclusions

In this section, different analyses were carried out to improve the understanding of the soil-wall interaction further.

First, an analysis of the unloading behaviour considering a refined structural model has been carried out. The results showed that the wall unloading process is insensitive to the proper modelling of the elastoplastic wall behaviour. In fact, the same earth pressure unloading was observed for a corroded wall and for an intact wall to which a rotation was imposed at its toe. Therefore, it was shown that the actions and reactions can be decoupled in assessing the failure of corrosion-damaged walls. The safety of the walls can then be evaluated by superposing the actions and reactions as in Fig. 63.

Then, the thermal analysis of an existing wall was carried out. Based on freely available meteorological data, it was possible to simulate the temperature field of a retaining wall with a good degree of accuracy. It was shown how temperature changes cause a cyclic action on the wall, resulting in additional displacement. The wall displacement measured in the field could be explained, although only partially (as the 24h-average had to be considered).

Further, the developed numerical model was employed to simulate full-scale structures. It was observed how the unloading behaviour is insensitive to the wall dimensions, and the applicability of the previously made conclusions applies to every wall dimension. In addition, the influence of the backfill inclination was investigated. Also in this case, only a marginal impact on the wall unloading process was observed.

Finally, a parametric study was carried out to study the effects of the soil friction and the geometry of the wall sections on the three-dimensional limit state. Higher friction and taller wall sections allow for a better stress redistribution in the backfill, leading to a lower limit state and a higher increase of the moment acting on the neighbouring sections.

10 Safety assessment of cantilever retaining walls

The present section is the synthesis of the two research projects AGB 2015/028 "Tragwiderstand und Verformungsvermögen von Winkelstützmauern bei lokaler Korrosion der Bewehrung" [3] and AGB 2015/029 "Failure Behaviour of Cantilever Retaining Walls - Soil-Retaining Wall Interaction" and has been elaborated in close cooperation. It is included in English in this report and in German in [3]. References to the listed literature concerning the structural behaviour can be found in [3].

For the verification of retaining walls affected by corrosion of the reinforcement, a multi-stage verification strategy (LoA: Level of Approximation) is proposed in analogy to [168], in which the verification effort is increased for each stage. It is to be decided on a case-by-case basis whether the effort for one stage is worthwhile (depending on the age of the structure, its general condition, superordinated project goals, and with regard to data collection), or whether strengthening measures or a new replacement construction should be examined directly.

10.1 Procedure

10.1.1 Overview

Fig. 174 shows the verification procedure in a flow chart. First, a triage is carried out, whereby the limit state analyses (A) and (B) according to Chapter 2.1 in [3] are used to determine whether sufficient structural safety can be verified based on simple methods (LoA I). If this is not the case, a decoupled analysis (LoA II) is performed. For simplification, the load-displacement behaviour of the retaining wall and the backfill are determined separately and combined for the verification. At this stage, simple, conservative assumptions are made regarding the corrosion damage. A possibly already occurred decrease of the earth pressure due to the tilt of the retaining wall about its base is neglected. If the simple decoupled analysis results in insufficient structural safety, a refined decoupled analysis (LoA III) can be carried out with less conservative assumptions regarding the corrosion distribution or the foundation stiffness, provided that the corresponding data can be collected with reasonable effort.

If there is a possibility of load redistribution in the longitudinal direction, for example if only individual sections of a dilated retaining wall are affected by corrosion, a coupled analysis (LoA IV) may be appropriate. In this case, the wall displacement and the earth pressure reaction are determined in each calculation step, considering the soil-structure interaction so that the influence of adjacent segments can be recorded.

Sufficient strengthening measures or a new replacement structure must be planned if the structural safety cannot be verified even with an in-depth analysis.
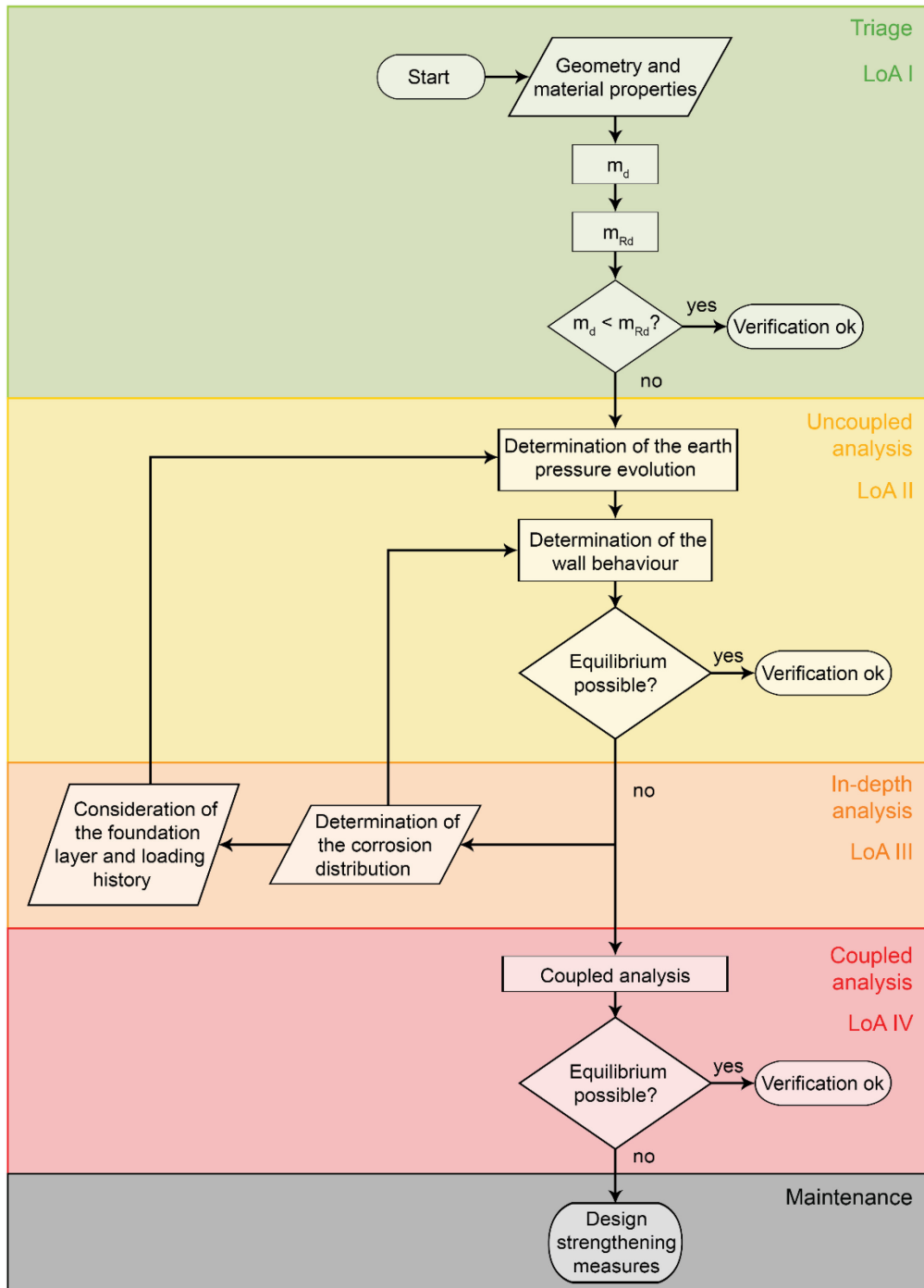
Fig. 174: Flowchart describing the stages of the verification procedure.

10.1.2 Triage (LoA I)

In the triage, it is checked whether the internal structural safety (ultimate limit state type 2 according to SIA standard 260) is ensured without verification of the deformation capacity of the wall. For this purpose, the limit state analysis (A) and (B) described in Chapter 2.1 in [3] are used.

Collection of geometry and material data

The following data is required for the verification:

- Geometry (wall height, wall thickness, geometry of the wall sections, backfill height)

- Materials (information on reinforcement: diameter, spacing, design value of yield stress; information on concrete: in particular, the design value of compressive strength)
- Geotechnical data (soil weight, shear strength, amount of possible water accumulation)
- Corrosion parameters (total section loss in the affected wall section and estimated number of affected bars)

For triage (LoA I), information from construction and design documentation and conservative assumptions are sufficient and can be obtained with little effort. For higher approximation levels (LoA II-IV), data from a sample of the structure and soil may be required.

Earth pressure

For the limit state analysis (A), it is assumed that the acting bending moment is the bending moment developed by the initial stress state (Sections 2.1 and 8). The latter can be estimated for uncompacted (or slightly compacted) soils according to Jáky's earth pressure at rest and for compacted soils according to Broms' theory. For the limit state analysis (B), the bending moment is determined according to Section 3.3 or with the active earth pressure according to Coulomb.

It should be emphasised that the theories of Jáky and Broms cannot be proved theoretically in a general way because of the underlying simplifications. However, for the cases considered in Section 8, it was shown experimentally that both theories provide conservative estimates of the earth pressure. A comparison with data from the literature confirmed this observation. Nevertheless, the input parameters should be estimated with caution to apply the two theories in practice. Alternatively, the initial stress state can be estimated with an FE analysis (see Section 8).

Resistance

The bending resistance at the construction joint is determined with a conventional cross-section analysis according to the SIA 262 and 269 standards, whereby only the total cross-sectional loss of the reinforcement is required. The favourable influence of a possible compressive normal force (due to wall friction, self-weight) can be considered, but it has little influence.

In the limit state analysis (A), the remaining cross-sectional area of the wall's reinforcement is considered. That is, the sum of the area of the undamaged bars and the reduced area of the damaged bars. In the limit state analysis (B), only the cross-sectional area of the uncorroded bars is considered (see Chapter 2.1 in [3]). If no information on the corrosion distribution is available, the number of affected bars can be estimated in the same way as in the simple coupled analysis (see Section 10.1.3).

Structural safety verification

For the structural safety verification in triage, the acting moments at the wall toe are compared with the respective bending resistance. If one of the two verifications (limit state analysis (A) or (B)) is fulfilled, no further measures need to be taken. Otherwise, a decoupled analysis is required.

10.1.3 Simple decoupled analysis (LoA II)

In the decoupled analysis, the load-displacement behaviour of the wall (as a function of the cross-sectional loss of the reinforcement) and the relationship between wall displacement and earth pressure distribution are determined separately and compared.

Estimation of the load-displacement behaviour of the wall

In the simple decoupled analysis, only the total section loss is assumed to be known. However, the load-displacement behaviour of the wall depends significantly on the distribution

of the total section loss over the different reinforcing bars. However, theoretical and experimental investigations carried out within project AGB 2015/028 have shown that there is a critical number of damaged bars in which the wall resistance and the deformation capacity are minimal. This critical number of damaged bars can be estimated using the following empirical approach [3]:

$$\frac{n_{\mathrm{c,crit}}}{n_{\mathrm{tot}}} \approx 0.2 + \zeta_m \qquad \zeta_m > 0. \tag{10.1}$$

where n_{tot} is the total number of bars and ζ_m is the average cross-sectional loss.

Thus, the load-displacement behaviour can be determined approximately for the critical number of corroding bars according to Equation (10.1) without further knowledge of the corrosion distribution. For the calculation, the corroded tension chord model (CTCM) according to Chapter 2 of the document attached to [3] is used and combined with the load-displacement behaviour of bending crack elements (Chapter 8 in the document attached to [3]) or, in a simplified way, with a cross-sectional analysis with subsequently considered tension stiffening. The length of the corrosion site (bar length affected by corrosion) must be estimated at this stage; it is recommended to assume it is in the range 10...30 mm.

The stress-strain relationship of the reinforcement should be modelled as realistically as possible, as this can significantly influence the results. Ideally, the relationship is known from tensile tests; otherwise, it is recommended to use the relationship according to Ramberg & Osgood (Chapter 2 of the document attached to [3]) with the correspondingly adjusted material parameters (see, for example, the steeldata.ch database). The assumption of a linear elastic-ideal plastic relationship is not helpful; the assumption of a bilinear relationship (linear elastic, linear hardening) may overestimate the deformation capacity and lead to nonconservative results.

Estimation of the wall displacement-earth pressure relationship

Determining the earth pressure development requires a reliable estimation of the soil parameters and the initial stress state in the backfill (at the beginning of the corrosion-induced wall displacement). Soil parameters are determined through triaxial tests or by reliable empirical values for the actual type of soil. The initial stress state is estimated by numerical simulations of the construction process (and any live loads) or by empirical approaches, the latter to be used with caution. If numerical simulations are performed, the uncracked and cracked elastic bending stiffness can be determined from the wall load-displacement curve (see the previous paragraph).

In current work, it has been shown that realistic modelling of the displacement behaviour of the corroding wall is not necessary to determine the development of the earth pressure in a decoupled analysis. Furthermore, the foundation stiffness may also be assumed to be infinite (i.e. rigid) in the first phase.

The development of the earth pressure results from an FE analysis of the corrosion-induced wall rotation, as in Sections 7 and 8. The soil hardening behaviour is to be modelled as realistically as possible with a suitable constitutive law (e.g. the *hardening soil model*), ideally calibrated by triaxial and oedometer tests. If this is impossible, calibration can be carried out using empirical results for similar soils from existing databases (see, for example, the soilmodels.com website).

Structural safety verification

The curves of the wall load-displacement behaviour (displacement-dependent resistance) and the relationship between earth pressure and wall displacement (displacement-dependent action) are superposed. If an equilibrium state is found (i.e. the action and resistance curves intersect), the structural safety verification is fulfilled. Otherwise, a refined decoupled analysis (Section 10.1.4) must be considered.

It should be noted that the displacement resulting from this analysis when reaching an equilibrium state has no relation to the displacements occurring in the structure due to the

partial safety factors used. Thus, it cannot be used to estimate displacement limit values (for example, to monitor a structure). Further analyses would be necessary based on a probabilistic approach (e.g. by assuming average values).

10.1.4 Refined decoupled analysis (LoA III)

By collecting additional data on the corrosion distribution or considering the stiffness of the foundation, it may be possible to achieve a more favourable result of the assessment.

Additional information on corrosion distribution

The simple decoupled analysis (Section 10.1.3) assumed that only the total cross-sectional loss was known, while the number of intact bars affected by corrosion was unknown. Therefore, the worst-case condition with the critical number of affected bars $n_{c,crit}$ was considered, for which the bearing resistance and the deformation capacity are minimal. If additional information on the corrosion distribution is available, it can be considered in the verification procedure.

If the number of corroding bars n_c is smaller than $n_{c,crit}$, the verification leads to the same result as the limit state analysis (B) from Section 10.1.2.

If $n_c > n_{c,crit}$, the calculation from Section 10.1.3 is repeated with the updated information. If an equilibrium state is found, the ultimate limit state design is fulfilled.

Consideration of the foundation and load history

Section 10.1.3 assumed a rigid foundation for the determination of the earth pressure. This assumption leads to a conservative estimate of the initial stresses, as a rigid-body rotation of the retaining wall during the backfill phase and the resulting decrease in earth pressure are neglected. However, if the material behaviour of the soil foundation (especially its stiffness) can be reliably estimated, this rotation may be considered, resulting in a more favourable value of the earth pressure.

On the other hand, it must be considered that the earth pressure could have increased between the time of construction and the occurrence of the first corrosion damage due to cyclic loading of the wall, for example due to variable live loads or temperature-related displacements. Furthermore, the effects of soil ageing can cause an increase in the coefficient of earth pressure (increased horizontal stress under constant vertical stress [169]). Even if this causes only minor changes in stress, it partially reduces the favourable wall unloading that occurred during the construction phase.

If the stiffness of the foundation is included in the calculation, it is recommended to model the construction process and the load history as realistically as possible. First, the excavation, the temporary earth stabilisation, and the spatially limited backfill between the wall and the temporary support must be considered. Neglecting these aspects leads to an incorrect estimate of the wall displacement that occurs during construction (see Section 8.4). Second, the load history in the service phase should be considered more carefully to identify a possible partial reloading of the wall backfill.

10.1.5 Coupled analysis (LoA IV)

If there is a possibility of load redistribution in the longitudinal direction of the wall, a coupled analysis can be carried out considering three-dimensional effects in the backfill and the soil-wall interaction, which can lead to a more favourable result. This is particularly possible if only individual segments of a dilated retaining wall are affected by corrosion. In such cases, depending on the geometry, a favourable three-dimensional stress state can result in the backfill. As a result of the greater displacement of the corroding segment, arching develops in the soil. Consequently, the horizontal soil stress is partially redistributed to the stiffer, noncorroding neighbouring segments. As a result, the corroding segment is un-

loaded, but the neighbouring segments are additionally loaded (Section 6.1.3) and deformed. Therefore, the behaviour of the soil and the corroding and noncorroding wall segments must be coupled and analysed step by step.

A prerequisite for the successful application of a coupled analysis is that the neighbouring segments have safety reserves and can withstand a higher load. If this is not the case, the coupled analysis will also not provide sufficient proof of structural safety.

10.1.6 Strengthening measures

If the previous verification stages cannot prove the safety of the wall, strengthening measures (anchoring of the wall, conversion to a gravity wall) or a new replacement wall must be considered.

10.2 Case study

The procedure described in Section 10.1 is illustrated in the following using a case study.

10.2.1 Description of the fictitious retaining wall

The fictitious retaining wall in Fig. 175 was built in 1972 along a road in a prealpine region. Its structural safety must be checked (ultimate limit state type 2, according to SIA 260).
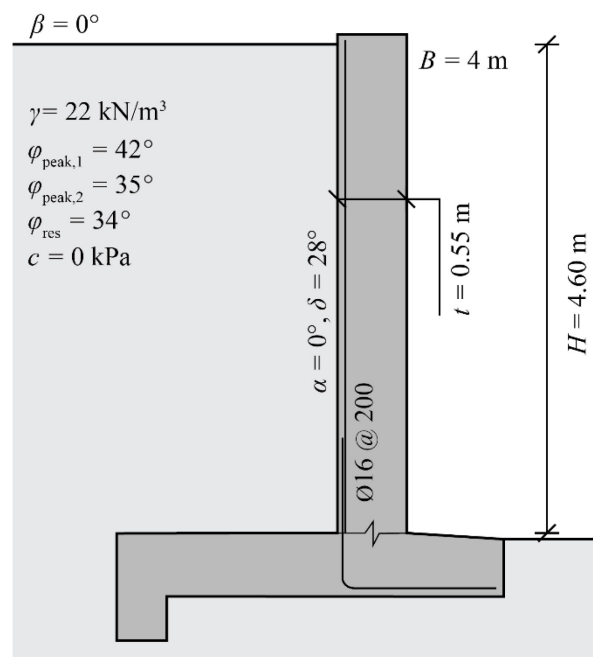
Fig. 175: Example wall, including details of geometry, reinforcement, and soil.

The 4.6 m high and 0.55 m thick hillside retaining wall is dilated in sections of 4 m length. It consists of concrete with compressive strength at design level f_{cd} = 40 MPa and is reinforced with Ø16@200 steel III (*Stahl III*) bars with the characteristic values given in Tab. 13. The reinforcement cover is 30 mm. The ground is homogeneous up to a depth of 15 m and consists of gravelly sand with a maximum (residual) shear strength of 42° (34°). The backfill of the retaining wall consists of excavated material and was only very lightly compacted. Increased compaction pressure can therefore be excluded.

A survey has shown that the wall reinforcement has corrosion damage directly above the construction joint due to honeycomb. It is estimated that the reinforcement cross-section is

reduced by a total of 30%. The distribution of corrosion among the different bars is unknown, but the expert in charge of the survey assumes that at least 50% of the bars are likely to be affected.

The characteristic values of the reinforcement are known from taken bars (Tab. 13). The stress-strain relationship of the reinforcement is assumed for these parameters according to Chapter 8 of the document attached to [3] and depicted in Fig. 176.

***Tab. 13:** Reinforcement properties.*

E_s	f_{sd}	f_{td}	A_{gt}
205 GPa	391 MPa	440 MPa	0.0043
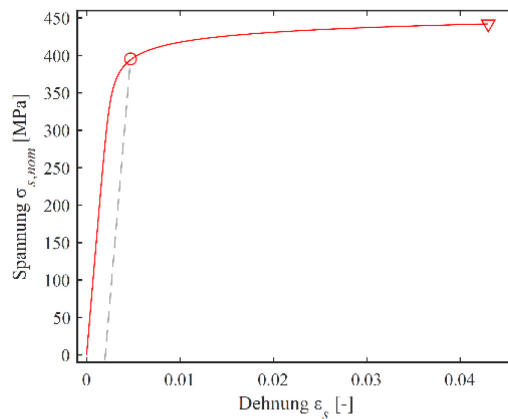
***Fig. 176:** Stress-strain relation of the reinforcement; circle = yield point, triangle = tensile strength.*

Also, a soil sample was taken in situ and tested in the laboratory. The most important soil properties are summarised in Tab. 14. The plastic soil behaviour (hardening law) is shown in Fig. 177. In situ measurements showed clear variations in soil deposition density between the eastern and western parts of the wall. Therefore, the wall stability should be investigated for both contractive and contractive-dilative behaviour. The two different soil deposition densities are referred to as type 1 and type 2 soil. The peak shear strength is 42° (type 1) respectively 35° (type 2), and the residual value is 34°. Since the soil was only very slightly compacted, the earth pressure coefficient is estimated as $K_0 = 1 - \sin \varphi_{\text{peak}}$ (see Sections 2.1.4 and 8.1).

***Tab. 14:** Soil mechanical properties.*

	E	φ_{peak}	φ_{res}	γ	K_0
Soil type 1	49.9 MPa	42°	34°	22 kN/m³	0.33
Soil type 2	23.8 MPa	35°	34°	22 kN/m³	0.43
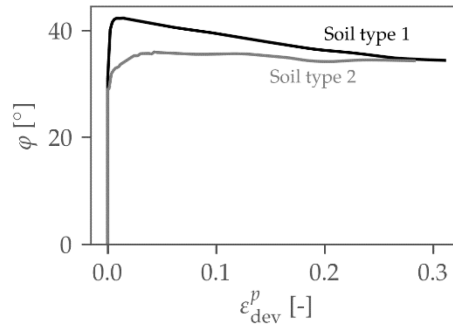
Fig. 177: *Soil hardening law.*

10.2.2 Triage (LoA I)

Limit state analysis (A)

The average cross-section on all bars (corroded and uncorroded) is $(1 - \zeta_m) \cdot a_s = 0.7 \cdot 1005 = 704 \text{ mm}^2/\text{m}'$. This results in a bending resistance in the construction joint of $m_{Rd} = 140 \text{ kNm/m}'$. The design value of the bending moment from the earth pressure is $m_{Ed} = 159 \text{ kNm/m}'$ for soil type 1 and $m_{Ed} = 207 \text{ kNm/m}'$ for type 2.

Limit state analysis (B)

The reinforcement cross-section of the noncorroded bars is $(1 - n_c/n_{tot}) \cdot a_s = 0.5 \cdot 1005 = 503 \text{ mm}^2/\text{m}'$ (n_c = number of corroded bars, n_{tot} = total number of bars). This results in a bending resistance of $m_{Rd} = 100 \text{ kNm/m}'$. The design value of the bending moment from the active earth pressure (after full mobilisation of the residual shear strength) is $m_{Ed} = 108 \text{ kNm/m}'$.

Conclusion

The ultimate limit state design can neither be fulfilled with the limit state analysis (A) nor (B). Therefore, a calculation according to LoA II is carried out.

10.2.3 Simple decoupled analysis (LoA II)

Estimation of the load-displacement behaviour of the wall

The critical number of corroding bars according to Equation (10.1) is assumed for the decoupled analysis in this approximation stage. Thus, for ζ_m = 0.3 half of all bars are considered corroded. For simplicity, the load-displacement behaviour of the wall is therefore determined for 2 m wall length and with 5 corroded and 5 intact bars according to the model from Chapter 8 of the document attached to [3]. The damaged length is assumed to be 20 mm and the cross-sectional loss per corroded bar is 60%.

The resulting load-displacement behaviour for ζ_m = 0.3 is shown in Fig. 178 (blue). The corresponding curves for different average section losses are also drawn in Fig. 178 (grey) to illustrate the influence of corrosion on the load-displacement behaviour of the wall. In each case, the critical number of corroding bars was assumed. A circle in the load-displacement curve indicates the failure of the retaining wall. The reduction in ultimate load and deformation capacity with increasing mean section loss is clearly visible. In a verification, it is advisable to record the behaviour for several degrees of damage to estimate the influence of corrosion development.

Estimation of the wall displacement-earth pressure relationship

FE analyses are carried out for the two soil types to estimate the earth pressure development as a function of the corrosion-induced wall displacement. The modelling procedure was described in Sections 7 and 8 and the same constitutive law was adopted. Since the

actual backfill is only slightly compacted, the initial stress state is modelled by depositing the fictitious backfill in ten layers of equal thickness. Subsequently, a wall rotation around the wall base point is imposed, and the bending moment acting at the construction joint is determined.

The resulting curves of the actions at the design level are shown in Fig. 178 (black). The typical characteristics of the different soil densities are observed: Soil type 2 (loose) has a higher initial moment and shows a contractive behaviour, characterised by a slower un-loading until the residual shear strength is reached. Soil type 1, on the other hand, shows a contractive-dilative behaviour and exhibits a minimum at $w/H \approx 7 \cdot 10^{-3}$ corresponding to the mobilisation of the peak shear strength, followed by a moment increase until the residual strength is reached.

Structural safety verification
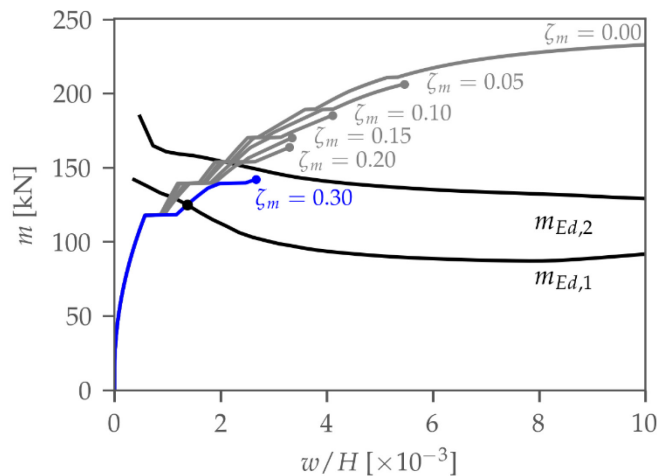
Fig. 178: *Acting moment from soil type 1 ($m_{Ed,1}$) and 2 ($m_{Ed,2}$) and resistance per mean section loss as a function of the wall displacement.*

As shown in Fig. 178, an equilibrium state can be found for soil type 1 with the mean section loss of ζ_m = 0.3 (intersection of the action and resistance curves). The structural safety for the eastern part of the retaining wall is thus proven.

However, no equilibrium can be found for soil type 2: the action curve runs above the re-sistance curve. This is even though the action from active earth pressure (with $\frac{w}{H} > 0.01$ and full mobilisation of the residual shear strength) is smaller than the load-bearing re-sistance of the wall, which shows that the limited deformation capacity of the wall can lead to failure in this case.

As the ultimate limit state could not be verified for the western part of the wall with a type 2 backfill, a refined decoupled analysis is carried out.

10.2.4 Refined decoupled analysis (LoA III)

The owner commissions a company specialising in structural surveys to perform ultrasound measurements at the base of the wall on the valley side. The measurement shows a high probability that honeycombs are present along 3/4 of the length of the wall section. There-fore, the wall load-displacement behaviour is calculated again according to Section 10.1.4, with the update that 75% of the bars are affected by corrosion. The loss of cross-section per bar is now 40%.
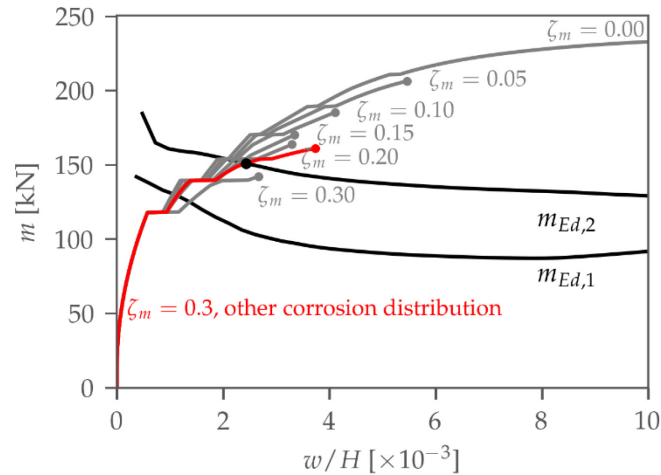
Fig. 179: *Acting moment from soil type 1 ($m_{Ed,1}$) and 2 ($m_{Ed,2}$) and resistance per mean section loss as a function of the wall displacement from Fig. 4 (grey) and load-displacement curve from the updated calculation (red).*

As a result of the updated assumptions, the structural resistance and the displacement capacity of the retaining wall could be increased, and an equilibrium state could also be found for the action curve of soil type 2 (Fig. 179). The ultimate limit state verification is thus fulfilled.

10.3 Closing remarks
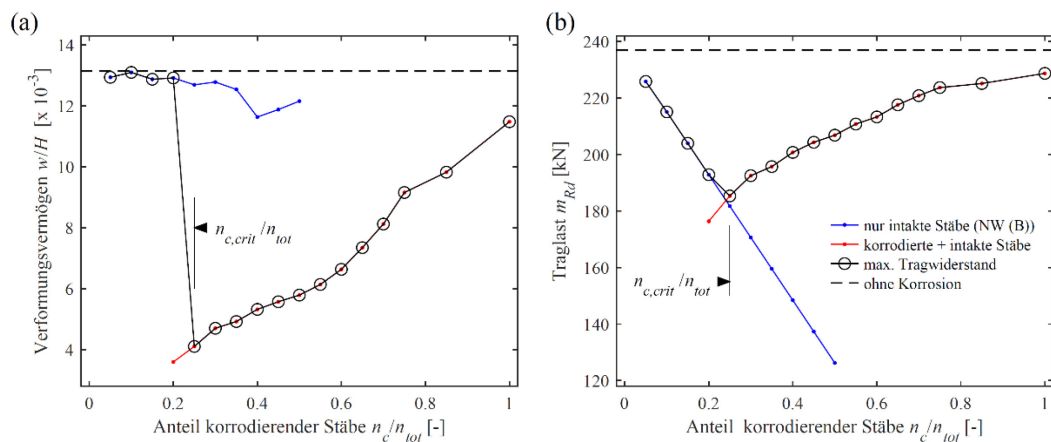
Fig. 180: *Influence of corrosion distribution: (a) deformation capacity and (b) bending resistance of the retaining wall considered in the above example for ζ_m = 10% mean section loss depending on the proportion of bars affected by corrosion.*

- The refined decoupled analysis in the case study highlights the variability of the results depending on the corrosion parameters. Determining the corrosion damage as accurately as possible can lead to a more favourable assessment of the structural safety. Fig. 180 illustrates the deformation capacity and the ultimate load for the case study for an average degree of damage of ζ_m = 0.1 (in this case $\frac{n_{c,crit}}{n_{tot}} \approx 0.3$) depending on the proportion of bars affected by corrosion. The comparison illustrates that (i) Equation (10.1) approximates well the critical number of affected bars leading to a minimum of bending resistance and deformation capacity, and (ii) the additional information on the actual number of bars affected by corrosion can lead to a significantly more favourable result.

- Concerning the action, retaining walls that are backfilled with contractive soil (i.e. loosely deposited) must be assessed more critically. Contractive soil implies a higher initial earth pressure, and the unloading to the residual value of the active earth pressure requires greater wall displacements.

- Strong compaction of the backfill has an unfavourable effect on the earth pressure development, as irreversible horizontal strain remain in the soil and larger wall displacements are required to achieve the residual value of the active earth pressure.

- From the point of view of both action and deformation capacity, stocky retaining walls are more critical because (i) they experience a greater initial earth pressure due to their high stiffness, (ii) the deformation capacity is generally smaller than for slender walls, and (iii) due to the smaller bending tensile forces, it is assumed that these walls have smaller diameter reinforcing bars for which the loss of cross-section increases rapidly as a result of progressive corrosion.

- For long retaining walls, for which a plane strain state can be assumed, the earth pressure may be conservatively estimated if the mechanical properties of the backfill are determined through triaxial tests, as the soil shear strength is then underestimated (Appendix II.2.2).

- From the results, no generally applicable strategy can be derived with regard to monitoring through displacement measurements. The expected displacements depend on the wall geometry, the reinforcement, the corrosion distribution, the compaction of the backfill soil, and the soil parameters. The likelihood of success of using the monitoring method must be assessed for each individual case. Limit/trigger values can only be defined for the individual case (or, possibly, for different classes of walls). It is generally recommended to measure the deformations due to further actions (e.g. temperature) by means of reference sensors (close to the construction joint), as a purely numerical consideration (e.g. estimation of the expected deformations due to temperature change) is more complex and potentially subject to uncertainties (see Section 9.2).

11   Summary and conclusions

Destructive tests on cantilever retaining walls have revealed significant corrosion of their main reinforcement, leading to a loss of strength and rotation capability that could result in a brittle structural failure mode. Due to the reduced rotation capacity, it is generally unknown whether the soil can reach the active limit state before the wall fails or the structure collapses under loads higher than the active earth pressure. Therefore, to assess the safety of existing structures, the correct quantification of the earth pressure between the initial and active states is crucial. Various studies have investigated the active earth pressure and the earth pressure unloading for different wall displacement modes in the past but often focused on just one aspect, missing a general applicability of the results.

In this work, a comprehensive analysis of the soil-structure interaction for corrosion-damaged cantilever retaining walls has been carried out. An improved understanding of the problem was obtained thanks to an experimental, numerical, and analytical study. As a result, a general framework was developed for the safety assessment of existing walls. It includes analytical solutions for the ultimate limit state and numerical models to simulate the unloading process. These analyses were complemented by numerical simulations at the particle state that provided helpful insight for developing and calibrating the constitutive model.

The governing failure mode for corrosion-damaged cantilever retaining structures is a bending failure, causing the wall stem to rotate about the damaged zone, which previous studies identified to be located at the construction joint (i.e. at the stem's toe). A bounded solution based on the limit analysis was proposed for this failure mode, which offers excellent accuracy. Although the soil flow is generally nonassociated, it has been shown that the proposed analytical solution can be successfully used to estimate the moment at the ultimate limit state. However, the solution does not represent strict bounds because of the flow nonassociativity. Conventional wall design methods were later analysed using the proposed limit analysis solution, showing that some procedures used in the past led to an overestimation of the bending moment. Thus, walls designed using these methods may have additional safety margins against structural failure. Practitioners may use the proposed solution to benchmark numerical models and verify existing walls.

An experimental study was carried out to investigate the unloading behaviour. The most influential parameters, the soil behaviour and the initial stress state, were varied to gain a complete understanding of the unloading process. An ad-hoc experimental setup that guarantees repeatable and reliable results was designed and built. In the tests, a higher initial moment was measured in loose samples than in dense samples. Due to the higher displacement required by loose soil to mobilise its strength, a more compliant moment-rotation response was also observed in the loose sample, thus needing a higher wall rotation to reach the residual value of the moment.

The initial earth pressure acting on retaining walls was further investigated using a stiffened steel wall, showing that a bilinear earth pressure distribution results due to friction at the soil-wall interface.

Compaction-induced earth pressures were studied by applying a static compaction to the backfill after the deposition of each layer to simulate higher stresses. The resulting earth pressure distribution featured a maximum close to the soil surface, leading to an earth pressure resultant force shifted toward the soil surface. Due to the higher location of the resultant force and the increased soil stiffness, a very fast unloading was observed in the compacted samples at the beginning of the rotation phase.

Furthermore, tests were carried out to investigate the three-dimensional effects in the backfill in the case of a single damaged wall section. A stress redistribution in the backfill is observed when a single wall section fails, originating a curved failure mechanism. Due to the stress redistribution, the limit load resulting on the damaged section is lower than under plane strain conditions; consequently, the moment acting on the intact neighbouring walls increases.

Based on the knowledge gained, a custom-tailored constitutive model was proposed to simulate the unloading process of corrosion-damaged walls. It is based on well-known and

widely used models, allowing the most straightforward use in practice. The proposed constitutive law is similar to the Hardening Soil model, which practitioners can employ to obtain an approximative quantification of the wall unloading process. A procedure was proposed to model the soil-structure interaction considering the entire loading history (from construction to the onset of corrosion damage). The model obtained was then validated against the experimental results, generally showing excellent agreement. Some challenges were encountered in modelling soil compaction, for which only approximate results could be obtained. Instead, a meshless method could be used to improve the quality of the results.

The soil behaviour was calibrated through laboratory and virtual element tests using the LS-DEM. The LS-DEM simulations showed that a higher strength is mobilised in a biaxial test (i.e. under plane strain conditions) than in a triaxial test. This explained the low earth pressure measured in the wall tests and could mean that the extended Matsuoka-Nakai model represents a better alternative to model soil yielding. However, as it is not widely known in practice, the Mohr-Coulomb failure criterion was calibrated to match plane strain conditions to ensure practitioners a more straightforward application of the proposed model. On the other hand, the results of a parametric study on the LS-DEM sample did not evidence any pressure dependence of the strength, disproving the proposition of a curved failure surface in the meridional stress plane.

Furthermore, a particle-scale study of the earth pressure at rest was carried out using the LS-DEM. The coefficient of earth pressure at rest K_0 was shown to depend on the soil density (or the coordination number) and the interparticle friction, just as the maximum shear strength. Therefore, Jáky's analytical solution delivered a rather good, conservative estimate for the K_0 coefficient of Perth Sand. In particular, Jáky's solution showed an excellent fit of the data of the dense sample. At the same time, the coefficient of loose sand was overestimated, although the qualitative trend of K_0 as a function of the peak strength was matched faultlessly. However, since there is no direct causation, this result must be treated with caution and cannot be generally applied, as additional research is needed.

The limit state under three-dimensional conditions was then studied numerically, showing good agreement with experimental data. The stress redistribution was confirmed to cause a lower limit state on the failing wall, and a stress increase in the neighbouring sections was measured. Some challenges were encountered in modelling the problem with the finite element method, and a solution was proposed to overcome them. Later, a parametric study showed how the soil strength and the geometry of the wall sections contribute to the stress redistribution, leading to lower limit loads on the failing sections and higher moment on the neighbouring sections.

The developed model was then applied to some practical situations in Section 9. The failure behaviour of cantilever retaining walls was studied by combining the model of the soil-structure interaction with a refined structural model. It was shown that the evolution of the earth pressure is basically independent of the wall corrosion degree, as the same evolution could be obtained by imposing a rotation to the intact wall at its toe. It follows that the actions and resistances can be decoupled, and the accurate modelling of the structural behaviour is not necessary for quantifying the earth pressure.

The thermal actions on cantilever retaining walls were then investigated. On the basis of simple meteorological data, the correct temperature field in the wall could be simulated and validated against field measurements. Temperature fluctuations were shown to contribute to wall displacement and generate a cyclic loading of the wall, leading to additional displacements in the vicinity of the construction joint. The proposed extension of the numerical model can be used to better understand the monitoring data and, possibly, to filter out temperature-caused wall displacements.

In addition, the influence of two parameters that could not be varied in the experiments, namely the wall height and the inclination of the backfill, was investigated using the numerical model. As was shown in the LS-DEM study, the pressure dependence of the material behaviour can be easily modelled by the proposed constitutive law (i.e. by assuming a pressure-dependent stiffness), meaning that the numerical model can be employed to model larger structures. The obtained results showed a similar behaviour as observed in the experiments, confirming that no scale effect at the soil-wall interface level influenced the results. Furthermore, the rotation required to reach the residual value of the moment was found to be constant with variable wall height.

The same was observed with the variable backfill inclination, which did not influence the soil behaviour in any significant way.

This work has proposed a complete framework to quantify the earth pressure acting on corrosion-damaged cantilever retaining walls, from the initial to the ultimate state. In addition, various aspects of the mechanical behaviour of granular soil were investigated at the grain scale, contributing to the general understanding of the behaviour of this important class of materials. Finally, the gained knowledge and the developed framework were applied to some practical cases to further investigate the soil-wall interaction.

The outcome of this work can be applied to the evaluation of the safety of existing walls, the interpretation of the results of the monitoring systems, and the development of a monitoring and maintenance strategy. A complete study on the wall unloading process was conducted under different conditions, setting the basis for an improved understanding of the earth pressure acting on corrosion-damaged walls. Based on the obtained framework, additional features can be added and studied, such as water pressures or cyclic loads such as, for example, traffic. Furthermore, these results can be considered to perform structural analyses (considering the structural model currently developed at the Institute for Structural Engineering) to identify the most critical wall profiles in terms of safety.

More specifically, some topics studied in this work deserve further investigation.

For example, the initial stress conditions in wall backfills should be studied further. Using the LS-DEM model, the effect of different particle shapes can be reviewed by only assuming a particular subset of the scanned material (e.g. only rounded grains), or a completely different material could be scanned. In addition, the role of contact anisotropy on the earth pressure at rest should be investigated. In a later step, the role of the wall interface friction on the initial earth pressure distribution could be investigated for a broader set of parameters. Furthermore, the effects of the layer thickness and compactor dimensions on the compaction-induced earth pressure should be analysed. Using the discrete element method, or another meshless method, could be advantageous.

The last Section, Section 10, synthesised the results of projects AGB 2015/028 and AGB 2015/029. A multistage verification procedure for cantilever retaining walls was proposed and detailed in a fictitious case study. Furthermore, the most critical retaining walls profiles were identified as (i) having low slenderness, (ii) being backfilled with loosely deposited soil, (iii) having compacted backfills. Instead, no generally applicable strategy can be derived regarding monitoring through displacement measurements. In fact, the expected displacements depend on the wall geometry, the reinforcement, the corrosion distribution, the compaction of the backfill soil, and the soil parameters. The applicability of the monitoring method must be assessed for each case or class of similar walls (considering the wall profile, the location, etc.).

Appendices

I Graphical determination of the active earth pressure

I.1 Poncelet's method

Fig. 1: Poncelet's method.

Given a wall and backfill geometry, soil friction angle φ, and wall friction angle δ, Poncelet's construction can be obtained as follows (Fig. 1):

1. Draw a line inclined by φ w.r.t. the horizontal passing through F. The intersection with the soil surface defines point G.
2. Draw a semicircle with centre M and radius $\overline{FM}$, where $\overline{FM}=\overline{GM}$.
3. Draw a line inclined by $(\varphi + \delta)$ w.r.t. the backface of the wall passing through A. The intersection with $\overline{FG}$ defines point B.
4. Draw a line perpendicular to $\overline{FG}$ and passing through B and intersecting the semicircle drawn before. The intersection defines point C.
5. Draw a circular arc centred at point F of radius $\overline{CF}$ that spans between C and $\overline{FG}$. The intersection with $\overline{FG}$ defines point D.
6. Draw a line parallel to $\overline{AB}$ passing through D. The intersection with the soil surface defines point E.
7. Connect E to the bottom of the wall F. The segment $\overline{EF}$ is the failure line, compliant with Coulomb's theory.
8. Draw a circular arc centred at point D, with radius $\overline{DE}$, that spans between E and $\overline{FG}$. The intersection with $\overline{FG}$ defines point E'.

The active earth pressure then reads:

$$E_{\mathrm{a}} = \gamma \cdot \|\triangle \mathrm{DEE'}\| , \tag{I.1}$$

where $\|\triangle \mathrm{DEE'}\|$ represents the area of triangle $\triangle$ DEE'.

It can indeed be shown that for the critical failure line, the line for which $\partial E_{\mathrm{a}}/\partial \chi = 0$, the following equality holds (e.g., [170, pp. 185–186]):

$$\|\triangle \mathrm{AEF}\| = \|\triangle \mathrm{DEF}\|. \tag{I.2}$$

Therefore,

$$G = \gamma \|\triangle\text{AEF}\| = \gamma \|\triangle\text{DEF}\| = \gamma \frac{\overline{\text{DF}} \cdot \overline{\text{EH}}}{2}. \tag{I.3}$$

Since the triangle $\triangle$ DEF and the force diagram (Fig. 1) are similar, it follows:

$$\frac{E_a}{\overline{\text{DE}}} = \frac{G}{\overline{\text{DF}}} \Leftrightarrow E_a = G\frac{\overline{\text{DE}}}{\overline{\text{DF}}} = \gamma \frac{\overline{\text{DE}} \cdot \overline{\text{EH}}}{2} = \gamma \cdot \|\triangle\text{DEE'}\|, \tag{I.4}$$

which proves Equation (I.1). The last equality in Equation (I.4) holds because $\overline{\text{DE}} = \overline{\text{DE'}}$.

I.2 Culmann's method

Fig. 2: Culmann's method.

Culmann's construction can be obtained as follows:

1. Draw the φ-line: a line inclined by φ w.r.t. the horizontal passing through A.
2. Draw the earth-pressure line: a line inclined by $(\varphi + \delta)$ w.r.t. the backface of the wall passing through A.
3. Draw a trial failure line $\overline{\text{AB'}}$.
4. Draw $\overline{\text{B'C'}}$ parallel to the wall backface.
5. Draw $\overline{\text{D'C'}}$ parallel to the earth-pressure line
6.
7. Repeat the same procedure from 3 to 5 until the locus of the point D, the "Culmann's E-line", can be inferred and drawn.
8. Find the point D on the E-line that maximises the length of $\overline{\text{DC}}$. From that point, draw the segment $\overline{\text{DC}}$ parallel to the earth-pressure line.
9. Draw $\overline{\text{BC}}$, by drawing a line parallel to the wall backface and passing through C.
10. Connect A and B to obtain the critical failure line.

Triangle $\triangle$ACD is similar to the force diagram. Hence,

$$E_a = G \cdot \frac{\|\overline{\text{DC}}\|}{\|\overline{\text{AC}}\|} = \frac{1}{2}\gamma \|\overline{\text{AE}}\| \|\overline{\text{BI}}\| \cdot \frac{\|\overline{\text{DC}}\|}{\|\overline{\text{AC}}\|} \tag{I.5}$$

where

$$G = \gamma \|\triangle\text{ABE}\| = \gamma \|\triangle\text{ACE}\| = \frac{1}{2}\gamma \|\overline{\text{AC}}\| \|\overline{\text{EG}}\|. \tag{I.6}$$

The second equality in Equation (I.6) holds because $\triangle$ABE and $\triangle$ACE share the same basis $\overline{\text{AE}}$ and have the same height $\overline{\text{BI}}$. Thus, Equation (I.5) becomes

$$E_a = \frac{1}{2}\gamma \, \|\overline{EG}\| \, \|\overline{DC}\| \; . \tag{I.7}$$

I.3 Mörsch's method

The following procedure can be used to determine the failure lines developed in the back-fills of cantilever retaining walls subjected to a horizontal rigid-body motion.
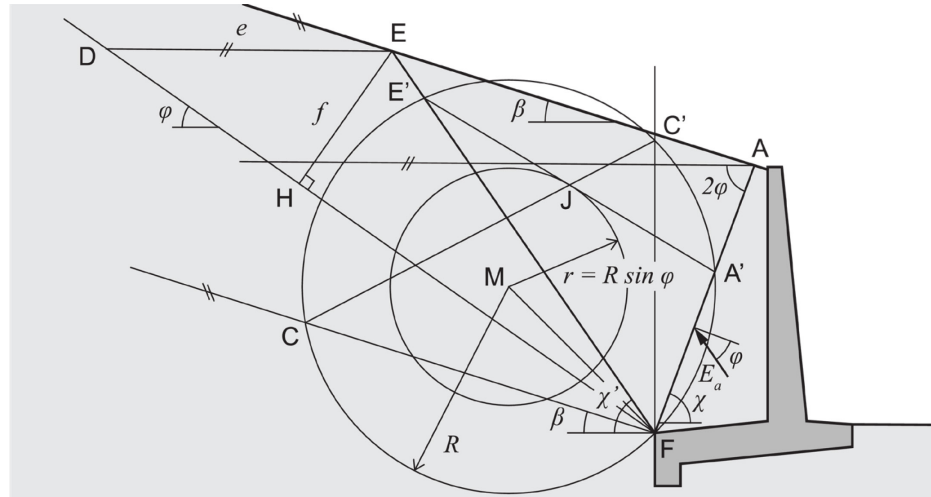

Fig. 3: Mörsch's method.

1. Arbitrarily choose a point M. Preferably on a straight line passing through F and making an angle of 45° with the horizontal.
2. Draw a circle of radius $R = \overline{MF}$ centred at M.
3. Draw a circle of radius $r = R \sin\varphi$ centred at M.
4. Draw a line parallel to the soil surface passing through F. Its intersection with the circle of radius R defines point C.
5. Draw a vertical line passing through A. Its intersection with the circle of radius R defines point C'.
6. Connect points C and C'. The intersection of $\overline{CC'}$ with the circle of radius r defines point J. [9]
7. Draw a line tangent to the circle of radius r at point J. The intersection of this line with the circle of radius R defines points A' and E', which lie on the two failure lines.
8. Connect $\overline{FA'}$ and $\overline{FE'}$ and, if necessary, extend the segments until they meet either the soil surface or the wall. $\overline{FA}$ and $\overline{FE}$ define the failure lines.
9. Draw a line s passing through A and inclined by 2φ to $\overline{AF}$.
10. Draw a line parallel to s through E. Its intersection with the natural slope line (i.e., the line making an angle of φ with the horizontal) defines point D. We define $e := \overline{DE}$.
11. Draw a line perpendicular to the natural slope line through E. its intersection with the natural slope line defines point H. We define $f := \overline{EH}$.

The active earth pressure then reads:

$$E_a = \gamma \, \frac{e \cdot f}{2} \; . \tag{I.8}$$

---

[9] In german, point J is defined *Involutionszentrum*.

II   Description of the test soil

This appendix describes the test soil used in this work and its mechanical behaviour. Experimental and numerical tests were carried out to obtain reliable results. First, the experimental results are presented. These represent the link to reality and are mainly used to calibrate the numerical models. Then, the numerical results (based on LS-DEM simulations, see Section 5.2.3) are presented. The numerical simulations allowed to gain information usually unavailable from laboratory tests and, in particular, to study the soil behaviour under plane strain conditions and at very low stresses.

II.1   Experimental description

The sieve curve determined in compliance with the DIN EN ISO 17892-4 standard [171] is shown in Fig. 4. The white dots represent the raw lab data. A line is interpolated between the raw points using piecewise cubic Hermite splines. As a reference, the supplier's specification is also plotted.
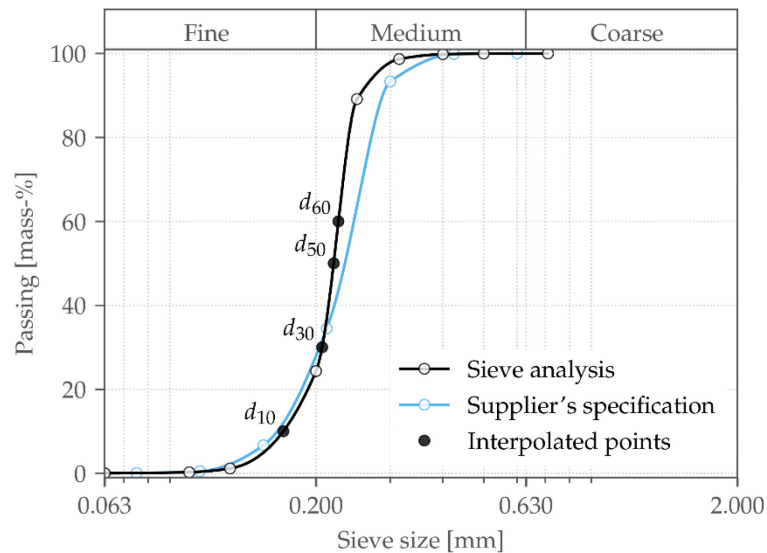
Fig. 4: Sieve curve of Perth sand.

Perth sand can be classified as medium-fine sand [9], [172], and its USCS classification is poorly graded sand (SP). The grain surface is relatively smooth [126].

The grain density of $\rho_{\mathrm{grain}} = 2.65\,\mathrm{g/cm^3}$ was determined using a pycnometer by Buchheister [126] and corresponds to the density of silica.
The bulk density of soil is variable and depends on the grain packing, which influences the porosity of a soil sample. In general, well-graded soil has a higher variability of porosity than poorly-graded soil.
The porosity of a granular sample is defined as

$$\phi = \frac{V_{\mathrm{vol}}}{V_{\mathrm{tot}}},\tag{II.1}$$

where V_{vol} is the volume of the voids, and V_{tot} is the total volume of the sample. In soil mechanics, the void ratio is often used instead of the porosity:

$$e = \frac{V_{\mathrm{vol}}}{V_{\mathrm{grains}}} = \frac{\phi}{1 - \phi},\tag{II.2}$$

where V_{grains} is the total volume of all grains in the sample.

The (dry) bulk density can therefore be defined as

$$\rho_d = (1 - \phi)\rho_{grain} = \frac{\rho_{grain}}{1 + e}. \tag{II.3}$$

The relative density of soil is defined, e.g., by ASTM Standard D4253-16 [131] as

$$D_d = \frac{e_{max} - e}{e_{max} - e_{min}} \cdot 100 = \frac{\rho_{d,max}(\rho_d - \rho_{d,min})}{\rho_d(\rho_{d,max} - \rho_{d,min})} \cdot 100, \tag{II.4}$$

where e_{max} and ρ_{min} correspond to the loosest possible packing, and e_{min} and ρ_{max} to densest possible packing. The relative density of soil indicates its plastic behaviour qualitatively. Dense soil dilates when sheared, while loose soil contracts.
The minimum and maximum density were determined as described by the ASTM Standards D4253-16 and D4254-16 [131], [173], using Method A and Method 2A, respectively. The resulting values are summarised in Tab. 1.

***Tab. 1:** Minimum and maximum density of Perth sand*

ρ_{min}	1.484 kN/m^3	95% CI [1.481, 1.488]
ρ_{max}	1.700 kN/m^3	95% CI [1.697, 1.703]
e_{min}	0.559	95% CI [0.554, 0.562]
e_{max}	0.785	95% CI [0.781, 0.788]

Shearing behaviour

A series of drained triaxial tests were performed to characterise the shearing behaviour of Perth sand. While it is impossible to reproduce the exact stress path developed in a wall backfill during unloading under plane strain conditions in a triaxial sample (due to its axial symmetry), triaxial testing is a standard procedure in geotechnics known to produce reliable results under controlled conditions. On the other hand, biaxial tests, which aim to guarantee plane strain conditions by design, are more complex and less reliable. The main challenges are the side friction and the preparation of a prismatic sample (e.g. [174]).

Axial compression tests were carried out. A list of the tests carried out is given in Tab. 2.

***Tab. 2:** Summary of triaxial tests. The identifier is composed of a letter indicating whether the sample was sheared in axial compression (c) or extension (e), a number indicating the consolidation pressure, and a letter describing the sample density (l: loose; d: dense).*

Identifier	Consolidation pressure	Initial void ratio	Initial relative density
c025d	25 kPa	0.59	84%
c050d	50 kPa	0.55	104%
c100d	100 kPa	0.56	99%
c025l	25 kPa	0.71	33%
c050l	50 kPa	0.74	19%

Different relative densities have been tested to match the backfill densities assumed in the wall tests.

All tests were carried out on saturated samples to allow accurate volume change measurements. Tatsuoka et al. [175] showed that the difference in friction angle between dry and fully saturated samples is less than one degree, which might be a random error caused by the soil variability. This result is confirmed by studies on the intergranular friction of uncontaminated quartz sand (i.e. clean sand with no traces of organic material) [116].

Evaluation

Geotechnical triaxial tests are usually evaluated by assuming a homogeneous stress state and displacement field over the whole sample. They are therefore evaluated in terms of the deviatoric stress

$$q = \sigma_a - \sigma_r,$$

(II.5)

the mean effective stress

$$p' = \frac{1}{3}(\sigma_a + 2\sigma_r),$$

(II.6)

the deviatoric strain

$$\varepsilon_{\text{dev}} = \frac{2}{3}(\varepsilon_a - \varepsilon_r),$$

(II.7)

and the volumetric strain

$$\varepsilon_v = \varepsilon_a + 2\varepsilon_r,$$

(II.8)

where index $_a$ indicates an axial quantity and $_r$ indicates a radial quantity.

This evaluation procedure usually provides reasonable estimations of the stiffness and strength parameters needed to design geotechnical structures. However, it is impossible to perform a triaxial test in the laboratory where the stress and displacement fields are homogeneous over the sample. Indeed, boundary effects are always present (e.g. the rough interface between the sample and the platens), and the sample deformation is not homogeneous.

Therefore, a different approach is applied to calibrate the constitutive models used in the following sections. Only tractions and displacements measured at the sample boundaries are used so that no assumption about the stress or displacement field over the sample must be made. The triaxial test will be simulated numerically as a boundary value problem in a second step. Here, the constitutive model will be calibrated to match the quantities measured in the laboratory.

The measured quantities in the triaxial tests are the axial force, the cell pressure and the backpressure in the soil specimen (their difference give the lateral pressure applied to the sample), the axial displacement at the sample's top, and the sample volume change. The initial geometry of the sample is carefully measured at the beginning of each test. The following quantities can therefore be derived. The traction acting at the sample top in the axial direction is

$$p_a = \frac{F_a}{A_0},$$

(II.9)

where F_a is the axial force exerted by the top platen on the sample and A_0 is the initial cross-sectional area of the sample. The pressure applied on the specimen's lateral surface is

$$p_r = p_{\text{cell}} - p_{\text{back}},$$

(II.10)

where p_{cell} is the cell pressure, and p_{back} is the backpressure applied to the sample. Both p_a and p_r are corrected to take the membrane stiffness into account following the procedure proposed by Kuerbis and Vaid [176]. For these corrections, assumptions regarding the deformation of the sample and the stress distribution must inevitably be made.

The normalised axial displacement at the sample top is

$$\bar{\delta}_a = \frac{u_a}{H}, \tag{II.11}$$

where u_a is the displacement at the sample top and H the sample height in the undeformed configuration. The normal displacement $\bar{\delta}_a$ is defined as an engineering strain. However, due to the inhomogeneous displacement field, it cannot be regarded as the strain at a material point in the sample.

The normalised volume change is

$$\bar{\delta}_{vol} = \frac{\Delta V}{V_0}, \tag{II.12}$$

where ΔV is the volume change and the V_0 the volume of the undeformed configuration.
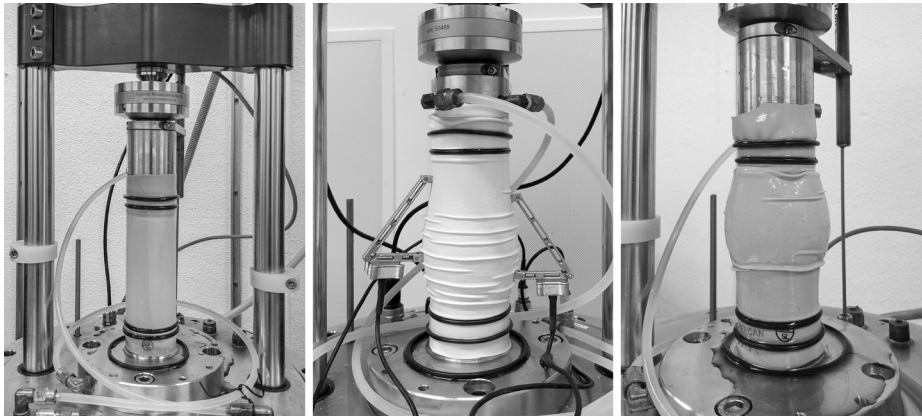
Results

Fig. 5: *Left: triaxial sample before filling the cell; centre: loose sample after shearing; right: dense sample after shearing.*

Fig. 5 shows the pictures of a loose (centre) and dense (right) sample. Both samples experienced bulging. In addition, two shear bands that cross diagonally could be observed by the naked eye in the dense sample. Two shear bands develop because of the constrained rotation of the top platen. On the other hand, no visible shear band was developed in the loose sample, although strain localisation occurs in loose sands at a smaller scale, as shown by Finno et al. [111]. The resulting deviatoric and volumetric behaviour is plotted in Fig. 6. Dense samples show hardening behaviour followed by a softening regime. The peak strength is mobilised at a normalised axial displacement of about 0.02-0.05, followed by a softening phase until the residual strength is mobilised. The volumetric behaviour is first slightly contractive, then dilative. At large deformations, the rate of dilation decreases, but a state of constant volume is not reached.

Loose samples show hardening behaviour until the residual state is reached at a normalised axial displacement of 0.15-0.2 and show a more pronounced contraction than dense samples, followed by slight dilation.
Samples c025d and c025l were subjected to an unloading-reloading cycle. Immediately after the load reversal, a steep elastic response is seen, followed by plastic yielding characterised by hardening. At the end of reloading, a higher sample strength is observed.
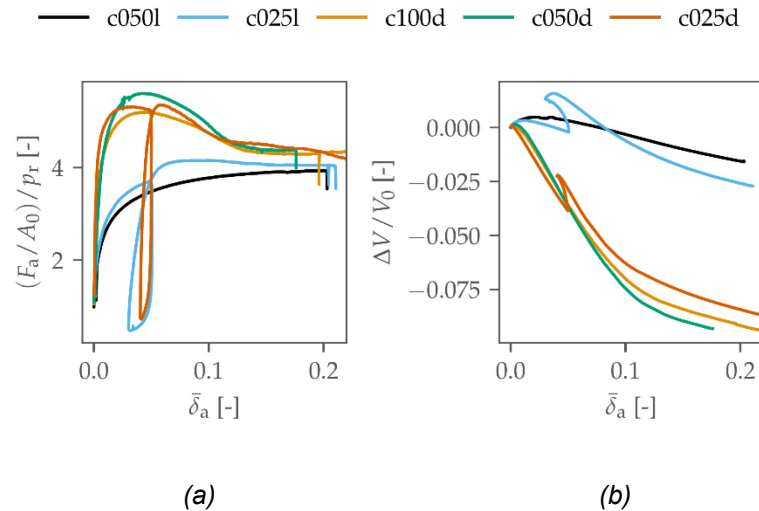
(a)   *(b)*

Fig. 6: *Results of axial compression tests on Perth Sand: (a) deviatoric behaviour as the normalised traction applied at the sample top versus the normalised displacement; (b) volumetric change of the samples tested in axial compression versus the normalised displacement (compression is positive).*

The samples tested at different consolidation stress levels do not show any correlation between the soil strength and the stress level (Fig. 6a). The variability of the soil sample (e.g. the slightly different relative densities) can explain the small deviations. This topic will be investigated more in detail in a later section. A pressure dependency of the stiffness is instead observed in the nonnormalised data.

A rough estimate of the soil strength can be obtained by assuming a homogeneous stress state over the whole sample.
In that case, the following relation (based on the Mohr-Coulomb failure criterion) holds:

$$\varphi = \arcsin\left(\frac{\frac{\sigma_{max}}{\sigma_{min}} - 1}{\frac{\sigma_{max}}{\sigma_{min}} + 1} \right), \tag{II.13}$$

where σ_{max} and σ_{min} are the maximum and minimum principal stress, respectively. The following relation approximately holds:

$$\frac{\sigma_{max}}{\sigma_{min}} \approx \frac{\frac{F_a}{A_0}}{p_r}. \tag{II.14}$$

Based on the test results, a peak friction angle of $\varphi_{peak} \approx 43°$ and a residual of $\varphi_{res} \approx 37°$ would result.

Oedometer tests

Two oedometer tests were carried out to study the soil consolidation properties: a loose and a dense sample were tested, as shown in Tab. 3.

Tab. 3: *Summary of oedometer tests.*

Identifier	Consolidation pressure	Initial void ratio	Initial relative density
oed96	25 kPa	0.57	96%
oed27	50 kPa	0.72	27%

Dry samples were prepared by air pluviation to the desired density and tested following the method described in ASTM D4186/D4186M−20e1 [135] and in VSS 70 349:2019 [136]

adjusted to a dry sample. In order to reduce the boundary effects, a sample having a maximum height-to-diameter ratio of 0.4 shall be used, and the minimum diameter is 50 mm [135]. In an attempt to further reduce the boundary effects, a sample with a diameter of 100 mm and a height of 40 mm was used.

Evaluation

The relationship between the soil elastic moduli and the pressure

$$\tilde{E} = f[(p')^n] := a\left(\frac{p'}{p'_{\text{ref}}}\right)^n, \tag{II.15}$$

has been observed experimentally (e.g. [137]) and micromechanically (e.g. [138], [139]). $\tilde{E}$ is a generic elastic modulus, p' the mean effective stress, and $0 < n \le 1$ is an empirically determined exponent. While exponent $n = 1$ shows good agreement with experimental data for clay [177], Li and Wang [178] showed that the behaviour exhibited by granular soil is better represented by a lower value of n. In their work, they propose $n \approx 0.3$ for the bulk modulus, while Schanz and Vermeer reported values ranging between 0.4 and 0.7 for the oedometric modulus [179].

Based on the definition of the bulk modulus

$$K = \frac{\mathrm{d}p'}{\mathrm{d}\varepsilon_v^e}, \tag{II.16}$$

and Equation (II.15), Li and Wang [178] derived a relationship based on a power-law describing the steady-state line of sands ($n \ne 1$). Their relationship can be reformulated to describe the unloading-reloading line (URL) as

$$e_{\text{URL}} = e_0 - \kappa\left(\frac{p'}{p'_{\text{ref}}}\right)^\alpha, \tag{II.17}$$

where $\alpha = 1 - n$, e_0 is the initial void ratio, p'_{ref} a reference pressure for normalisation, and

$$\kappa := \frac{1 + e_0}{a\alpha}{p'_{\text{ref}}}^\alpha. \tag{II.18}$$

Equation (II.17) only differs from the well-known formula for clays [157] by the natural logarithm being substituted by a power law.

By analogy, the virgin compression line (VCL) can be formulated as

$$e_{\text{VCL}} = e_0 - \lambda\left(\frac{p'}{p'_{\text{ref}}}\right)^\alpha. \tag{II.19}$$

From Eqs. (II.15), (II.17), and (II.18), the bulk modulus can be derived:

$$K = \frac{1 + e_0}{\kappa\alpha}{p'_{\text{ref}}}^\alpha\left(\frac{p'}{p'_{\text{ref}}}\right)^{1-\alpha}. \tag{II.20}$$

On the other hand, Equation (II.19) and the parameter λ from can be used to formulate the volumetric hardening rule of Perth sand.

Motivation of the chosen evaluation method

In an oedometer sample, the mean effective stress reads

$$p' = \frac{\sigma_v'}{3}(1 + 2K_0), \qquad \qquad \text{(II.21)}$$

where σ_v' is the applied effective vertical stress, and $K_0 = \sigma_h'/\sigma_v'$ the lateral earth pressure coefficient at rest. Talesnick et al. [57] showed that K_0 is constant during the virgin compression of sand but varies as a function of the applied vertical stress σ_v' during unloading and reloading. In the same work, the same authors validated the formula for K_0 in overconsolidated soil first proposed by Schmidt [180]

$$K_0 = K_{0,NC} \cdot \text{OCR}^\beta, \qquad \qquad \text{(II.22)}$$

where $\text{OCR} = \frac{\sigma_{v,\max}'}{\sigma_v'}$. Because the horizontal stress is rarely measured in an oedometer test (due to the technical challenges such a measurement poses), test results are usually evaluated in terms of the void ratio e and the effective vertical stress σ_v'. As a result, the oedometric modulus is determined. In order to be used for the simulation of boundary value problems, however, soil parameters shall be defined as functions of stress or strain invariants (since arbitrary stress paths can arise). In fact, as a consequence of Equations (II.21) and (II.22), σ_v' is not proportional to the first invariant of the stress tensor during unloading and reloading. For this reason, in this work, the test results are evaluated in terms of the mean effective stress.

Results

The proper evaluation of the oedometer test requires knowledge of the mean stress p of the sample, which, in turn, requires measurements of the lateral stress. As these measurements could not be carried out in the laboratory, the mean pressure p is estimated by Equations (II.21) and (II.22) assuming the values for $K_{0,nc}$ and a that will be derived in Section 8.1. Fig. 7 shows the results obtained in the dense sample on a linear and power-law axis. The power-law scaling of the axis was obtained assuming the exponent α in Equations (II.17) and (II.19) to be 0.5, as is often reported in the literature. It is observed that this value indeed provides a good fit (i.e. the VCL and URL are approximately linear), although higher values up to $n \leq 0.7$ would work as well. A power-law fit of the URL and VCL were computed assuming the same value $\alpha = 0.5$. The resulting fitting lines are plotted in Fig. 7, which can be used to visually confirm the good agreement of Equations (II.21) and (II.22) with experimental data.

Legend:
— $\lambda = 9.107e - 04$, $\alpha = 0.500$, $e_0 = 0.572$
--- $\kappa = 5.832e - 04$, $\alpha = 0.500$, $e_0 = 0.570$
⋯ $\kappa = 5.492e - 04$, $\alpha = 0.500$, $e_0 = 0.566$

Fig. 7: Void ratio e versus mean stress p in test oed96. The fitted VCL and URL are plotted over the experimental data. On the left, the p-axis has a linear scale; on the right, it is scaled by a power law with an exponent 0.5. The fitting parameters λ and κ are referred to the reference pressure $p_{\text{ref}} = 1\,kPa$.

Fig. 8, analogously, shows the results of the loose specimen. Here, the same exponent α was assumed and kept fixed. Again, the obtained fitting lines fit the data well, especially along the VCL at higher pressures (where the boundary effects become less important) and along the URL at low to medium OCR values.
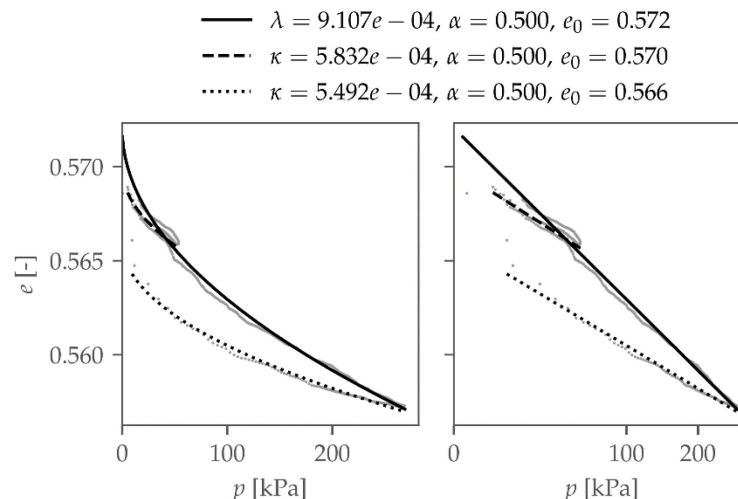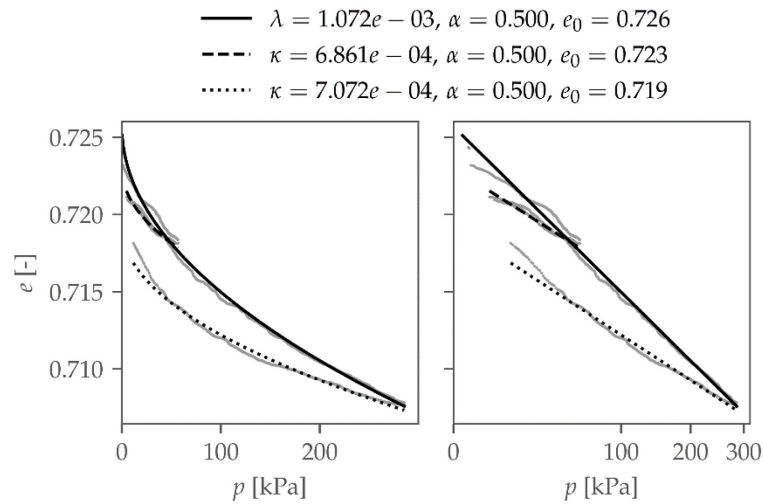

Fig. 8: *Void ratio e versus mean stress p in test oed27. The fitted VCL and URL are plotted over the experimental data. On the left, the p-axis has a linear scale; on the right, it is scaled by a power law with an exponent 0.5. The fitting parameters λ and κ are referred to the reference pressure $p_{\mathrm{ref}} = 1\ kPa$.*

Based on the fitted values and Equation (II.20), it is possible to determine the bulk moduli of Perth Sand in a dense and loose state. The elastic bulk modulus results from the fit of the URL, while an elastoplastic modulus can be derived from the VCL fit. The resulting values are summarised in Tab. 4 and are referred to the mean effective stress of 25 kPa to stay consistent with other mechanical properties calculated in this work at that stress level.

Tab. 4: *Bulk moduli of Perth sand determined in oedometer tests in the laboratory at the mean stress of 25 kPa.*

	K^{ep} (VCL)	K^{e} (URL)
oed96	17.3 MPa	28.0 MPa
oed27	16.1 MPa	24.8 MPa

II.2   Numerical description

The theoretical background of LS-DEM and the methodology adopted in this section were described in [9] and omitted in this work for conciseness. Instead, the interested reader is referred to [9]. The grain shape was reconstructed from a three-dimensional X-ray computer tomography scan of a sample containing about 38'000 grains of Perth sand. A subset of these grains is depicted in Fig. 9.
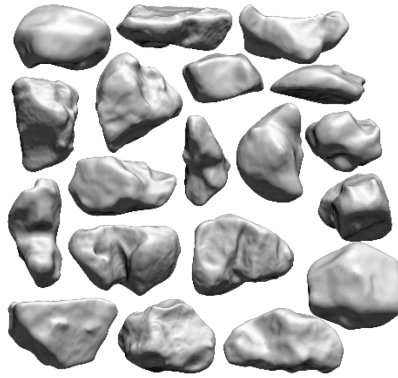
Fig. 9: Three-dimensional reconstruction of Perth sand grains based on an XRCT scan.

The governing parameters in LS-DEM are the intergranular contact stiffness (normal and tangential) and the intergranular friction. These three parameters were calibrated based on the triaxial and odometer tests presented in the previous section [9] (see, e.g., Fig. 10). Then, the soil behaviour was studied by running oedometer, triaxial, and biaxial tests on a cubic sample (Fig. 11). The sample size was chosen to minimise strain localisation.

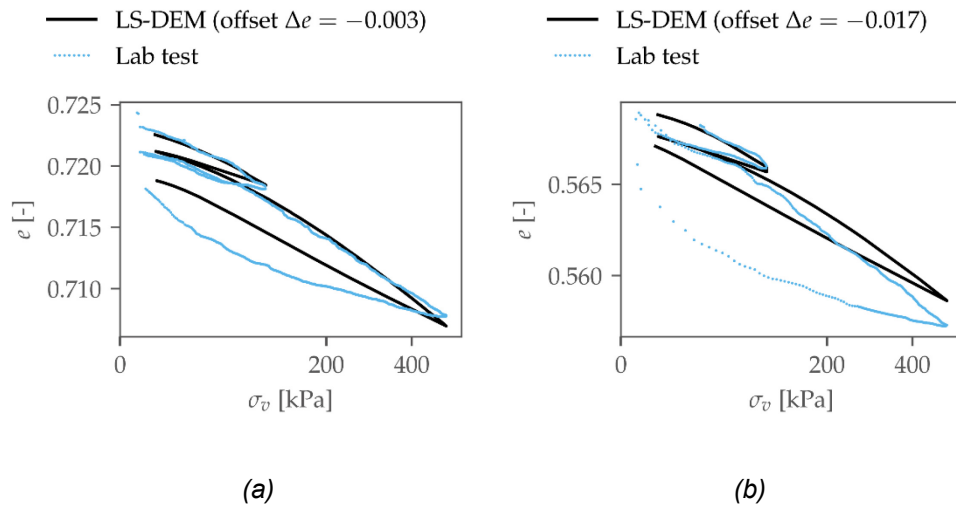(a)   (b)

Fig. 10: One-dimensional consolidation behaviour of the LS-DEM samples compared to the laboratory tests: (a) loose sample (b) dense sample. Please note that the vertical scale differs for the dense and loose samples.
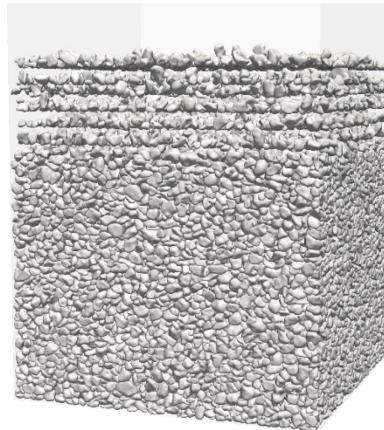

Fig. 11: Preparation of a dense sample in LS-DEM.

From these tests, the elastic and plastic parameters were determined for later use in the numerical modelling of the wall unloading process. In particular, the mobilisation of the plastic parameters φ and ψ as a function of the deviatoric plastic strain and the elastic parameters were determined with triaxial tests (see Fig. 9 and Tab. 5). On the other hand, the oedometer tests confirmed the results obtained in Tab. 4.
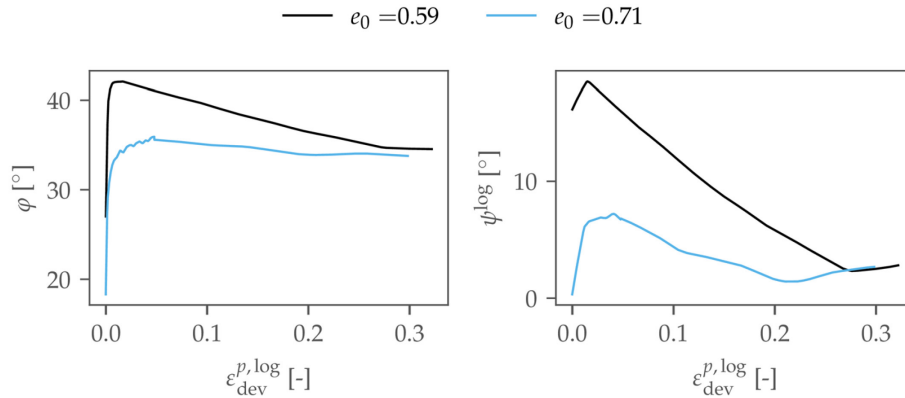

Fig. 12: *Plastic parameters φ and ψ as a function of the deviatoric plastic strain in a triaxial test.*

Tab. 5: *Mechanical properties of Perth Sand at a confining pressure of 25 kPa determined with LS-DEM.*

	E	ν	φ_{peak}	φ_{res}	ψ_{max}
Dense	49.9 MPa	0.18	42.1°	34.6°	18.5°
Loose	23.8 MPa	0.21	35.9°	33.8°	7.2°

Furthermore, during the calibration phase, it was observed that the peak friction angle depends on the sample relative density and the intergranular friction coefficient. Instead, the residual strength showed no sensitivity on the intergranular friction, suggesting that only the particle shape determines it.

II.2.1 Investigation of the pressure dependence of Perth Sand mechanical behaviour

Several studies in the past reported a pressure dependence of the soil friction angle, characterised by higher values at low stress levels and giving rise to curved Mohr-Coulomb failure surfaces [181], [182]. For example, Lee and Seed [183] performed several drained triaxial compression tests on sand at different confining pressures and identified the following components of shearing strength: sliding friction, dilation, and particle crushing and rearranging. The authors assumed sliding friction to be independent of the confining pressure, while dilation contributed the most to the shear strength at low stresses and had a negative contribution at high stresses. Instead, particle crushing and rearranging were assumed to contribute the most at high pressures while being irrelevant at low pressures. The resulting failure envelope is then curved at low stresses and almost linear at higher stresses (see, e.g., [100]).
Bolton [184] obtained similar results by analyzing the results of 17 different sands and derived a well-established empirical relationship between the peak shear resistance and the soil density and confining pressure. In addition, Bolton identified the residual shear strength of soil as independent of the confining stress, giving a value of about 33° for quartz sand. This value is indeed very close to the values obtained for Perth Sand in the current work.

However, published two years earlier, Fukushima and Tatsuoka's results [185] contradicted Bolton's. They showed that accurate results of the soil strength at low pressures could only be obtained if the effects of the membrane and the sample's self-weight are considered in

determining the stress. Further, drained triaxial compression tests showed an almost irrelevant pressure dependence of the soil strength, especially for stress levels below 50 kPa. More recently, Fannin et al. [186], Cabarkapa [187], and Winters et al. [188] showed a pressure dependence of the friction angle experimentally, while Wichtmann [62] observed a negligible influence of the pressure on the soil friction.

This section uses LS-DEM to shed light on this topic from a different perspective. LS-DEM considers the real grain shape, which is known to contribute significantly to soil dilatancy (e.g., [114], [189]) and is an adequate tool.
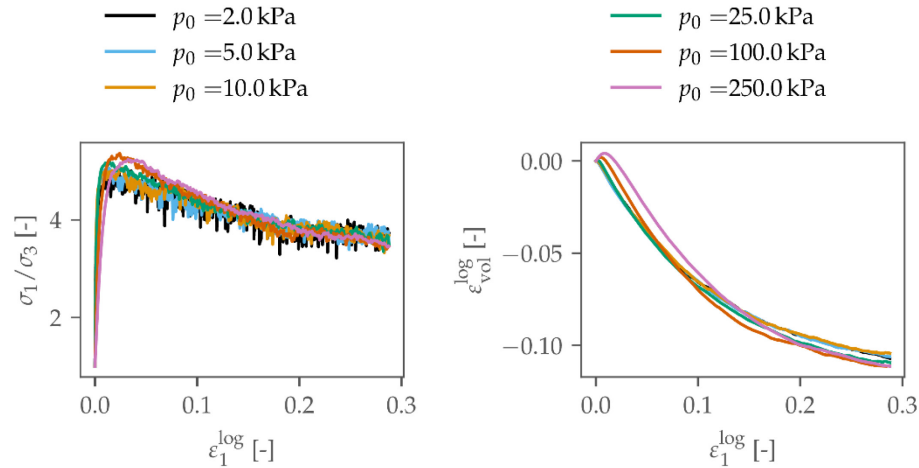

Fig. 13: Deviatoric and volumetric response of dense samples tested in axial compression at different confining pressures. Left: stress ratio σ_1/σ_3 as a function of the axial strain; right: volumetric strain as a function of the axial strain.

Fig. 12 presents the results of triaxial tests on dense specimens at different isotropic consolidation pressures. It is observed that the soil strength and the volume dilation are practically constant over the tested pressure range. The peak and residual friction angles, and the dilatancy angle for the tested pressures are summarised in the bottom graphs in Fig. 15 and only denote a negligible increase with increasing pressure for $p_0 < 100 \, kPa$.
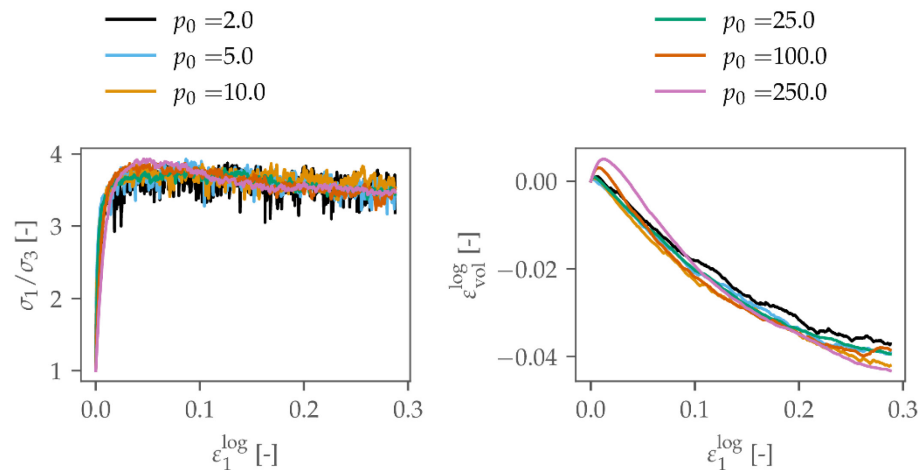
Fig. 14: Deviatoric and volumetric response of dense samples tested in axial compression at different confining pressures. Left: stress ratio σ_1/σ_3 as a function of the axial strain; right: volumetric strain as a function of the axial strain

Similarly, Fig. 14 depicts the results of triaxial tests on loose specimens at different isotropic consolidation pressures. As for dense soil, an important correlation between the friction

angle and the confining pressure is missing, as confirmed by the characteristic values extracted and plotted in Fig. 15.
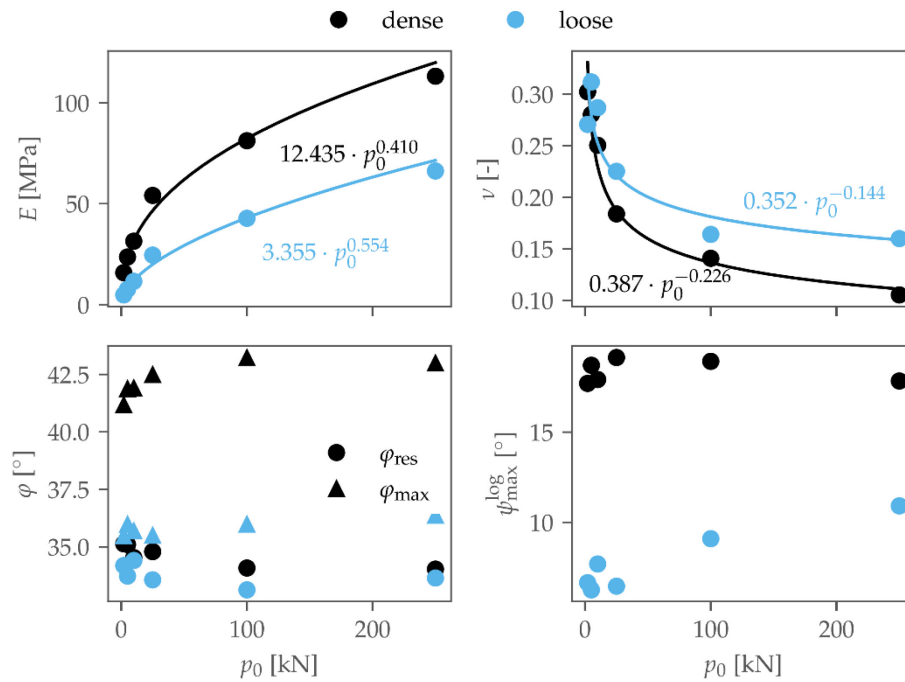

Fig. 15: Pressure dependence of Perth Sand's elastic and plastic parameters. From top to bottom, left to right: Young's modulus E, Poisson's ratio ν, peak and residual friction angle $\varphi_{\max}$ and φ_{res}, and dilatancy angle ψ.

Thus, the numerical results do not support the theory of curved failure envelopes at low stresses and a higher dilatancy contribution to the soil shear strength.

It may be argued that particle breakage is not modelled in the employed LS-DEM implementation (while it is in others, see e.g. [190]), thus undermining the validity of the results. However, particle breakage is usually considered to impact the soil behaviour at higher stress levels than those tested here (e.g. [191]–[194]), and LS-DEM without breakage has been validated against physical experiments performed at a confining stress of 100 kPa [114], [128].

Thus, only an increased intergranular friction coefficient with decreasing contact forces would produce a higher dilatancy and peak friction angle at small pressures in LS-DEM. This, however, would violate Amonton's law, which a multitude of studies has corroborated [195]–[197].

The two plots in Fig. 15 show the pressure dependency of the elastic parameters. A power law can fit both parameters (see also Tab. 6) . While little data is present in the literature about the Poisson's ratio, it is well-known that a power law well describes the pressure dependence of the Young's modulus of granular soil with an exponent of about 0.5. This may serve as an additional confirmation that LS-DEM can reliably predict the soil pressure dependency.

Tab. 6: Equations defining Perth Sand's pressure-dependent elastic parameters.

Dense	$E = 12.435\,\text{MPa} \cdot p^{0.41}$	$\nu = 0.387 \cdot p^{-0.226}$
Loose	$E = 3.355\,\text{MPa} \cdot p^{0.554}$	$\nu = 0.352 \cdot p^{-0.144}$

II.2.2   Soil behaviour under plane strain conditions

Plane strain conditions represent an additional kinematic constraint to the soil deformation. This additional constraint was observed to influence the strength (e.g. [198]). Tatsuoka et al. [199] conducted a series of plane strain compression tests to study this phenomenon and the pressure dependence of strength. Their study observed no pressure dependence of the friction angle on the lateral stress but a significant anisotropy of the strength under plane strain conditions depending on the inclination δ of the maximum principle stress to the bedding plane. The lowest strength was observed for $\delta = 23°$ and was very similar to the strength determined in a triaxial test. For $\delta = 90°$ (i.e. the maximal principle stress is perpendicular to the bedding plane) values of φ of about 50° were observed.

As biaxial testing presents more technical challenges than triaxial tests, the latter are often preferred in geotechnical laboratories to characterise the soil strength. However, plane strain conditions characterise a multitude of geotechnical problems. Therefore, Hanna [200] proposed a simple semiempirical method based on Rowe's theory [201] to predict the friction angle for plane strain conditions from the results of triaxial tests. The relationship reads

$$\tan \varphi_{\mathrm{ps}} \cos \varphi_{\mathrm{res}} = \frac{(K \cdot D - 1)\sqrt{(12D - 3D^2)}}{(4K \cdot D - K \cdot D^2 + 3D)},$$ (II.23)

where φ_{ps} is the friction angle for plane strain conditions, φ_{res} the residual friction angle determined in a triaxial test, D is an empirical dilatancy factor, expressed as a function of the relative porosity of the soil, and

$$K = \tan^2 \left[45° + \frac{\varphi_{\mathrm{res}}}{2} \right].$$

The values obtained in Tab. 5 for the dense sample, together with the dilatancy factor $D \approx 2$ read from Fig. 4 in [200] would result in a friction angle $\varphi_{\mathrm{ps}} \approx 52°$.

The deviatoric and volumetric response of the numerical biaxial tests carried out on the LS-DEM loose and dense samples are summarised in Fig. 16. The most notable difference to the triaxial test results is the higher peak strength reached by the dense sample. Indeed, the maximum stress ratio is higher than 8, leading to a maximum friction angle of $\varphi_{\mathrm{max}} = 51.7°$. This value agrees well with that derived using Hanna's procedure. A higher residual strength is observed, resulting in a friction angle of $\varphi_{\mathrm{res}} = 37°$ (Fig. 17).

The consequence of this result is that the strength of a granular material depends on the intermediate principal stress as well, rather than only the minimal and the maximal, as assumed by the Mohr-Coulomb (MC) failure criterion. Thus, the employment of the MC failure criterion for plane strain problems leads to an underestimation of the soil strength if triaxial tests were used for its calibration, as was also shown by Griffiths and Huang [202]. In this work, the Mohr-Coulomb model is calibrated considering the results of the biaxial tests to ensure the applicability of this work's findings in practice. Indeed, the MC model remains the most widely used in soil engineering practice. Alternatively, the extended Matsuoka-Nakai model could be employed instead [202].
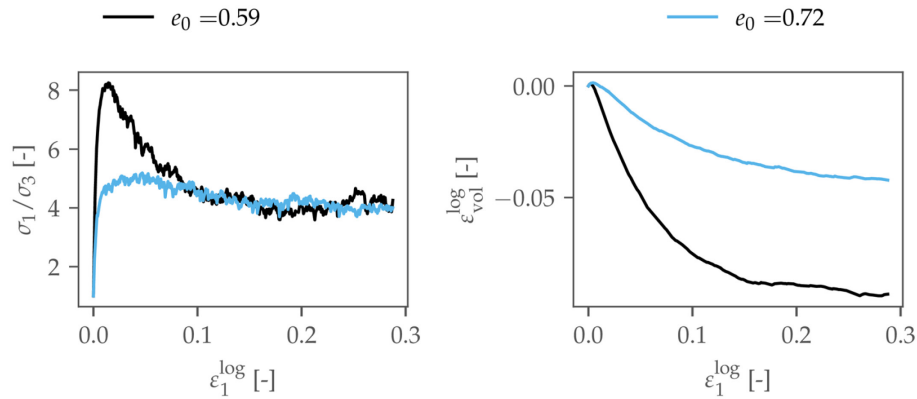
Fig. 16: *Deviatoric and volumetric response of the dense and loose sample tested in axial compression under plane strain conditions. Left: stress ratio σ_1/σ_3 as a function of the axial strain; right: volumetric strain as a function of the axial strain.*

Furthermore, the biaxial test on the dense sample shows a sharper peak than in the triaxial test on the same sample. The reason is that shear bands are observed in the biaxial test, as shown in Fig. 18a. While strain localisation in the triaxial sample could be avoided by the proper choice of the sample size, the same is not possible in the biaxial test (at least not without affecting the results) because of the more constrained kinematics. Fig. 18b shows the grain rotations accumulated over the isotropic consolidation and shearing phases. Unlike under plane strain conditions, the rotation is evenly distributed over the sample volume and no shear bands can be detected, even by slicing the sample.

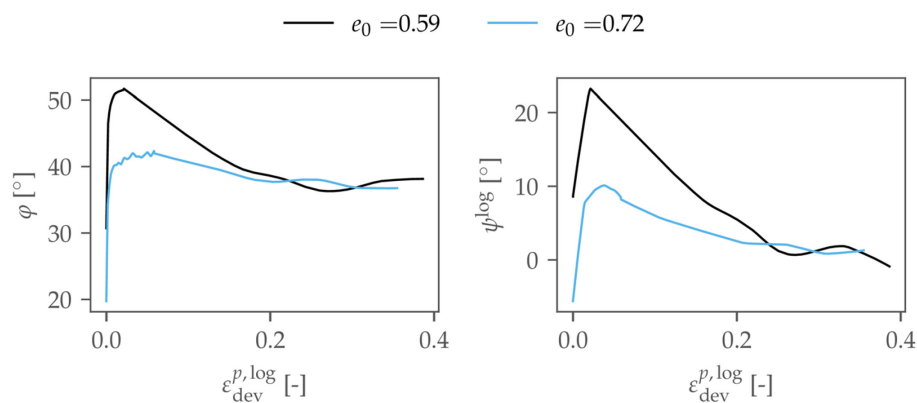**Fig. 17:** *Plastic parameters φ and ψ as a function of the deviatoric plastic strain.*

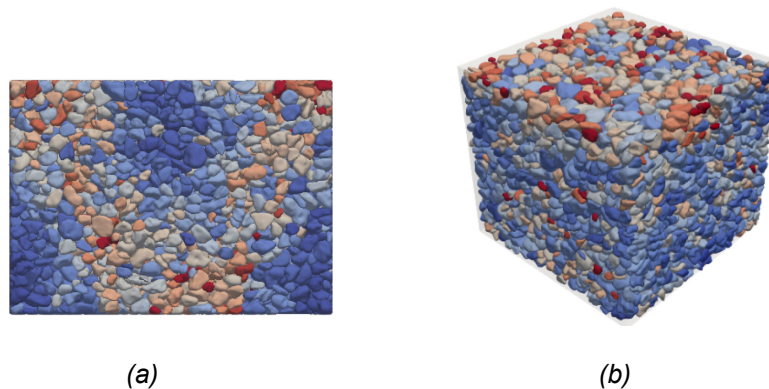(a)   (b)

Fig. 18: *Accumulated particle rotation during shearing of a dense specimen: (a) biaxial test; (b) triaxial test.*

III Numerical analysis: wall unloading process

III.1 Strain regularisation and mesh dependency

A simple regularisation technique proposed by Pietruszczak and Mróz [149] is employed to avoid a significant mesh dependency of the FE-based solutions. In the constitutive law presented in Section 7.1.1, softening is governed by the cumulative plastic deviatoric strain. Therefore, the deviatoric plastic strain increment is scaled according to Equation (7.9). The efficacy of this technique is verified by simulating the wall unloading as in Section 7.2 by changing the mesh size and applying the regularisation.

The resulting moment-rotation curves are shown in Fig. 19, which confirm the effectiveness of the adopted regularisation scheme, as the mesh dependency of the solution stays in an acceptable range.
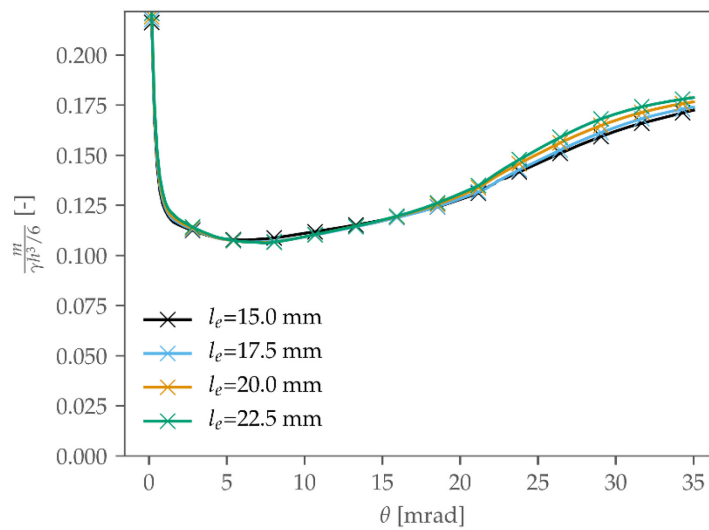
Fig. 19: Simulation of the wall unloading for a dense, uncompacted sample with different mesh sizes and applying the regularisation as in Section 7.1.2.

III.2 Sample calibration of the hardening soil model

The hardening soil model assumes the following relationship to describe the stress-strain response of a triaxial test [148]:

$$-\varepsilon_1 = \frac{1}{E_i} \frac{q}{1 - \frac{q}{q_a}},$$ (III.1)

where q is the deviatoric stress, $q = q_a$ is an asymptote of Equation (III.1) defined as

$$q_a = \frac{q_f}{R_f}$$ (III.2)

where q_f is the ultimate deviatoric stress and $0 < R_f \leq 1$, and E_i is a stiffness value defined as

$$E_i = \frac{2E_{50}}{2 - R_f}.$$ (III.3)

For cohesionless soil, the stiffness E_{50} is defined as

$$E_{50} = E_{50}^{\text{ref}} \left(\frac{\sigma_3}{p_{\text{ref}}}\right)^m.$$ (III.4)

where σ_3 is the minor principal stress, m is an empirical exponent ($m \approx 0.5$ for granular soil), and E_{50}^{ref} the reference stiffness modulus corresponding to the reference confining pressure p_{ref}.

Furthermore, the ultimate deviatoric stress q_f is assumed to be a function of σ_3 (see [148, p. 68]). As σ_3 is constant in a triaxial test, a constant q_f can be assumed for the calibration.

By carrying out triaxial tests in the laboratory, an accurate fit of Equation (III.1) to the observed stress-strain response can be obtained, as in Fig. 131 (Section 7.4). The obtained parameters are summarised in Tab. 7.

Tab. 7: *Parameters of the hardening soil model for the triaxial tests of Fig. 131.*

	Dense		**Loose**	
	Residual	***Peak***	***Residual***	***Peak***
E_{50}^{ref}	90 MN/m^2		20 MN/m^2	
p_{ref}		25 kPa		
m		0.5		
q_f	65 kPa	104 kPa	65 kPa	70 kPa
R_f		0.9	0.95	

Glossary

Term	Meaning
FEM	Finite Element Method.
DEM	Discrete Element Method.
LS-DEM	Level Set Discrete Element Method
PIV	Particle Image Velocimetry
SF	Safety factor

Glossary

References

[1] GUMA, 'Evaluation de l'état des murs de soutènement béton à semelles. Etude pilote. Rapport de synthèse des phases 1 et 2.', Neuchâtel, 2014.

[2] Dr. Vollenweider AG, 'Gefährdung von Winkelstützmauern durch Korrosion. Untersuchung des Bruchverhaltens – Phase 2 Zürich. Technischer Bericht', Bundesamt für Strassen ASTRA, Zürich, 2014.

[3] S. Häfliger and W. Kaufmann, 'Tragwiderstand und Verformungsvermögen von Winkelstützmauern bei lokaler Korrosion der Bewehrung', FEDRO Report, 2023.

[4] Marmota Engineering AG, M. Iten, and F. Fischli, 'Automatisiertes faseroptisches Überwachungssystem an einer Winkelstützmauer', 2021.

[5] Vereinigung Schweizerischer Strassenfachleute, 'SNV 640 389 Stützmauern'. 1969.

[6] Vereinigung Schweizerischer Strassenfachleute, 'SN 640 383a Stützbauwerke'. VSS, Zürich, 2002.

[7] S. M. Springman, C. Jommi, and P. Teysseire, 'Instabilities on moraine slopes induced by loss of suction: a case history', *Géotechnique*, vol. 53, no. 1, pp. 3–10, 2003, doi: 10.1680/geot.2003.53.1.3.

[8] P. Teysseire, 'Geotechnische Eigenschaften von Moränen', ETH Zurich, 2006. doi: 10.3929/ETHZ-A-005166289.

[9] D. Perozzi, 'Quantification of the earth pressure acting on corrosion-damaged cantilever retaining walls: An analysis of the soil-structure interaction', Doctoral thesis, ETH Zurich, 2022. https://doi.org/10.3929/ethz-b-000591353

[10] Schweizerischer Ingenieur- und Architektenverein, *Dokumentation D 0197. Geotechnik. Bemessungsbeispiele zur Norm SIA 267*. Trunimger Druck AG, 2004.

[11] H.-J. Lang, J. Huder, P. Amann, and A. M. Puzrin, *Bodenmechanik und Grundbau*. Berlin, Heidelberg: Springer Berlin Heidelberg, 2011. doi: 10.1007/978-3-642-14687-9.

[12] Cubus AG, 'Larix 9'. Zürich, 2022.

[13] 'DIN EN 1997-1, Eurocode 7 – Entwurf, Berechnung und Bemessung in der Geotechnik – Teil 1: Allgemeine Regeln; Deutsche Fassung EN 1997-1:2004 + AC:2009 + A1:2013'. 2014.

[14] S. L. P. Vauban, *Traité de la défense des places. Ouvrage original de M. le maréchal de Vauban*. Paris: C.-A. Jombert père, Libraire du Génie & de l'Artillerie, 1769.

[15] P. Bullet, *L'architecture pratique (etc.)*. Paris: Estienne Michallet, 1691.

[16] P. Couplet, 'De la poussée des terres contre leur revestement, et la force des revestements qu'on leur doit opposer (Seconde partie)', *Hist. Académie R. Sci. Avec Mém. Mathématique Phys.*, vol. MDCCXXVII, pp. 139–178, 1729.

[17] B. F. de Belidor, *La science des ingénieurs dans la conduite des travaux de fortification et d'architecture civile*. Paris: Claude Jombert, 1729. doi: 10.3931/e-rara-26982.

[18] H. Gautier, *Dissertation sur l'epaisseur des culées des ponts, sur la largeur des piles, sur la portée des voussoirs, sur l'erfort & la pesanteur des arches à differens surbaissemens [...]*. Paris: André Cailleau, 1717. doi: 10.3931/e-rara-20230.

[19] C.-A. Coulomb, 'Essai sur une application des règles de Maximis & Minimis à quelques Problèmes de Statique, relatifs à l'Architecture', in *Mémoires de Mathématique et de Physique, présentés à l'Académie Royale des Sciences, par divers Savans, & lûs dans ses Assemblées*, Paris: Imprimerie Royale, 1776, pp. 343–382.

[20] K. Culmann, *Die graphische statik*. Zurich: Meyer & Zeller, 1866. doi: 10.3931/e-rara-20052.

[21] R. Prony, *Recherches sur la poussée des terres, et sur la forme et les dimensions à donner aux murs de revêtement*. Paris: Imprimerie de la République, 1802.

[22] K. Mayniel, *Traité Expérimental, Analytique Et Pratique De La Poussée Des Terres Et Des Murs De Revêtement*. Paris: Bachelier librairie, 1808.

[23] Français, 'Recherches sur la poussée des terres, sur la forme et les dimensions des murs revêtement et sur les talus d'excavation', in *Mémorial de l'officier du génie, no. 4*, Paris: Imprimerie Royale, 1820.

[24] J.-V. Poncelet, 'Mémoire sur la stabilité des revêtements et de leurs fondations', in *Mémorial de l'officier du génie, no. 13*, Paris: Imprimerie et librairie de Bachelier, 1840, pp. 7–270.

[25] Schweizerischer Ingenieur- und Architektenverein, *SIA 261, Einwirkungen auf Tragwerke*. 2014.

[26] Elektro-Watt Ingenieurunternehmung AG, 'A63 Schin-Strasse, Stützmauer A17 747'. Tiefbauamt des Kantons Graubünden, 1973.

[27] W. J. M. Rankine, 'On the stability of loose earth', *Philos. Trans. R. Soc. Lond.*, vol. 147, no. January, pp. 9–27, 1857, doi: 10.1098/rstl.1857.0003.

[28] A. Caquot and J. Kérisel, *Grundlagen der Bodenmechanik*. Berlin, Heidelberg: Springer Berlin Heidelberg, 1967. doi: 10.1007/978-3-642-92937-3.

[29] Á. Kézdi, *Erddrucktheorien*. Berlin, Heidelberg: Springer Berlin Heidelberg, 1962. doi: 10.1007/978-3-642-92838-3.

[30] H. Ravizé, *Poussée des terres : étude des équations de l'équilibre limite : nouvelle méthode de détermination des coefficients de poussée et de butée*. Paris: Dunod, 1945.

[31] W.-F. Chen, *Limit analysis and soil plasticity*. Amsterdam: Elsevier scientific publishing company, 1975.

[32] F. Kötter, 'Die Bestimmung des Drucks an gekrümmte Gleitflächen, eine Aufgabe aus der Lehre vom Erddruck', *Sitzungsberichte Akad. Wiss.*, pp. 229–233, 1903.

[33] V. V. Sokolovskii, *Statics of Granular Media*. Oxford: Pergamon Press, 1965. doi: 10.1115/1.3625019.

[34]   E. H. Davis, 'Theories of plasticity and the failure of soil masses', in *Soil Mechanics : selected topics*, I. K. Lee, Ed. London: Butterworths, 1968, pp. 341–380.

[35]   *DIN 4085:2017-08, Baugrund – Berechnung des Erddrucks Subsoil*. Germany, 2017.

[36]   J. Résal, *Poussée des terres. Stabilité des murs de soutènement*. Paris: École des Ponts et Chaussées, 1903.

[37]   G. Gilbrin, 'Die wirtschaftlichste Form der Eisenbeton-Winkelstützmauer', *Beton Eisen*, no. 10, pp. 233–235, 1912.

[38]   J. Schultze, 'Erddruck auf Winkelstützmauern', *Zentralblatt Bauverwalt.*, vol. 28, no. 36, pp. 198–199, 1916.

[39]   K. Kabelae, 'Die wirtschaftlichste Form der Eisenbeton-Winkelstützmauer', *Beton Eisen*, vol. 19, no. 20, pp. 218–221, 1919.

[40]   A. Ostenfeld, 'Ueber Winkelstützmauern', *Beton Eisen*, no. 1, pp. 11–14, 1921.

[41]   E. Mörsch, 'Die Berechnung der Winkelstützmauern', *Beton U Eisen*, no. 20, pp. 327–339, 1925.

[42]   Vereinigung Schweiz. Strassenfachmänner (VSS), *Stützmauern. Grundlagen zur Berechnung und Konstruktion. Bemessungstabellen*. Zürich: Gebr. Fretz AG, 1966.

[43]   A. Piaskowski and Z. Kowalewski, 'Application of Thixiotropic Clay Suspensions for Stability of Vertical Sides of Deep Trenches without Strutting', in *Proceedings of the Sixth International Conference on Soil Mechanics and Foundation Engineering*, Toronto, 1965, pp. 526–529.

[44]   J. P. Karstedt, 'Untersuchungen zum aktiven räumlichen Erddruck im rolligem Boden bei hydrostatischer Stützung der Erdwand', Grundbauinstitut der Technischen Universität Berlin, Berlin, 1982.

[45]   F. tom Wörden, 'Untersuchungen zum räumlichen aktiven Erddruck auf starre vertikale Bauteile im nicht-bindigen Boden', Leibniz Universität Hannover, Hannover, 2010.

[46]   B. Walz and J. Prager, 'Der Nachweis der äusseren Standsicherheit flüssigkeitsgestützter Erdwände nach der Elementscheibentheorie', Veröffentlichungen des Grundbauinstituts der Technischen Universität Berlin, Berlin, 1978.

[47]   K. Terzaghi, 'Distribution of the lateral pressure of sand on the timbering of cuts', in *Proc. 1st Int. Conf. on SMFE*, Cambridge, MA, USA, 2018, pp. 211–215. doi: 10.1007/978-3-319-73568-9_174.

[48]   K. Terzaghi, *Theoretical Soil Mechanics*. Hoboken, NJ, USA: John Wiley & Sons, Inc., 1943.

[49]   K. Terzaghi and R. B. Peck, *Die Bodenmechanik in der Baupraxis*. Berlin, Heidelberg: Springer Berlin Heidelberg, 1961. doi: 10.1007/978-3-642-92829-1.

[50]   J. Jáky, 'The coefficient of Earth Pressure at Rest', *J. Soc. Hung Archit. Eng.*, vol. 78, no. 22, pp. 355–358, 1944.

[51]   J. Jáky, 'Pressure in silos', in *Proc. 2nd International Conference on Soil Mechanics and Foundation Engineering*, Rotterdam, 1948, pp. 103–107.

[52]   R. L. Michalowski, 'Coefficient of Earth Pressure at Rest', *J. Geotech. Geoenvironmental Eng.*, vol. 131, no. 11, pp. 1429–1433, Nov. 2005, doi: 10.1061/(ASCE)1090-0241(2005)131:11(1429).

[53]   G. Mesri and T. M. Hayat, 'The coefficient of earth pressure at rest', *Can. Geotech. J.*, vol. 30, no. 4, pp. 647–666, Aug. 1993, doi: 10.1139/t93-056.

[54]   P. W. Mayne and F. H. Kulhawy, 'K0-OCR Relationships in Soil', *J. Geotech. Eng. Div.*, vol. 108, no. 6, pp. 851–872, 1982.

[55]   J. Lee, D. Park, D. Kyung, and D. Lee, 'Effect of Particle characteristics on K0 Behavior for Granular Materials', *18th Int. Conf. Soil Mech. Geotech. Eng. Chall. Innov. Geotech. ICSMGE 2013*, vol. 1, no. Wroth 1973, pp. 377–380, 2013.

[56]   J. Lee, T. S. Yun, D. Lee, and J. Lee, 'Assessment of K0 correlation to strength for granular materials', *Soils Found.*, vol. 53, no. 4, pp. 584–595, 2013, doi: 10.1016/j.sandf.2013.06.009.

[57]   M. Talesnick, S. Nachum, and S. Frydman, 'K 0 determination using improved experimental technique', *Géotechnique*, vol. 71, no. 6, pp. 509–520, Jun. 2021, doi: 10.1680/jgeot.19.P.019.

[58]   M. L. Talesnick, R. Avraham, and M. Ringel, 'Measurement of contact soil pressure in physical modelling of soil-structure interaction', *Int. J. Phys. Model. Geotech.*, vol. 14, no. 1, pp. 3–12, 2014, doi: 10.1680/IJPMG.13.00008.

[59]   X. Gu, J. Hu, and M. Huang, 'K0 of granular soils: a particulate approach', *Granul. Matter*, vol. 17, no. 6, pp. 703–715, 2015, doi: 10.1007/s10035-015-0588-7.

[60]   E. W. Brooker and H. O. Ireland, 'Earth Pressures at Rest Related to Stress History', *Can. Geotech. J.*, vol. 2, no. 1, pp. 1–15, Feb. 1965, doi: 10.1139/t65-001.

[61]   C. S. Chang and R. V. Whitman, 'Drained Permanent Deformation of Sand Due to Cyclic Loading', *J. Geotech. Eng.*, vol. 114, no. 10, pp. 1164–1180, Oct. 1988, doi: 10.1061/(ASCE)0733-9410(1988)114:10(1164).

[62]   T. Wichtmann, A. Niemunis, and Th. Triantafyllidis, 'Strain accumulation in sand due to cyclic loading: Drained cyclic tests with triaxial extension', *Soil Dyn. Earthq. Eng.*, vol. 27, no. 1, pp. 42–48, Jan. 2007, doi: 10.1016/j.soildyn.2006.04.001.

[63]   H. Spotka, 'Einfluss der Bodenverdichtung mittels Oberflächen-Rüttler auf den Erddruck einer Stützwand bei Sand', Universität Stuttgart, 1977.

[64]   T.-J. Chen and Y.-S. Fang, 'Earth Pressure due to Vibratory Compaction', *J. Geotech. Geoenvironmental Eng.*, vol. 134, no. 4, pp. 437–444, Apr. 2008, doi: 10.1061/(ASCE)1090-0241(2008)134:4(437).

[65]   B. B. Broms, 'Lateral earth pressures due to compaction of cohesionless soils', in *Proc. 4th Conf. on Soil Mechanics*, Budapest, 1971, pp. 373–384.

[66] T. S. Ingold, 'The effects of compaction on retaining walls', *Géotechnique*, vol. 29, no. 3, pp. 265–283, Sep. 1979, doi: 10.1680/geot.1979.29.3.265.

[67] J. Boussinesq, 'Application des potentiels à l'étude de l'équilibre et du mouvement des solides élastiques: principalement au calcul des déformations et des pressions que produisent, dans ces solides, des efforts quelconques exercés sur une petite partie de leur surface'. Gauthier-Villars, 1885.

[68] J. M. Duncan and R. B. Seed, 'Compaction-Induced Earth Pressures Under K0-Conditions', *J. Geotech. Eng.*, vol. 112, no. 1, pp. 1–22, Jan. 1986, doi: 10.1061/(ASCE)0733-9410(1986)112:1(1).

[69] M. A. Sherif, Y. Fang, and R. I. Sherif, 'KA and K0 Behind Rotating and Non-Yielding Walls', *J. Geotech. Eng.*, vol. 110, no. 1, pp. 41–56, Jan. 1984, doi: 10.1061/(ASCE)0733-9410(1984)110:1(41).

[70] Y. Fang and I. Ishibashi, 'Static Earth Pressures with Various Wall Movements', *J. Geotech. Eng.*, vol. 112, no. 3, pp. 317–333, Mar. 1986, doi: 10.1061/(ASCE)0733-9410(1986)112:3(317).

[71] R. L. Handy and M. Asce, 'The arch in soil arching', *J. Geotech. Eng.*, vol. 111, no. 3, pp. 302–318, 1985, doi: 10.1061/(ASCE)0733-9410(1985)111:3(302).

[72] M.-F. Chang, 'Lateral earth pressures behind rotating walls', *Can. Geotech. J.*, vol. 34, no. 4, pp. 498–509, Aug. 1997, doi: 10.1139/t97-016.

[73] S. Patel and K. Deb, 'Study of Active Earth Pressure behind a Vertical Retaining Wall Subjected to Rotation about the Base', 2020, doi: 10.1061/(ASCE)GM.1943-5622.0001639.

[74] S. S. Nadukuru and R. L. Michalowski, 'Arching in Distribution of Active Load on Retaining Walls', *J. Geotech. Geoenvironmental Eng.*, vol. 138, no. 5, pp. 575–584, 2012, doi: 10.1061/(ASCE)GT.1943-5606.0000617.

[75] Schweizerischer Ingenieur- und Architektenverein, 'SIA 260, Grundlagen der Projektierung von Tragwerken'. Zürich, 2013.

[76] 'DIN EN 1990:2021-10 Eurocode: Grundlagen der Tragwerksplanung', 2021.

[77] Elektro-Watt Ingenieurunternehmung AG, 'A 63 Schinstrasse, Stüetzmauer talseits km 9120-9240', Tiefbauamt des Kantons Graubünden, Zürich, 1972.

[78] Haas + Tschupp Ingenieurbüro AG, 'N3 Stütmauer Rossau, km 170.114-170.503. Ausführungsstatik', Kantonsingenieur St. Gallen, Jona, 1981.

[79] Schweizerischer Ingenieur- und Architektenverein, *SIA 267, Geotechnik*. 2013.

[80] Heiniger & Partner, 'Stützmauer v3.00'. 1990.

[81] Prim+Partner Ingenieurbüro für Hoch und Tiefbau, 'SN1 Abschnitt Wil-St. Margrethen, Anschluss Kreuzbleiche, km 380-400. Statik', ASTRA, St. Gallen, 1984.

[82] R. Wüllimann, 'Grundlagen der Erddruckberechnung', *Bodenmechanische Grundlagen Stützmauerberechnung*, no. Sonderdruck aus Strasse und Verkehr Nr. 2, pp. 71–76, 1964.

[83] U. Vollenweider, 'Norm SIA 267: Geotechnik', *Tec Doss. Sonderh. Von Tec21*, vol. 129, pp. 26–27, 2003, doi: 10.5169/seals-108796.

[84] Stiftung Umwelteinsatz SUS, 'Ergänzungen zum Buch Trockenmauern, Grundlagen, Bauanleitung, Bedeutung. Anhang: Sicherheitsfaktoren', 2014. https://data.umwelteinsatz.ch/T/Anhang-Sicherheit.html (accessed Aug. 30, 2021).

[85] D. J. Rohner, 'Zum Problem der Fundamentdimensionierung', *Bodenmechanische Grundlagen Stützmauerberechnung*, no. Sonderdruck aus Strasse und Verkehr Nr. 2, pp. 79–87, 1964.

[86] R. Wullimann and D. Rohner, 'Stuetzmauern - Grundlagen für Berechnung und Konstruktion. Vorentwurf zu den Stützmauernbemessungstabellen des VSS', Versuchsanstalt für Wasserbau und Erdbau an der ETH, Erdbauabteilung, Zürich, 1962.

[87] T. Belytschko, W. K. Liu, B. Moran, and K. I. Elkhodary, *Nonlinear Finite Elements for Continua and Structures*. Chichester: Wiley, 2014.

[88] R. L. Michalowski, 'Three-dimensional analysis of locally loaded slopes', *Geotechnique*, vol. 39, no. 1, pp. 27–38, 1989, doi: 10.1680/geot.1989.39.1.27.

[89] D. C. Drucker, W. Prager, and H. J. Greenberg, 'Extended limit design theorems for continuous media', *Q. Appl. Math.*, vol. 9, no. 4, pp. 381–389, 1952.

[90] D. C. Drucker, 'Coulomb Friction, Plasticity, and Limit Loads', *J. Appl. Mech.*, vol. 21, no. 1, pp. 71–74, Mar. 1954, doi: 10.1115/1.4010821.

[91] O. Mohr, 'Welche Umstände bedingen die Elastizitätsgrenze und den Bruch eines Materials', *Z. Vereines Dtsch. Ingenieure*, vol. 44, pp. 1524–1530, 1900.

[92] M. Sayir, J. Dual, S. Kaufmann, and E. Mazza, *Ingenieurmechanik 1*. Wiesbaden: Springer Fachmedien Wiesbaden, 2015. doi: 10.1007/978-3-658-10047-6.

[93] D. Capecchi, *History of Virtual Work Laws*, vol. 42. Milano: Springer Milan, 2012. doi: 10.1007/978-88-470-2056-6.

[94] E. Christiansen, 'Limit analysis of collapse states', in *Handbook of Numerical Analysis*, vol. 4, 1996, pp. 193–312. doi: 10.1016/S1570-8659(96)80004-4.

[95] S. W. Sloan, 'Upper bound limit analysis using finite elements and linear programming', *Int. J. Numer. Anal. Methods Geomech.*, vol. 13, no. 3, pp. 263–282, May 1989, doi: 10.1002/nag.1610130304.

[96] K. H. Roscoe, 'The Influence of Strains in Soil Mechanics', *Géotechnique*, vol. 20, no. 2, pp. 129–170, 1970, doi: 10.1680/geot.1970.20.2.129.

[97] P. A. Vermeer and R. de Borst, 'Non-Associated Plasticity for Soils, Concrete and Rock.', in *Heron*, vol. 29, no. 3, Delft University of Technology, 1984.

[98] A. Drescher and E. Detournay, 'Limit load in translational failure mechanisms for associative and non-associative materials', *Géotechnique*, vol. 43, no. 3, pp. 443–456, Sep. 1993, doi: 10.1680/geot.1993.43.3.443.

[99] K. Krabbenhoft, M. R. Karim, A. V. Lyamin, and S. W. Sloan, 'Associated computational plasticity schemes for nonassociated frictional materials', *Int. J. Numer. Methods Eng.*, vol. 90, no. 9, pp. 1089–1117, Jun. 2012, doi: 10.1002/nme.3358.

[100] W. F. Chen and X. L. Liu, *Limit Analysis in Soil Mechanics*. Amsterdam: Elsevier, 1991.

[101] C. Thornton and L. Zhang, 'A numerical examination of shear banding and simple shear non-coaxial flow rules', *Philos. Mag.*, vol. 86, no. 21–22, pp. 3425–3452, 2006, doi: 10.1080/14786430500197868.

[102] R. Hill, *The mathematical Theory of Plasticity*. Oxford: Oxford University Press, 1998, 1950.

[103] J. Ai, P. A. Langston, and H.-S. Yu, 'Discrete element modelling of material non-coaxiality in simple shear flows', *Int. J. Numer. Anal. Methods Geomech.*, vol. 38, no. 6, pp. 615–635, Apr. 2014, doi: 10.1002/nag.2230.

[104] D. Radenkovic, 'Limit theorems for a Coulomb material with a non standard dilatation', *CR Acad Sci Paris*, pp. 4103–4104, 1961.

[105] Optum Computational Engineering, 'Optum G2'. Copenhagen, 2021. [Online]. Available: https://op-tumce.com/

[106] S. Haefliger and W. Kaufmann, 'Experiments on locally corroded retaining wall segments and their assessment with the Corroded Tension Chord Model', in *Proc. of the 3rd CACRCS Workshop Capacity Assessment of Corroded Reinforced Concrete Structure*, 2021. doi: 10.3929/ethz-b-000527046.

[107] R. Lancellotta, 'Analytical solution of passive earth pressure', *Géotechnique*, vol. 52, no. 8, pp. 617–619, Oct. 2002, doi: 10.1680/geot.2002.52.8.617.

[108] R. Lancellotta, 'Lower-bound approach for seismic passive earth resistance', *Géotechnique*, vol. 57, no. 3, pp. 319–321, Apr. 2007, doi: 10.1680/geot.2007.57.3.319.

[109] G. T. Houlsby, 'How the dilatancy of soils affects their behaviour', *Proceedings of the 10th European Conference on Soil Mechanics and Foundation Engineering*. pp. 26–30, 1991.

[110] I. Vardoulakis, 'Shear band inclination and shear modulus of sand in biaxial tests', *Int. J. Numer. Anal. Methods Geomech.*, vol. 4, no. 2, pp. 103–119, Apr. 1980, doi: 10.1002/nag.1610040202.

[111] R. J. Finno, W. W. Harris, M. A. Mooney, and G. Viggiani, 'Shear bands in plane strain compression of loose sand', *Geotechnique*, vol. 47, no. 1, pp. 149–165, 1997, doi: 10.1680/geot.1997.47.1.149.

[112] J. R. Rice, 'The localization of plastic deformation', *14th Int. Congr. Theor. Appl. Mech.*, pp. 207–220, 1976.

[113] D. Bigoni and T. Hueckel, 'Uniqueness and localization—I. Associative and non-associative elastoplasticity', *Int. J. Solids Struct.*, vol. 28, no. 2, pp. 197–213, 1991, doi: 10.1016/0020-7683(91)90205-T.

[114] R. Kawamoto, E. Andò, G. Viggiani, and J. E. Andrade, 'All you need is shape: Predicting shear banding in sand with LS-DEM', *J. Mech. Phys. Solids*, vol. 111, pp. 375–392, Feb. 2018, doi: 10.1016/j.jmps.2017.10.003.

[115] M. Ryser, E. Kölz, A. Steiger, and Y. Schiegg, 'Gefährdungsanalyse bestehender Stützmauern', 707, 2021.

[116] T. W. Lambe and R. V. Whitman, *Soil mechanics*. New York: Wiley, 1969.

[117] S. Haefliger and W. Kaufmann, 'Corroded Tension Chord Model: Load-deformation behavior of structures with locally corroded reinforcement', *Struct. Concr.*, vol. 23, no. 1, pp. 104–120, Feb. 2022, doi: 10.1002/suco.202100165.

[118] Dassault Systèmes Simulia Corp., 'Abaqus 2019'. Johnston, RI, 2019.

[119] J. Clausen, L. Damkilde, and L. Andersen, 'An efficient return algorithm for non-associated plasticity with linear yield criteria in principal stress space', *Comput. Struct.*, vol. 85, no. 23–24, pp. 1795–1807, 2007, doi: 10.1016/j.compstruc.2007.04.002.

[120] J. Clausen, L. Damkilde, and L. V. Andersen, 'Robust and efficient handling of yield surface discontinuities in elasto-plastic finite element calculations', *Eng. Comput.*, vol. 32, no. 6, pp. 1722–1752, Aug. 2015, doi: 10.1108/EC-01-2014-0008.

[121] J. Clausen, L. Damkilde, and L. Andersen, 'Efficient return algorithms for associated plasticity with multiple yield planes', *Int. J. Numer. Methods Eng.*, vol. 66, no. 6, pp. 1036–1059, 2006, doi: 10.1002/nme.1595.

[122] Material-Archiv, 'Polyvinylchlorid ohne Weichmacher. PVC-U', 2009. www.materialarchiv.ch/detail/99 (accessed Sep. 02, 2016).

[123] Vinidex, 'PVC Properties', 2016. http://www.vinidex.com.au/technical/material-properties/pvc-properties/ (accessed Sep. 02, 2016).

[124] Kern GmbH, 'Polyvinylchlorid (PVC-U)', 2022. https://www.kern.de/de/technisches-datenblatt/polyvinylchlorid-pvc-u?n=2690_1 (accessed Feb. 02, 2022).

[125] Schweizerischer Ingenieur- und Architektenverein, 'SIA 262, Betonbau'. Zürich, 2013.

[126] J. A. Buchheister, 'Verflüssigungspotenzial von reinem und siltigem Sand unter multiaxialer Belastung', ETH Zürich, Zürich, 2009.

[127] P. Nater, 'Belastungs- und Verformungsverhalten von geschichteten Bodensystemen unter starren Kreisfundationen', ETH Zürich, Zürich, 2005.

[128] R. Kawamoto, E. Andò, G. Viggiani, and J. E. Andrade, 'Level set discrete element method for three-dimensional computations with triaxial case study', *J. Mech. Phys. Solids*, vol. 91, pp. 1–13, Jun. 2016, doi: 10.1016/j.jmps.2016.02.021.

[129] F. Oliveira, A. Freitas, P. Morais, B. Mendes, A. T. Carvalho, and J. B. Serra, 'A Travelling Sand Pluviator To Reconstruct Large Soil Specimens', *15th Int. Conf. Exp. Mech.*, 2012.

[130] A. Cresswell, M. Barton, and R. Brown, 'Determining the Maximum Density of Sands by Pluviation', *Geotech. Test. J.*, vol. 22, no. 4, pp. 324–328, 1999, doi: 10.1520/GTJ11245J.

[131] 'ASTM D4253-16 Standard Test Methods for Maximum Index Density and Unit Weight of Soils Using a Vibratory Tab.'. ASTM International, 2016. doi: 10.1520/D4253-16.

[132] F. Adjemian and P. Evesque, 'Experimental study of stick-slip behaviour', *Int. J. Numer. Anal. Methods Geomech.*, vol. 28, no. 6, pp. 501–530, May 2004, doi: 10.1002/nag.350.

[133] T. Doanh, M. T. Hoang, J. N. Roux, and C. Dequeker, 'Stick-slip behaviour of model granular materials in drained triaxial compression', *Granul. Matter*, vol. 15, no. 1, pp. 1–23, Feb. 2013, doi: 10.1007/S10035-012-0384-6.

[134] A. Ozbay and A. F. Cabalar, 'Effects of triaxial confining pressure and strain rate on stick-slip behavior of a dry granular material', *Granul. Matter*, vol. 18, no. 3, Aug. 2016, doi: 10.1007/S10035-016-0664-7.

[135] C. H. Scholz, 'Rock friction', in *The Mechanics of Earthquakes and Faulting*, Cambridge University Press, 2019. doi: 10.1017/9781316681473.

[136] W. F. Brace and J. D. Byerlee, 'Stick-Slip as a Mechanism for Earthquakes', *Science*, vol. 153, no. 3739, pp. 990–992, Aug. 1966, doi: 10.1126/science.153.3739.990.

[137] L. E. Roussel, 'Experimental investigation of stick-slip behavior in granular materials', Lousiana State University and Agricultural and Mechanical College, 2005. Accessed: Mar. 30, 2022.

[138] D. Hauswirth, 'A study of the novel approaches to soil displacement monitoring using distributed fiber optic strain sensing', ETH Zürich, 2015. doi: 10.3929/ethz-a-010476493.

[139] M. Arnold, 'Zur Berechnung des Erd- und Auflastdrucks auf Winkelstützwände im Gebrauchszustand', TU Dresden, 2004.

[140] O. Mohr, *Abhandlungen aus dem Gebiete der technischen Mechanik*. Berlin: Wilhelm Ernst & Sohn, 1906.

[141] T. Schanz, P. A. Vermeer, and P. G. Bonnier, 'The hardening soil model: Formulation and verification', in *Beyond 2000 in Computational Geotechnics*, Routledge, 1999, pp. 281–296. doi: 10.1201/9781315138206-27.

[142] P.-A. von Wolffersdorff, 'A hypoplastic relation for granular materials with a predefined limit state surface', *Mech. Cohesive-Frict. Mater.*, vol. 1, no. 3, pp. 251–271, Jul. 1996, doi: 10.1002/(SICI)1099-1484(199607)1:3<251::AID-CFM13>3.0.CO;2-3.

[143] Y. F. Dafalias and M. T. Manzari, 'Simple Plasticity Sand Model Accounting for Fabric Change Effects', *J. Eng. Mech.*, vol. 130, no. 6, pp. 622–634, Jun. 2004, doi: 10.1061/(ASCE)0733-9399(2004)130:6(622).

[144] M. Taiebat and Y. F. Dafalias, 'SANISAND: Simple anisotropic sand plasticity model', *Int. J. Numer. Anal. Methods Geomech.*, vol. 32, no. 8, pp. 915–948, Jun. 2008, doi: 10.1002/nag.651.

[145] D. Kolymbas, 'Introduction to Hypoplasticity : Advances in Geotechnical Engineering and Tunnelling 1', *Introd. Hypoplasticity*, Jan. 2000, doi: 10.1201/9781482283785.

[146] A. Eisenring, 'Numerical Study on the Soil-Retaining Wall Interaction', ETH Zurich, 2020.

[147] A. M. Puzrin, *Constitutive Modelling in Geomechanics*. Berlin, Heidelberg: Springer Berlin Heidelberg, 2012. doi: 10.1007/978-3-642-27395-7.

[148] I. Bentley Systems, 'PLAXIS V21.01 Material Models Manual', 2021.

[149] St. Pietruszczak and Z. Mróz, 'Finite element analysis of deformation of strain-softening materials', *Int. J. Numer. Methods Eng.*, vol. 17, no. 3, pp. 327–334, 1981, doi: 10.1002/nme.1620170303.

[150] I. Anastasopoulos, G. Gazetas, M. F. Bransby, M. C. R. Davies, and A. El Nahas, 'Fault Rupture Propagation through Sand: Finite-Element Analysis and Validation through Centrifuge Experiments', *J. Geotech. Geoenvironmental Eng.*, vol. 133, no. 8, pp. 943–958, Aug. 2007, doi: 10.1061/(ASCE)1090-0241(2007)133:8(943).

[151] A. Stöcklin, 'Sedimentation, Seismic Triggering and Post-failure Evolution of Submarine Landslides', ETH Zurich, Zurich, 2019. doi: 10.3929/ethz-b-000380139.

[152] V. Galavi and H. F. Schweiger, 'Nonlocal Multilaminate Model for Strain Softening Analysis', *Int. J. Geomech.*, vol. 10, no. 1, pp. 30–44, Feb. 2010, doi: 10.1061/(ASCE)1532-3641(2010)10:1(30).

[153] H. B. Mühlhaus and I. Vardoulakis, 'The thickness of shear bands in granular materials', *Geotechnique*, vol. 37, no. 3, pp. 271–283, Sep. 1987, doi: 10.1680/GEOT.1987.37.3.271.

[154] E. Andò, S. A. Hall, G. Viggiani, J. Desrues, and P. Bésuelle, 'Grain-scale experimental investigation of localised deformation in sand: a discrete particle tracking approach', *Acta Geotech.*, vol. 7, no. 1, pp. 1–13, Mar. 2012, doi: 10.1007/s11440-011-0151-6.

[155] Optum Computational Engineering, 'Optum G3'. Copenhagen NV, 2021.

[156] Y. Gao and Y. H. Wang, 'Experimental and DEM Examinations of K0 in Sand under Different Loading Conditions', *J. Geotech. Geoenvironmental Eng.*, vol. 140, no. 5, p. 04014012, May 2014, doi: 10.1061/(ASCE)GT.1943-5606.0001095.

[157] K. H. Roscoe and J. B. Burland, 'On the generalized stress-strain behaviour of "wet" clay', in *Engineering plasticity*, Cambridge, 1968, pp. 535–609.

[158] P. A. Vermeer, 'A double hardening model for sand', *Géotechnique*, vol. 28, no. 4, pp. 413–433, Dec. 1978, doi: 10.1680/geot.1978.28.4.413.

[159] L. Lampach, 'Initial stress conditions for L-shaped cantilever walls', ETH Zurich, Zurich, 2016.

[160] W. Kaufmann, 'Integrale Brücken - Sachstandsbericht', 2008.

[161] D. Santillán, E. Salete, D. J. Vicente, and M. Á. Toledo, 'Treatment of Solar Radiation by Spatial and Temporal Discretization for Modeling the Thermal Response of Arch Dams', *J. Eng. Mech.*, vol. 140, no. 11, Nov. 2014, doi: 10.1061/(ASCE)EM.1943-7889.0000801.

[162]	Y. A. Çengel and A. J. Ghajar, *Heat and mass transfer: fundamentals & applications.* Boston: McGraw-Hill, 2007.
[163]	ASHRAE, *Handbook of Fundamentals*. New York: ASHRAE, 1972.
[164]	Agroscope, 'Agrometeo', 2019. https://www.agrometeo.ch (accessed Oct. 24, 2019).
[165]	Meteo Schweiz, 'Solarenergie', 2019. https://www.meteoschweiz.admin.ch/home/klima/schweizer-klima-im-detail/solarenergie.html (accessed Oct. 31, 2019).
[166]	ub.de Fachwissen GmbH, 'photovoltaik.org - Diffuse Strahlung', 2019. https://www.photovoltaik.org/wissen/diffuse-strahlung (accessed Oct. 31, 2019).
[167]	National Oceanic and Atmospheric Administration, 'NOAA Solar Calculator', 2019. https://gml.noaa.gov/grad/solcalc/ (accessed Oct. 20, 2019).
[168]	A. Muttoni and M. F. Ruiz, 'Levels-of-Approximation Approach in Codes of Practice', *Struct. Eng. Int.*, vol. 22, no. 2, pp. 190–194, May 2012, doi: 10.2749/101686612X13291382990688.
[169]	R. L. Michalowski, Z. Wang, and S. S. Nadukuru, 'Maturing of contacts and ageing of silica sand', *Géotechnique*, vol. 68, no. 2, pp. 133–145, Feb. 2018, doi: 10.1680/jgeot.16.P.321.
[170]	Á. Kézdi, *Erddrucktheorien*. Berlin, Heidelberg: Springer Berlin Heidelberg, 1962. doi: 10.1007/978-3-642-92838-3.
[171]	'DIN EN ISO 17892-4:2017-04, Geotechnische Erkundung und Untersuchung –Laborversuche an Bodenproben –Teil 4: Bestimmung der Korngrößenverteilung'. 2017.
[172]	'DIN EN ISO 14688-1:2020-11, Geotechnische Erkundung und Untersuchung — Benennung, Beschreibung und Klassifizierung von Boden — Teil 1: Benennung und Beschreibung'. 2020.
[173]	'ASTM D4254-16 Standard Test Methods for Minimum Index Density and Unit Weight of Soils and Calculation of Relative Density'. ASTM International, 2016. doi: 10.1520/D4254-16.
[174]	J. Alabdullah, 'Testing Unsaturated Soil for Plane Strain Conditions : A New Double-Wall Biaxial Device', pp. 1–208, 2010.
[175]	F. Tatsuoka, S. Goto, and M. Sakamoto, 'Effects of Some Factors on Strength and Deformation Characteristics of Sand at Low Pressures', *Soils Found.*, vol. 26, no. 1, pp. 105–114, Mar. 1986, doi: 10.3208/sandf1972.26.105.
[176]	R. Kuerbis and Y. Vaid, 'Corrections for Membrane Strength in the Triaxial Test BT - Corrections for Membrane Strength in the Triaxial Test', pp. 361–369, 1990.
[177]	J. B. Burland, 'On the compressibility and shear strength of natural clays', *Geotechnique*, vol. 40, no. 3, pp. 329–378, 1990, doi: 10.1680/GEOT.1990.40.3.329.
[178]	X. S. Li and Y. Wang, 'Linear representation of steady-state line for sand', *J. Geotech. Geoenvironmental Eng.*, vol. 124, no. 12, pp. 1215–1217, 1998, doi: 10.1061/(ASCE)1090-0241(1998)124:12(1215).
[179]	T. Schanz and P. A. Vermeer, 'On the Stiffness of Sands', *Pre-Fail. Deform. Behav. Geomaterials*, no. JANUARY 1998, pp. 383–387, 1998, doi: 10.1143/PTPS.37.451.
[180]	B. Schmidt, 'Earth Pressures at Rest Related to Stress History', *Can. Geotech. J.*, vol. 3, no. 4, pp. 239–242, Nov. 1966, doi: 10.1139/t66-028.
[181]	R. Baker, 'Nonlinear Mohr Envelopes Based on Triaxial Data', vol. 130, no. May, pp. 1–9, 2004.
[182]	M. Maksimovic, 'Nonlinear Failure Envelope for Soils', *J. Geotech. Eng.*, vol. 115, no. 4, pp. 581–586, Apr. 1989, doi: 10.1061/(ASCE)0733-9410(1989)115:4(581).
[183]	K. L. Lee and H. B. Seed, 'Drained Strength Characteristics of Sands', *J. Soil Mech. Found. Div.*, vol. 93, no. 6, pp. 117–141, Nov. 1967, doi: 10.1061/JSFEAQ.0001048.
[184]	M. D. Bolton, 'The strength and dilatancy of sands', *Géotechnique*, vol. 36, no. 1, pp. 65–78, 1986, doi: 10.1680/geot.1986.36.1.65.
[185]	S. Fukushima and F. Tatsuoka, 'Strength and Deformation Characteristics of Saturated Sand at Extremely Low Pressures', *Soils Found.*, vol. 24, no. 4, pp. 30–48, Dec. 1984, doi: 10.3208/sandf1972.24.4_30.
[186]	R. J. Fannin, A. Eliadorani, and J. M. T. Wilkinson, 'Shear strength of cohesionless soils at low stress', *Géotechnique*, vol. 55, no. 6, pp. 467–478, 2005, doi: 10.1680/geot.2005.55.6.467.
[187]	Z. Cabarkapa, 'Discussion: Shear strength of cohesionless soils at low stress', *Géotechnique*, vol. 56, no. 6, pp. 439–441, Aug. 2006, doi: 10.1680/geot.2006.56.6.439.
[188]	K. E. Winters, O.-D. S. Taylor, W. W. Berry, W. R. Rowland, and M. D. Antwine, 'Cohesionless Soil Fabric and Shear Strength at Low Confining Pressures', in *Geo-Chicago 2016*, Reston, VA, Aug. 2016, pp. 212–221. doi: 10.1061/9780784480151.022.
[189]	K. A. Alshibli and M. B. Cil, 'Influence of particle morphology on the friction and dilatancy of sand', *J. Geotech. Geoenvironmental Eng.*, vol. 144, no. 3, pp. 1–12, 2018, doi: 10.1061/(ASCE)GT.1943-5606.0001841.
[190]	J. M. Harmon, 'Predicting the Strength of Planetary Surfaces', Caltech, Pasadena, California, 2022.
[191]	J. P. De Bono and G. R. McDowell, 'DEM of triaxial tests on crushable sand', *Granul. Matter*, vol. 16, no. 4, pp. 551–562, Apr. 2014, doi: 10.1007/S10035-014-0500-X/FIGURES/14.
[192]	D. Shi, L. Zheng, J. Xue, and J. Sun, 'DEM Modeling of Particle Breakage in Silica Sands under One-Dimensional Compression', *Acta Mech. Solida Sin.*, vol. 29, no. 1, pp. 78–94, Feb. 2016, doi: 10.1016/S0894-9166(16)60008-3.
[193]	Z. Zhu, J. Wang, and M. Wu, 'DEM simulation of particle crushing in a triaxial test considering the influence of particle morphology and coordination number', *Comput. Geotech.*, vol. 148, Aug. 2022, doi: 10.1016/J.COMPGEO.2022.104769.
[194]	J. M. Harmon, D. Arthur, and J. E. Andrade, 'Level set splitting in DEM for modeling breakage mechanics', *Comput. Methods Appl. Mech. Eng.*, vol. 365, Jun. 2020, doi: 10.1016/J.CMA.2020.112961.

[195] J. Gao, W. D. Luedtke, D. Gourdon, M. Ruths, J. N. Israelachvili, and U. Landman, 'Frictional Forces and Amontons' Law: From the Molecular to the Macroscopic Scale', *J. Phys. Chem. B*, vol. 108, no. 11, pp. 3410–3425, Mar. 2004, doi: 10.1021/jp036362l.

[196] H. M. Horn and D. U. Deere, 'Frictional characteristics of minerals', *Geotechnique*, vol. 12, no. 4, pp. 319–335, 1962, doi: 10.1680/GEOT.1962.12.4.319.

[197] M. H. Müser, L. Wenning, and M. O. Robbins, 'Simple Microscopic Theory of Amontons's Laws for Static Friction', *Phys. Rev. Lett.*, vol. 86, no. 7, pp. 1295–1298, Feb. 2001, doi: 10.1103/PhysRevLett.86.1295.

[198] N. S. El-Nasrallah, 'Shear Strength of A Cohesionless Soil Under Plane Strain and Triaxial Conditions', McMaster University, Hamilton, Ontario, 1976.

[199] F. Tatsuoka, M. Sakamoto, T. Kawamura, and S. Fukushima, 'Strength and Deformation Characteristics of Sand in Plane Strain Compression at Extremely Low Pressures', *Soils Found.*, vol. 26, no. 1, pp. 65–84, Mar. 1986, doi: 10.3208/sandf1972.26.65.

[200] A. Hanna, 'Determination of plane-strain shear strength of sand from the results of triaxial tests', *Can. Geotech. J.*, vol. 38, no. 6, pp. 1231–1240, Dec. 2001, doi: 10.1139/t01-064.

[201] P. W. Rowe, 'The Relation Between the Shear Strength of Sands in Triaxial Compression, Plane Strain and Direct', *Géotechnique*, vol. 19, no. 1, pp. 75–86, Jan. 1969, doi: 10.1680/geot.1969.19.1.75.

[202] D. V. Griffiths and J. Huang, 'Observations on the extended Matsuoka-Nakai failure criterion', *Int. J. Numer. Anal. Methods Geomech.*, vol. 33, no. 17, pp. 1889–1905, Dec. 2009, doi: 10.1002/nag.810.

Project completion

Schweizerische Eidgenossenschaft
Confédération suisse
Confederazione Svizzera
Confederaziun svizra

Eidgenössisches Departement für
Umwelt, Verkehr, Energie und Kommunikation UVEK
Bundesamt für Strassen ASTRA

FORSCHUNG IM STRASSENWESEN DES UVEK
Version vom 09.10.2013
Formular Nr. 3: Projektabschluss

erstellt / geändert am: 08.12.2022

Grunddaten

Projekt-Nr.:   AGB 2015/029

Projekttitel: Failure Behaviour of Cantilever Retaining Walls. Soil-Retaining Wall Interaction

Enddatum: 31.03.2023

Texte

Zusammenfassung der Projektresultate:

Das Ziel dieses Projektes war ein verbessertes und quantitatives Verständnis der Erddruckeinwirkung auf durch Bewehrungskorrosion geschwächte Winkelstützmauern. Es wurden analytische, numerische und experimentelle Analysen durchgeführt, um den Verlauf des Erddrucks von der Errichtung der Wand bis zum Zeitpunkt eines möglichen Einsturzes zu quantifizieren.

Zuerst wurden die gängigsten Erddrucktheorien und Bemessungsmethoden besprochen. Der relevante Versagensmodus für korrosionsgeschädigte Winkelstützmauern wurde dann identifiziert und analysiert: Ein rigoroses Nachweisverfahren wurde für den Grenzzustand der Tragfähigkeit vorgeschlagen. Darauf aufbauend werden die konventionellen Methoden analysiert und bewertet.

Der massgebende Versagensmodus wurde in massstäblichen Experimenten weiter untersucht, bei denen verschiedene Anfangsspannungsbedingungen und Bodenparameter untersucht wurden. Zunächst wurden ebene Dehnungsbedingungen untersucht. Dann wurde es gezeigt, wie eine inhomogene Verteilung des Korrosionsgrads zu eine Spannungsumlagerung in der Hinterfüllung und folglich zu tiefere Erddrücke auf dem geschädigten Wandabschnitt führen kann. Darüber hinaus wurden die Anfangsspannungsbedingungen für den Fall einer nahezu starren Wand untersucht. Basiert auf experimentellen Beobachtungen und allgemein bekannten Stoffgesetzen wurde ein numerisches Framework zur Quantifizierung des Erddrucks auf Winkelstützmauern entwickelt. Das Framework ist allgemein anwendbar und liefert zuverlässige Ergebnisse, da er anhand experimenteller Daten validiert wurde. Darüber hinaus wurde das "Level Set Discrete Element Method" verwendet, um den Erdruhedruckkoeffizienten zu analysieren.

Schliesslich wurden die entwickelten numerischen Modelle auf einige Fallstudien angewandt. Beispielsweise wurden die Auswirkungen zyklischer Temperaturänderungen simuliert und diskutiert, wobei die Auswirkungen auf die Wandüberwachung berücksichtigt werden. Zum Schluss wurden die Ergebnisse aus dem aktuellen Projekt und dem AGB 2015/028 kombiniert, um eine Nachweisstrategie für Winkelstützmauern vorzuschlagen, die auch allgemeine Rückschlüsse auf dem Bruchverhalten von korrosionsgeschädigten Wänden ermöglichte.

Schweizerische Eidgenossenschaft
Confédération suisse
Confederazione Svizzera
Confederaziun svizra

Eidgenössisches Departement für
Umwelt, Verkehr, Energie und Kommunikation UVEK
Bundesamt für Strassen ASTRA

Zielerreichung:

Die Zielsetzungen dieses Forschungsprojekt wurden erreicht. Die experimentelle Studie lieferte sehr zuverlässige Ergebnisse mit einem hohen Detaillierungsgrad und ermöglichte eine eingehende Analyse des Entlastungsprozesses von korrosionsgeschädigten Wänden. Die erzielten Ergebnisse ermöglichten den Aufbau eines zuverlässigen Frameworks, das für die Bewertung von Wänden in der Praxis verwendet werden kann.
Im Laufe des Projekts stellte die Forschungsstelle fest, dass einige Aspekte mehr Aufmerksamkeit erforderten, und beschloss, mit Zustimmung der Begleitkommission zusätzliche Analysen durchzuführen (z. B. die Analysen zum initialen Spannungszustand und die Analysen mit dem Level Set Discrete Element Method).
Zusätzlich wurde das Thema der Temperatureinflüsse auf Wunsch der Begleitkommission tiefer untersucht.

Folgerungen und Empfehlungen:

Diese Arbeit beschreibt den korrosionsbedingten Entlastungsprozess der Wände in einem mechanisch konsistenten Rahmen. Das Ergebnis dieser Arbeit ist ein verbessertes Wissen, das zur Bewertung der Sicherheit von Wänden auf einer umfassenden Ebene (d. h. zur Identifizierung der kritischsten Wände), zur Planung von Verstärkungsmaßnahmen und zur Entwicklung von Überwachungsstrategien verwendet werden kann.

Für eine umfassende Überprüfung der Stabilität von Winkelstützwänden auf nationaler Ebene, kann aufgrund der Variabilität der Boden- und Wandeigenschaften sowie der Anfangsspannungsbedingungen in der Hinterfüllung der Wände ein probabilistischer Ansatz angewendet werden, um zuverlässigere Ergebnisse zu gewährleisten.

Publikationen:

D. Perozzi, "Quantification of the earth pressure acting on corrosion-damaged cantilever retaining walls: An analysis of the soil-structure interaction", Doctoral thesis, ETH Zurich, 2022.

Weitere Publikationen in akademischen Fachzeitschriften sind geplant.

Der Projektleiter/die Projektleiterin:

Name: Puzrin   Vorname: Alexander M.

Amt, Firma, Institut: ETH Zürich, Institut für Geotechnik

Unterschrift des Projektleiters/der Projektleiterin:

Schweizerische Eidgenossenschaft
Confédération suisse
Confederazione Svizzera
Confederaziun svizra

Eidgenössisches Departement für
Umwelt, Verkehr, Energie und Kommunikation UVEK
Bundesamt für Strassen ASTRA

FORSCHUNG IM STRASSENWESEN DES UVEK

Formular Nr. 3: Projektabschluss

Beurteilung der Begleitkommission:

Beurteilung:

Die Begleitkommission beurteilt das Forschungsprojekt, den Schlussbericht und die darin enthaltenen Daten und Folgerungen als sehr positiv. Nach einem kurzen Überblick zu in der Praxis üblichen Theorien für Erddruck und Bemessung von Winkelstützmauern, werden Theorie und numerische Modellierung von Einwirkungen, Verformungsverhalten und Traglast von Winkelstützmauern dargestellt und mit Resultaten von Versuchen in reduziertem Massstab im Labor verglichen. Mit weiteren numerischen Modellierungen wird zudem der Einfluss verschiedener Parameter untersucht, welche in den Versuchen nicht simuliert werden konnten. Der Bericht wird abgeschlossen mit einem "Level of Approximation" Vorgehen für die Beurteilung der Sicherheit von Winkelstützmauern. Die Zielsetzungen des Projekts wurden vollumfänglich erfüllt.

Umsetzung:

Der Schlussbericht gibt detaillierte Verfahren und Vorgehen für die Beurteilung der Einwirkungen (Erddruck), des Verformungsverhaltens und der Tragsicherheit von Winkelstützmauern in der Praxis. Es wird ein "Level of Approximation" Vorgehen für die Beurteilung der Sicherheit von Winkelstützmauern gegeben, welches sich je nach Stand der Kenntnisse der Parameter eines bestimmten Projektes anwenden und stufenweise verfeinern lässt.

weitergehender Forschungsbedarf:

Die Untersuchungen im Projekt zeigen auf, dass die globalen Verformungen (Auslenkung der Wand oder deren Oberkante) wohl nicht als Monitoring-Methode geeignet sind, um die Sicherheit von Winkelstützmauern zu beurteilen. Es besteht Bedarf, andere Monitoring-Methoden zu finden und zu bestätigen.

Einfluss auf Normenwerk:

Die Angaben in SIA 267, SIA 269/7 und in Wegleitungen / Richtlinien für Winkelstützmauern sollten überprüft und wo erforderlich entsprechend der Folgerungen und Empfehlungen dieses Projekts aktualisiert werden.

Der Präsident/die Präsidentin der Begleitkommission:

Name: Ganz   Vorname: Hans Rudolf

Amt, Firma, Institut: GANZ Consulting

Unterschrift des Präsidenten/der Präsidentin der Begleitkommission:

Acknowledgements